MOTIVATION FOR FUTURE ATMOSPHERIC MEASUREMENTS FOR THE EXPLORATION OF MARS AND TITAN

ELISA DONG

A DISSERTATION SUBMITTED TO THE FACULTY OF GRADUATE STUDIES
IN PARTIAL FULFILMENT OF THE REQUIREMENTS
FOR THE DEGREE OF

DOCTOR OF PHILOSOPHY

GRADUATE PROGRAM IN EARTH AND SPACE SCIENCE
YORK UNIVERSITY
TORONTO, ONTARIO

JULY 2026

© ELISA DONG, 2026

Abstract

The atmosphere is the interface between the planetary surface and space. A strategically placed instrument at the surface of a planetary body can provide insight into the present day atmospheric dynamics of the planet and context for past and present processes. In this dissertation, I demonstrate how a single instrument can be used to constrain the movement of trace gases and characterize impactors entering a planetary atmosphere.

The formation, transport, and removal of methane in the Martian atmosphere remains difficult to explain. The first part of this dissertation explores the spatial variaibility of methane in a Martian analog environment for methane microseepage as part of the ongoing development of new methane spectrometers for Mars. I found that the current resolution of the sole methane spectrometer on the surface of Mars is sufficient to measure methane spatial variability as observed at the analog site over a few meters. Second, I simulated the transport of methane in the Martian atmosphere at Gale Crater using three different atmospheric models and estimated the required methane flux from the surface to satisfy the existing surface measurements. I incorporated a recently characterized rapid methane destruction mechanism that relies on the presence of UV-activated perchlorate. Perchlorate is expected to be distributed on dust throughout the atmosphere. I found that it was generally possible for the methane concentration in the atmospheric column observable from orbit to fall below the observational limit.

The history of impactors on Titan is not well constrained, in part due to the lack of data and distance of Titan from Earth. The final project in this dissertation takes place on Titan, where I leverage the meteorological instrument package on the upcoming Dragonfly mission to evaluate whether airbursts from outer solar system comets would be detectable by the changes in pressure and seismic coupling at the surface. I found that they were generally within observational limits by both the pressure sensor and seismometer. Observations of such airbursts may revise our understanding of the outer solar system.

Dedication

To the dreamers and the doers.

Acknowledgements

I'd like to acknowledge my two wonderful co-supervisors, Dr. Catherine Neish and Dr. John Moores for their patience, curiosity, and mentorship. Working with them has been an incredible experience of push and pull. Despite the challenges of my degree and external complications, they were always supportive of my well-being and my academic career. I had the good fortune in dabbling in many side projects that did not all come to fruition during my term, knowing that science is not always a straight path forward. This dissertation could only happen because of your support, thank you!

As for my fellow lab mates, past and present, y'all are awesome. Words cannot express how grateful I am for you all. Roadtrips to London, icecream downtown, plant browsing weekends, lunch under the trees, scribbling away at whiteboards, tagging along for silly ideas, letting me know when they're too silly... It has been an honour and a pleasure. Thank you!

I'd like to acknowledge a few of the other mentors I have gained along the way, Ralph Lorenz for providing guidance on work and keen insight into my methods, Elizabeth Silber for extended applications of my work, Benjamin Fernando on math and fun, and Charles-Édouard Boukarée on research pivots in the future. For those that took the time to chat with me at meetings and conferences, thank you!

The time during my PhD was not solely academic. I'd like to thank the Founder's captains, Matthew, Reilly, and Quinton for having good heads on their shoulders. To those who worked on making the workplace better for all of us, Marcelle-Anne, James, and Matthew, thank you. To the friends that have stuck around through the worst of times, Max, James, Joshua, Catheryn, and the RPG friends to take my mind off things, Jamie, James, Rachel, Lukas, Thomas, Ryan, Nathan, Sophie, and countless others, thank you! To my parents and grandparents that sacrificed much of their lives so I could explore my interests and to my brother that takes care of my pets when I'm gone for extended periods without complaining, thank you! To Mauritz, who was with me every step of the way, has an uncanny knack of always picking up when a car issue pops up, and for providing cats, thank you!

I would have struggled far harder during my degree without animal companionship. I'd like to acknowledge Grizabella who trusted me enough to patiently brush out mats towards the end, Calypso, for suddenly becoming cuddly when I'm feeling down, Paisley, for demonstrating inertia and demonstrating incredible focus, and Edith, for keeping me company during the first year. Over the last two years, I've seen Xavion, Spicy, Froggy, Katana and Wheelbarrow become adults. It has been rewarding seeing them grow and become comfortable in my space.

Lastly, I want to acknowledge those who contributed to the financial support of my degree. I received support from both the Carswell Family Foundation and the Dr. Diane Michelangi Memorial Scholarship. To the folks over at NSERC, thank you for thinking some of my ideas are worth supporting. These awards support the research of scientists like myself. Alongside the direct support, I'd like to thank the Writing Centre, especially Ali Hadidi, for helping me communicate my ideas on paper. Thank you all!

Table of Contents

Abstract . . . . . **ii**

Dedication . . . . . **iii**

Acknowledgements . . . . . **iv**

Table of Contents . . . . . **vi**

List of Tables . . . . . **ix**

List of Figures . . . . . **x**

1 Introduction **1**

1.1 Motivation 1

1.2 A Brief Overiew of Mars 2

1.2.1 Gale Crater, Curiosity Rover Atmospheric Measurements 4

1.2.2 Methane on Mars 6

1.2.3 The Need for a Fast Methane Destruction Mechanism 10

1.2.4 Martian Methane Microseepage Analog 13

1.3 An Overview to Titan 15

1.4 The Dragonfly Mission 16

1.4.1 Titan's Atmospheric and Surface Properties 17

1.4.2 Impactors in the Solar System 19

1.4.3 Modelling Meteors 21

1.5 Summary and Overview of Dissertation 21

2 Methane in the Arctic **23**

2.1 Introduction 24

2.2 Methods 24

2.2.1 Site Description and Sample Procedure 24

2.2.2 2022 Sample Campaign 26

2.2.3 2023 Sample Campaign 27

2.2.4 2024 Sample Campaign 27

2.2.5 Quick-Look Analysis . . . 29
2.2.6 Data Processing . . . 30
2.3 Results . . . 31
2.3.1 2022 Sample Campaign . . . 31
2.3.2 2023 Sample Campaign . . . 32
2.3.3 2024 Sample Campaign . . . 37
2.4 Discussion . . . 39
2.4.1 Spatial Variability . . . 39
2.4.2 Implications for Martian Methane Sampling . . . 42
2.5 Conclusions . . . 43

3 Martian Methane Diffusion and Destruction . . . 44
3.1 Introduction . . . 45
3.1.1 Zhang et al. (2022)'s Methane and Perchlorate Experiment . . . 46
3.1.2 Goal of this Work . . . 47
3.2 Methods . . . 47
3.2.1 1D Diffusion in the Vertical Diffusion Model (VDM) . . . 48
3.2.2 Box Modelling - 10 km to the Exobase . . . 63
3.3 Results . . . 64
3.3.1 Methane Flux Estimates . . . 65
3.3.2 Diurnal Methane Variability . . . 68
3.3.3 Methane At and Above 10 km . . . 74
3.3.4 Plume Dissipation . . . 76
3.3.5 Effect of the Destruction Mechanism . . . 78
3.4 Discussion and Implications . . . 82
3.4.1 Eddy Diffusivity Coefficients . . . 83
3.4.2 Plumes of Methane . . . 85
3.4.3 Model Limitations . . . 86
3.4.4 Gale Crater as a Proxy for All of Mars . . . 87
3.4.5 Atmospheric Mixing in the Daytime . . . 88
3.5 Conclusions . . . 89

4 Titan Airbursts . . . 91
4.1 Introduction . . . 92
4.2 Methods . . . 96
4.2.1 Meteor Properties . . . 101
4.2.2 Overpressure Estimations . . . 103
4.2.3 Seismic Response . . . 110
4.3 Simulation Results . . . 112
4.3.1 Burst Heights . . . 112

4.3.2 Overpressure Estimations . . . 117
4.3.3 Travel Times and Signal Length . . . 121
4.3.4 Additional Peaks . . . 123
4.3.5 Overpressure Estimations using iSALE-2D . . . 124
4.3.6 Seismic Response . . . 125
4.4 Discussion . . . 128
4.4.1 Overpressure . . . 129
4.4.2 Seismicity . . . 132
4.4.3 Applications to DraGMet . . . 133
4.5 Conclusions and Future Work . . . 135

5 Conclusions . . . 136

6 Future Work . . . 139
6.1 Next Steps in Understanding Martian Methane . . . 139
6.2 Next Steps in Undestanding Airbursts in Titan's Atmosphere . . . 141

References . . . 143

Appendices . . . 170

A Atmospheric Dynamics and Eddy Diffusivity . . . 170
A.1 Dynamical Atmospheric Modelling Theory . . . 170
A.1.1 GEM-Mars . . . 172
A.1.2 1D University Helsinki/Finnish Meteorological Institute (1D UH/FMI) Model 173
A.1.3 Laboratoire de Météorologie Dynamic Mars GCM - The LMD Model . . . 173

B Effect of Varying Dust Distributions for Methane Diffusion and Destruction . 174
B.1 Varying Dust Distributions . . . 174
B.2 Discussion of Dust Profiles . . . 178

List of Tables

2.1 Polygon 1 sample methane data from 2023 30

3.1 Distribution of selected levels for the VDM. 50
3.2 SAM-TLS enriched measurements of methane acquired over MY32 - 34 53
3.3 Number of mie particles as retrieved from the radiative transfer model 57
3.4 Estimated surface flux E_0 required to match enriched SAM-TLS measurements at the surface in units of $kg/m^2/sol$ 66

4.1 Initiating parameters for the Separate Fragments Model. 103
4.2 Average compressional velocities of common materials on Earth and approximate Martian regolith and bedrock properties 112

List of Figures

1.1 Mars' orbit around the Sun . . . 3
1.2 Curiosity rover landing ellipse and Gale Crater . . . 4
1.3 Key Martian methane measurements . . . 6
1.4 Theoretical Methane Sources and Sinks . . . 7
1.5 SAM-TLS and ACS Measurements of Methane in and near Gale Crater . . . 9
1.6 Map of Axel Heiberg Island with sources of methane . . . 14
1.7 Approximate Dragonfly landing ellipse and context . . . 17
1.8 Density profile of Titan's atmosphere as measured by HASI during descent. Data from Fulchignoni et al. (2005). . . . 19

2.1 Illustration of hypothetical polygonal feature cross section. . . . 25
2.2 Google maps overview of the polygonal terrain next to Colour Lake. . . . 26
2.3 Sample point schematic for Polygon 2 in the 2024 field campaign as recorded by the operator. . . . 28
2.4 Photo taken of 2024 field site . . . 29
2.5 Raw data for sample site Polygon 1 and running averages . . . 30
2.6 Polygon A 2022 location and methane measurements . . . 31
2.7 Relative methane concentration differences for Polygon A with data taken in 2022. . . . 32
2.8 Drone images of sample sites Polygons 1-4 . . . 33
2.9 Methane concentrations for polygon sample sites taken during the 2023 field campaign 34
2.10 Relative methane concentration plotted as a function of distance from the polygon centers. . . . 36
2.11 Relative methane concentration for Polygons 1 – 4 and Polygon A (2023 data) plotted as a function of distance from the polygon centers. . . . 37
2.12 Polygon 2a and 2b mean methane measurements from the 2024 dataset. . . . 38
2.13 Relative methane concentration to the center measurement for Polygon 2a and 2b as taken in 2024. . . . 39

3.1 VDM time steps . . . 52
3.2 Various Conrath profiles . . . 56
3.3 Eddy diffusion profiles from three atmospheric models . . . 58
3.4 Eddy diffusion throughout a sol from three atmospheric models . . . 59

3.5 Methane concentration at 1 m for three different atmospheric models targeting the SAM-TLS value . . . 65
3.6 Methane fluxes required to achieve SAM-TLS values . . . 68
3.7 Methane concentration at 1 m altitude and in the box model - well-mixed dust profile 70
3.8 Example of methane concentration at 10 km and in the box model for stability . . . 71
3.9 Methane concentration throughout the VDM over $L_s = 30°$ and 220° . . . 72
3.10 Methane concentration throughout the VDM over $L_s = 30°$ and 220° - specified altitudes . . . 73
3.11 Maximum methane concentration above 10 km. . . . 75
3.12 Simulated methane plume of 21 ppbv 10 m in height for $L_s = 30°$ and $L_s = 70°$. . . . 77
3.13 Relative methane in VDM without destruction. . . . 79
3.14 Relative methane in VDM without destruction over 7 sols. . . . 81
3.15 Methane concentration at 1 m above the surface and suggested measurement time at 1500 LTST . . . 89

4.1 Meteor entry geometry . . . 98
4.2 Energy release curve example . . . 100
4.3 Temperature and pressure profile used in iSALE . . . 106
4.4 Illustration of the overpressure pulse from a point source . . . 108
4.5 Energy release curve examples and meteor trajectories . . . 113
4.6 Burst height at a variety of incoming meteor incident angles, radii, and strengths for an incident velocity of $v = 11\ \mathrm{km\,s^{-1}}$ and $\rho = 500\ \mathrm{kg\,m^{-3}}$ . . . 114
4.7 Energy release curves for varying incidence angles with increasing incident strength. 115
4.8 Examining the relationship between entry velocity and burst height. . . . 116
4.9 Examining the relationship between density and burst height. . . . 117
4.10 Estimates of burst energy . . . 118
4.11 Overpressures for variable velocities, strength, and radius with all other variables fixed at incident angle $a = 45°$, density $\rho = 500\ \mathrm{kg\,m^{-3}}$. . . . 119
4.12 Overpressures with varying incident angle, initial strength, and radius with fixed velocity $v = 11\ \mathrm{km\,s^{-1}}$ and density $\rho = 500\ \mathrm{kg\,m^{-3}}$ . . . 120
4.13 Overpressures with varying incident angle, initial strength, and radius with fixed velocity $v = 11\ \mathrm{km\,s^{-1}}$ incident angle $a = 45°$. . . . 121
4.14 Overpressure signal length for the positive phase . . . 123
4.15 Example of energy release curve with two apparent airburst peaks . . . 124
4.16 Peak vertical velocity of the surface . . . 126
4.17 Vertical velocity for varying surface density ρ_s and surface P-wave velocity V_p . . . 127
4.18 Vertical velocity generated for a wet sand surface using an exponentially decaying function . . . 128
4.19 Peak overpressure fall-off with increasing horizontal distance from burst . . . 130

B.1 Methane concentration 1at m altitude and in the box model - Conrath profile of $\nu = 3175$
B.2 Difference between the well-mixed dust profile and the Conrath profile for the GEM-Mars atmospheric model. 177
B.3 Difference between the well-mixed dust profile and the Conrath profile for the 1D UH/FMI and LMD atmospheric models. 178

Chapter 1

Introduction

1.1 Motivation

Understanding of planetary atmospheres and how particles propagate through them is part of investigating other planetary bodies. The atmosphere is often the most accessible part of a planet to observe and sample to learn about the planet, both remotely and via landed missions. Light transmitted through the atmosphere can be used identify atmospheric composition from their unique spectral signatures from the surface, orbit, and telescopes from Earth. Instruments at the surface and remote observations can be used to track trace gases, such as methane, as they are diffused in varying climate conditions to understand their sources and sinks. Sounds and pressure waves can transfer signatures of short-lived phenomena such as wind gusts and airbursts. Investigations of the atmosphere provide insight not only into the processes taking place within the atmosphere, but also the surface and atmospheric interactions such as the rate of gas exchange and transfer of shockwaves through the atmosphere/surface interface.

In this dissertation, I study the atmospheres of Earth, Mars, and Saturn's moon Titan. I consider the seismoacoustic signatures of bolides in Titan's atmosphere, the potential methane destruction mechanisms on Martian atmospheric methane, and application of methane detection instrumentation for a future Martian mission in the context of an analog study in the Arctic. The work in the dissertation is a blend of theoretical modelling to describe processes in the atmosphere and analog research to further the development of future mission instruments.

In this chapter, I provide an overview to Mars' present day atmosphere, the Curiosity rover and Gale Crater site selection, a history of methane measurements on Mars, and previous efforts to reconcile spatiotemporal methane variability. Additionally, I include a short background to the Martian methane microseepage analog studied in Chapter 2 that takes place at the polygonal terrain in the Canadian Arctic. Following the section on Mars, I highlight key characteristics of Titan that make it a compelling location for investigation and provide an overview to estimates of impacts on Titan's surface. I then provide an explanation for how the upcoming Dragonfly mission will have relevant instruments for detecting airbursts to further our knowledge of impactors in the outer Solar System.

1.2 A Brief Overiew of Mars

The present day Martian atmosphere is predominantly carbon dioxide (95.3%), with low concentrations of nitrogen, argon, and oxygen (2.7%, 1.6%, and 0.1%, respectively). The atmosphere also includes trace levels of water vapour (210 ppm) and methane (sub-ppm levels) (Owen et al., 1977, Moroz, 1998, Trainer et al., 2019, Vandaele et al., 2024, NAS, 2020). The thickness of the Martian atmosphere and its composition changes throughout a Martian year as the polar icecaps respond to solar forcing. Carbon dioxide gas falls as snow at the poles during the winter and sublimates in spring and summer (Jakosky and Farmer, 1982, Hayne et al., 2014). During this process, up to 30% of the atmosphere is solidified as it comes out of gaseous form (James et al., 1992). Overall, the atmosphere of Mars is significantly thinner than that of Earth's, with a mean surface pressure of only 6.1 mbar (Haberle, 2015). Naturally, the surface pressure varies depending on altitude, with higher altitudes corresponding to lower surface pressures. The average temperature of the atmosphere near the surface of Mars is 210 K, with a strong diurnal variability (NAS, 2020).

Due to its elliptical orbit (eccentricity ~ 0.094), the seasons on Mars have varying lengths. Furthermore, Mars has an axial tilt of 25°, leading to opposing seasons on the Northern and Southern hemisphere. The seasons on Mars can be divided into various L_s, where L_s is the solar longitude in degrees and denotes the relative position of Mars in orbit around the Sun. Similar to Earth, the seasons are made in reference to the relevant hemisphere. For example, northern summer takes place at the same time as southern winter. Furthermore, times of year on Mars can fall into Dust Storm Season, when the atmosphere tends to be more dusty and localized dust storms may become regional and global dust storms, and Aphelion Cloud Belt Season, when a characteristic belt of clouds forms near the equator around aphelion. Dust Storm Season typically falls into $L_s = 140°$ to 250°, though there are secondary and tertiary seasons as well (Kass et al., 2016, Battalio and Wang, 2021), whereas Aphelion Cloud Belt Season is well defined and falls between $L_s = 150°$ and 180°(Smith, 2008).

Aphelion, when Mars is the farthest from the Sun and receives the least solar insolation, takes place around $L_s = 71°$ (Fig. 1.1). Perihelion, when Mars is the closest to the Sun, takes place at $L_s = 251°$. During perihelion, the proximity of the Sun corresponds to an increase in solar flux and additional energy available on Mars.

A full Martian year corresponds to 668 sols ($\sim$ 688 Earth days), where each sol is 24 hours and 39 minutes and 35.244 Earth seconds long. Further references to Martian Year (MY) use the conventional start of MY 1 to take place on April 11, 1955 (Clancy et al., 2000). Time keeping on Mars can be represented by the local mean solar time (LMST), where the Sun is assumed to have a uniform motion across the celestial equator. Alternatively, time can be described using local true solar time (LTST) where the mean Sun corresponds to the Sun elevation (e.g. 1200 LTST is when the Sun is highest in the sky). The difference between the two time keeping conventions typically is less than 1 hour at any given time.

Dust lifting on Mars is not uncommon, as numerous dust devils and dust storms have been observed there. Dust Storm season corresponds to the time of year where regional and even global

dust storms tend to occur. These storms lift dust between 40 and 70 km in altitude (Martín-Rubio et al., 2025). During the non-dusty season, there is still suspended dust closer to the surface, and detached haze layers that correspond to dust around 20 - 40 km above the surface (Heavens et al., 2011, Guzewich et al., 2013, Määttänen et al., 2013).

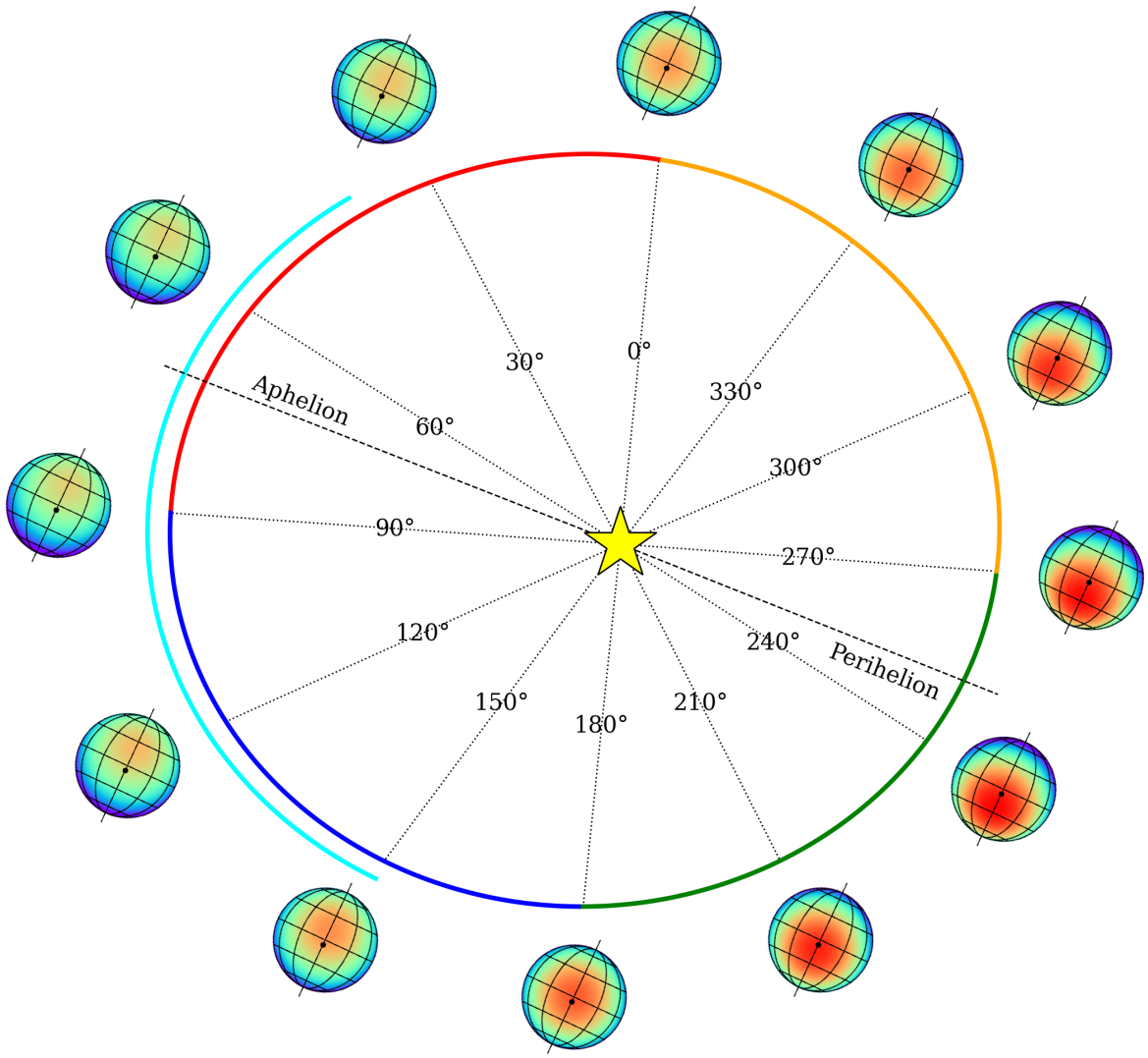


Figure 1.1: Mars' orbit around the Sun and corresponding L_s. The different colours along the orbital path correspond to the southern seasons as experienced by the Curiosity rover shown by the black dot (green: spring, yellow: summer, red: fall, blue: winter). The light blue arc corresponds to aphelion cloud belt season. Image provided by: Diana Hayes.

The planetary boundary layer (PBL) on Mars is the atmospheric layer closest to the surface and responds to surface changes. Within the PBL, momentum transfer is assumed to be due to drag forces from the atmospheric motion interacting with the surface, resulting in instabilities that lead to turbulent motion (Petrosyan et al., 2011). These instabilities arise from wind shear and surface

heating that transport momentum and atmospheric constituents such as trace gases. Within the PBL, dust is often assumed to be well-mixed (e.g. Guzewich et al. (2017)). Typically, one can assume the PBL ranges between 1-10 km on Mars (Petrosyan et al., 2011, Hinson et al., 2008). However, the PBL varies seasonally and diurnally and can be as thin as a few meters at night (Guzewich et al., 2017, Smith et al., 2006, Savijäärvi, 2012). Understanding the PBL is important, as it is the atmospheric layer in which landers and rovers take measurements from. For Mars, orbital measurements of methane, the topic of two chapters in this dissertation, typically do not observe sufficiently far down enough to observe the PBL.

1.2.1 Gale Crater, Curiosity Rover Atmospheric Measurements

Gale Crater was the selected landing site for the Curiosity rover due to the potential for observing different geological layers exposed at the surface. Additionally, clay layers were detected that possibly have evidence of past and present life (Grotzinger et al., 2012). The landing ellipse itself consists of several fluvial features such as alluvial fans (Grotzinger et al., 2012) (Fig. 1.2). Since landing, Curiosity has been gradually driving up Mount Sharp (Olympus Mons) and increasing in altitude. This has lead to changes to atmospheric pressure, air temperature, and relative humidity as Curiosity continues to drive. However, the biggest driver of variability for temperature is dust in the atmosphere (Martín-Rubio et al., 2025).

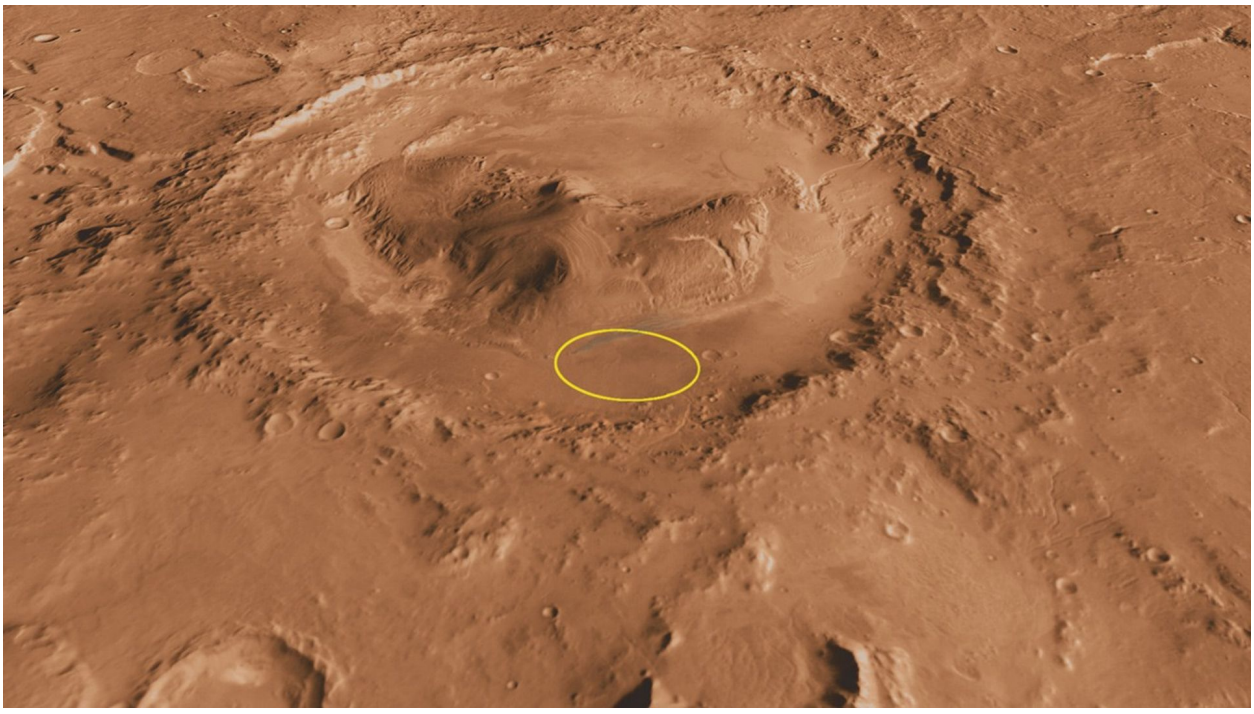


Figure 1.2: Gale Crater shown with Curiosity rover landing site ellipse marked in yellow. The dimensions of the ellipse correspond to 20 km by 25 km. Source: NASA/JPL-Caltech/ASU/UA

Since landing on Aug 5, 2012, Curiosity rover has travelled a total of 36860 m (as of Sol

4908, or May 27, 2026). Curiosity is equipped with meteorological equipment - the Rover Environmental Monitoring Station, REMS, that consists of temperature, pressure, UV, and wind sensors. Temperature and pressure changes have been documented throughout the duration of the mission (Gómez-Elvira et al., 2012, Gõmez-Elvira et al., 2014, Harri et al., 2014, naki Ordonez-Etxeberria et al., 2018), with seasonal and diurnal pressure change reproduced within the Mars Climate Database and deviations corresponding to dust storms and dust abundance (naki Ordonez-Etxeberria et al., 2018). The surface temperature at Gale Crater ranges between $\sim$ 180 - 290 K with a diurnal variability of 50 - 90 K, and surface pressures range between $\sim$6 - 9 mbar, with the lowest surface pressure recorded around $L_s = 170°$ and a diurnal variability of $\sim$0.5 - 0.9 mbar naki Ordonez-Etxeberria et al. (2019), Haberle et al. (2014), Harri et al. (2014).

Due to the depth of Gale Crater, the PBL is expected to reduce to a few meters and fall well below the crater rim, such that the atmosphere within Gale Crater is trapped overnight (Moores et al., 2015, Guzewich et al., 2017, Fonseca et al., 2018). Additionally, the PBL only exceeds the crater rim for up to 3.64 hours between $L_s = 180°$ to $370°$ (Fonseca et al., 2018), with the most dramatic atmospheric mixing in and out of the crater taking place around $L_s = 270°$ (Rafkin et al., 2016). Thus, when describing atmospheric activity within Gale Crater, it is necessary to consider the local topographical effects such as up and downslope winds (e.g. Newman et al. (2019)).

Atmospheric measurements have also been taken by the onboard cameras such as the navigational camera system Navcam, and the camera system mounted on the main mast, Mastcam. Measurements include wind direction, cloud altitudes and direction, dust lifting movies, and opacity measurements. The measurement of dust is particularly important on Mars, as the presence of dust changes atmospheric dynamics. Dust has a role in absorption and radiation that correspond to forced atmospheric tides, resulting in oscillations in the atmosphere and changes in pressure and temperature (Leovy and Zurek, 1979, Zurek and Leovy, 1981, Guzewich et al., 2016). To evaluate the presence of dust in the atmosphere, observations such as the Line of Sight and Mastcam tau (where tau is a measurement of opacity) are able to estimate the relative opacity in the Martian atmosphere over several Martian years (Moore et al., 2016, Smith et al., 2019, 2020), including over a global dust storm were incident UV plummeted by 97% (Guzewich et al., 2019). Outside of dust storms, dust opacity within Gale Crater shows consistent seasonal variability (Guzewich et al., 2017). The density of suspended dust in Gale corresponds to a minimum opacity at $L_s = 90°$ and maximum opacity at $L_s = 270°$.

The Curiosity rover is also equipped with a suite of chemistry equipment that allow for the sampling of drilled and ablated surface samples, and the atmosphere. The chemistry of the surface measurements has varied over Curiosity's traverse as well. As part of the atmospheric measurements, there have been unexpected and difficult to explain variations in oxygen and methane concentrations (Lo et al., 2024, Webster et al., 2015, 2018, Trainer et al., 2019).

1.2.2 Methane on Mars

The Martian methane mystery has been the subject of debate over the last two decades. This controvery has spanned several Earth based observations (Mumma et al., 2009, Krasnopolsky et al., 2004), and has influenced the development of instrumentation for both rover and orbital missions (Webster and Mahaffy, 2011, Metcalfe et al., 2018). This includes the Curiosity rover and Trace Gas Orbiter. In the past few years, several methane measurements hae been taken at the surface in Gale Crater and also from orbit, with the Trace Gas Orbiter taking over 3000 solar occultation measurements for methane retrieval between 2018 and 2020 (Formisano et al., 2004, Geminale et al., 2008, Fonti et al., 2015, Korablev et al., 2019, Knutsen et al., 2021, Montmessin et al., 2021) (Fig. 1.3). Methane sparks particular interest, as the variability of methane observed during the early observations and its presence potentially could indicate a biosignature (Yung et al., 2018, Atreya et al., 2011), produced by possible methanogenic life on Mars. The lifetime of methane in the Martian atmosphere is approximately 330 years (Summers et al., 2002, Wong et al., 2003, Atreya et al., 2007). Thus, the presence of methane would suggest an active source of methane that provides a new supply or resupply of methane into the atmosphere in recent geological history.

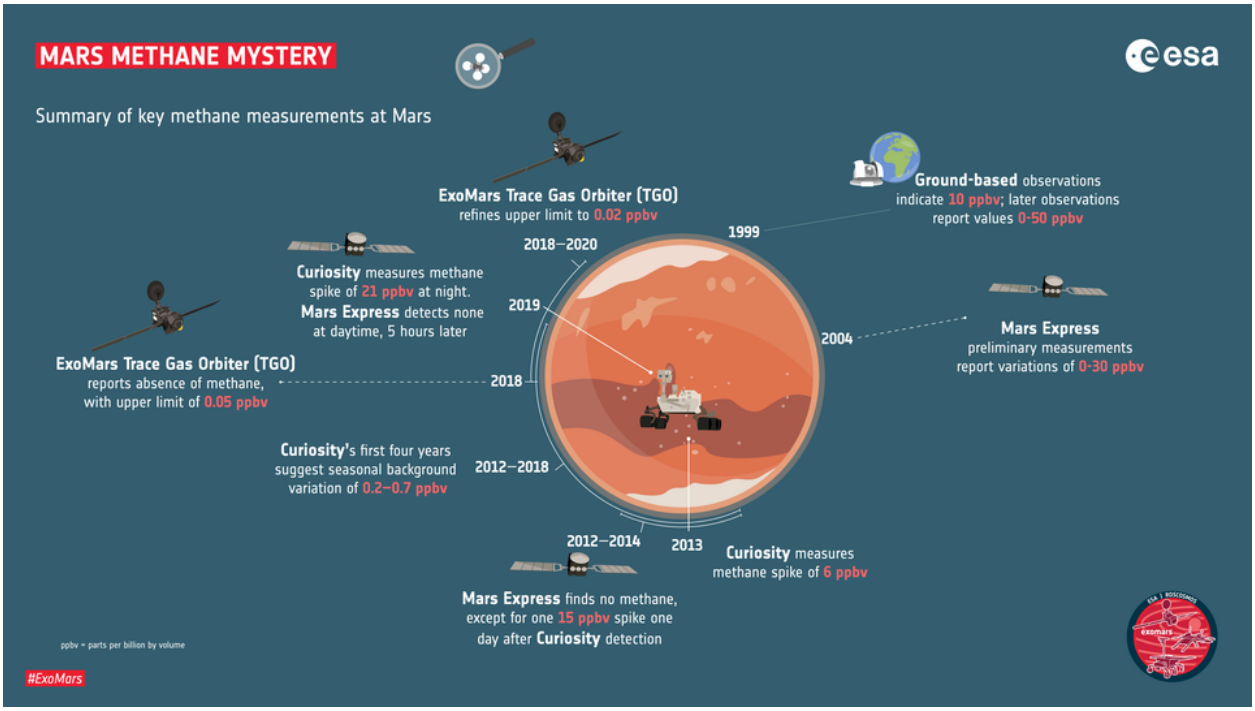


Figure 1.3: Key Martian methane measurements starting in 1999. The first measurement, though a false signal, kickstarted the investigations of the possibility of methane on Mars. Measurements of methane include telescope, orbital, and rover measurements. Source: ESA/ExoMars

However, it is difficult to produce methane on Mars considering the current climate of Mars. It is possible that methane could have formed earlier in Martian history and is now being released from ancient storage via barometric pumping or slow diffusion from geological storage (Ortiz et al., 2024,

Gough et al., 2010, Etiope and Oehler, 2019, Oehler and Etiope, 2017, Chassefière, 2009) (Fig. 1.4). More recent sources of methane production such as interactions with interplanetary dust particles and UV do not produce enough methane to explain the observed levels of methane measured at the surface (Moores and Schuerger, 2012, Moores et al., 2017, 2024). Furthermore, methane destruction mechanisms are likely necessary to explain the temporal variability of methane observed on Mars. The presence of methane on Mars is interesting as it appears to vary seasonally and diurnally, has strong spatial variability, and should not be this difficult to find in the atmosphere if it were readily available (Zahnle et al., 2011, Viscardy et al., 2016, Lefèvre and Forget, 2009). As such, further investigation of methane formation, transport, and removal are warranted.

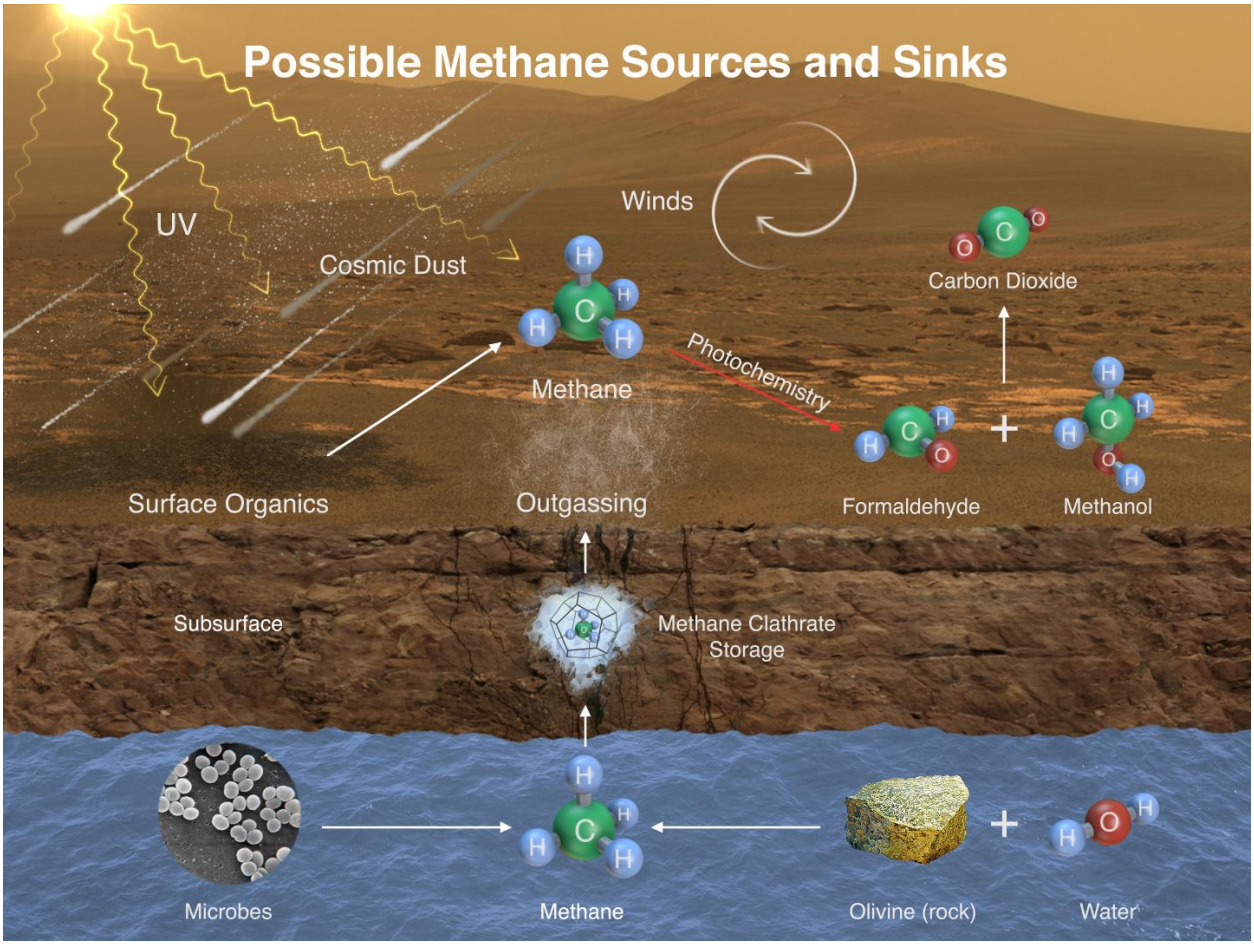


Figure 1.4: Theoretical methane sources and sinks. Source: NASA's Goddard Space Flight Center/JPL-Caltech/University of Michigan

While it is difficult to dig below the surface of Mars to investigate the sources of methane and constrain their spatial location, sampling the atmosphere is significantly more practical. To address some of the questions around methane, the Curiosity rover instrumentation suite was developed to include a spectrometer capable of sampling methane in the atmosphere, the Sample Analysis at Mars - Tunable Laser Spectrometer (SAM-TLS) (Webster and Mahaffy, 2011). SAM-

TLS measurements indicated that methane was present within Gale Crater with levels varying from 0.2 - 21 ppbv when considering the higher-resolution measurements (Webster et al., 2015, 2018, 2021).

Additionally, the Trace Gas Orbiter (TGO) was equipped with two different spectrometers that are suited for targeting methane specifically (Zurek et al., 2011). Interest in methane and existing observations spurred the development of the Atmospheric Chemistry Suite (ACS) and the Nadir and Occultation for Mars Discovery (NOMAD) instruments. These instruments are capable of measuring methane by observing specific spectral bands where the presence of methane could be detected. However, neither ACS nor NOMAD measurements from 2019 - 2022 resulted in positive detections of methane (Korablev et al., 2019, Knutsen et al., 2021, Montmessin et al., 2021). Specifically, methane concentrations measured by the Trace Gas Orbiter (TGO) Atmospheric Chemistry Suite (ACS) and Nadir and Occultation for Mars Discovery (NOMAD) instruments at dawn and dusk observe no methane, with an upper limit of 0.02 ppbv when measured ith ACS (Korablev et al., 2019, Montmessin et al., 2021). Furthermore, TGO has taken several measurements within 600 km of Gale Crater, where the Curiosity rover has measuremed methane up to 21 ppbv at the surface. It is surprising that TGO was unable to find methane in the Martian atmosphere over the hundred of measurements taken.

Methane Measurements from SAM-TLS

Gale Crater currently hosts one active Martian rover (Curiosity rover). The Curiosity rover is equipped with several sophisticated instruments to investigate organic compounds, geology, planetary and surface processes taking place on Mars. This includes the Sample Analysis at Mars instrument suite, that consists of three instruments including a quadrupole mass spectrometer, a gas chromatograph, and a tunable laser spectrometer (TLS). The TLS takes in gas samples in two modes, direct ingest and enriched mode. The enriched mode increases the methane abundance by a factor of 25 in comparison to CO_2 and H_2O, typically taking an additional 2 hours to run in comparison to the 20 minute direct ingest mode requires to fill the sample cell (Webster et al., 2018). Given the length of the measurement and power demands to run SAM-TLS, measurements of methane in enriched mode are relatively sparse. However, both sets of measurements indicate the presence of methane within Gale Crater and represent the only measurements of methane at the surface of Mars thus far.

The precise concentration of methane near the surface and the measurements from SAM-TLS are contested in the literature (Zahnle et al., 2011, Viscardy et al., 2025). Nonetheless, methane measurements taken on Mars by SAM-TLS have led to the inference of two main categories of methane, background microseepage with an average of $\sim$0.4 ppbv, and higher concentration measurements that can be described as methane plumes up to $\sim$21 ppbv (Trainer et al., 2019, Webster et al., 2015, 2018). The background level of methane has been described as having a seasonal cycle (Webster et al., 2018), though such descriptions have been contested due to insufficient data Gillen et al. (2020). Methane on Mars may also have a diurnal cycle (Webster et al., 2021)(Fig. 1.5). Pos-

sible sources of this background methane include outgassing from methane clathrates, production through serpentinization of olivine (Oze and Sharma, 2005), adsorption interactions with surface regolith that are temperature dependent in parallel with barometric pumping from the subsurface (Gough et al., 2010, Ortiz et al., 2024), and more speculatively, byproducts of methanogenic life-forms (Oehler and Etiope, 2017, Chassefière, 2009, Ortiz et al., 2024, Yung et al., 2018, Atreya et al., 2007).

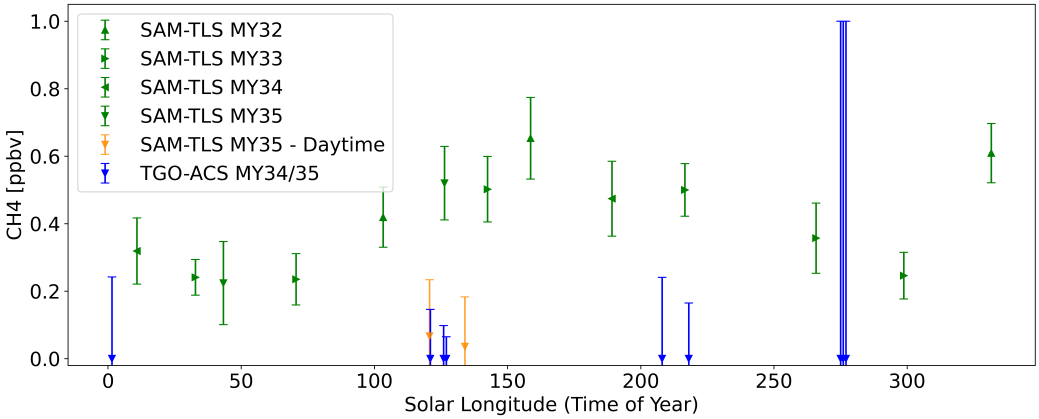


Figure 1.5: Plot showing all MY32-34 measurements of methane from SAM-TLS in enrichment mode with 1 standard error of the mean (Webster et al., 2018). Green points correspond to night time measurements, with orange points around $L_s = 125°$ correspond with daytime measurements (Webster et al., 2021). Measurements from TGO ACS solar occultations (blue) within a 600 km radius from Gale Crater are all plotted at 0 ppbv with the upper limits of each measurement indicated by the size of the error bar (Montmessin et al., 2021).

Additionally, there are instances of high concentration measurements of as much as 21 ppbv at the surface (Webster et al., 2021) that are suggestive of an intermittent source of methane may originate from the northwest of Gale Crater, based on back-trajectory analysis(Luo et al., 2021). (Luo et al., 2021) indicate that this external origin is only likely if methane is being destroyed. The plume observed in Mumma et al. (2009) corresponds to a source stretched latitudinally with a peak methane signal at 315°W (Mischna et al., 2011). However, the observation of a 33 ppbv plume were contested and the upper limit of the observation was revised to 3 ppbv (Zahnle et al., 2011). Overall, proposed sources of methane remain difficult to verify.

Despite ongoing work, the typically low levels of methane coupled with infrequent measurements that are sparsely scattered across Gale Crater do not allow for discrimination of different source mechanism theories. Additionally, the spatial distribution of background methane is not well described due to the limited data. Constraining the potential spatial variability is critical in the next step of a Martian methane sampling campaign.

1.2.3 The Need for a Fast Methane Destruction Mechanism

As noted, the photochemical lifetime of methane is around 330 years on Mars (Summers et al., 2002, Wong et al., 2003, Atreya et al., 2007). Past work has investigated the possibility of faster removal of methane in the Martian atmosphere. Following the observation and subsequent disappearance of methane from Earth-based observations over a 4 month period (Mumma et al., 2009), Lefèvre and Forget (2009) used the Laboratoire de Météorologie Global Climate Model to investigate the rapid disappearance of a large source of methane. Lefèvre and Forget (2009) found that the disappearance of a large methane plume required an atmospheric lifetime of at most 200 sols (or one sol when considering heterogeneous chemistry), in contrast to the expected $\sim$ 330 year e-fold reduction expected.

In preparation for the TGO measurements, Viscardy et al. (2016) demonstrated that the atmospheric mixing on Mars would result in methane mixing throughout the atmosphere within months. The high concentration measurements observed by Curiosity should also be detected by TGO as distinct vertical layers of methane (Viscardy et al., 2016). However, no such layers have been observed, with all methane measurements by TGO observing no methane, with at most 0.02 ppbv based on the error for the measurements (Korablev et al., 2019, Montmessin et al., 2021). It is possible that methane is being destroyed in the atmosphere, though. The main methane destruction mechanisms that are well understood include oxidation near the surface and Lyman-α photolysis when methane is mixed into the upper atmosphere which collectively produce a 330 year e-fold reduction time scale for methane produced in the Martian atmosphere (Krasnopolsky et al., 2004, Summers et al., 2002, Wong et al., 2003, Atreya et al., 2007). Combined, these mechanisms are insufficient to explain the disparity in methane observations between SAM-TLS surface measurements and TGO atmospheric column measurements. These examples highlight the need for a rapid methane destruction mechanism.

However, Moores et al. (2019b) demonstrated it was possible for the regular background concentrations of methane to become sufficiently dilute to fall below the threshold for TGO detection without requiring novel destruction mechanisms. One noted caveat is that their method relied on a relatively small methane emitting area, as if methane is sourced only from Gale Crater (Moores et al., 2019b). During the nighttime, atmospheric mixing and convective activity is suppressed within Gale Crater. Considering a scenario where the source of methane is persistently seeping from the surface within Gale Crater, this leads to increasing concentration of methane in the stable near-surface layer of the atmosphere throughout the night. During the daytime, the planetary boundary layer is expanded, and methane is more readily mixed throughout the lowest few kilometers of the atmosphere. Under these circumstances, Moores et al. (2019b) found it was possible that the methane flux from the surface could range between an average of $7.47 - 13.5 \times 10^{-11}$ kg/m^2/sol while still resulting in sufficient dilution of the methane concentration to fall to several pptv, below the reported TGO upper limit of 0.05 ppbv at the time (Korablev et al., 2019).

In response to Moores et al. (2019b), additional daytime measurements were acquired by SAM-TLS within Gale Crater to investigate whether methane tends to build up at night and is relatively

lower in concentration during the day. These daytime measurements revealed methane concentrations below 0.05 ppbv, an order of magnitude lower than nighttime concentrations, demonstrating diurnal variability in the background measurements (Fig 1.5). Overall, the SAM-TLS daytime measurements demonstrated that it is likely daytime measurements are typically lower than that of nighttime measurements. Thus, TGO observations could be partially explained by the dilution of methane.

Following up on Moores et al. (2019b), Walters (2023) simulated the transport of methane from the surface within Gale Crater at a higher resolution and incorporated atmospheric dynamics that varied throughout the day. Walters (2023) found that the required methane flux was an order of magnitude higher than the estimates from Moores et al. (2019b), and the methane at the top of their model exceeded that of TGO's observational limts. Moreover, recent refinements to the lower limits of TGO observations have been reduced to 0.02 ppbv as the upper bound for methane (Montmessin et al., 2021), and it remains likely that a faster methane destruction mechanism is necessary to explain the difference in methane concentrations at different altitudes.

Our experience with rapid methane production and destruction on Earth suggests that biological mechanisms may be one solution (Krasnopolsky et al., 2004, Yung et al., 2018). However, it is unlikely that present-day Mars supports life in the near-surface, though methane created or sequestered deeper in the subsurface may reasonably be transported from 200 m below the surface (Ortiz et al., 2024) or from even deeper depths (Oehler and Etiope, 2017), which is potentially a more habitable environment. Additional mechanisms for methane removal via short term sequestration within the Martian regolith itself have been proposed. Gough et al. (2011) demonstrated physisorption by methane adsorbing onto Martian regolith simulant, where adsorption increased with decreasing temperatures and increased methane partial pressure. A similar proposal came from Moores et al. (2019a), where they demonstrated it was possible to replicate seasonal variability at Gale Crater via absorption and desorption. Jensen et al. (2014) investigated olivine and silicate tumbling interactions with methane and found that methane bonded with the silicates after months of tumbling. Thøgersen et al. (2021) observed that triboelectricity (such as that sparked by energetic dust collisions) could also reduce methane. The oxidation of methane with peroxide (H_2O_2) has been proposed, as peroxide is strongly oxidizing (Atreya et al., 2007). Another mechanism involves a reaction with perchlorate (ClO_4^-), a highly reactive salt species observed at both the Phoenix (0.4 – 0.6 wt%) and Curiosity sites (up to 1.2 wt%) on Mars (Sutter et al., 2017, Hogancamp et al., 2018, Hecht et al., 2009, Kounaves et al., 2010, Clark and Kounaves, 2016). Most of these mechanisms have their limitations, whether the condition for the destruction is limited or insufficient to make sense of the current methane observations, or restrict methane seepage to very limited areas of Mars.

In this dissertation, I focus on perchlorate. It is possible that the presence of perchlorate contributes to methane destruction in the atmosphere. However, experiments reacting magnesium and sodium perchlorate do not show evidence for rapid destruction (Gough et al., 2011). Gough et al. (2011) identified that the lifetime of methane would be greater than 4 years (constrained by

observations from Mumma et al. (2009)), unless the layer of Martian soil containing perchlorate exceeded 500 m in depth. More recent work by Zhang et al. (2022) experimented with magnesium perchlorate reactions with methane in the presence of UV. They found drastically different results, with a reaction rate several orders of magnitude faster than that estimated by Gough et al. (2011). Assuming an 0.5 wt% fraction of perchlorate, the lifetime of methane was reduced to hours to days. Since this research has been published, a detailed investigation coupling the dilution of methane via diffusion, and the fast destruction mechanism of methane has not been done.

While efforts have been made to reconcile the methane measurements made by SAM-TLS and TGO by considering the effect of a varying PBL height and changing pressure (e.g. Moores et al. (2019b), Ortiz et al. (2024)), it is prudent to consider the effects of a rapid methane destruction mechanism in the Martian atmosphere. I once again consider the work by Walters (2023) where they demonstrated using a detailed subdiurnal vertical diffusion model within Gale Crater that diffusion of methane alone does not explain the difference in observed concentration from the surface and from orbit. Their results suggested that the methane flux at the surface of Gale Crater was one order of magnitude higher than that estimated by Moores et al. (2019b) to achieve the concentrations observed by SAM-TLS. The difference in flux estimation likely is due to the atmospheric model used in the two different papers. Moores et al. (2019b) use eddy diffusivity values as estimated from the Rover Environmental Monitoring Station of 9.4×10^{-4} m^2/s (Martínez et al., 2017) and the molecular diffusivity limit at night to evaluate two end-members of night-time mixing, while Walters (2023) and Walters et al. (2024) considered the values retrieved from the Global Environemental Multiscale Model for Mars (GEM-Mars) over a full sol including more complex dynamics with varying eddy diffusivity values over 3 km and different times of the Martian year. The eddy diffusivity values near the surface from GEM-Mars generally exceed the upper limit of mixing used by Moores et al. (2019b) with the lowest GEM-Mars nighttime values on the order of 10^{-2} m^2/s near the surface. As the eddy diffusivity values represent turbulent atmospheric mixing, greater amounts of mixing and subsequent transport of atmospheric constituents near the surface would require an increased methane flux to achieve the observed surface methane measurements.

The description presented in Walters (2023) in the GEM-Mars based model was incomplete as they imposed two unrealistic constraints. First, the methane accumulation was limited in the model by removing methane from the top of the vertical diffusion model. Second, their model does not include altitudes observable by TGO as the model was limited to 3 km in altitude. Furthermore, in both Moores et al. (2019b) and Walters (2023) and Walters et al. (2024) did not investigate plume-like sources of high methane concentration.

Chapter 3 expands upon Walters (2023)'s methodology by incorporating a destruction mechanism and a wider range of modelled eddy diffusivity values (which change the rate at which the atmosphere mixes). Additionally, my work explores the effect of the rapid methane destruction mechanism proposed by Zhang et al. (2022), where dust is suspended in the atmosphere and methane can be destroyed when in contact with dust during the daytime. I simulate this destruction effect in conjunction with a detailed diffusion model of methane that extends to the lower

observational altitude of TGO (10 km). I estimate the required methane flux from the surface to achieve the reported SAM-TLS methane concentrations using three different atmospheric models to simulate diffusive processes and two different dust profiles to estimate methane destruction. If the methane concentration at 10 km and above is consistently well below the TGO detection threshold, then it is possible that both TGO and Curiosity rover measurements of methane may be consistent with each other.

1.2.4 Martian Methane Microseepage Analog

While the specific observations of methane remain contested, it is reasonable to investigate and understand the origin, distribution, and transport of methane on Mars if it is present. To support future methane measurements on Mars, the Canadian Space Agency has sponsored the development and testing of the Martian Atmospheric Gas Evolution (MAGE) instrument. As part of the development of an instrument, it is necessary to demonstrate that the instrument has potential to evaluate the problem being posed, or has heritage in resolving the issue. For methane on Mars, SAM-TLS is the prime example of a spectrometer at the surface that has successfully observed methane with reasonably high precision. However, the number of measurements is very low, and studies have suggested that the seasonal trends observed could easily be within error of a flat line (Gillen et al., 2020). Additionally, the frequency of the measurements relative to the physical distance between each measurement does not contribute to the identification of a methane source if it can be spatially resolved.

Axel Heiberg Island as a Methane Analog

The purpose of an analog study is to understand processes that take place on Earth to interpret data from other planetary bodies, such as Mars. An analog site should represent and approximate in some manner the geological, environmental, and biological conditions for a planetary body in the present or at some point in the past (Osinski et al., 2006). In this instance, the analog serves as a testing ground for instrument performance to understand the performance requirements of future methane instruments on Mars. Canada has several analogues available to understand the Martian environment, including several in Nunavut with periglacial landforms that have been observed on Mars and others with extreme conditions that are useful in the study of astrobiology (Osinski et al., 2006).

The Off-Axis Integrated Cavity Output Spectrometer is a commercial spectrometer produced by ABB Inc., and is the basis for the MAGE instrument intended for future measurements of methane on Mars. As part of the development of MAGE, I took a spectrometer to a Martian methane analog in the Canadian Arctic to investigate the methane spatial varibility. At the site, the methane varies both spatially and temporally, with the main control on methane production and removal being microbial organisms in the subsurface. Specifically, I evaluated the spatial variability of methane over polyonal terrain at an analog site in the Canadian Arctic on Axel Heiberg Island (AHI, also Umingmat Nunaat), a high fidelity Martian analog (Pollard et al., 2009).

AHI is particularly suitable for the investigation of methane variability, with several hypersaline springs that act as point sources (Pollard et al., 2009), and polygonal terrain (Lau et al., 2015) that presents an opportunity for investigating meter-scale methane concentration variability (Fig. 1.6). Thus, AHI serves as an appropriate location to investigate the spatial variability of methane and both the microseepage and plume type release mechanisms. In this dissertation, I focus on microseepage.

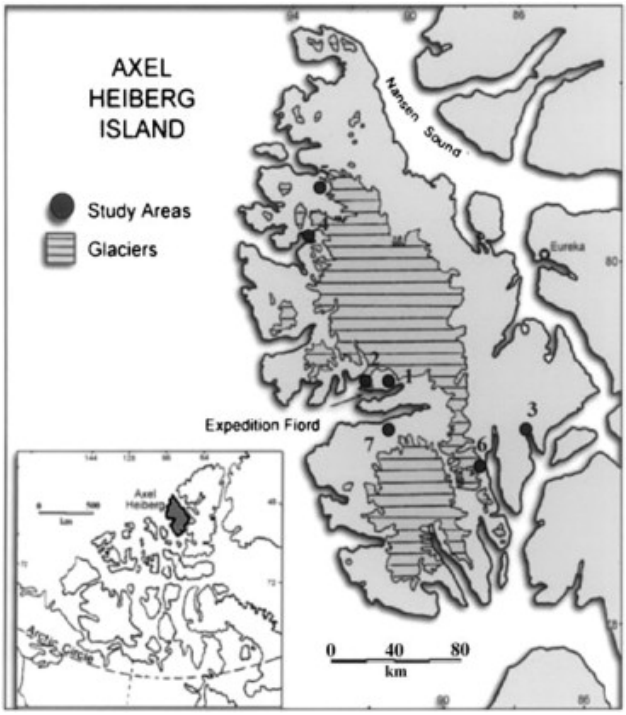


Figure 1.6: Map of Axel Heiberg Island with sources of methane. Point 1 marks Expedition Fiord, where polygons have been sampled by (Lau et al., 2015) and act as a net methane sink. Point 7 marks the Lost Hammer site, where strong surges of methane have been observed (Pollard et al., 2009). Source: Pollard et al. (2009).

Background methane flux at the surface of polygonal terrains such as those found on AHI has been observed to vary based on environmental factors, with an overall net negative flux into the surface (Christensen, 1993, Lau et al., 2015, McCalley et al., 2014, Voigt et al., 2023). In addition to thermogenic sources of methane from long-buried organics, variability in the background methane near the surface is expected, as methanogenic (methane-emitting) and methanotrophic (methane-consuming) microbial populations are present (Douglas et al., 2016, Liebner et al., 2009, McCalley et al., 2014). Factors affecting methane producers and oxidizers (consumers) have previously been documented relating depth, temperature, water concentration, and other abiotic factors to methane oxidation across short spatial distances (Lau et al., 2015, Martineau et al., 2014, Stackhouse et al., 2017). While methane microseepage-producing mechanisms will likely be different at the Martian surface, we can leverage this population diversity in situ to investigate methane variability across meter-length spatial scales.

In Chapter 2, I report on a Martian methane microseepage analog study conducted at AHI using a methane spectrometer to investigate meter-scale variability of methane in an analog environment. The field test is an opportune time to evaluate the requirement for future methane spectrometer resolution and frequency. This work informs future Martian methane instrument development and provides insight into potential spatial variability of methane.

1.3 An Overview to Titan

Farther out in the Solar System lies Titan, Saturn's largest moon. Much like Mars, Titan is an important site for understanding the origins of life. Titan is the destination of NASA's upcoming Dragonfly mission set to land in the early 2030s (Barnes et al., 2021, Turtle and Lorenz, 2024). This moon is uniquely Earth-like in several aspects, including having a dense atmosphere and a hydrological cycle, with methane taking the role of water (Lorenz et al., 2018). Compositionally, Titan's atmosphere predominantly consists of nitrogen and a few percent of methane. Estimates of methane at the surface are 5.65% ± 0.18% (Niemann et al., 2010). Given the distance from the Sun, Titan receives significantly less solar flux than that of Earth and Mars, with a surface temperature of 94 K (Fulchignoni et al., 2005, Schinder et al., 2011). The surface pressure of Titan is close to 1.5 bar, and the atmospheric density decreases with greater altitudes. Methane is close to its triple point at the surface and can be present in both gas and liquid forms. The presence of liquid and gaseous methane on Titan in conjunction with the presence of water-ice molecules in a reducing atmosphere makes Titan an excellent candidate for investigating prebiotic chemistry (Hörst et al., 2012, Hörst, 2017, He and Smith, 2014, Raulin et al., 1995).

Titan's surface is likely coated in organic solids that form as atmospheric aerosols and are deposited on the surface (Waite et al., 2007, Cable et al., 2011, Hörst, 2017). Some noteworthy features on Titan's surface include the organic-rich dunes, methane and ethane lakes, cryovolcanoes, and the large Menrva impact crater. The absence of numerous impact craters indicates that the surface of Titan is geologically relatively young, around 300 - 1000 Myr (Wakita et al., 2026, Hedgepeth et al., 2020, Neish and Lorenz, 2012). The investigation of impacts on Titan is relevant for the potential of prebiotic life, as impacts transfer heat and energy, thereby allowing for critical reactions to take place in aqueous environements, while larger impacts may penetrate Titan's icy crust to a potential subsurface ocean, leading to mixing of organics from the surface with liquid water (Crósta et al., 2021, Neish et al., 2024).

Crater counting and age dating the surface to estimate the frequency of impactors is an imprecise science, particularly when coverage of a planetary body is incomplete as in the case of Titan (e.g. (Shah et al., 2025)). For example, the apparent age of Menrva crater is anomalously young given its size, deviating from the crater-size distribution. Furthermore, despite the recent improved observations that double the crater count from early work (Hedgepeth et al., 2020, Neish and Lorenz, 2012), (Hedgepeth et al., 2020) found an apparent undercount for craters less than 10 km in diameter relative to past work by Neish and Lorenz (2012). This is unexpected considering

Artemieva and Lunine (2003) demonstrated impactors as small a 100 m are likely to reach the surface. Given a minimum size of an impactor must be to reach the surface of Titan intact (at least 100 m), this corresponds to craters approximately 1 km or larger in diameter. Smaller meteors do not result in an impact with the surface and subsequent crater formation. As there is no evidence of smaller impactors on Titan's surface, the overall mass from sub-km meteors is poorly constrained. Overall, the cratering rates in the Saturnian system remain poorly constrained, with no data to constrain the sub km impactor rate.

1.4 The Dragonfly Mission

The Dragonfly mission was developed as a response to NASA's New Frontiers 4 opportunity to address the habitability of ocean worlds (Lorenz et al., 2018). Dragonfly is currently progressing through its integration and testing phase, and is expected to launch in 2028 with an arrival in late 2034. While some of the main science objectives include understanding of the potential for prebiotic chemistry on Titan, Dragonfly was developed as a multi-disciplinary mission with multiple mission goals (Barnes et al., 2021). Other science objectives include the measurement of atmospheric conditions to better understand transport processes on the surface and in the atmosphere and to characterize seismic activity to constrain the subsurface structure of Titan (Turtle and Lorenz, 2024, Barnes et al., 2021, Lorenz et al., 2019, Rafkin et al., 2018). The prime mission timeframe consists of approximately 3 Earth years, or 70 Titan sols. The landing is expected to take place during northern hemisphere winter, close to the time of Titan year Cassini-Huygens arrived in the Saturnian system (Barnes et al., 2021). Note that Titan is tidally locked to Saturn, thus the length of day and night correspond to around 192 hours each, with night time activities focused on battery recharge.

The mission craft consists of a relocatable lander equipped with 8 sets of rotors for flight. Due to the atmospheric density on Titan and lower gravity (1/7th of Earth's), powered flight is considerably easier on Titan in comparison to Earth and Mars (Lorenz et al., 2018). The landing ellipse of Dragonfly is located in the equatorial dune field south of Selk Crater, an $\sim$ 80 km diameter crater (Fig. 1.7) (Turtle and Lorenz, 2024). Dragonfly will conduct several short flights over dunes with the goal of reaching Selk Crater within a total of 30 - 40 total flights. Given the lack of information regarding the surface of Titan, the flights are expected to return a wealth of information on the surface materials and variability across the Dragonfly traverse. The traverse is expected to pass through different surface materials including: dark dune sand, interdune gravels, crustal material, ejecta blanket and impact melt from Selk Crater (Barnes et al., 2021). The sand seas are expected to consist of organic sands and sand-free areas 2.0 - 3.5 km across (Savage et al., 2014, Barnes et al., 2021). During the landings between flights, the Dragonfly Geophysical and Meteorology package (DraGMet) will be actively sampling the atmosphere and measuring surface properties, including recording seismic activity (Panning et al., 2020). Dragonfly will also be equipped with a Drill for Acquisition of Complex Organics (DrACO) for ingestion into the Dragonfly Mass Spectrometer

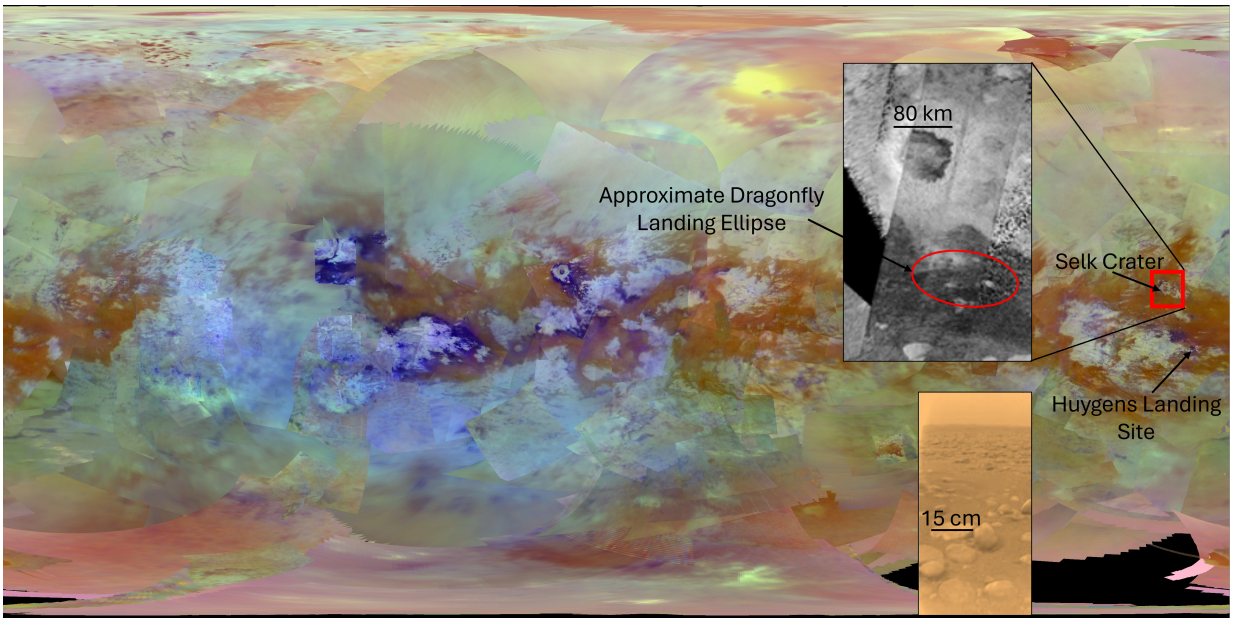


Figure 1.7: Map of Titan and approximate Dragonfly landing ellipse. The expected traverse areas are shown in the red square (Turtle and Lorenz, 2024) and the approximate landing ellipse for Dragonfly is shown by the red ellipse over an inset image of the area surrounding Selk Crater (approximately 80 km wide). The context image for Selk Crater in grey shows the reflectance data from the Cassini Radio Detection and Ranging (RADAR) instrument (Elachi et al., 2005). Dragonfly is expected to land on a surface covered in sand (Lorenz et al., 2021). The background image shows Titan using Cassini Visual and Infrared Mapping Spectrometer (VIMS) data produced by Mouélic et al. (2019) over an interpolated grid. The inset Huygens landing photo is shown for surface context.

(DraMS) to study the chemical composition of surface materials (Lorenz et al., 2018, Turtle and Lorenz, 2024). Unlike landed Martian missions that have several orbiters that can support data return, Dragonfly will be returning data using a high-gain antenna directly back to Earth (Turtle and Lorenz, 2024).

This dissertation takes advantage of the instruments onboard the meteorological suite (DraGMet) to measure pressure disturbances in the atmosphere (Lorenz et al., 2018, Rafkin et al., 2018, Panning et al., 2020). Atmospheric disturbances include winds and weather intrinsic to the moon, but also include external sources such as meteor airbursts. Currently, the characteristics and population distribution of outer Solar System meteors remain poorly constrained by very few observations (Bottke et al., 2023, Nesvorný et al., 2023). If impactors encounter Titan's atmosphere during the Dragonfly mission, it may be possible to learn more about them via DraGMet.

1.4.1 Titan's Atmospheric and Surface Properties

The discovery of Titan's atmosphere is attributed to José Comas-Solá in 1908 who believed he observed limb-darkening (Solá, 1908). The observation of methane around Titan by Gerard Kuiper demonstrated that it was likely Titan had an atmosphere (Kuiper et al., 1944). However, it was later

found that methane was only a small component of Titan's atmosphere (Danielson et al., 1973). Lewis (1971) hypothesized that the dominant species in Titan's atmosphere was N_2, and this was later confirmed by Pioneer 11 (Tomasko, 1980). Later encounters by Voyagers 1 and 2 narrowed down the surface temperature to 94 K with a surface pressure of 1.5 bar (Lindal et al., 1983). In 2004, the Cassini-Huygens mission reached the Saturnian system, with the Huygens probe landing on Titan's surface in 2005. Cassini continued to orbit Saturn for 13 more years before completing its Grand Finale by entering Saturn's atmosphere, continuing to make observations of Titan's meteorology over the course of the mission (Turtle et al., 2018, Teanby et al., 2019).

The Huygens probe descent provided the most complete atmospheric profile we have of Titan to date. Huygens was equipped with the Huygens Atmospheric Structure Instrument (HASI), which measured temperature and pressure. Other instruments collected and analyzed the composition of the atmosphere, and took photos during the descent (Jaffe and Herrell, 1997). The pressure profile from HASI descent indicates that the atmosphere follows a similar pressure profile to that of Earth's, though Titan's scale height is more elongated over 15 - 50 km in comparison to Earth's 8.5 km scale height (Fig. 1.8). Based on the temperature profile collected by HASI, the PBL was located at 300 m at the time of descent (Fulchignoni et al., 2005), though simulations suggest that the diurnal PBL varies between the near surface and 800 m throughout the day (Charnay and Lebonnois, 2012). Titan's atmosphere is 4.4x the density of Earth's, capable of supporting powered flight with smaller rotors on Titan (Lorenz et al., 2018). Zonal wind speeds near the surface are expected to be lower than 1 m/s, though we note that seasonal storm activity has been observed on Titan and can lead to higher wind speeds and atmospheric transport near the surface (Lorenz et al., 2021).

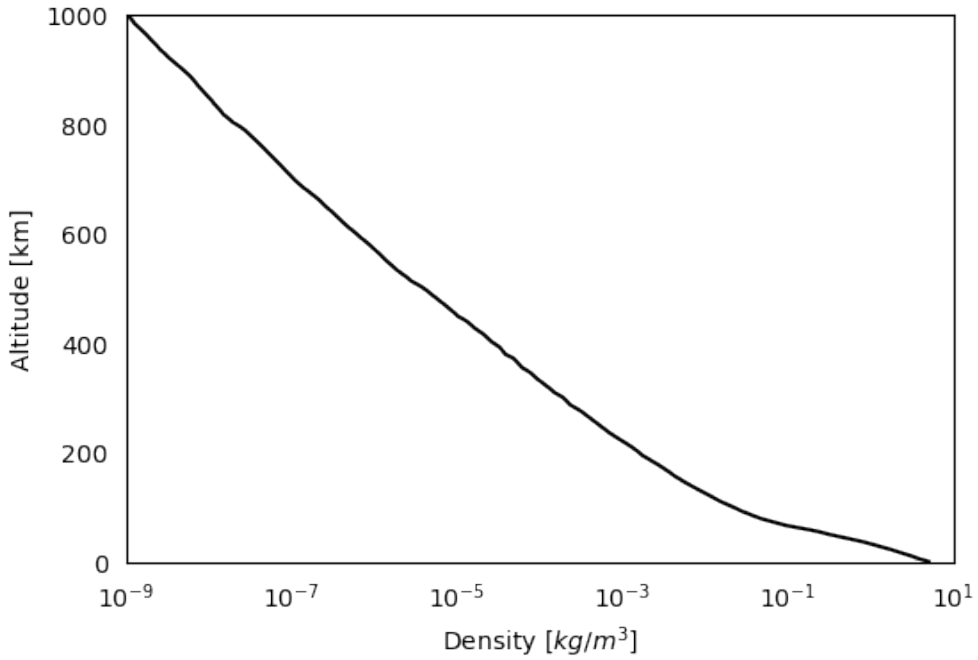


Figure 1.8: Density profile of Titan's atmosphere as measured by HASI during descent. Data from Fulchignoni et al. (2005).

While detailed data about Titan's atmospheric temperature and pressure profile are restricted to a singular location and time, we can infer that the speed of sound on Titan is lower than that of Earth's, at 195/ ms - 200 m/s (Petculescu and Lueptow, 2007, Lorenz et al., 2018). Acoustic waves are expected from Titan, with sources such as tidal cracking, slow winds, microseisms, and general atmospheric noise (Panning et al., 2020). Such waves are expected to be relatively efficient in comparison to Earth, Venus, and Mars at all frequencies with several orders of magnitude less acoustic attenuation (Petculescu and Lueptow, 2007). Furthermore, attenuation through Titan's atmosphere with altitude are also considerably less than that of Earth, Venus, and Mars (Petculescu and Lueptow, 2007). Consequently, acoustic propagation in Titan's atmosphere can potentially be detected by the DraGMet suite of instruments. An example of acoustic propagations that may be observed include airbursts, the explosion of meteors that occur when the external pressure exceeds the internal strength of the meteors.

1.4.2 Impactors in the Solar System

Large impactors (meteorites) can leave craters on the surface, whereas smaller ones ablate away in the atmosphere before reaching the surface (meteors), potentially leaving trace signals at the end of their fiery and explosive lives (bolides). When a sufficiently rapid breakup of the meteor occurs, as in the case of bolides, the corresponding explosion is referred to as an airburst, and is accompanied by a shockwave. Descriptions of shockwaves travelling through the atmosphere can be described via hydrodynamical simulations, including those used for crater impacting, and also via empirical

equations.

The empirical equations that can be used to describe airburst shockwaves were initially developed to evaluate the behaviour of nuclear explosions. Glasstone and Dolan (1977) identified several scaling relations to describe the nuclear explosions during testing in the early 1960s that related relative temperature and pressure from the source to the ground (Glasstone and Dolan, 1977). The behaviour of nuclear explosions are similar to point source booms that occur from sonic booms, and more general explosions. The empirical equations assume an atmospheric density increasing exponentially towards the surface, which is similar to the atmospheric profile for Titan. Furthermore, these equations assume no meaningful winds during the propagation towards the surface after the explosions occur. The equations and caveats are further expounded upon in Chapter 4.

In the outer solar system beyond the ice line, most meteors would be expected to be cometary in nature. Estimates of impactors in the Saturnian system are dependent on crater counting, inferences, and very few limited observations of impacts (Korycansky and Zahnle, 2005, Bottke et al., 2023, Wood et al., 2010, Neish and Lorenz, 2012, Hedgepeth et al., 2020, Artemieva and Lunine, 2005). It is easy for the estimated distribution of impactors to be skewed by the scant measurements available, especially those of smaller objects. This matters as they influence the expected mass distribution in the solar system and can constrain simulations for solar system formation models. More generally, there is evidence that it is feasible to detect airbursts, and they occur at a higher rate within the inner solar system than previously anticipated. Thus, it may be meaningful to investigate the occurrence rate on Titan.

Seismometers are particularly suitable for the detection of airbursts, as they have distinct seismic signatures that are akin to those of explosions. On Earth, the Chelyabinsk event is the largest airburst event on record, where shockwaves were recorded 4000 km away from the source (Heimann et al., 2013). Chelyabinsk is not the only recorded event, however. Airbursts in Earth's atmosphere are regularly detected by the seismic array associated with the Comprehensive Test Ban Treaty, initially implemented for nuclear testing detection (Pilger et al., 2015, Edwards, 2009a).

Airbursts are associated with meteors, where the trajectory and mass loss from meteors can be tracked by observing the intensity of light in the sky. The greatest light flare is associated with a major breakup event for the meteor. Given an array of meteor parameters, such as initial trajectory, velocity, mass, and internal strength, it is possible to simulate an incoming meteor and estimate the trajectory of the meteor and breakup sequence after it enters the atmosphere (Brown et al., 2016, McFadden et al., 2021).

Sonic booms are also associated with manmade objects in the atmosphere. Kanamori et al. (1992) demonstrated that seismic activity was excited by acoustic coupling from the atmosphere to the surface when space shuttles returned to Earth, travelling through the atmosphere at hypervelocity. They found that the seismic wave generated from the coupling was a distinct N-shape when coupled with bedrock, and the overpressure in the acoustic wave could be accurately estimated from the seismic wave alone as the surface seismic velocity was known. Later research by Revelle (2005) and Edwards et al. (2007) confirmed that the airbursts from meteors and hypersonic shuttles was

similar and the same methods could be used for ray-tracing and estimating the initial trajectory of the travelling hypersonic objects. Silber et al. (2024) and Fernando et al. (2024) had similar findings, where the shockwaves from OSIRIS-REx re-entry were seismoacoustically coupled.

1.4.3 Modelling Meteors

The study of meteor physics has a long history of Earth, and Titan's atmosphere shares enough similarities to Earth's atmosphere that we can draw direct comparisons. When a meteor enters Earth's atmosphere, at a hypervelocity velocity with a mean 16.7 km/s (∼11 km/s on Titan), the meteor experiences friction from the atmosphere and begins to heat up and loses its outer shell via ablation. This can be observed as a "shooting star", the visible portion of a meteor. If the meteor continues on an Earth-bound (Titan-bound) trajectory towards the surface, then pressure increases exponentially. If the pressure exerted on the meteor is greater than the internal strength of the meteor, then it will break apart. When a meteor breaks apart, it loses some kinetic energy. If there are successive and rapid break up events, this can translate to an airburst which manifests as a sonic boom and a large flash of light. While it is unlikely that a meteor causing an event the magnitude of Cheylabinsk will enter the atmosphere, or a crater forming meteor will impact Titan during the Dragonfly mission, it is reasonable to expect that smaller impactors may occur and result in small airbursts. The physics of an airburst from a small meteor are the same as those of larger meteors, nuclear tests, and hypersonic velocity space shuttles. A sonic boom is generated and travels radially outwards from the source. As the blastwave travels outwards, its amplitude decreases and its speed drops to the speed of sound. Upon arrival at the surface, the acoustic wave couples into the surface, transforming into a seismic wave.

The upcoming Dragonfly mission serves as an excellent opportunity to learn about the outer Solar System more broadly. In particular, the DraGMet package has microphones, several pressure sensors, and a seismometer. This equipment is suitable for the detection of blastwaves that travel at the speed of sound. The chapter on Titan Airbursts targets two major signals, the overpressure and the seismic velocity of the surface. I consider the theoretical presentation of the waveforms and whether the instruments onboard are sufficient to detect airburst events. If Dragonfly can detect these events, it may be possible to constrain the number of outer solar system meteors.

1.5 Summary and Overview of Dissertation

This dissertation includes three projects that investigate how planetary atmospheres can inform us about properties of the coupled surface-atmosphere interface including: the limitations of methane spectrometers for the understanding of methane on Mars, the detailed transport and dynamics of methane in the Martian atmosphere, and the propagtion of seismoacoustic waves in Titan's atmosphere. The chapters are organized by investigation area and proximity to Earth, starting on our home planet with an analog experiment to better constrain methane spatial variability, then to Mars to track the diffusion of methane in the atmospheric column, then to Titan where incoming

meteors provide insight into outer Solar System cometary populations and surface properties.

In Chapter 2, we investigate the results of a deployment to a Martian methane analog site in the Canadian Arctic. Methane that is typically measured on the surface of Mars is most likely released from the surface (microseepage). With the current limitations of the instruments on Mars, future investigations are interested in constraining the source and spatial variability of methane to test the various hypotheses of the origin of methane on Mars. Several microseepage mechanisms have been proposed but have not been validated due to the paucity of data. To support the development of future methane instruments, I investigated methane spatial variability across three field seasons in a Martian analog environment, the polygonal terrain on Axel Heiberg Island. The polygonal terrain on Axel Heiberg Island has previously been studied for methane producing and oxidizing microbial organisms, with environmental conditions such as temperature and water affecting the methane flux. I leveraged this population diversity to investigate the methane spatial variability across individual polygons with applications to future Martian methane measurements.

In Chapter 3, the approach to understanding methane on Mars shifts towards a simulation based method. Measurements of methane on the surface are several orders of magnitude higher than the lower limit of the TGO satellite measurements, which find no methane at all. Based on the circulation models of the Martian atmosphere, one expects methane mixed into the atmosphere from the surface should result in detections by satellite observations. However, the methane mixed into the upper atmosphere can be reduced if the methane itself is destroyed near the surface prior to transport. I investigate a recently evaluated methane destruction mechanism that relies on the presence of perchlorate and UV, both of which are available on Mars. As part of the simulations, I used three different atmospheric models to describe the transport of methane from the surface and estimate the required methane flux to achieve the surface level methane concentration corresponding to measurements taken by the Curiosity rover at Gale Crater. I evaluate whether the diffusion and destruction of methane from the surface leads to methane concentrations at altitudes observable by the Trace Gas Orbiter below their detection threshold.

In Chapter 4, I evaluate the transport of acoustic waves in Titan's atmosphere. Less is known about Titan's atmosphere in comparison to Mars. However, the atmospheric pressure profile is similar to what is observed on Earth. Thus, the formation and propagation of shockwaves from meteor airbursts is expected to follow similar behaviour to the that of tests conducted on Earth. I consider realistic simulations of meteor descent through Titan's atmosphere and track the airburst height, associated energy with the airburst, and the propagation of the associated shockwaves. I also evaluated the final magnitude of the shockwave and compared the magnitude to the resolution to the Dragonfly instrument.

Chapter 5 provides an overview of Future Work inspired by the research described in Chapters 2, 3, and 4. Chapter 6 concludes with a brief summary of the scientific problems presented in this dissertation and the results I obtained following my investigations.

Chapter 2

Methane in the Arctic

The work in this chapter has been published previously as the following:

Elisa Dong, John E. Moores, Haley M. Sapers, Lucas Beckering Vinckers Stofer, Alex C. Innanen "A Mars Analog for Spatially Varying Methane Microseepage based on observations acquired in an Analog Deployment to Polygons at Expedition Strip, Axel Heiberg Island", in *Acta Astronautica*, [2025]

and has been updated and extended here for the purposes of this document. CRediT: Elisa Dong: Writing – original draft, Methodology, Investigation, Formal analysis, Conceptualization. John E. Moores: Writing – review & editing, Supervision, Funding acquisition. Haley M. Sapers: Project administration, Investigation. Lucas Beckering Vinckers Stofer: Investigation, Data curation. Alex C. Innanen: Methodology, Investigation.

2.1 Introduction

The primary focus of this chapter is the presentation and analysis of methane concentration measurements conducted at the Expedition landing strip, which consists of polygonal terrain. I leverage this spatial variability to measure methane across meter-scales to evaluate the potential for spatial variability of methane at Mars. I describe our field campaign results and conclude with implications for future martian methane sampling campaigns and exploration.

2.2 Methods

An Off-Axis Integrated Cavity-enhanced Output Spectrometer (OA-ICOS) was brought to Axel Heiberg Island for 3 field seasons. Methane concentration measurements were taken on July 16, 2022; July 5, 6, and 16, 2023; and July 14, 2024. Samples were taken by different operators for each of the field seasons. The OA-ICOS was housed in a Pelican case that sampled gas via an inlet into the case. The OA-ICOS was used to measure levels of methane, carbon dioxide, and water vapour in and around the island. Further details on the OA-ICOS and its development as part of the Mars Atmospheric Gas Evolution can be found in Walters et al. (2024). For this paper, I focus on the methane concentration measurements, and provide the water vapour and carbon dioxide values in the Appendix found in Dong et al. (2025). Data for the environmental conditions potentially affecting the measurements were recorded by hand in 2023, and recorded via a handheld Kestrel 5500 Weather Meter.

2.2.1 Site Description and Sample Procedure

The Expedition landing strip consists of polygonal terrain next to a large water feature (Colour Lake). Polygonal terrain is often observed within periglacial environments, and forms from freeze-thaw cycles which cause cracks to open. These cracks are further developed by the formation of ice and/or sand wedges (Mackay, 1974, De and Leffingwell, 1915). Similar terrain has been observed on Mars, which may form from a similar mechanism (Levy et al., 2010, Mellon et al., 2009, 2008). However, I do not anticipate that the martian polygons will host a microbial ecology similar to what we observe in the arctic and will not create small-scale variation in methane concentration. Therefore, the polygons at AHI are not analogs for martian polygons. Our field site consists of

individual high-centered polygons, with the center of the polygon being relatively elevated and lighter in tone compared to the recessed, darker, troughs that form the edges of the polygon (Fig. 2.1). In 2023, I observed ponding at some of the trough locations, with the most ponding at the corners where troughs met.

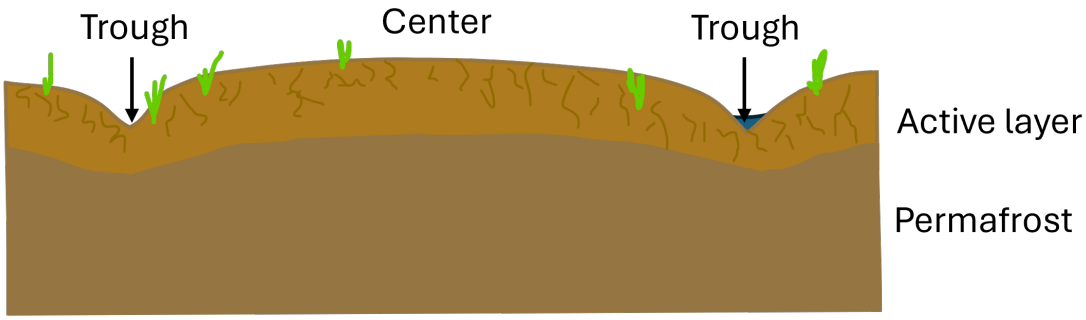


Figure 2.1: Illustration of hypothetical polygonal feature cross section. The center of the polygon is relatively elevated in comparison to the edges of the polygon forming the troughs. The troughs are deep cracks that can span several centimeters across that are visually darker than the rest of the polygon. Some troughs were observed to be partially flooded. The polygon is cracked throughout, with scrubby and sparse vegetation present. Variation in microbial communities is expected across the polygon due to differences in subsurface environment. I expect differences to be strongly represented at the center and trough locations.

At each sample point, I ran the OA-ICOS instrument for approximately 12 minutes to retrieve 10 minutes of data following the boot up sequence. Samples were taken every 0.908 s once the instrument was fully booted up. The placement of the instrument was such that the inlet of the OA-ICOS was pointed in the upwind direction at the beginning of the sample procedure for each sample point for consistency. During sampling, the operator stood downwind, over 2 m away from the instrument. To remove any influence caused by the operator moving close to the instrument when powering off the device, all data after 10 minutes was removed. The team collected data over 3 field seasons from 2022 – 2024 across 5 different polygons at the Expedition landing strip. Note that during these field campaigns, AHI experienced 24 hours of sunlight.

The sample sites for the polygonal terrain are as follows: Polygon 1, Polygon 2, Polygon 3, and Polygon 4 are shown in order of closest to farthest from the lake (Fig. 2.2). Polygons 3 and 4 are also on the other side of the regular landing strip and at a slightly higher elevation. Samples were taken at the approximate centers of the polygon, and at trough locations. I expected that methane flux would vary most between the polygon centers and troughs, given that the centers

were typically drier than the troughs. Photographs of individual polygons were taken using a DJI Mini SE at 30 m elevation with a 90 degree pointing with the intent of keeping the polygon in frame.



Figure 2.2: Google maps overview of the polygonal terrain next to Colour Lake. Sample sites are outlined with red markers indicating the trough sample locations, and blue markers corresponding to center sample locations. A faint track from the plane landings and runway can be seen between Polygons 2 and 3 and is approximated with the dashed line on the map.

2.2.2 2022 Sample Campaign

In 2022, sampling at the center and troughs of a polygon was conducted as part of a field test and demonstration (Polygon A). The sample points representing the troughs were taken mid-way along the polygon edges and one at a corner. The sample measurement of Polygon A took place when the temperature reached 18°C. Measurements of Polygon A in 2022 were taken between 10:55 and 12:30.

2.2.3 2023 Sample Campaign

For the 2023 sampling campaign, I set out to evaluate methane variability across individual polygons. I was also interested whether any observed trends for methane variability were similar at different sample sites. Given my assumption about surface morphology differences between the troughs and face of the polygon, I sampled the center and selected trough locations. In addition, temperature and relative humidity were taken near the OA-ICOS using a Honeywell dual sensor for most of the 10-minute sampling intervals and recorded (see Supplementary Information in the associated paper). I also noted the approximate wind direction using a temporary windsock.

Trough measurements were typically taken at polygon vertices and, in the case of Polygon 1, an additional sample point where a new trough appeared to be forming. Detailed GPS coordinates, sample times, and dates are provided in the Appendix of Dong et al. (2025). During the daytime, wind was typically observed to flow parallel to the valley and lake, sometime coming downslope from the campsite and across the lake. Measured daytime temperatures ranged from 14 to 28°C, and I recorded relative humidities between 28 – 52% during our operations. Our starting sample times took place between 10:42 and 18:49.

2.2.4 2024 Sample Campaign

In the 2024 field campaign, sampling was limited to one day of operations on July 14, 2024. I selected a target polygon to increase our spatial sample density following the results of previous years. The sample site with approximate spacings for the sample points relative to the center and trough are marked in Figure 3. Instead of sampling multiple trough locations, I adjusted measurement locations such that trough measurements were taken at the midpoint of the edges and crossed into adjacent polygons as two transects.

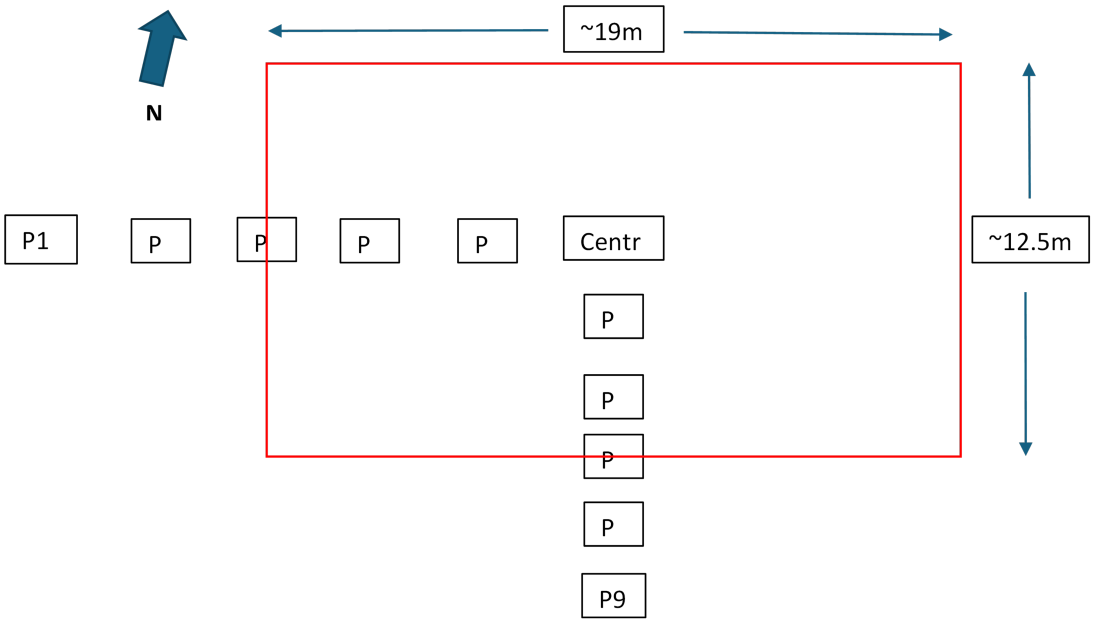


Figure 2.3: Sample point schematic for Polygon 2 in the 2024 field campaign as recorded by the operator.

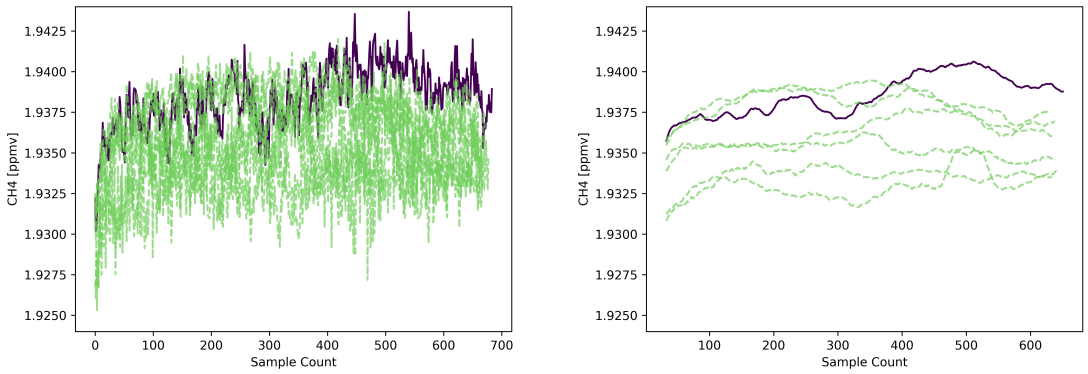
In 2024, environmental data was recorded using a Kestrel 5500 Weather Meter. The Kestrel unit recorded temperatures ranging between 0.3 – 3.2°C, with wind speeds ranging between 0 m/s and 3.4 m/s. Data was obtained between 11:00 and 13:25. The sample site was heavily obscured by fog throughout the sampling, and snow was present during the earlier measurements as seen in Figure 2.4.



Figure 2.4: Photo taken of 2024 field site during the first sample collection. Snow is visible as white streaks in the photo. Fog is visible at the surface.

2.2.5 Quick-Look Analysis

Data was not available in real-time when at the field site. Starting in 2023, I produced quick look results after each field day to evaluate the data to confirm the sample was indeed taken. This included generating raw data plots, smoothed plots with a 1-minute running average of our raw data, and finding the means and standard deviation for each of the sample runs. An example of the raw data and the smoothed running average are shown in Figure 2.5, with means and standard deviations of the data from Polygon 1 provided in Table 2.1.



(a) **(b)**

Figure 2.5: Raw data for sample site Polygon 1 (2.5a) and smoothed out with running average of 1 minute (2.5b). The center measurement is plotted in dark purple, and the trough measurements are plotted with dashed green lines. The mean and standard deviation of each run was also calculated.

Measurement Type	**Mean (ppmv)**	**Standard Deviation (ppmv)**
Center	1.9384	0.0019
Trough	1.9378	0.0017
Trough	1.9329	0.0019
Trough	1.9334	0.0016
Trough	1.9351	0.0016
Trough	1.9363	0.0015
Trough along newly forming crack	1.9378	0.0015

Table 2.1: Table of means and standard deviation from raw data retrieved from Polygon 1 (2023) sample point measurements for methane concentration. This data was not directly used for later analysis, and was produced to provide guidance on our initial hypothesis that the center of polygons would be different than that of troughs.

2.2.6 Data Processing

From the field site analysis, I observed a consistent ramp-up across all our sample point measurements (e.g. values measured between sample numbers between 0 and 100 in Figure 2.5). Consequently, I removed the first 100 samples in each sample point during subsequent analysis and all of the results.

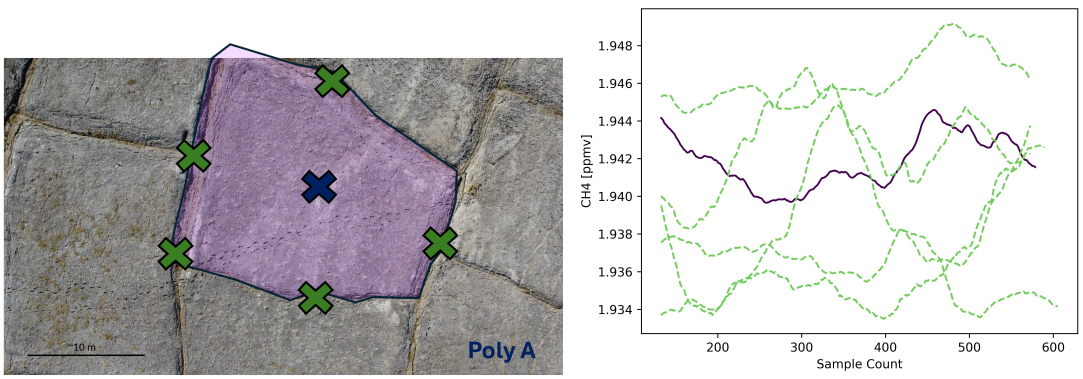
After collecting all of the sample site data, I overlaid the center and trough means for each of the sample sites to evaluate the relative methane concentrations at these locations. I also plotted the relative distance of the trough measurements from the selected center point to observe whether

there is a spatial control on the methane that can be measured at the surface.

2.3 Results

2.3.1 2022 Sample Campaign

The sample site for 2022 and the corresponding running averages are shown in Figure 2.6. 6 samples were taken at the sample points marked in the figure, with one sample point at the center, and several at trough locations. There was no observation of a strong difference between the center and trough measurements in terms of methane concentration ($p = 0.34$). However, I noted that the methane concentration at the center measurement was generally higher than 3 of the 5 trough measurements (Fig. 2.7).



(a) **(b)**

Figure 2.6: Figure 2.6a shows Polygon A highlighted in purple with sample points shown at the center (black) and trough locations (green). On the right I show the running average for the 2022 data, smoothed over 1 minute sample intervals with the same cutoff as used for the 2023 data. The center is measurement is plotted in dark purple, and the trough measurements are shown as green dashed lines.

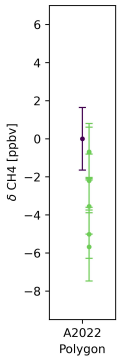
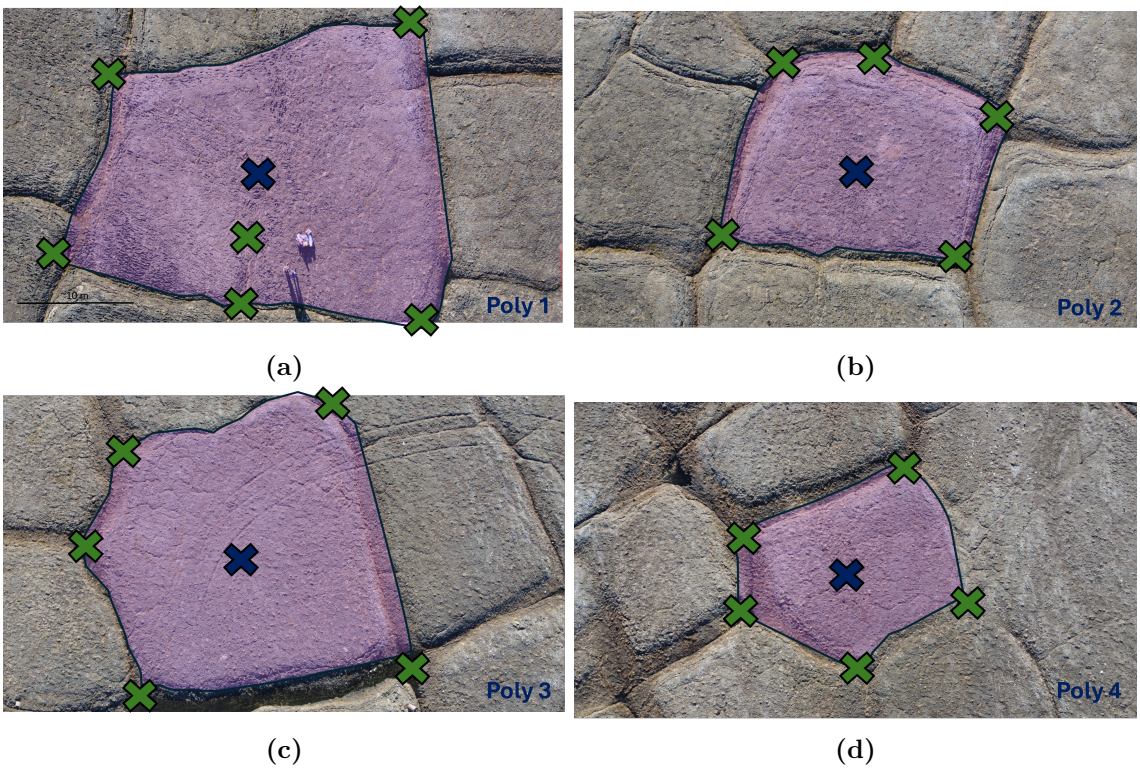


Figure 2.7: Relative methane concentration differences for mean methane measurements at Polygon A with data taken in 2022. Three of the trough measurements are below the center mean and outside of the standard deviation.

2.3.2 2023 Sample Campaign

Following the 2022 field campaign, we expanded our measurements to four additional polygons as shown in Figure 2.8 in 2023, with means and standard deviation plotted in Figure 2.9f alongside the 2022 data. I confirmed visually that the soil at the surface of the polygons was drier (paler) than that at the troughs, thus providing at least one environmental difference between the two sample site types. I also noted that some of the samples taken at some of the trough sample point locations demonstrated ponding at the surface in the 2023 field campaign as shown in blue in Figure 2.9. These trough sample points were taken at the nearest dry spot to the polygon corner.



(a) (b) (c) (d)

Figure 2.8: Drone images of sample sites Polygons 1-4 from left to right. Images were taken using a DJI SE Mini at 30 m starting altitude from the center of Polygon 1 on July 5, 2023 with a 90 degree downwards pointing. In the image from Polygon 1, a slight blurry orange in the corner is from the 3D printed skids in the camera frame. The yellow box in the picture of Polygon 1 is the OA-ICOS instrument. As Polygon 1 had a notable crack across one of the Polygon edges, I also sampled at this intersection, treating it as a trough sample point. Polygon 2 has no notable features. Polygon 3 was selected to not intersect the main airstrip, though the surface features show tracks from a plane turn in past years. Polygon 4 has poorly defined polygon edges on two sides. The markers are my best attempt to match the sample location to the image.

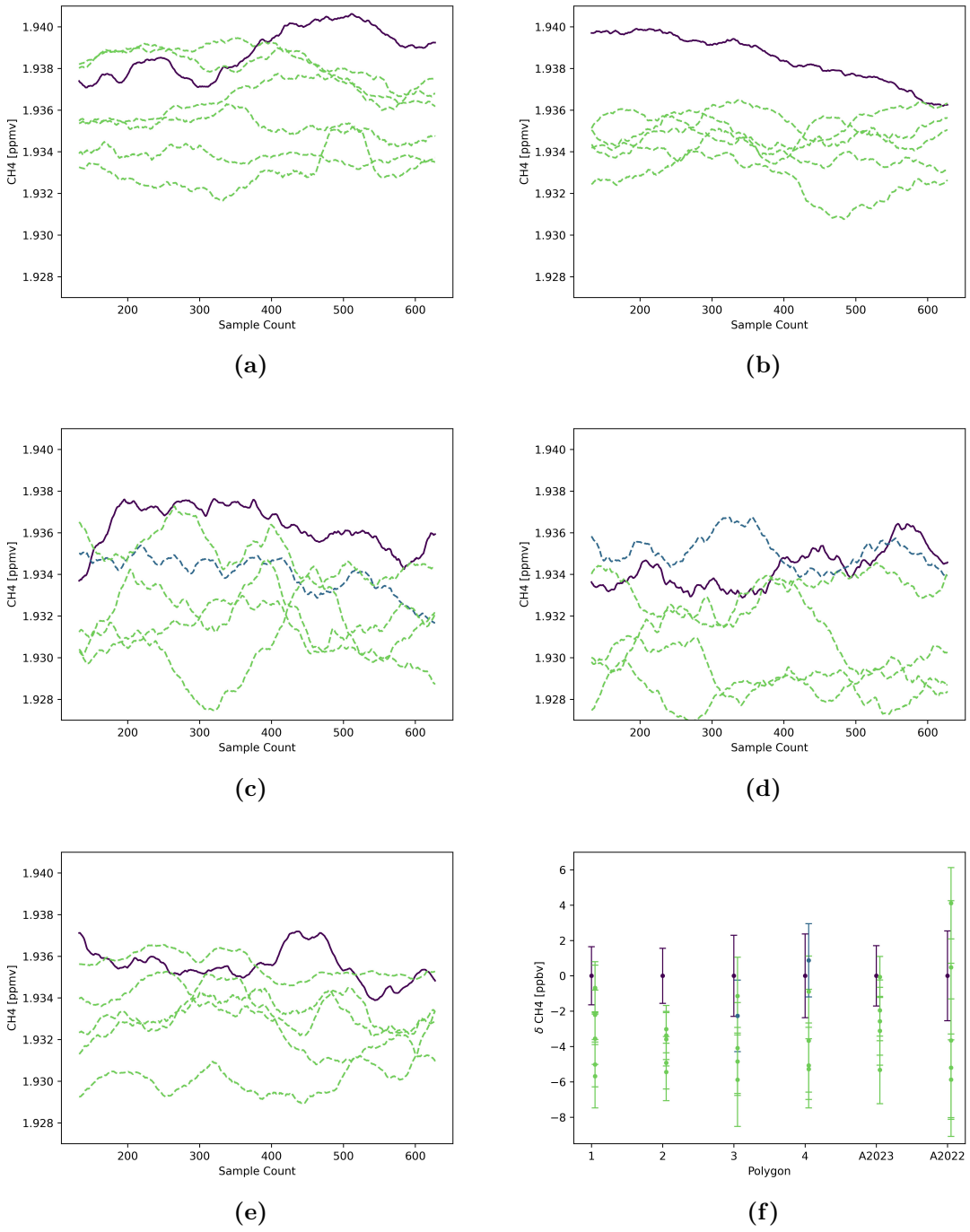


Figure 2.9: Methane concentrations for polygon sample sites taken during the 2023 field campaign plotted as running averages over 1-minute intervals. For each polygon, the center measurements are shown as solid dark purple lines, and the trough locations are as dashed green lines, where trough locations that demonstrated visible water ponding at the surface at Polygons 3 and 4 are shown as blue dashed lines. Figure 2.9f shows a of mean methane concentrations for center (dark purple) and trough (green) measurements relative to the center mean value where error bars correspond to the sample error of the mean. Trough measurements that were taken at flooded corners are indicated with a blue marker. Sample points correspond to the sampling done in the 2022 and 2023 campaigns. The center measurement generally displays a higher methane concentration than the trough measurements. The trough measurements have been shifted in time so that they are more easily discernable from the center measurements. Error bars for the trough measurements overlap.

We can observe that the average values suggest there may be some difference between the center and trough measurements in methane concentration. p-values for each polygon sampled in 2023 is as follows: $p_1 = 0.02$, $p_2 < 0.01$, $p_3 = 0.01$, $p_4 = 0.08$, $p_{A2023} = 0.04$. Similar to the observations made in 2022, the sample site data taken in 2023 show that most of the center means for respective sample sites are higher than that of the trough mean measurements at the same site. However, I note that some of the error bars do span the range and crossover into the mean value of our center and trough measurements for all polygons excepting Polygon 2.

I additionally plotted the relative distances between the center and the troughs to evaluate the potential for a general trend of decrease by plotting each sample point mean as a relative value from the corresponding center measurement. Specifically, I consider measurements from 2023 in Polygons 1 – 4 as the sampling locations were selected based on the same criteria in Figure 2.10. We can observe that many sample sites correspond with a decrease in relative methane concentration as they increase in distance from the center of the polygons. However, there is a wide spread of these methane concentration values, including one trough measurement that exceeds the corresponding center sample point. We do not find a good fit to a generally decreasing relative methane with distance trend when observing these values collectively and as individual sample sites (Fig. 2.11. While a general trend for methane variation can be observed, I were unable to satisfactorily solve for fits including a logarithmic function and the inverse square-law. I also found that a simple linear fit relating distance and methane concentration was a poor fit with the exception of Polygon 2.

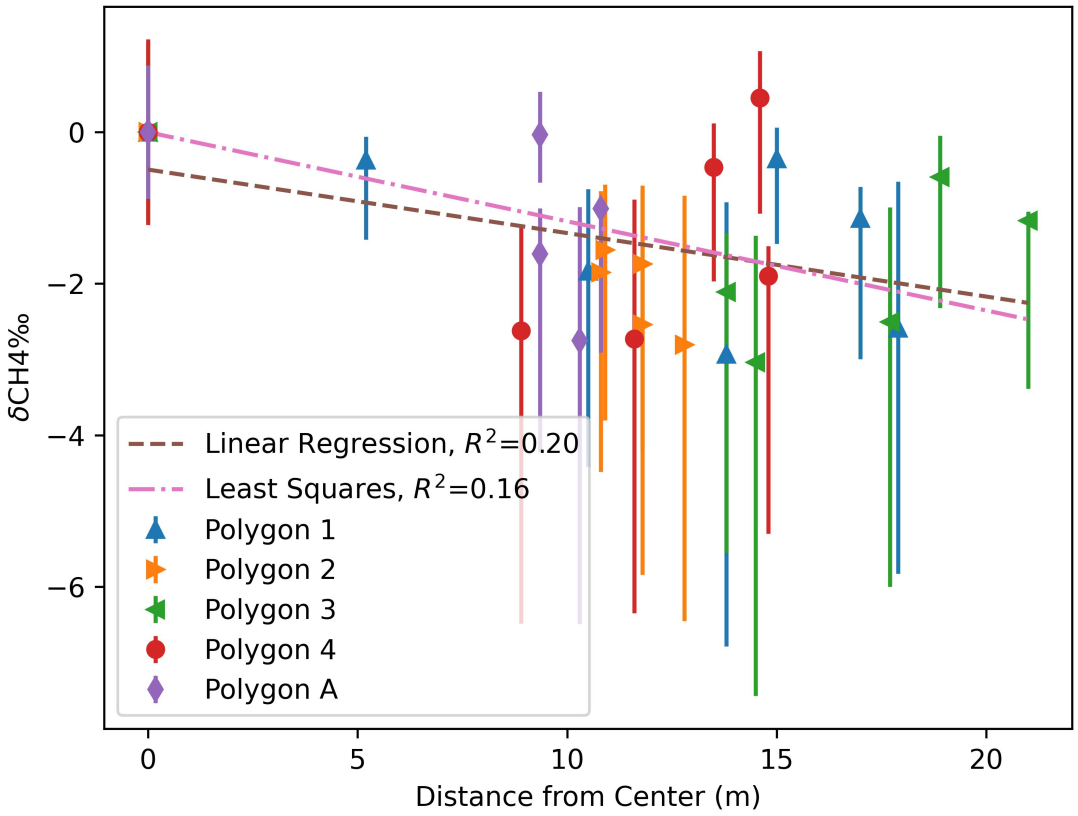


Figure 2.10: Relative methane concentration plotted as a function of distance from the polygon centers. A linear regression and least squares line has been fitted to all the data. Both fits result in low R^2 values.

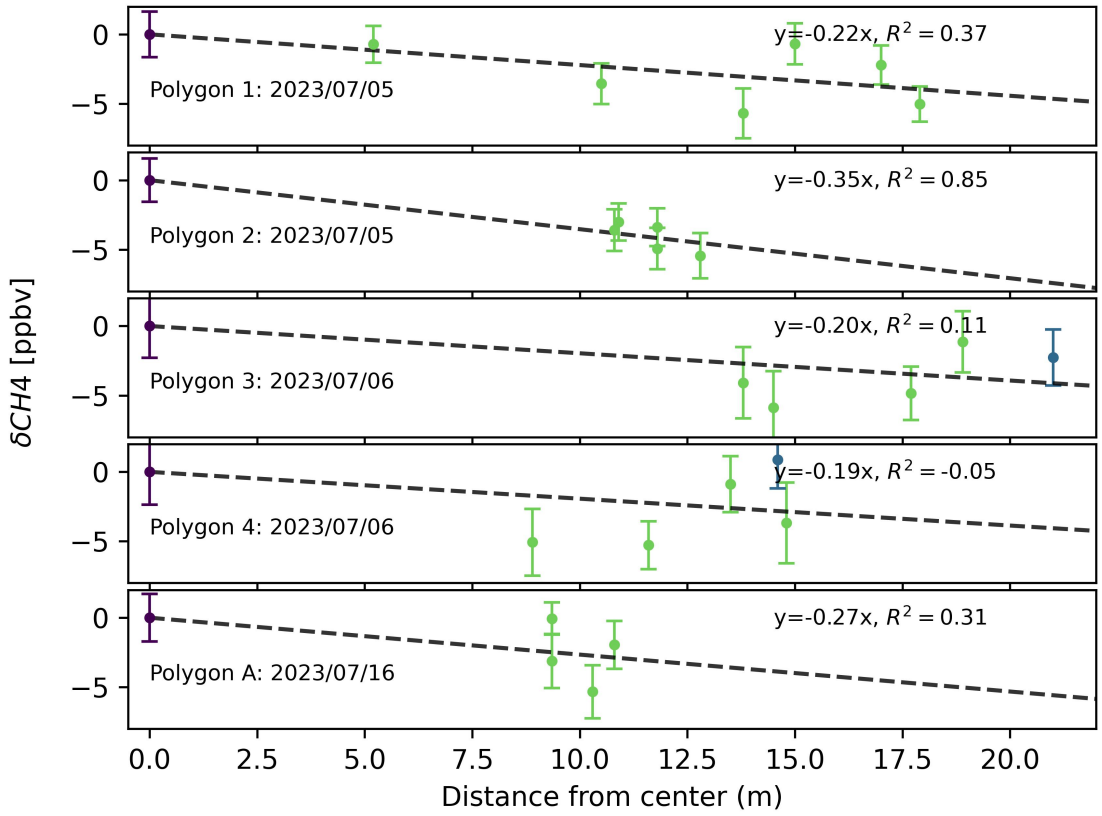


Figure 2.11: Relative methane concentration for Polygons 1 – 4 and Polygon A (2023 data) plotted as a function of distance from the polygon centers. Due to the minimal data available, I fit a straight line to our data. We observe that all of our data result in a negative slope, indicating that methane concentration is lower at a greater distance from the center.

2.3.3 2024 Sample Campaign

I treat the sample data taken in the 2024 sample campaign as two separate transects from the center of Polygon 2 crossing into the adjacent polygon. For convenience, I will refer to these datasets as Polygon 2a and Polygon 2b. We can observe that the methane concentration is consistently highest across the time series in both Polygon 2a and 2b. However, unlike 2022 and 2023, the samples taken by the operator were in between the trough measurements and into the adjacent polygon. In both 2a and 2b, we can clearly observe that the trough measurement is not the lowest methane concentration, and the intermediate measurements dip below the average trough value (Fig. 2.12). For Polygon 2b, I note that the polygon center measurement used is the same data

taken for Polygon 2a and was taken 2 hours prior to sampling the remainder of the Polygon 2b.

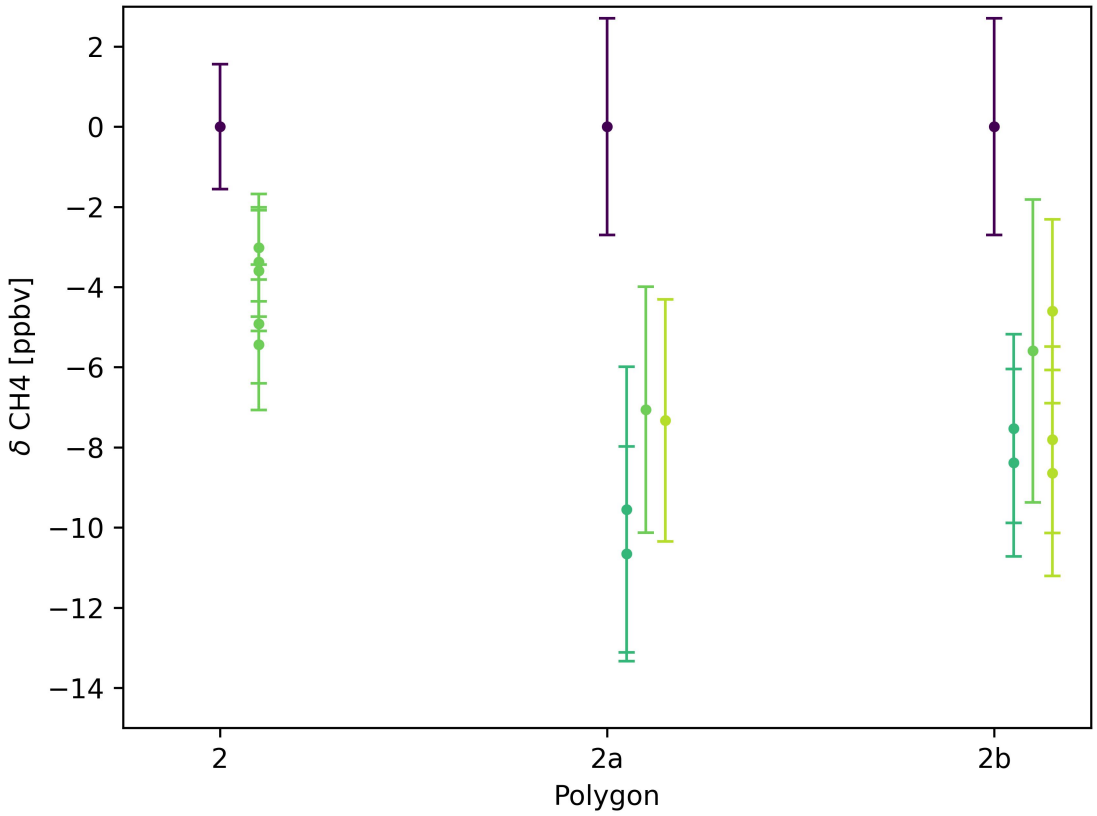
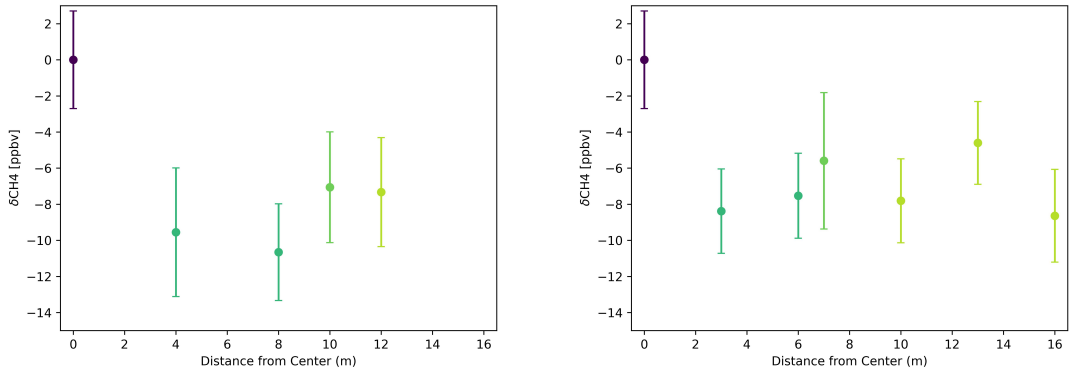


Figure 2.12: Polygon 2a and 2b mean methane measurements from the 2024 dataset. The center of Polygon 2a and 2b are shared measurements, shown as a dark purple marker. Moving outwards from the center, the dark green markers are the measurements between the center and the trough, the green marker is the trough measurement, and the light green markers are measurements taken outside of the main polygon. The 2023 data Polygon 2 is plotted for reference, with all green markers corresponding to trough measurements. For all measurements at Polygon 2, observe that the methane concentration is lower at sample points away from the center of the polygon.

The average methane concentrations are shown for both in Figure 2.13 as a function of distance from the center measurement. Observe that the mean methane concentration decreases in both cases before the trough measurement as sample locations were moved away from the center, rising at the trough, then decreasing again before nearing the center of the adjacent polygon where the concentration value begins to rise again. We did not obtain the spatial characteristics of the adjacent polygons and cannot confirm whether our measurements ended near their centers. My general observation from 2023 that our center and trough measurements are likely to be from

different populations remains the same. However, note that the generally decreasing trend that I had assumed for our 2023 data does not fit our observations from 2024. Instead, we can observe a strong similarity between all non-center measurements. In comparing the center measurement and the remainder measurements, I find p-values of less than 0.01 for both Polygon 2a and 2b, suggesting that non-center measurements belong to a different population than that of the center. I am less certain that the intermediate measurements can be separated from the trough measurements ($p_{2a} = 0.16$, $p_{2b} = 0.07$).



(a) **(b)**

Figure 2.13: Relative methane concentration to the center measurement for Polygon 2a and 2b as taken in 2024. The non-center measurements are clearly different from the center measurement values. However, the remainder measurements all fall within each other's error bars and cannot be confidently stated to be different populations. Overall, we observe a difference in the methane measurement populations, with the center measurement corresponding to the highest methane concentrations.

2.4 Discussion

2.4.1 Spatial Variability

Following the 2022 and 2023 sample campaigns, I observed that the differences in methane concentration across our sample sites and sample points indicated that methane tended to be highest at the centers of the polygons. This relationship also was observed for each individual polygon, where 4 of the 5 sample sites in 2023 resulted in a p-value > 0.05 when evaluating whether the trough measurements were a different population from the center measurements. When trying to plot the variability as a function of distance however, I found that a linear fit was not suitable for most of

our sample sites with the exception of Polygon 2 ($R^2 = 0.84$).

In 2024, I further investigated Polygon 2 by directing sampling in between the center and trough measurements and sampling outwards from the polygon along two different transects. I expected that as the operator moved outwards from the center to the trough, that the methane concentration would fall in a consistent manner, decreasing to a minimum value at the trough and thereby informing us if there was a more suitable function to describe the methane concentration decrease. I then expected the methane concentration to rise as we moved into the next polygon. While I was able to support the observation from 2022 and 2023 that the methane concentration at the center was higher than that at the troughs, the spatial variability in 2024 was different than I expected. Rather than observing the lowest values at the trough as had been previously assumed based on the 2022 and 2023 data, I found methane concentrations of similar values within several meters of the trough boundaries. While I was not able to definitively demonstrate that the center and trough locations are environmental end-members of the individual polygons, the similar methane concentration values nearby the troughs does suggest a local feature that acts as a net methane sink.

Here I note some of the shortcomings with this analog study. First is the selection of the sample points themselves. I selected the sample points based on the perceived environmental conditions, which thereby affect the population of methanogenic and methanotrophic bacteria (Lau et al., 2015, Martineau et al., 2014, Stackhouse et al., 2017). However, I did not directly sample the microbial populations nor the subsurface water saturation, temperature, soil chemistry, that would have affected the methane flux. I also noted that some of the sample trough locations were inundated with water (e.g. at Polygons 3 and 4 in 2023). This could alter gas exchange between the surface and atmosphere, limiting oxidative activity of microbial communities, and changing the community distribution and subsequent methane concentration near the surface (Christensen, 1993, McCalley et al., 2014). The effect of flooding on the local methane concentration at two of our sample points is unknown. However, I did choose to sample adjacent to the flooded areas, which may have limited these effects. Lastly with regards to sample point selection, I did not have a standardized method for selecting the centers of polygons for central measurements as the polygons were somewhat irregular.

Second, the sample device was not directly coupled to the surface when measuring the methane

concentration. The surface methane that I measured was instead mixed and diluted by the atmosphere, the most likely mode of operation for a Mars mission. I also observed changes in wind direction at some of our sample sites during the time of sampling. Changes in wind direction change the entire back trajectory of the air parcel being measured and therefore precisely what surfaces over which that air has passed. Thus, my measurements also incorporate the effects of mixing from other nearby sources and sinks of methane, and fluxes from farther sources during windy conditions.

Third, the environmental conditions were different for each field season. Specifically, the typical temperature range at our field site varied significantly between each year. While these values were not recorded with precision instruments, I can surmise that during the field season in 2022, the weather was chilly but not stormy, 2023 was unseasonably warm with clear skies, and 2024 was very cold and damp. This in turn likely affected the methane flux at the surface and the spatial distribution of different microbial communities as soil temperature and water saturation are known factors for activity of these communities (Lau et al., 2015, Stackhouse et al., 2017). As I did not have the data to disentangle these environmental factors, I evaluated each year's data independently of each other. While most sample measurements for a given Polygon were taken with a 1.5-hour span, we did note that there were changes to temperature and wind direction during these shorter intervals as well.

Furthermore, the error in the instrument itself is not characterized in this work. The OA-ICOS was not calibrated prior to field use, though it produced similar results to another spectrometer available in the field. Thus, the specific methane concentration values may not be reflective of the true methane concentration. The plots showing averages of the methane concentration are shown with the standard error of the mean. While the populations between center and troughs were different based on their p-values, the mean methane concentration has an SEM of ~ 1 ppbv. This value represents the variability of the methane concentration over the 10 minute sampling time, with the SEM shown as error bars in line with how measurements of methane on Mars are currently reported (i.e. Webster et al. (2018), Montmessin et al. (2021)).

2.4.2 Implications for Martian Methane Sampling

My work directly contributes towards future methane sampling method. As part of this, I noted several shortcomings in our methods, including the inability to directly measure methane flux from the surface and the changes in environment between field seasons. However, these shortcomings in methodology are the reality for Mars missions. It is likely that future Mars missions that measure methane will also be unable to isolate methane flux directly from the surface, and will be sampling air parcels that include a history of diffusion and incorporation of other sources and sinks. While on Mars we do not expect the changes in environment to modify methanogen and methanotroph populations as they are unlikely present, we will not be able to disentangle the effects of the seasonality and changes in weather on methane flux unless we repeatedly take measurements at the same location over several years. Thus, my work shared several characteristics of a potential methane sample campaign. Despite these restrictions, I successfully observed methane variability across meter-length scales in a Martian analogue and demonstrate the relationship between methane concentration and features in the terrain. In 2023, I was able to observe that methane varies as much as ∼3.5 ppbv over 10 m. This suggests that with the current SAM-TLS on Mars, similar spatial variability would be easily observable with an instrument comparable to the direct ingest mode with an SEM error of 2.1 ppbv, or the enrichment mode with an SEM error of 0.1 ppbv (Pla-Garcia et al., 2019, Webster et al., 2013).

Thus far, meter scale methane measurements have not been attempted on Mars due to the paucity of measurements. However, I have shown that with the instrumentation currently on Mars, it is possible to observe methane variability at the meter-scale even when methane emission is diffuse (e.g. not originating from a point source, such as a vent). Additionally, the ability to sample at high frequency spatial intervals can be important, as we observed with our second visit to Polygon 2 in 2024. Despite my initial expectation that methane would decrease in some fashion, I was unable to confirm this relationship nor were we able to find an appropriate function to match our data. However, I was able find two distinct populations of methane concentration measurements. If we can isolate the spatial distribution of different microseepage rates and methane contributions to the atmosphere on Mars, we can then progress on testing the proposed mechanisms for microseepage.

2.5 Conclusions

I found an overall trend of decreasing methane across Polygons 1 – 4 and A by evaluating the difference between the center and trough measurements. These locations represented extremes in the local environment for each polygon. We returned for a third field campaign to further investigate Polygon 2 and subsampled within the polygon face. I found that the methane concentration was lower than expected at intermediate locations between the center and troughs of the polygon rather than decreasing in a consistent fashion between the center and the trough concentrations.

I also demonstrated that methane variability due to processes comparable to Martian microseepage can be detected without penetrating the surface directly or necessitating the use of a flux chamber. I observed these relationships regardless of the different environmental conditions between the 3 field campaigns. Specifically, I find that methane concentration variability of ∼3.5 ppbv over 10 m can theoretically be observed by an instrument equivalent to the SAM-TLS onboard the MSL rover.

By constraining the spatial variability of methane at a Martian analog, I was able to relate the surface condition to the methane concentration. SFuture observations using the same methods may identify the relative contribution and distribution of methane from localized sources such as cracks and microseepage sources for a future methane sample campaign on Mars. I successfully demonstrated the use of this analog for identifying trends in methane variability. Future sampling with meter-scale frequency may better characterize the microseepage and constrain the origins and transport mechanisms of methane in the Martian atmosphere.

Chapter 3

Martian Methane Diffusion and Destruction

The work in this chapter has the following contributions:

CRediT: Elisa Dong: Writing – original draft, Validation, Methodology, Investigation, Formal analysis. Grace Bischof: Software, Methodology. John E. Moores: Conceptualization, Resources, Writing – review & editing, Supervision. Mark Gordon: Software. Madeline E. Walters: Methodology. Germán Martínez: Software, Methodology. Catherine D. Neish: Writing – review & editing, Supervision. Daniel Lo: Conceptualization.

3.1 Introduction

Observations of methane concentrations on Mars have been inconsistent with each other over the last two decades and do not align with our current knowledge of its production, destruction, and transport there. At the surface, the average background methane concentration is $\sim$ 0.4 ppbv during the nighttime. The methane concentration appears to have seasonal and diurnal variability, where methane is an order of magnitude lower during the daytime (Webster et al., 2018, 2021). All measurements at the surface of Mars have been taken within Gale Crater by the Sample Analysis at Mars Tunable Laser Spectrometer (SAM-TLS) on the Curiosity rover. SAM-TLS has also measured higher concentrations of methane up to $\sim$21 ppbv (Webster et al., 2018). Orbital measurements taken by the Atmospheric Chemistry Suite (ACS) and Nadir and Occultation for Mars Discovery instruments (NOMAD) onboard the Trace Gas Orbiter (TGO) measure no methane and an upper limit of 0.02 ppbv when accounting for the error in measurement (Korablev et al., 2019, Montmessin et al., 2021, Knutsen et al., 2021).

However, SAM-TLS, ACS, and NOMAD take measurements at drastically different altitudes. SAM-TLS samples air approximately a meter above the surface, while ACS and NOMAD observe the atmospheric column with varying depths. The theoretical optimum depths are between 15 and 25 km above the surface, though observations have probed to 5 km above the surface (Korablev et al., 2019, Montmessin et al., 2021). Furthermore, the TGO measurements are optimized for solar occultation such that methane measurements are taken at dawn and dusk. These measurements are taken several hours apart from the typical SAM-TLS measurement timing, which is near midnight. Regardless of the measurement time disparity, studies have shown that methane plumes should be readily detected from orbit. In particular, global climate model (GCM) simulations have suggested observed methane concentrations should be readily mixed into the atmosphere and detected within a few weeks (Viscardy et al., 2016, Lefèvre and Forget, 2009). It is therefore surprising that TGO consistently observes no methane.

In 2019, Moores et al. (2019b) considered the required methane flux from the surface to achieve the methane concetrations measured by SAM-TLS at the surface, and demonstrated that their estimates of methane would fall to a few parts per trillion of methanewhen mixed within the planetary boundary layer during the daytime. However, Walters (2023) modelled the atmosphere in

Gale Crater with greater resolution and found a much higher methane flux was required to satisfy the SAM-TLS methane measurements. These higher fluxes corresponded to higher a methane concentration during the daytime at the top of their model of 3 km, exceeding the TGO detection threshold. However, neither of these simulations accounted for rapid methane removal. In addition, Walters (2023)'s work presented some short-comings such as unrealistic boundary conditions and did not investigate altitudes observable by TGO.

Methane in the Martian atmosphere is generally reported to have a *e*-fold lifetime of ∼330 years (Summers et al., 2002, Wong et al., 2003, Atreya et al., 2007). However, reactions including perchlorate, a highly reactive salt thought to be widely present on the Martian surface, have been investigated for the possibility of accelerating methane destruction. Interactions with perchlorate as a methane destruction mechanism are particularly promising when we consider that perchlorate is not only at the present surface, but also readily available as a component of atmospheric dust.

Perhaps surprisingly, a study by Gough et al. (2011) demonstrated that adsorbed methane in the presence of perchlorate did not produce additional CO_2, an expected product from methane oxidation. Their results suggested that the presence of perchlorate did not contribute towards methane destruction on a meaningful time scale. Zhang et al. (2022) later revisited perchlorate as a reactant and considered the effects of incorporating UV in their simulation. In their laboratory study, they found that CO_2 and CO were produced rapidly (on the time scale of hours), but only when UV was present. In the absence of UV, they also found that their experiment had the same result as Gough et al. (2011). Zhang et al. (2022)'s work demonstrates that a rapid destruction mechanism could be operating on Mars, though this mechanism would only be active during the daytime, when UV light is available from the Sun. Using their estimated destruction rate, they found that for a simplified Martian atmosphere, methane can be destroyed on the order of hours to days in the presence of UV-activated perchlorate.

3.1.1 Zhang et al. (2022)'s Methane and Perchlorate Experiment

In Zhang et al. (2022)'s experiement, they set up a room temperature vacuum chamber pumped down to 1 mTorr. They included samples of solid magnesium perchlorate hexahydrate in the chamber. Methane was then pumped into the chamber to a partial pressure of ∼30-265 Torr such that the gas within the vacuum chamber consisted nearly entirely of methane gas. When

exposed to a UV lamp that produced light predominantly at the 254 nm wavelength, Zhang et al. (2022) observed spectral signatures indicative of methane and perchlorate reactions. They proposed that perchlorate decomposes into oxygen and chlorine reactions, and the excited oxygen reacts with methane to produce both carbon monoxide (CO) and carbon dioxide (CO_2). Zhang et al. (2022) estimated that UV activated perchlorate could remove methane at a rate of 4.8×10^{12} molecules/m^2/s if methane destruction was photon limited.

However, Zhang et al. (2022) conducted their experiement under Earth surface pressures and reacting with 100% methane instead of a Martian atmosphere representative gas. Furthermore, their estimates assumes that methane and perchlorate are evenly distributed in the entire atmospheric column, which is unrealistic.

3.1.2 Goal of this Work

In this work, I consider the effect of the fast methane destruction mechanism proposed by Zhang et al. (2022) in conjunction with the diffusion model used by Walters (2023) which includes atmospheric dynamics to simulate methane diffusion throughout the atmosphere. I evaluate whether this destruction mechanism is sufficient to explain both the diurnal variability and the methane concentration differences observed by Curiosity and TGO. As part of the simulations, I incorporate different models of eddy diffusivity, UV flux, and dust distribution to span a wide range of possible scenarios. I report on my initial findings and determine if the methane destruction mechanism and rate investigated by Zhang et al. (2022) can produce a model consistent with measurements from Curiosity and TGO. I also consider how rapidly a high concentration methane "plume" would dissipate in my simulations. In this study, I do not directly investigate the putative processes that create methane on Mars.

3.2 Methods

To investigate the fast methane destruction mechanism, it is necessary to consider the perchlorate present in Martian atmospheric dust and its reaction with methane. To track methane in the atmosphere, I implement the 1-D vertical diffusion model (VDM) from Walters (2023) to track the concentration of methane in the atmosphere between the surface and 10 km in altitude. The VDM

is run over an entire sol for sols corresponding to SAM-TLS observations taken at night (Section 3.2.1). The VDM is supported by three different atmospheric models where values of eddy diffusivity, temperature, and pressure are retrieved from. These atmosheric models are the 3D Global Environmental Multiscale Model adapted for Mars (GEM-Mars) (Neary and Daerden, 2018); the 1D University of Helsinki/Finnish Meteorological Institute model (1D UH/FMI) (Savijärvi et al., 2020); and, the Laboratoire de Météorologie Dynamique (LMD) model whose outputs are accessible via the Mars Climate Databse (Lewis et al., 2001). To incorporate the methane destruction mechanism, I describe the relationship between dust, perchlorate, photon flux, and methane partial pressure. I then prescribe two different dust profiles in the atmosphere.

In Section 3.2.2, I introduce an additional modification to the VDM by adding a simple box model at the top of the VDM spatial grid (10 km), covering the range between an altitude of 10 km and the exobase. In the box model, methane is destroyed at the typical described rate of ∼330 years (Summers et al., 2002, Wong et al., 2003, Atreya et al., 2007). The methane concentration is constant throughout this part of the atmosphere and represents the atmospheric column visible to TGO. Exchange of methane between the box and VDM is governed by the concentration of the top layer of the VDM and the box. For the coupled VDM and the box model, I repeat each sol within the entire model (VDM and box model) such that there are 30 Mars Years for model spin-up and then evaluate the concentration at the surface on the last sol of the simulation.

In Section 3.2.1, I provide an example of how I solve the coupled VDM and box model, iteratively updating the methane flux from the surface until the resulting methane concentration at the SAM-TLS measurement height (1 m) matches the observations at the time they are taken.

3.2.1 1D Diffusion in the Vertical Diffusion Model (VDM)

I use a Vertical Diffusion Model to simulate the diffusion and destruction of methane in the Martian atmosphere between the surface and an altitude of 10 km (Stroud et al., 2005, Walters, 2023). The change in methane concentration is described by

$$\frac{dC_j}{dt} = E_j - f_j + \frac{d}{dz}\left(\frac{\kappa(z_j) dC_j}{dz}\right) \tag{3.1}$$

In Equation 3.1, C_j is the concentration of methane in the jth model layer, E_j is the change

in methane concentration due to emissions from the jth layer, $\kappa(z_j)$ is the eddy diffusivity at height z_j, and f_j is the methane rate of change due to chemical reactions. In my simulations, f_j is the methane loss due to reactions with perchlorate. Additionally, E_j is a positive value and corresponds to an increase in methane concentration, f_j is a negative value and describes the decrease in methane concentration. The last term in the equation $\frac{d}{dz}(\frac{\kappa(z_j)dC_j}{dz})$ describes the change in methane concentration with time and is proportional to the eddy diffusivity coefficient. Note that eddy diffusivity is further classified into heat eddy diffusivity and momentum eddy diffusivity. I use heat eddy diffusivity here, as heat diffusivity accounts for the effects of temperature fluctuation and when different from the momentum eddy diffusivity, is larger (Tien, 1959). Note that eddy diffusivities are typically several orders of magnitude greater than molecular diffusivities (Arya, 2001). Transport from the top level into the box model is described in Section 3.2.2.

Each layer j represents an altiude within the VDM. The vertical domain consists of 10 km with 29 levels and altitudes starting at 0.3 m, 0.7 m, 1.0 m, and so on, increasing in size of levels with increasing altiude, and ending with 5000.0 m, 7000.0 m, 10000.0 m (Table 3.1). The vertical grid is chosen such that the maximum afternoon extent of the Planetary Boundary layer lies within the VDM spatial domain and align with the highest resolution atmospheric model used in this work, the 1D UH/FMI model (Moores et al., 2015, Guzewich et al., 2017, Fonseca et al., 2018). Additional levels are added at 1.0 m, 3.0 m, 4.0 m, and 5.0 m for analysis.

The model is initiated with no methane in the atmosphere such that $C_j(t = 0) = 0$ for all levels j. $E_j = 0$ at all layers except for the surface layer, as I consider the only source of methane in this model to be microseepage from the surface. Methane flux into the VDM is described in Section 3.2.1.

$\kappa(z_j)$ and f_j are updated at each half hour time-step of the VDM. Note that the half hour time-step is to match the time step of the atmospheric models where the eddy diffusivity, temperature, and pressure values are retrieved from. The values used for the eddy diffusivity coefficient $\kappa(z_j)$ at each level vary depending on the atmospheric model from which the values are sourced. I considered values from Mars Year 35 for the following atmospheric models for the closest L_s in 10°intervals: the 3D GEM-Mars model (Neary and Daerden, 2018); the 1D UH/FMI model (Savijärvi et al., 2020); and, the LMD model (Lewis et al., 2001). In instances where the eddy diffusivity coefficient was not available at each vertical grid point, I interpolate the values between the vertical grid points in

Table 3.1: Distribution of selected levels for the VDM. There are 29 levels starting at 0.3 m up to 10 km. The levels are follow those of the 1D UH/FMI model. Additional levels added for analysis are marked with an asterisk (*).

Level (j)	Altitude (m)
1	0.3
2	0.7
3	1.0*
4	1.6
5	2.0
6	3.0*
7	3.5
8	4.0*
9	5.0*
10	8.0
11	17.0
12	40.0
13	100.0
14	165.0
15	250.0
16	350.0
17	500.0
18	750.0
19	1100.0
20	1500.0
21	2000.0
22	2500.0
23	3000.0
24	3500.0
25	4000.0
26	4500.0
27	5000.0
28	7000.0
29	10000.0

the atmospheric model $\kappa(z_j)$. From each of these atmospheric models, I additionally incorporate the temperature and pressure values at each half hour time step as part the destruction mechanism for f_j (Section 3.2.1). In the previous version of this work, Walters (2023) did not incorporate f_j as there was no destruction mechanism.

During the VDM simulation, the volumetric number density of the methane is tracked in units of mol/m^3 for the diffusion and destruction rate at each time step and is converted into ppbv for analysis. In the canopy model, the diffusion and emission/destruction steps are simulated separately each minute. As the VDM is updated each half hour, I increase the length of each half hour into 31 minutes to accomodate for the longer Martian day. Each minute is repeated twice, once for diffusion and once for emission/destruction. The specific procedure is as follows: 30 s of diffusion at 1 s intervals, 1 minute of emission from the surface and destruction at 1 s intervals, and then another 30 s of diffusion at 1 s intervals (Fig. 3.1). The net effect on the methane contribution from these two steps is then combined. For each 1 s step, I solve Eq. 3.3 using the Crank-Nicholson method. After 1860 s (the half hour time step), I save the present concentration C_j and update the eddy diffusivity values E_j and destruction rates f_j for the next half hour time step of the VDM simulation. After the completion of a full sol, I repeat the sol-scenario such that there are 30 Martian years of spin-up with the intent of reaching a steady state, and I evaluate the methane concentrations on the final sol. I did test a shorter spin-up time, but found that 30 Martian years was needed to reach a steady state (see Section 3.3.2 for an example of how the diurnal trends were repeatable over the final year of simulations at the 10 km altitude and within the box model). As the box model concentration is relevant to investigating the observable methane concentration by TGO, it was sensible to ensure equilibrium at the VDM and box model boundary. Furthermore, the duration for spin-up was increased due to the VDM setup. I initiated the VDM with no methane in the atmosphere and allow for methane to build up as the spin-up progresses. As the destruction mechanism is active during the spin-up, this extends the time required to find a steady state. Note that the number of seconds does not correspond perfectly to a full Martian sol as 48 half-hours consisting of 1860 s each (31 minutes) results in an overrepresentation by approximately 505 s. Increasing the length of the sol by 505 s better reflects the length of a Martian sol than an underestimate of 2375 s, the case if each half-hour only consisted on 30 minutes.

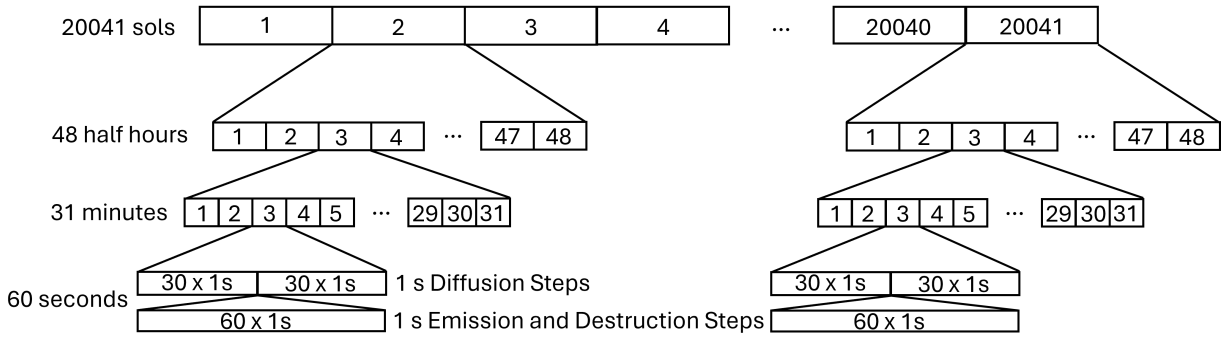


Figure 3.1: VDM simulation time steps. The simulation is spun-up for a time equivalent of 30 Mars years by repeating the same sol and atmospheric behaviour for the relevant L_s and one additional sol for evaluation. Each sol is split into 48 half-hours where the eddy diffusivity, temperature, and pressure are updated using the values from the atmospheric models, that is, one of GEM-Mars, the 1D UH/FMI model, or the LMD model. Each half hour consists of 31 minutes such that there are 1860 seconds per half hour. I run diffusion, emission, and destruction each minute separately, with the cumulative effects representing a single minute. Diffusion and emission/destruction time steps are 1 s each. As these processes are different, I first run 30 s of diffusion, then 60 s of emission and destruction, then another 30 s of diffusion to represent 1 minute of time when combined. The concentration of methane is output every half hour.

Setting Surface Emissions E_0

As part of the VDM, I provide a flux of E_0 (kg/m^2/s) from the surface. I then run the combined VDM and box model. Using the final sol of the outputs, I obtain the methane concentration at 1 m (level 3) at the half-hour closest to the SAM-TLS measurement I am comparing to (Table 3.2). I then iteratively update E_0 if the methane concentration of my simulation C_3 does not match the targeted methane concentration near the surface, e.g. fails to match the SAM-TLS measurement within a tolerance of 0.01 ppbv at the closest half hour, and rerun the full simulation including spin-up until C_3 is within the target methane value.

For example, for the SAM-TLS measurement at$L_s = 10.84°$, I run the VDM at the closest L_s for one of the atmospheric models, $L_s = 10°$. I compare the concentration of methane at an altitude of 1 m from the VDM at 0000 hours on the final sol of the simulation to the measured value of 0.319 ppbv. If $C_3(t = 0000)$ does not correspond to measured value of 0.319 ppbv, I update the value of E_0 by increasing or decreasing the flux E_0 and rerun the VDM, including the full spin-up time. I repeat this until the final sol concentration at 0000 $C_3(t = 0000)$ reaches with 0.01 ppbv of 0.319 ppbv.

Table 3.2: SAM-TLS enriched measurements of methane acquired over MY32 - 34, table adapted from Webster et al. (2018). Ingest times are reported in Local Mean Solar Time (LMST) and the standard error of the mean (SEM) values are also reported.

Ls	Ingest Time (LMST)	Simulated L_s	Comparison Time (LMST)	CH_4 (ppbv)	Error $\pm$ 1 SEM (ppbv)
10.84	0003	10	0000	0.319	0.098
32.81	0123	30	0130	0.241	0.053
70.57	0023	70	0030	0.235	0.076
103.48	0157	100	0200	0.419	0.089
142.46	2355	140	0000	0.502	0.097
158.61	0122	160	0130	0.653	0.121
216.58	0121	220	0130	0.500	0.078
265.78	0130	270	0130	0.357	0.104
298.76	2353	300	0000	0.246	0.069
331.57	2351	330	0000	0.609	0.088

Destruction Mechanism f_j

I begin with the methane destruction equation from Zhang et al. (2022)

$$f_j = \alpha A \phi \tag{3.2}$$

where f_j is the reaction rate, α is the efficiency of destroying methane molecules by UV photons ($\alpha = 3.5 \times 10^{-3}$ molecules/photon), A is the perchlorate surface area in m^2 that corresponds to the cross-sectional area that would be illuminated by sunlight such that $A = \pi r^2$, and ϕ is the photon flux in photons/m^2/s. The photon flux can be calculated from the energy flux of UV photons $P = 7.0$ W/m^2 by considering the energy for one UV photon, $\epsilon = \frac{hc}{\lambda}$, where h is Planck's constant, c is the speed of light, and $\lambda = 254$ nm, the monochromatic wavelength of Zhang et al. (2022)'s experiment. Though Zhang et al. (2022) used a UV lamp with 90% of the UV contribution from one wavelength of light, I will treat all UVC wavelengths (e.g. 200 nm – 280 nm) as capable of participating in the Zhang et al. (2022) fast destruction mechansim. For convenience, the UVC is broken down into four 20 nm bands where the photon energy for each band is represented by the average wavelength at 210, 230, 250, and 270 nm.

In Zhang et al. (2022)'s experiment, A is the entire surface area available. I assume that for Martian aerosols, there is a 1% surface area fraction where perchlorate is present given the estimated weight fraction of perchlorate in Martian regolith (Sutter et al., 2017, Hogancamp et al.,

2018, Hecht et al., 2009, Kounaves et al., 2010, Clark and Kounaves, 2016). I further restrict the area in which the reaction can take place by considering only the incident surface where UV would first encounter a dust particle. This is the cross-sectional area for each dust particle during daylight hours. Additionally, unlike Zhang et al. (2022) experiment, methane is present only in small quantities in the atmosphere. Thus, I also consider that the reaction will only take place when methane is in contact with dust which varies per level.

$$f_j = \alpha A_j \phi_j \tag{3.3}$$

where the area available for the reaction is $A_j = 0.01\pi r^2 q_j$ for the number of dust particles in each layer, q_j, where each dust particle has a radius r. The energy available for the reaction is ϕ_j.

I assume that the reaction in Equation 3.3 only takes place if methane is in contact with perchlorate. I consider adsorption to be the primary means of contact, which depends on the methane concentration, temperature, and pressure. Then, I can update Equation 3.2 such that at each level of my simulation is represented by

$$f_j = \alpha A_j \theta_j(C_j, P_j, T_j)\phi_j \tag{3.4}$$

where θ_j is the fractional area of absorption onto the dust, which is a function of methane concentration C_j, pressure P_j, and temperature T_j. I can estimate the surface area available for adsorption within each atmospheric layer θ_j is based on the partial pressure of methane, P_{CH_4}, using the Langmuir equation (Moores et al., 2019b)

$$\theta_j = \frac{k_{eq} P_{CH_4}}{1 + k_{eq} P_{CH_4}} \tag{3.5}$$

where

$$k_{eq} = 6.073 \times 10^{-6} T_j^{-\frac{3}{2}} \frac{\gamma}{\eta} \exp \frac{\Delta H}{R T_j} \tag{3.6}$$

and

$$P_{CH_4} = P_j C_j 10^{-9} \tag{3.7}$$

When C_j is provided in ppbv and P_j is the pressure provided by the atmospheric models described in Section 3.2.1. I choose the enthalpy of adsorption $\Delta H = 25$ kJ/mol where ΔH ranges between 16 to 25 kJ/mol and $R = 8.314$ J/mol/K is the universal gas constant (Moores et al., 2019a). Note that Moores et al. (2019a) uses a higher enthalpy constant of $\Delta H = 31.5$ kJ/mol for their equilibrium absortion constant. T_j is the temperature at each altitude provided by the atmospheric models in Section 3.2.1, γ and η are the uptake and evaporation coefficient respectively, which I set such that $\frac{\gamma}{\eta} = 1$,as in Moores et al. (2019b) and Gough et al. (2010).

To distribute the number of dust particles in each jth layer, I assume the total number of dust particles, q_0, can be estimated from the number of mie particles estimated by the radiative transfer model (Griffith et al., 2012, Smith et al., 2020). I further assume that all of the dust is present within the 10 km VDM. To distribute the dust throughout the VDM, I consider a well-mixed dust profile and a Conrath profile described by (Conrath, 1975)

$$q_j = q_0 \exp(\nu(1 - \frac{1}{\exp -\frac{z_j}{H}})). \tag{3.8}$$

Here, q_j is the number of dust particles above altitude z_j, q_0 is the number of dust particles above the surface, and H is the scale height. In this case, I set $H = 11$ km following Savijärvi et al. (2020). ν is the Conrath coefficient, which typically ranges between 1 - 4 (Heavens et al., 2011). I use $\nu = 3$ for the vertical profile. Note that $\nu = 0$ is equivalent to a well-mixed dust profile (Fig. 3.2).

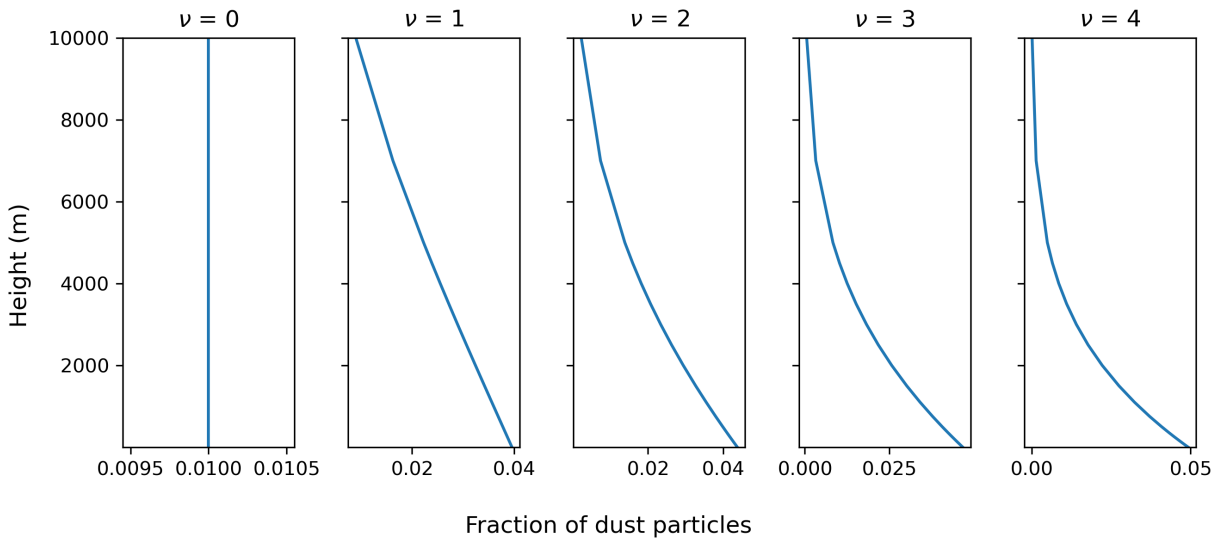


Figure 3.2: Fraction of total dust particles in the atmosphere for varying Conrath coefficients and corresponding dust profiles over 10 km. When $\nu = 0$, the dust profile is well-mixed. As ν increases, the concentration of dust increases towards the surface. The total amount of dust in these profiles is the same.

To estimate the total amount of dust in the atmospheric column and UV flux at each sol L_s, I use the radiative transfer model described by Griffith et al. (2012), Smith et al. (2020) in 20 nm increments. This model outputs the surface flux at different times of the sol and the atmospheric column opacity at a given wavelength using an input from the total number of mie particles in the atmosphere.

To first find the number of mie particles, q_{mie}, the radiative transfer model is run at the 880 nm wavelength. I use the 880 nm wavelength as the model outputs can be validated against regular observations taken within Gale Crater by the Mastcam camera. The Mastcam camera on the Curiosity rover regularly makes observations of the total atmospheric column opacity, τ_0 at 880 nm from within Gale Crater (Smith et al., 2020, Bischof et al., 2024). The number of mie particles is adjusted until the radiative transfer model outputs a total column opacity that matches the average observed opacity, τ_0, at solar longitude of interest (Table 3.3) (Smith et al., 2020).

The mie particles have an optical radius of 1.4 μm, following Griffith et al. (2012), Smith et al. (2020). However, I am interested in a representative dust particle and the mean dust particle radius is $r = 0.5\mu$m using Equation 12 in Tomasko et al. (1999). The number of dust particles q_0 for each sol can then be calculated by redistributing the mass of the gamma distribution for a mean dust

Table 3.3: Number of mie particles q_{mie} as retrieved from the radiative transfer model. q_{mie} is adjusted until the opacity as observed from the surface at 880 nm matches the observations from the average Mastcam tau observations for a given L_s.

Simulated L_s	Total number of mie particles q_{mie}	τ_0
10	2.96E+06	0.579
30	1.98E+06	0.376
70	1.57E+07	0.330
100	1.87E+06	0.336
140	2.54E+06	0.338
160	4.09E+06	0.604
220	1.02E+07	0.980
270	7.17E+06	1.000
300	5.67E+06	0.705
330	6.07E+06	0.939

particle radius of $r = 0.5\mu$m. The total number of dust particles q_0 are then distributed amongst the layers, z_j, following either a well-mixed dust profile, or a Conrath profile of $\nu = 3$ (Eqn. 3.8).

I assume that the photons from the UVC band between 200 and 280 nm may contribute to the Zhang et al. (2022) derived destruction rate (Eqn. 3.3). To find the UV flux contribution at each UVC band, I rerun for my target wavelengths (200 – 280 nm in 20 nm band sections) with the same number of mie particles from the 880 nm run. I can then estimate the available UV flux at each layer ϕ_j for each 20 nm UVC band $n = 200n - 200(n + 1)$ based on the relationship between the opacity τ_j (which corresponds to the dust concentration) at each layer,

$$\phi_j(n) = \phi_0 \exp(-\Delta\tau_j) \tag{3.9}$$

where $\Delta\tau_j = \tau_0(\frac{q_j}{q_0})$ is the relative difference in opacity between each layer j, and τ_j is proportional to the number of particles at q_j above layer j. The total UV flux at each level is the sum of each 20 nm UVC band contribution such that $\phi_j = \sum_{i=0}^{3} \phi_i$.

I now have an updated destruction and removal mechanism for each level to solve for Equation 3.4 that incorporates the dust distribution profiles, the surface area in which perchlorate is exposed to UV, the adsorption of methane, and the available UVC flux.

Methane Transport - Eddy Diffusivity Coefficients $\kappa(z_j)$, Pressure P_j, and Temperature T_j

The heat eddy diffusivity coefficients (from here on, eddy diffusivity) at each layer are estimated using three different atmospheric models, with an example shown in Figures 3.3 and 3.4. Generally, eddy diffusivity approximates the transport of atmospheric constituents by mixing. From each atmospheric model, I retrieve the relevant eddy diffusivity, pressure, and temperature profiles for the relevant L_s.

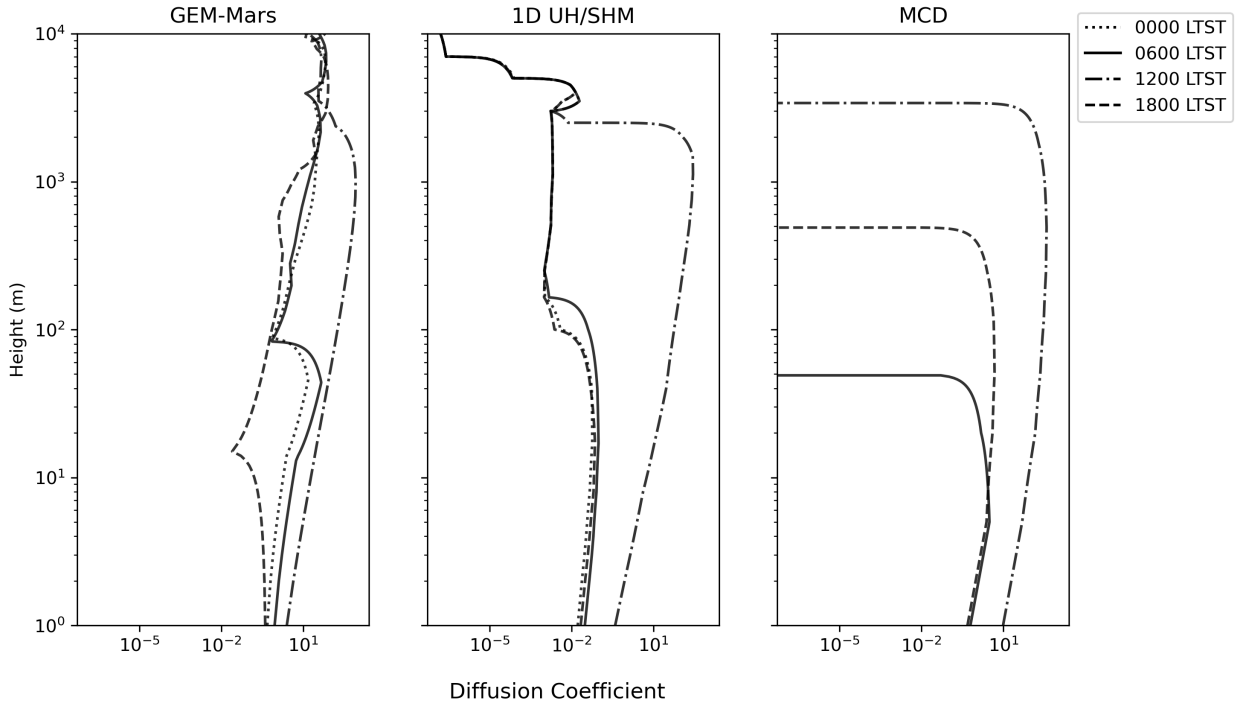


Figure 3.3: Example of eddy diffusivity coefficients from three different atmospheric models at $L_s = 220°$. The three atmospheric models show a wide range of eddy diffusivity coefficients both at the surface and throughout the 10 km profile. At all times of sol, the 1D UH/FMI model shows a sharp decline in eddy diffusivity near the top of the 10 km profile, whereas the GEM-Mars model generaly shows an increase in eddy diffusivity as the atmospheric profile increases. The LMD model shows a sharp cutoff in the atmosphere where the eddy diffusivities fall to the molecular diffusivity limit. Note that the LMD model eddy diffusivity coefficients are 0 m^2/s at midnight for all L_s.

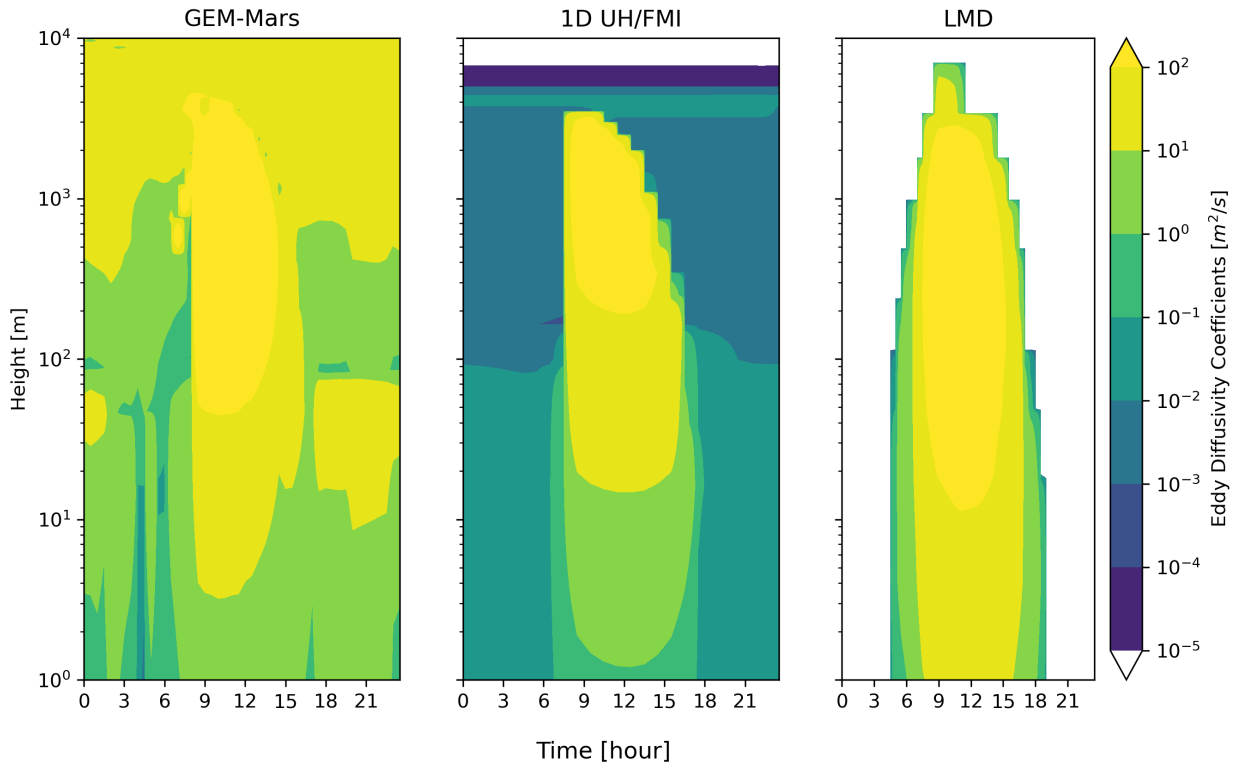


Figure 3.4: Example of eddy diffusivity coefficients for three different atmospheric models for $L_s = 220°$. This plot captures the same information as the previous image (Fig. 3.3) but includes eddy diffusivities representative of the entire sol for each atmospheric model. Higher values correspond with increased atmospheric mixing and transport between levels. Generally, mixing near the surface is increased during the daytime with the greatest mixing between dawn and midday for all models. Eddy diffusivity values are highest during the daytime between ∼100 - 5000 m in the atmosphere. In both the 1D UH/FMI and LMD models, atmospheric mixing is inefficient towards the top of the VDM. In contrast, GEM-Mars is expected to efficiently transport methane from the mid-altitudes to the top of the VDM.

I choose to use three different atmospheric models as their behaviours vary depending on the assumptions within each model. For example, I observe that the LMD model produces no atmospheric mixing at midnight, which differs from the GEM-Mars and the 1D UH/FMI model. Additionally, the atmospheric models exhibit altitudes where atmospheric mixing is reduced, and in the case of the LMD model, entirely suppressed. These differences are expected to lead to different methane concentrations throughout the atmosphere. GEM-Mars generally has increased atmospheric mixing throughout the column compared to the other atmospheric models, and thus increased methane transport with increasing altitude, while both the 1D UH/FMI and LMD model are expected to have inefficient methane mixing higher in the atmosphere. I briefly describe each

of the models and their governing physics in Section 3.2.1.

Atmospheric Models

In this work, I considered two 3D Global Climate Models, GEM-Mars and the LMD model, and a 1D model, the 1D UH/FMI model. These three atmospheric models are run separately from the VDM. The eddy diffusivity, temperature, and pressure values from the atmospheric models for MY35 are then used in the VDM. In the GCMs, the topographical information was retrieved from the Mars Orbiter Laser Altimeter (MOLA). All of the atmospheric models have vertical layers that are more densely packed near the surface, with the distance between layers increasing higher in the atmosphere. Other atmospheric models such as the Mars Weather and Research Forecasting model (MarsWRF) and the NASA-Ames GCM exist, though were not available for comparison at the time of this study.

An overview to the stability functions and how eddy diffusivity coefficients are calculated for the respective models is summarized in Appendix A. Note that the eddy diffusivity values as interpolated from these models sometimes falls to 0. In such instances, I update the diffusivity to align with the molecular diffusion limit as described in Moores et al. (2019b) as molecular diffusivity may be greater than mixing from turbulence under conditions of low winds and low convection and a diffusivity of zero is non-physical.

GEM-MARS GEM-Mars is a 3D global climate model (GCM) based on the Global Environmental Multiscalemodel Model (GEM 4.2.0), the standard GCM for operational weather forecasting by Environment Canada adapted for Mars. I use the version with the most recent update in 2018 (Neary and Daerden, 2018). This model was previously used to demonstrate that methane on Mars can have variability in its vertical distribution, taking several weeks for it to be uniformly mixed in the atmosphere (Viscardy et al., 2016).

GEM-Mars includes carbon dioxide, dust, water, and atmospheric chemistry including photochemistry and gas-phase chemistry. The vertical grid has 103 thermodynamic layers and 102 momentum layers up to 150 km altitude. The levels are spaced more closely near the surface, starting at 2 m above the surface, and farther apart towards the top of the model excepting the spacing between 10 and 50 km, where the spacing between levels is $\sim$1 km to vertical details in the atmo-

sphere Daerden et al. (2015). Overall the vertical resolution aligns well with the solar occulation measurements from NOMAD. The horizontal resolution of the model is 4° x 4° corresponding to 237 x 237 km at the equator. The topography obtained from MOLA is binned into a 0.25° x 0.25° grid. The surface heat budget is estimated from solar and infrared sources using radiative transfer calculations, outbound infrared emissions, and thermal conduction in the soil. Notably, the base of this model where $z_0 = 0$ m is higher than that of the true surface of Gale Crater, as Gale Crater is only 154 km in diamater, too small to be resolved by the model. The eddy diffusivity coefficients from GEM-Mars begin at -2.2 km below the datum (the triple point of water), corresponding to approximately 2 km above the surface of Gale Crater (Vasavada et al., 2014). While the model has accounted for this difference by adjusting the model surface pressure hydrostatically, the pressures at Gale Crater deviate up to 20 Pa in most instances, with an overestimate of pressure during northern winter and underestimate in southern winter (Neary and Daerden, 2018).

Performance testing of GEM-Mars considered datasets from TES for thermal profiles and total dust opacities, the Mars Climate Sounder (MCS) for long term temperature, dust and ice vertical profiles, surface temperature and pressure measurements from the Rover Environmental Monitoring Station (REMS) aboard Curiosity (Neary and Daerden, 2018).

Within the PBL, the eddy diffusivity coefficients describing vertical transport are derived using a turbulent parameterization scheme by calculating turbulent diffusivity (Holtslag and Boville, 1993). GEM-Mars follows Holtslag and Boville (1993) by using a non-local scheme that deviates from the one described in Appendix A that uses the bulk Richardson number rather than the gradient Richardson number. The countergradient term γ_c was removed from the flux equation per Daerden et al. (2015). Above the PBL, eddy diffusivities are calculated using a mixing length of 500 m and the stability is dependent on the gradient Richardson number Ri (Holtslag and Boville, 1993). The surface energy flux drives the evolution of the soil temperature via heat diffusion, which then transfers into the atmosphere. The soil temperature prediction model follows Savijarvi (1992). Surface albedo, thermal inertia, and surface roughness length come from the Thermal Emission Spectrometer (TES) (Christensen et al., 2001, Putzig et al., 2005, Hébrard et al., 2012, Neary and Daerden, 2018).

1D University of Helsinki/Finnish Meteorological Institute Column Model (1D UH/FMI Model) The second model I consider is a 1D column model based on the University of Helsinki/Finnish Meteorological Institute model (Savijärvi et al., 2020), which was previously developed to simulate data for both the Phoenix and Viking landers. The latest version of this model incorporates more detailed soil temperature profile and geostrophic winds with a diffusion-adsorption model for water vapour (Savijarvi, 1999). The soil temperature profile is estimated from the thermal inertia as measured by the Mars Odyssey Thermal Emission Imaging System (THEMIS). Additionally, the Visible and Infrared Mineralogical Mapping Spectrometer, OMEGA, onboard Mars Express was used to derive albedo. The water vapour content was taken from co-located Compact Reconnaissance Imaging Spectrometer for Mars (CRISM) values from the Mars Reconnaissance Orbiter (MRO), which are in good agreement with the Curiosity ChemCam measurements. Opacity and surface pressures are provided by the Mastcam and Rover Environmental and Monitoring Station (REMS) instruments onboard Curiosity, respectively, with the change in pressure controlled by a scale height of 11 km. Dust is well-mixed in this model.

This model has a higher resolution at the surface than the other two atmospheric models as it was developed to reproduce measurements taken at 2 m above the surface (Savijarvi, 1999). This model also incorporates the effects of a full hydrological cycle and ice cloud and fog physics. The base of this model corresponds to the true altitude of Curiosity as the values are estimated based on REMS local surface pressures. Winds are provided by a constant geostrophic wind. Depending on the surface roughness length that is assumed, the values for diffusivity change significantly when close to the surface. The 1D UH/FMI model used in this work assumes a surface roughness length of 10 cm.

The surface flux and turbulence in this model follow Monin-Obhukov similarity theory at the surface as where the stability function at the surface is defined in Appendix A. Above the surface, the Blackadar (1962) approach is followed.

Laboratoire de Météorologie Dynamic Mars GCM - The LMD Model Third, I use the Mars Climate Database (MCD) to retrieve atmospheric values of eddy diffusivity, pressure, and temperature from the Laboratoire de Météorologie Dyanmique Mars Global Climate Model v3.0. This model has a vertical range of 0 to 120 km with 32 vertical layers, MOLA topography at

a resolution of 32 pixels/degree, and thermal inertia data from the Mars Global Surveyor TES. This model also incorporates solar and thermal infrared fluxes at the surface and at the top of the atmosphere. Realistic dust scenarios are incorporated from observations from MGS. The horizontal resolution of the MCD output is 5° x 5°.

The initial development of the model regarding the methodology for radiative transfer, impact of CO_2, dust absorption/emission and diffusion employed by this model are described in (Forget et al., 1999). Updated dust properties in the newest version includes optical properties of dust and vertical dust interactions from Madeleine et al. (2011) and Wolff et al. (2009). The vertical distribution of dust in the LMD model follows an adapted form of the Conrath profile. I chose to use a scenario for MY35 for dust loading and daily solar extreme ultraviolet input. I did not include small scale variability (e.g. gravity waves which propagate with increasing altitude) nor large scale variability represented by the Empirical Orthogonal Functions for large scale variance in space and time to describe horizontal correlations.

The surface temperature is controlled by an 11-layer soil model as described by Hourdin et al. (1993). Turbulence at the surface is a function of wind velocity and surface drag, which is then dependent on the von Kármán constant and surface roughness coefficient, in this case, 0.01 m as suggested by Haberle et al. (1993) and is the same as the roughness coefficient used for the 1D UH/FMI model. Mixing coefficients above the surface are based on an equation for turbulent kinetic energy evolution with a turbulent mixing length following (Blackadar, 1962). Mixing within the PBL utilises a thermal plume model described in Colaïtis et al. (2013).

3.2.2 Box Modelling - 10 km to the Exobase

To investigate the upper atmosphere including the portion of the atmosphere that is visible to TGO, I also include a simple box model to track the methane concentration above the first 10 km from the base of the atmospheric models (e.g. the vertical span covered by the VDM). This box represents the remainder of the atmosphere up to the exobase. Methane enters the box model when the gradient between the top level of the VDM is positive in the direction of the box (e.g. Fick's first law).

$$F_{box} = -\kappa_{top} \frac{C_{box} - C_{top}}{z_{box-top}} \tag{3.10}$$

Once methane enters the box, it is instantaneously mixed throughout the box such that the concentration in the box is the same throughout. Methane is not allowed to re-enter the VDM. I assume there is no dust present in the box, and thus, the destruction mechanism from Zhang et al. (2022) does not apply. The only removal of methane from the box is the typical ∼330 year life time for methane (Summers et al., 2002, Wong et al., 2003).

3.3 Results

This section presents results of my combined VDM and box model using a well-mixed dust profile and Conrath profile of $\nu = 3$ using the destruction rate proposed in Equation 3.3. Most examples shown are of $L_s = 30°$ (moving towards aphelion) and $L_s = 220°$ (moving towards perihelion), which are roughly half a Martian year apart and representative of the general trends I observed. Where images and results only describe the well-mixed dust profile, the results for the Conrath profile of $\nu = 3$ dust profile are similar.

I report on the estimated flux required in each of the scenarios for different dust profiles and atmospheric models required to match the SAM-TLS methane values at 1 m close to the time of the SAM-TLS measurements (Section 3.3.1). In most scenarios, it is possible to both satisfy the SAM-TLS concentration at the time of measurement and remain below the detection threshold of TGO. I also describe the overall trends in methane concentration throughout the atmospheric column throughout a full sol as methane is added from the surface. Section 3.4.2 demonstrates how large plume-like sources of methane can be quickly removed from the atmosphere. Lastly, I show that the destruction mechanism has an impact on the methane concentration in the atmosphere in comparison to a model simulation without destruction (Section 3.3.5). The effect of different dust-profiles was minimal, as such, commentary on the different dust-profiles can be found in the Appendix B.

3.3.1 Methane Flux Estimates

The microseepage fluxes were constrained by matching the model results to the closest L_s from SAM-TLS enriched measurements during Mars Year 35, an example solution is shown in Figure 3.5. Table 3.4 shows the resultant fluxes that are required across the three different diffusivity models to obtain a methane concentration within 0.01 ppbv of the SAM-TLS measurements for a Conrath profile of $\nu = 3$ and a well-mixed dust profile. Where not possible, I report the methane flux estimate that corresponds with the closest methane concentration to the SAM-TLS values.

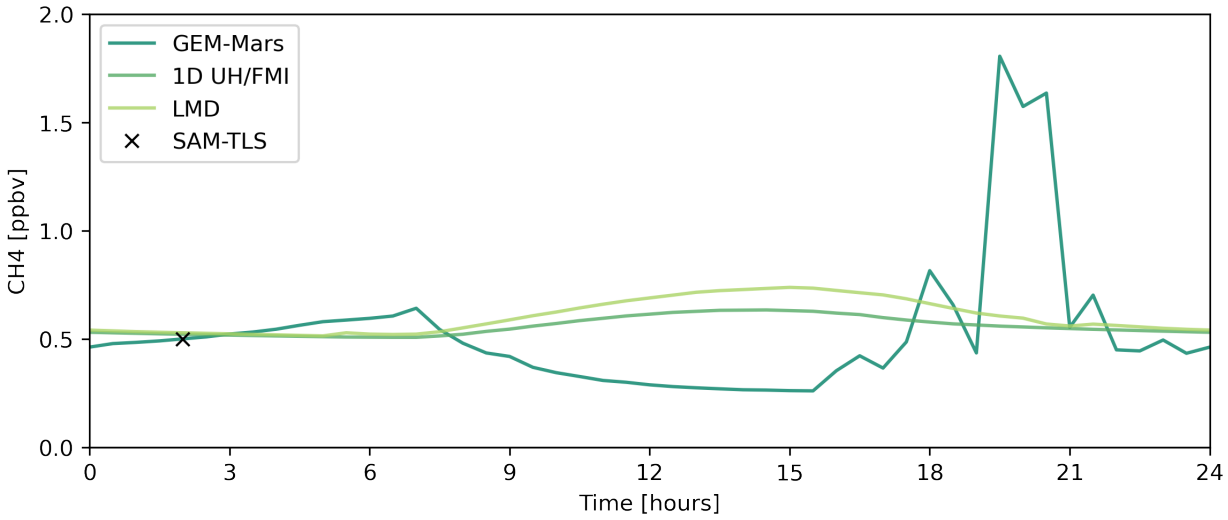


Figure 3.5: Methane concentration at 1 m on the final sol of the simulation for three different atmospheric models targeting the SAM-TLS value of 0.5 ppbv (marked with an "x") for an example of a well-mixed profile at $L_s = 220°$. Here, the methane concentration near the surface for GEM-Mars shows expected behaviour with methane showing a relative increase in the nighttime and decrease during the daytime. In contrast, both the 1D UH/FMI and LMD models show that methane stays relatively stable throughout the nighttime with a gradual increase in methane at 1 m above the surface during the day. Explanations for the behaviour of methane concentration variability throughout a Martian sol can be found in Section 3.3.2

In all of the simulations using the GEM-Mars eddy diffusivity values, I was able to find a methane flux that resulted in a surface methane concentration close to the SAM-TLS values. In contrast, over half of the solutions I found using the LMD eddy diffusivity values resulted in surface methane concentrations that were in excess of a 0.01 ppbv deviation despite an iterative approach for methane flux estimates. However, I note that the surface methane concentrations were still within one standard error of the mean from SAM-TLS values. Simulations using the 1D UH/FMI model had solutions that were within 0.01 ppbv of the SAM-TLS values, in excess of the 0.01 ppbv

Table 3.4: Estimated surface flux E_0 required to match enriched SAM-TLS measurements at the surface in units of kg/m^2/sol. The table is split into two parts for readability. Values from Moores et al. (2019b) are also included for comparison. The values I estimated for the three different atmospheric models are listed for the well-mixed dust profile and the Conrath profile of $\nu = 3$. Where flux estimates are different for the two different dust profiles, the Conrath profile is reported as the second value. Flux values marked with an asterisk(*) are estimates where I was unable to find a flux that resulted in a methane concentration at 1 m above the surface close to the SAM-TLS measurement timing within 0.01 ppbv.

Webster et al., 2021 (rounded)	Moores et al., 2019 (well-mixed)	Moores et al., 2019 (stably stratified)	GEM-Mars (well-mixed)	GEM-Mars ($\nu = 3$)
10.84 (10)	10.3E-11	5.7E-11	8.48E-10	8.48E-10
32.81 (30)	8.41E-11	4.72E-11	7.14E-10	7.14E-10
70.57 (70)	8.06E-11	4.52E-11	6.00E-10	6.00E-10
103.48 (100)	13.3E-11	7.38E-11	1.04E-09	1.04E-09
142.46 (140)	16.7E-11	9.16E-11	1.15E-09	1.15E-09
158.61 (160)	21.1E-11	11.6E-11	1.59E-09	1.59E-09
216.58 (220)	14.6E-11	8.04E-11	1.52E-09	1.52E-09
265.78 (270)	11.9E-11	6.62E-11	1.31E-09	1.31E-09
298.76 (300)	10.0E-11	5.67E-11	8.83E-10	8.83E-10
331.57 (330)	25.1E-11	14.1E-11	1.82E-09	1.82E-09
Average	13.5E-11	7.75E-11	1.15E-09	1.15E-09

Webster et al., 2021 (rounded)	1D UH/FMI (well-mixed)	1D UH/FMI ($\nu = 3$)	LMD (well-mixed)	LMD ($\nu = 3$)
10.84 (10)	1.93E-11*	1.94E-11*	2.58E-12	2.58E-12
32.81 (30)	1.03E-11	1.03E-11	2.60E-12*	2.60E-12*
70.57 (70)	1.29E-11	1.30E-11	3.04E-12*	3.05E-12*
103.48 (100)	1.70E-11*	1.69E-11*	2.29E-12*	2.29E-12*
142.46 (140)	2.03E-11*	2.03E-11*	4.16E-12	4.16E-12
158.61 (160)	2.41E-11*	2.41E-11*	7.37E-12*	7.37E-12*
216.58 (220)	1.77E-11*	1.77E-11*	4.79E-12*	4.80E-12*
265.78 (270)	1.21E-11	1.21E-11	3.81E-12	3.81E-12
298.76 (300)	8.41E-12*	8.41E-12*	1.78E-12*	1.77E-12*
331.57 (330)	2.32E-11*	2.32E-11*	4.68E-12*	4.68E-12*
Average	1.65E-11	1.65E-11	3.71E-12	3.71E-12

tolerance but within one SEM.

Strikingly, the different atmospheric models allowed for methane fluxes over three orders of magnitude. This difference is strongly linked to the eddy diffusivity and methane transport efficiency at night. The LMD model reduces surface mixing into the atmosphere at night to the molecular diffusion limit, allowing methane to quickly build up near the surface. At the SAM-TLS measuring altitude of 1 m, methane concentration is stable overnight. In contrast, the GEM-Mars model is variable throughout the night and transports methane from the 1 m SAM-TLS measurement more efficiently into the remainder of the atmosphere thereby requiring a higher methane flux to compensate for the diffusion. The 1D UH/FMI model behaviour at nighttime falls between the two other atmospheric models as mixing takes place during the night, but generally at a lower rate compared to the GEM-Mars model.

The behaviour of the estimated surface methane flux E_0 is similar in all of my simulations throughout MY35 (Fig. 3.6). Methane flux peaks at $L_s = 160°$ and 330°, consistent with seasonal increases in eddy diffusivity near the surface Figure 3.6. I additionally observe a consistent dip in methane concentration for all of the atmospheric models at $L_s = 300°$. These peaks and dips align with methane surface flux estimates derived by (Moores et al., 2019b) despite the simplified assumptions they used. However, I do not consistently observe a similar dip at $L_s = 30°$ and 70° to Moores et al. (2019b).

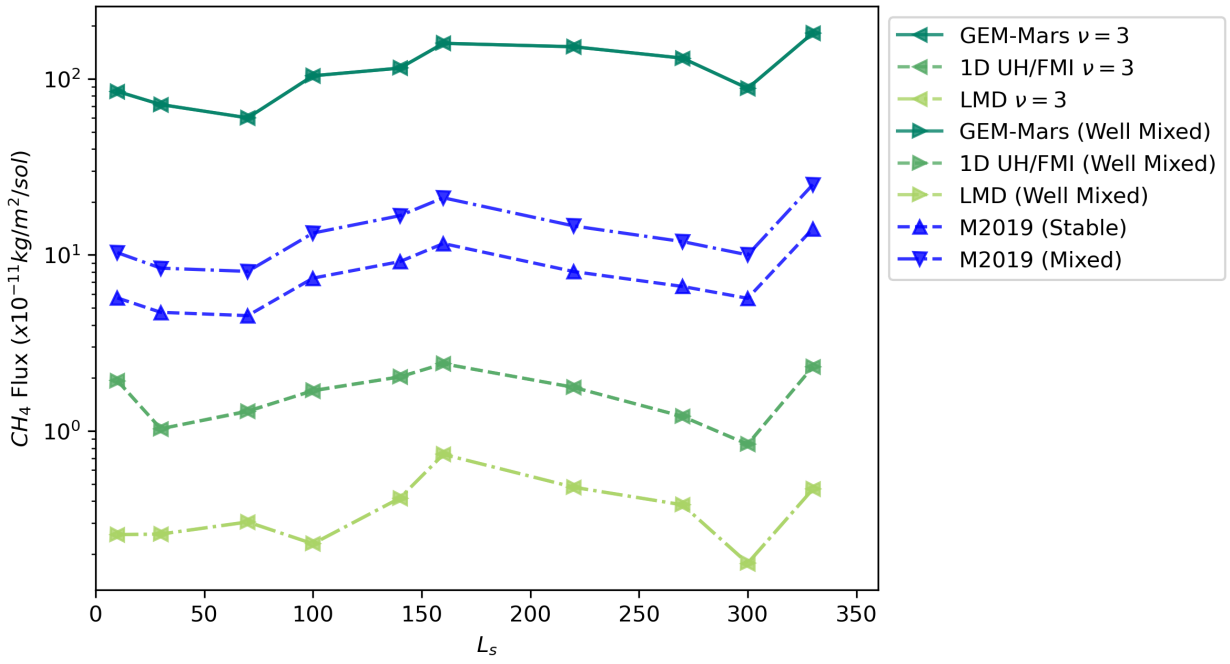


Figure 3.6: Methane flux from the surface required to achieve measurements of SAM-TLS concentrations at 1 m above the surface for both the well-mixed dust profile and the Conrath $\nu = 3$ dust profile. In many instances, the estimated fluxes are nearly identical for both dust profiles. The general trends across the different atmospheric models are similar, with a slight increase in methane flux towards $L_s = 160°$ and 330° representing times of the Martian year where mixing near the surface is increased.

The three atmospheric models I considered diverge in behaviour between $L_s = 10°$ and 70°, where the flux for the LMD model decreases rather than following the general increase that is exhibited by the other models. For each atmospheric model, the methane flux solutions for the different dust profiles are nearly identical, suggesting that eddy diffusivities and the transport of methane are more significant than the difference in methane destruction near the surface.

3.3.2 Diurnal Methane Variability

Methane concentrations at the top of the VDM and within the box model are periodic, reflecting the diurnal variability in the final few sols of the model simulations (Fig. 3.7). As the target methane concentration within 0.01 ppbv of SAM-TLS values at the surface was not feasible in some of the simulations (see Section 3.3.1). In these instances, figures show the closest solutions instead. As the concentration at the top of the VDM and within the box model are repeatable, the overall solutions throughout the atmosphere are stable and the spin-up time of 30 Martian years is

sufficient (Fig. 3.8). Note that the LMD atmospheric model limits the mixing such that methane never enters the box model. As such, the stability for the simulations using the LMD atmospheric model is evaluated at 5 km instead.

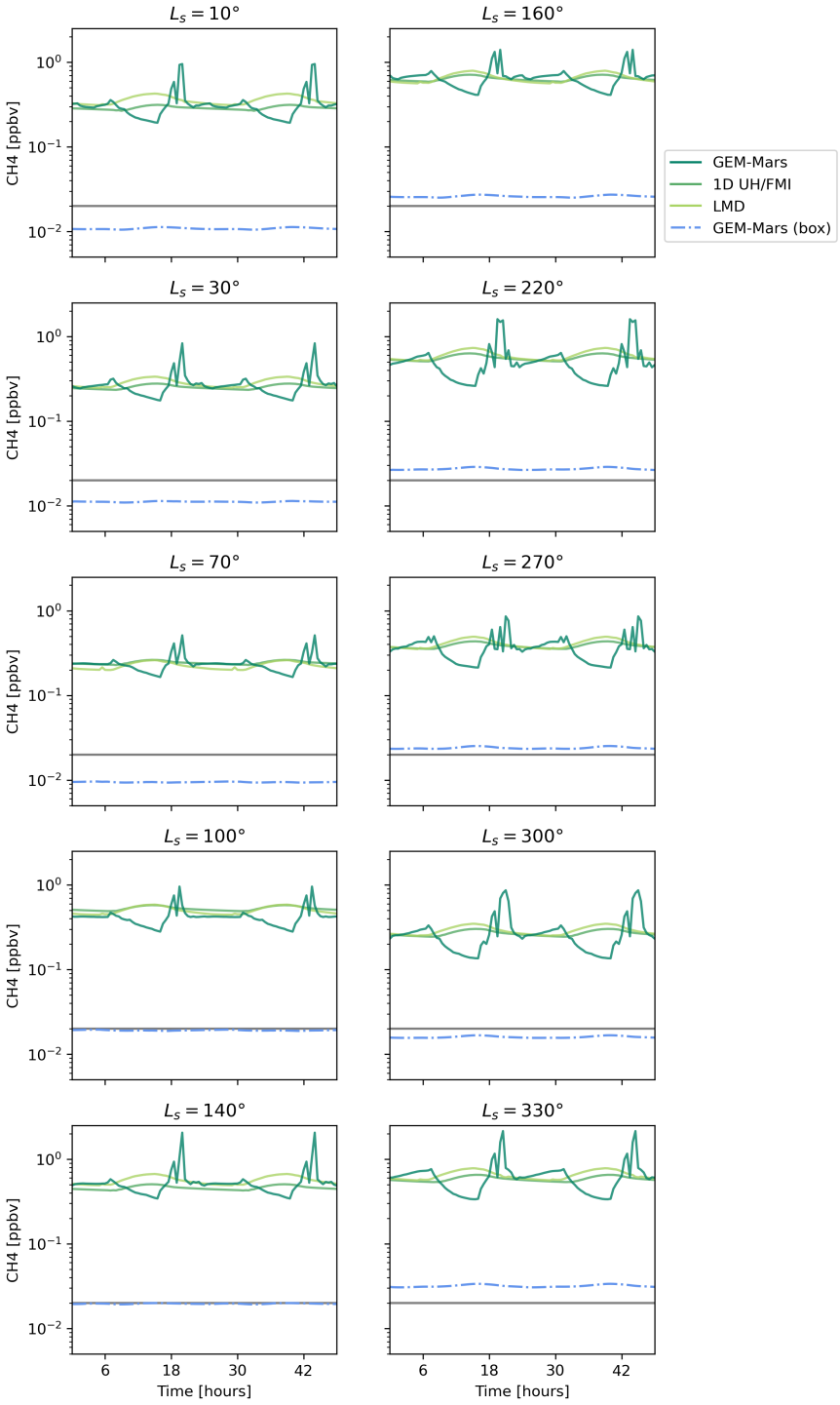


Figure 3.7: Examples of surface methane concentration at 1 m (green) and box model (blue) concentration for the last 48 hours in the simulation for a well-mixed dust profile. They grey line corresponds to a value of 0.02 ppbv. The methane concentrations shown for each model repeats over 24 Martian hours, reflective of the diurnal nature of atmospheric mixing. Note that the 1D UH/FMI box model concentrations are scaled up by a factor of 1E17 to show some of the repetition. Where they are not plotted, they fall below the methane concentration range plotted. Additionally, the LMD box model value is consistent with 0 ppbv and is not plotted.

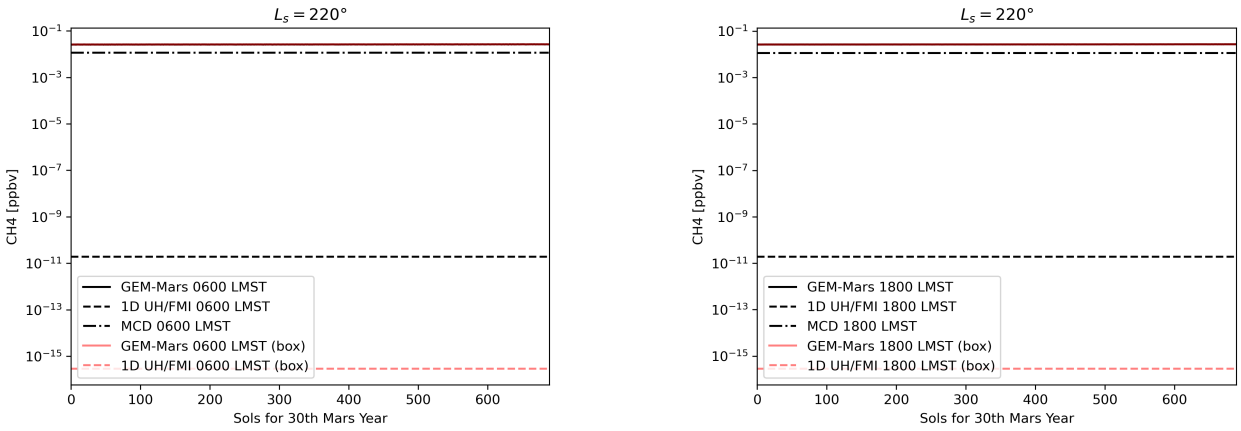


Figure 3.8: Example of methane concentration at 10 km altitude in the VDM for the GEM-Mars and 1D UH/FMI models, and 5 km for the LMD model (black) and in the box model (red) for all atmospheric models at 0600 LTST (left) and 1800 LTST (right) for $L_s = 220°$ over last 669 sols of the simulation. The GEM-Mars 10 km value and box model overlap each other on the plot. I observe no meaningful drift at the same time each sol, indicating that the simulation has reached stability. Note that the LMD model consistently produces 0 ppbv methane concentration in the box in the simulation and is therefore not shown on the plot.

I observe that the GEM-Mars atmospheric model produces a build up of methane at the surface overnight and decreases during the daytime (Figs. 3.9 and 3.15). Behaviour from the GEM-Mars model overnight is more complex in comparison to the 1D UH/FMI and LMD models as mixing is not suppressed during the evening. This corresponds to a gradual increase in methane at 1 m altitude overnight. Methane decreases relatively sharply starting at dawn as the methane is diluted by mixing into the atmosphere more quickly than the other two models while methane destruction is also taking place. During the evening, mixing is supressed near the surface shortly after nightfall with the exception of are two distinct spikes of methane that are transported up several meters above the surface, with a strong evening peak around 1900h (Fig. 3.15). These spikes are a direct result of the eddy diffusivity coefficients and atmospheric transport in conjunction with the methane flux from the surface, as destruction is not active during this time. Eddy diffusivities for the GEM-Mars model where they briefly fall at sunset throughout the lower 1 km altitudes then form a localized region of higher mixing and increased transport between 10 and 100 m (Fig. 3.3). This area of increased mixing perhaps corresponds with a noctural low-level jet or slope winds despite the relatively low resolution of GEM-Mars as described in Rafkin et al. (2016). Methane in all altitudes for the GEM-Mars model decreases sharply towards noon near the surface as the solar

flux increases, reaching similar daytime methane measurements taken by SAM-TLS. The methane decreases slower higher in the atmosphere as methane is also being mixed up into the atmosphere. These features do not appear in the 1D UH/FMI and LMD models.

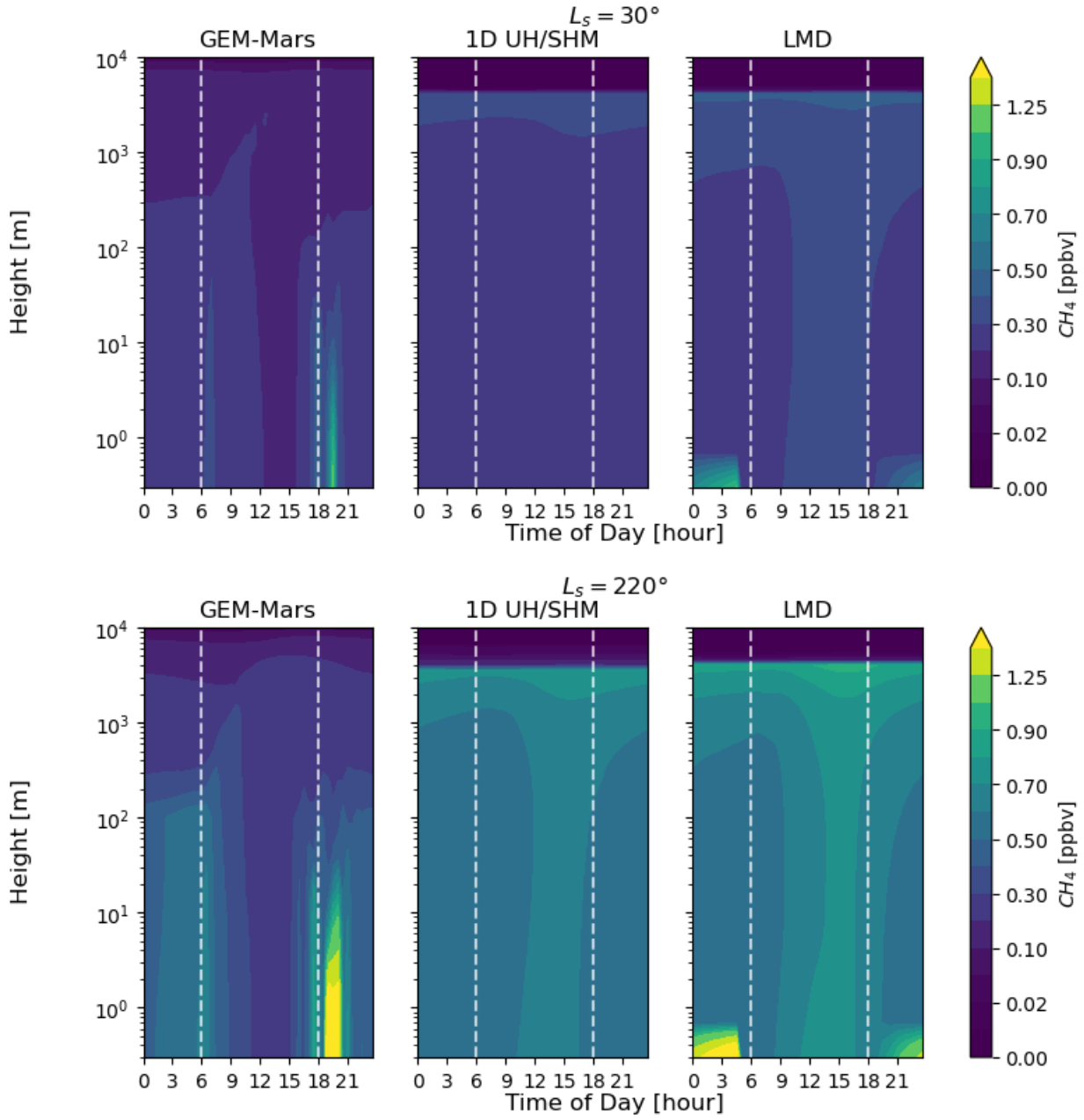


Figure 3.9: Methane concentration on sol 26481 plotted as a function of time of day over the entire10 km VDM shown for two example sols $L_s = 30°$ and 220° for a well-mixed dust profile. Two dashed lines are shown on each plot to indicate 0600 and 1800 LMST, which correspond to the approximate measurements times by TGO.

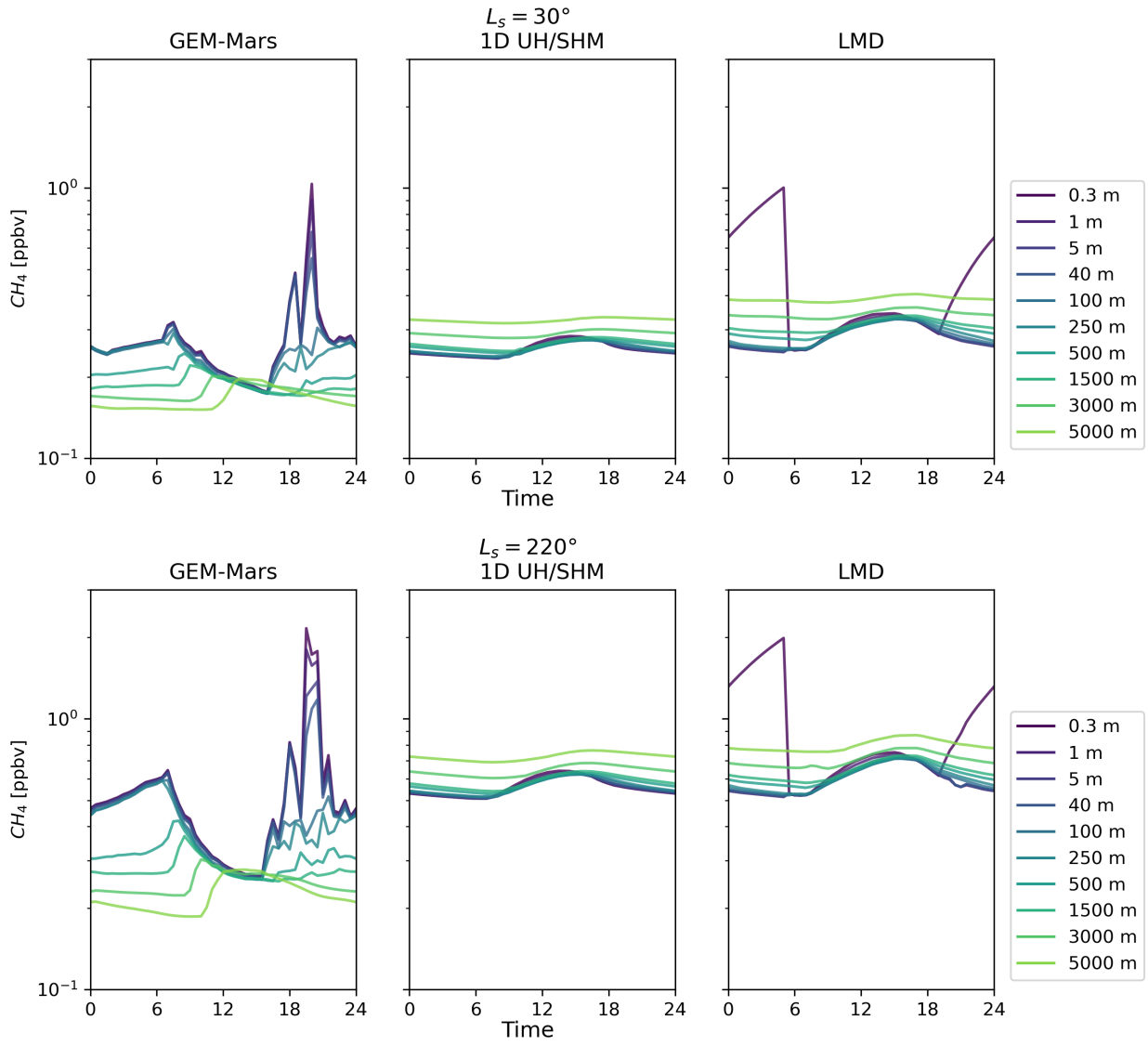


Figure 3.10: Methane concentration shown for the final sol of the simulation plotted as a function of time of day and altitude over the 10 km VDM. Results are shown for two example sols $L_s = 30°$ and 220° for a well-mixed dust profile for specified altitudes. Methane is added into the model as E_0 at the surface layer and is diffused as a function of concentration C_j and eddy diffusivity κ_j (see Equation 3.1). During the nighttime, only E_0 and $\frac{d}{dz}(\frac{k(z_j)dC_j}{dz})$ act to change the methane concentration in the atmospheric column. Note that in the 1D UH/FMI and LMD models, methane appears to build up around 3 km due to low eddy diffusivity. During the daytime, the methane destruction mechanism represented by f_j in Equation 3.1 becomes active. This can be observed by the relative decrease in methane in the GEM-Mars model. The relationship between these three factors is more complicated for the 1D UH/FMI and LMD models, where methane is transported downwards towards the surface during the daytime.

Note that the vertical profile of methane concentration does not always decrease with increasing altitude. For example, there is a band of varying thickness around 500 km in the 1D UH/FMI

and LMD models (Fig. 3.9). This indicates that methane is being transported faster than the destruction mechanism can remove methane in these areas. The decrease in methane concentration at the top of the VDM for the 1D UH/FMI and LMD models indicates a sharp decrease in methane transport that corresponds with a decrease in eddy diffusivity. I observe that there is an overall increase in methane concentration between the surface and the first 0.5 m of the LMD model. However, I expect SAM-TLS to be taking measurements at 1 m. At 1 m altitude, the LMD model indicates that methane increases during the daytime. Methane does not penetrate the upper section of the VDM and accumulates in the lower portion of the atmosphere. Furthermore, methane is continuously supplied to the VDM. The increase in methane during the daytime demonstrates that methane is being transported faster from the surface than it is being removed from the first few meters. Additionally, In the evening, the atmospheric mixing and eddy diffusivity gradually decrease such that methane does not reach 1 m. However, if the 0.3 m layer (Fig. 3.15, dark purple line) is more representative of the SAM-TLS measurements, I observe that methane increases steadily during the nighttime, decreases extremely quickly at sunrise (corresponding with diffusion of methane via transport), and gradually increases during the daytime as methane production and transport into higher layers exceeds destruction.

The 1D UH/FMI model behaves similarly to the LMD model without the strong diurnal variability in the first layer of the VDM as overnight mixing at the surface is more efficient in the 1D UH/FMI model (Fig. 3.3). During the daytime, methane is generally well-mixed in the VDM when using the 1D UH/FMI atmospheric model (Fig. 3.9).

3.3.3 Methane At and Above 10 km

I investigate the difference between my simulations of the upper atmospheric column and the lower limit of observation for TGO (0.02 ppbv) by plotting the atmospheric concentration of methane in the box model at 0600 LTST and 1800 LTST, typical observation times for TGO (Fig. 3.11). I find that the methane concentration above 10 km is consistently below 0.02 ppbv for the simulations using the 1D UH/FMI eddy diffusivity values, as mixing is suppressed within the upper layers of the VDM itself and methane is removed via the destruction mechanism before entering the box model. The LMD atmospheric model does not allow for the entry of methane into the box model at all, and is thus consistently below the TGO detection threshold.

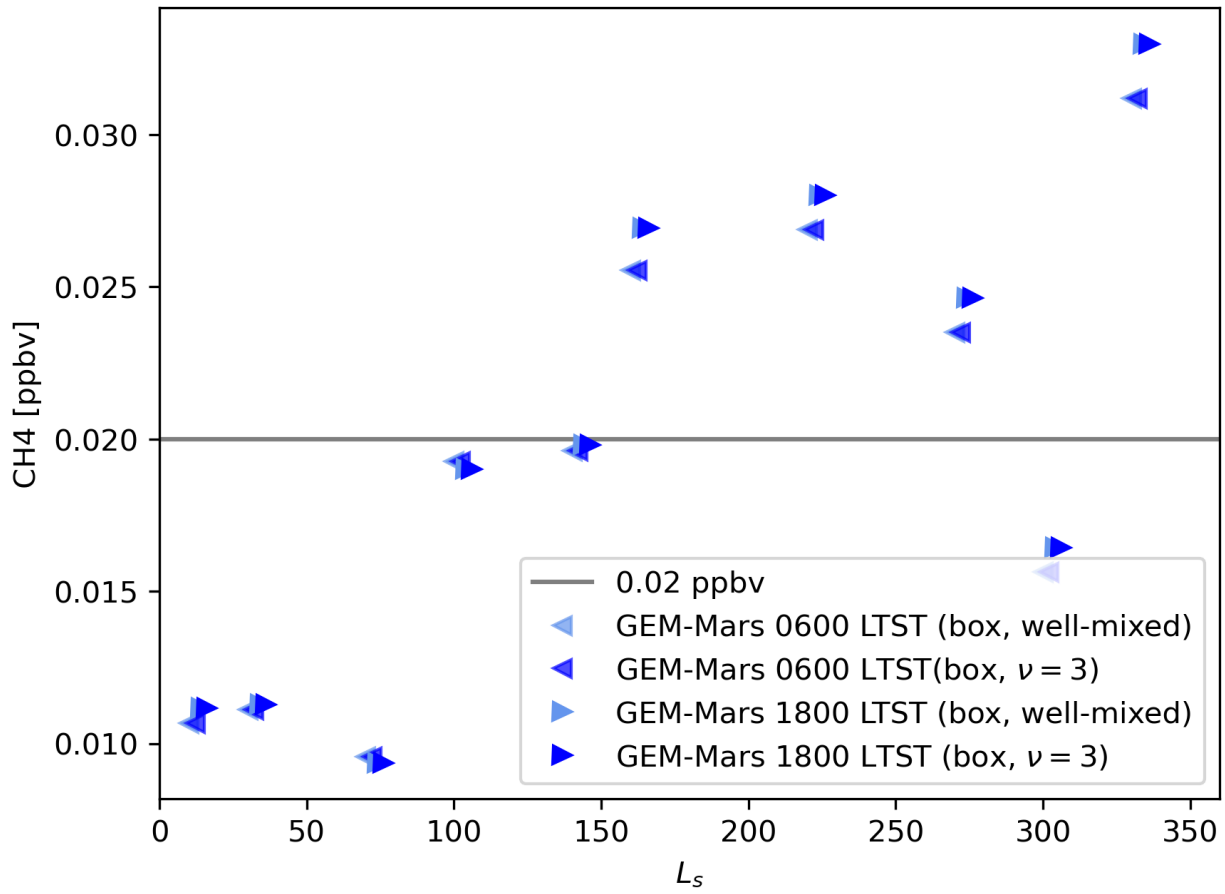


Figure 3.11: Right: Both the well-mixed and Conrath profile of $\nu = 3$ for GEM-Mars concentrations at 0600 LTST and 1800 LTST are plotted with horizontal offsets for visibility. Methane in the box model is generally below the threshold, but exceeds 0.02 ppbv when using the GEM-Mars at sols $L_s = 160°, 220°, 270°, 330°$. For values in excess of 0.02 ppbv, the methane concentration in the afternoon at 1800 LTST consistently exceeds that at 0600 LTST with a maximum value of $\sim$ 0.033 ppbv. Values from the 1D UH/FMI model from the VDM at 10 km and in the box model are over 10 orders of magnitude below the 0.02 ppbv threshold, and values from the LMD model are consistently at 0 ppbv.

In contrast, the simulations using the eddy diffusivity values from GEM-Mars model have varying results. The methane concentration in the box model increases during the aphelion to perihelion transition and exceeds 0.02 ppbv. The methane concentration then decreases below this threshold at $L_s = 300°$ before increasing again at $L_s = 330°$. The maximum methane concentration in the box model is at 0.033 ppbv. There is a subtle diurnal variation in the box model reflective of the TGO observational space where the methane concentration is highest in the afternoon at 1800 LMST (Figs. 3.7 and 3.11). Note that the individual upper limit for TGO measurements of

methane near Gale Crater exceeds 0.033 ppbv, with the lowest upper limit of 0.065 ppbv taken around $L_s = 127°$ (Montmessin et al., 2021). Thus, my simulations show that the modelled methane concentration visible to TGO consistently remains lower than the TGO observational limits close to Gale Crater.

3.3.4 Plume Dissipation

I simulated the effect of a large source of methane entering Gale Crater by adding methane at 21 ppbv between the surface and 10 m above the surface to evaluate how quickly the methane would disperse. Additionally, I evaluated whether such a high concentration of methane could be transported into the upper atmospheric column and be detected by TGO. The 21 ppbv source was chosen to replicate an apparent methane plume observation made by SAM-TLS in the enriched mode measured at night around $L_s = 41.5°$. Observations the day prior from the Mars Express orbiter (upper limit of 2 ppbv) did find any methane, and SAM-TLS measurements 4 sols later found that the methane concentration fell to 0.224 ppbv (ESA, 2019, Webster et al., 2021). This suggests that the plume-like source both appeared and disappeared quickly.

For simplicity, I ran the simulation without the previously estimated surface methane flux and distribution in the atmosphere. I find that the plumes in these simulations are diluted and destroyed such that the methane concentration in the entire atmospheric column falls below 0.02 ppbv within two sols using the GEM-Mars atmospheric model and below 0.05 ppbv for both the 1D UH/FMI and LMD models (Fig. 3.12). At the top of the VDM, the methane concentration remains consistently below 0.01 ppbv. As such, it is unlikely a large methane plume on the order of 21 ppbv would be detected by TGO based on these simulations. I note that SAM-TLS would also not observe this higher concentration plume if the GEM-Mars and 1D UH/FMI models accurately reflects the surface dynamics as methane will be rapidly diluted over the timespan of the SAM-TLS ingest (say, over a 2 hour ingest as in Webster et al. (2021)) and would instead correspond to ∼1-5 ppbv, a potential limitation of the atmospheric models.

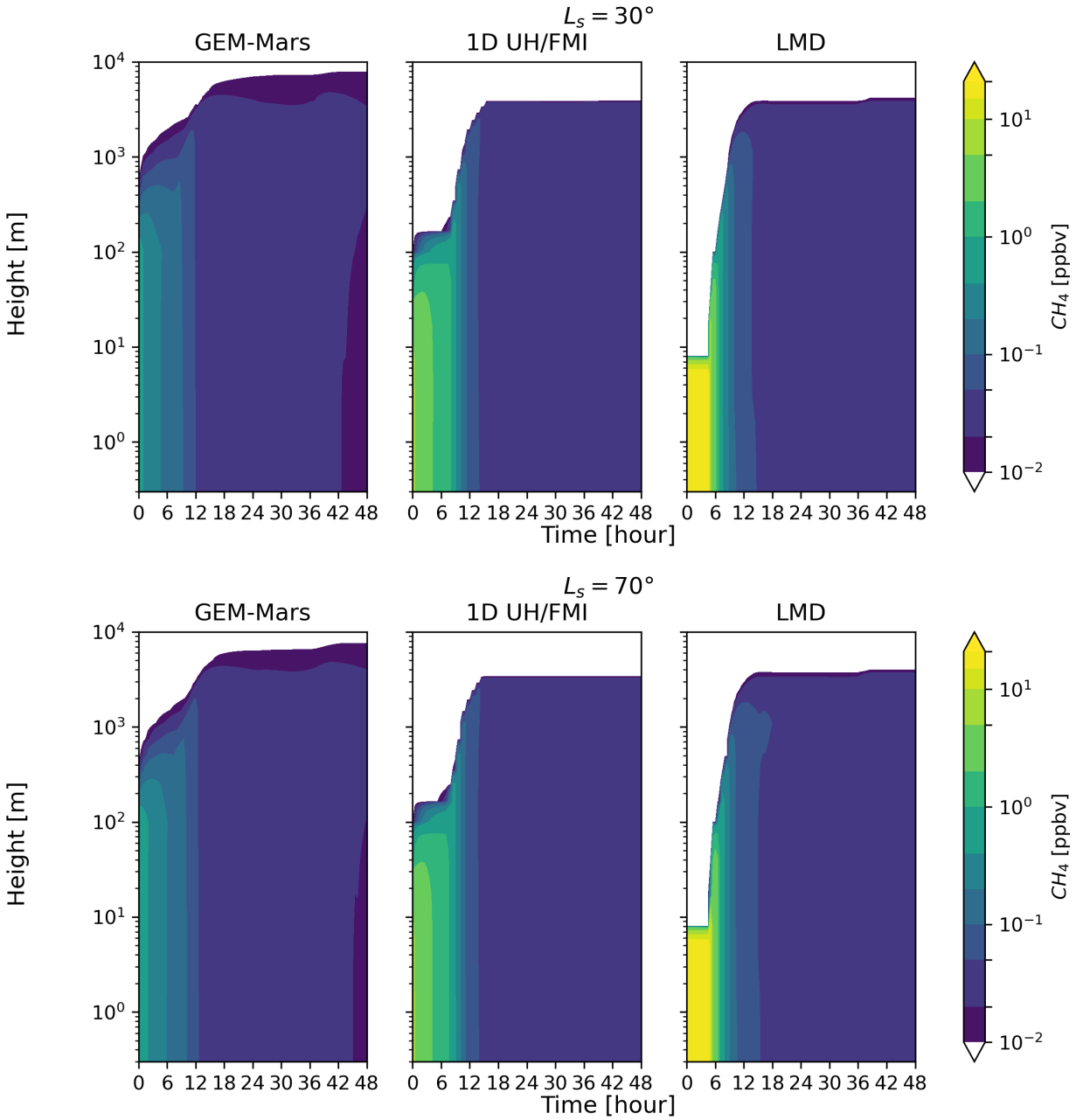


Figure 3.12: Simulated methane plume 10 m in height initialized at 21 ppbv shown for $L_s = 30°$ (left) and $L_s = 70°$ (right) for a well-mixed dust profile. As my simulations did not cover $L_s = 41.5°$, the selected sols are the closest seasonally to the SAM-TLS detection of 21 ppbv. The white shading indicates methane concentrations below 0.01 ppbv. The Conrath profile of $\nu = 3$ demonstrates similar methane dilution and destruction.

3.3.5 Effect of the Destruction Mechanism

To test the relative effect that the destruction mechanism has on the overall concentration of methane in the atmosphere during my simulations, I ran an additional sol (using the solutions from the prior sections as spin-up) without destruction. When running the additional sol, I use the methane flux solution, E_0, I had previously solved for in Section 3.3.1. In Figure 3.13, I plot the relative difference in total methane in the first 10 km of the atmosphere to demonstrate the effect of my simulation with, and without the rapid methane destruction.

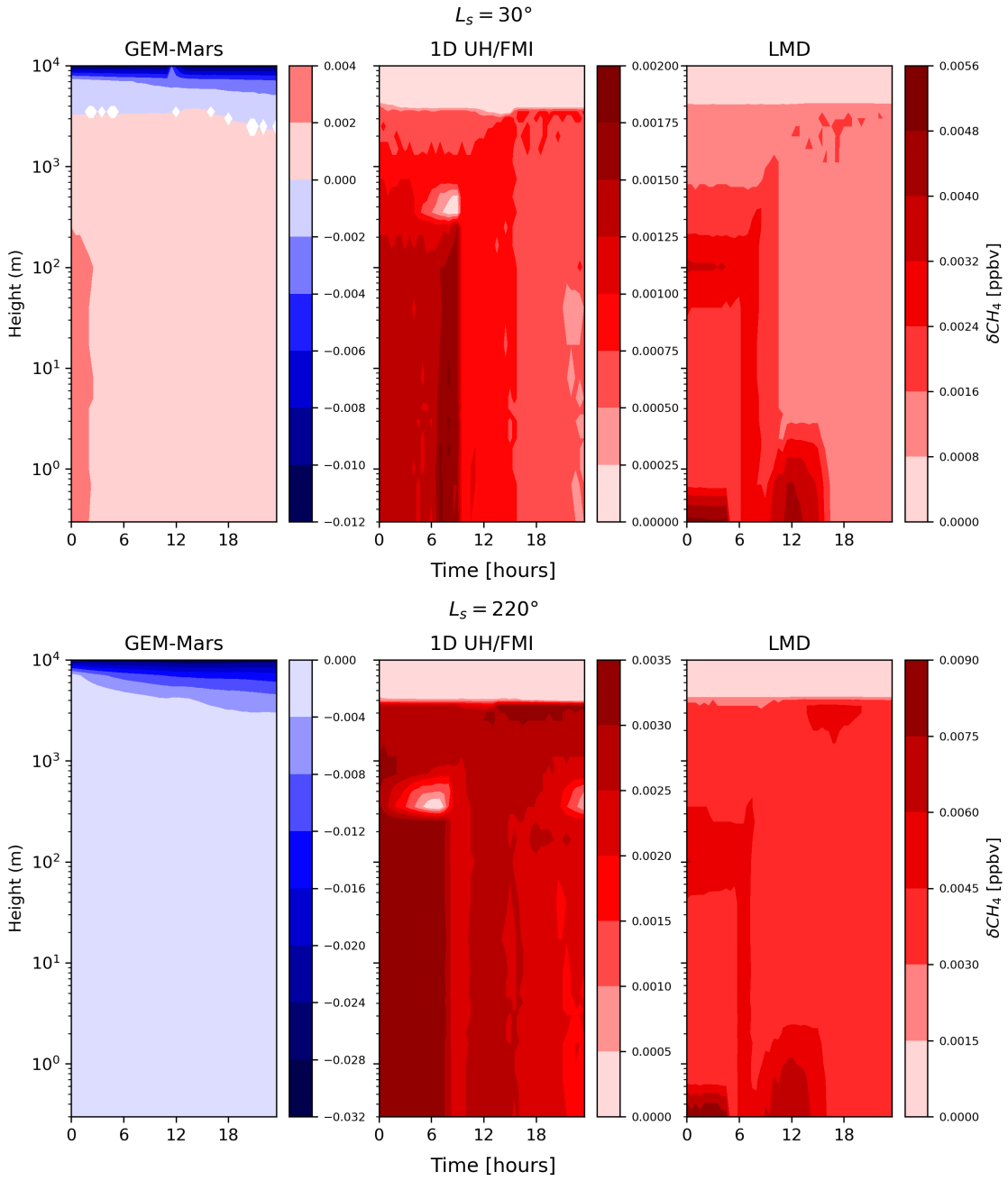


Figure 3.13: The relative concetration of methane in the VDM without the methane destruction mechanism shown for a well-mixed profile in comparison to the VDM with the methane destruction mechanism. Positive values reflect more methane in the simulation without reduction (red) and negative values correspond with more methane in the VDM when the destruction mechanism is active (blue). Methane is consistently higher in the VDM when there is no destruction mechanism active for the 1D UH/FMI and LMD models. The effect of the destruction mechanism is more variable for the GEM-Mars model, where the example of $L_s = 30°$ shows a relative increase in methane below 3 km in the VDM when the methane destruction mechanism is not active, but a relative loss of methane above 3 km. $L_s = 220°$ demonstrates less methane in the VDM when the destruction mechanism is not active throughout the entire sol.

As expected, methane overall is higher when the methane destruction mechanism is removed for the 1D UH/FMI and LMD models. Methane is added via the surface flux, but does not move into the box model faster than the addition of methane into the VDM. Methane does not increase quicky within the VDM, however, it is also evident that the methane will build up over time and in comparison to the model with destruction, the simulation is not stable (Fig. 3.14).

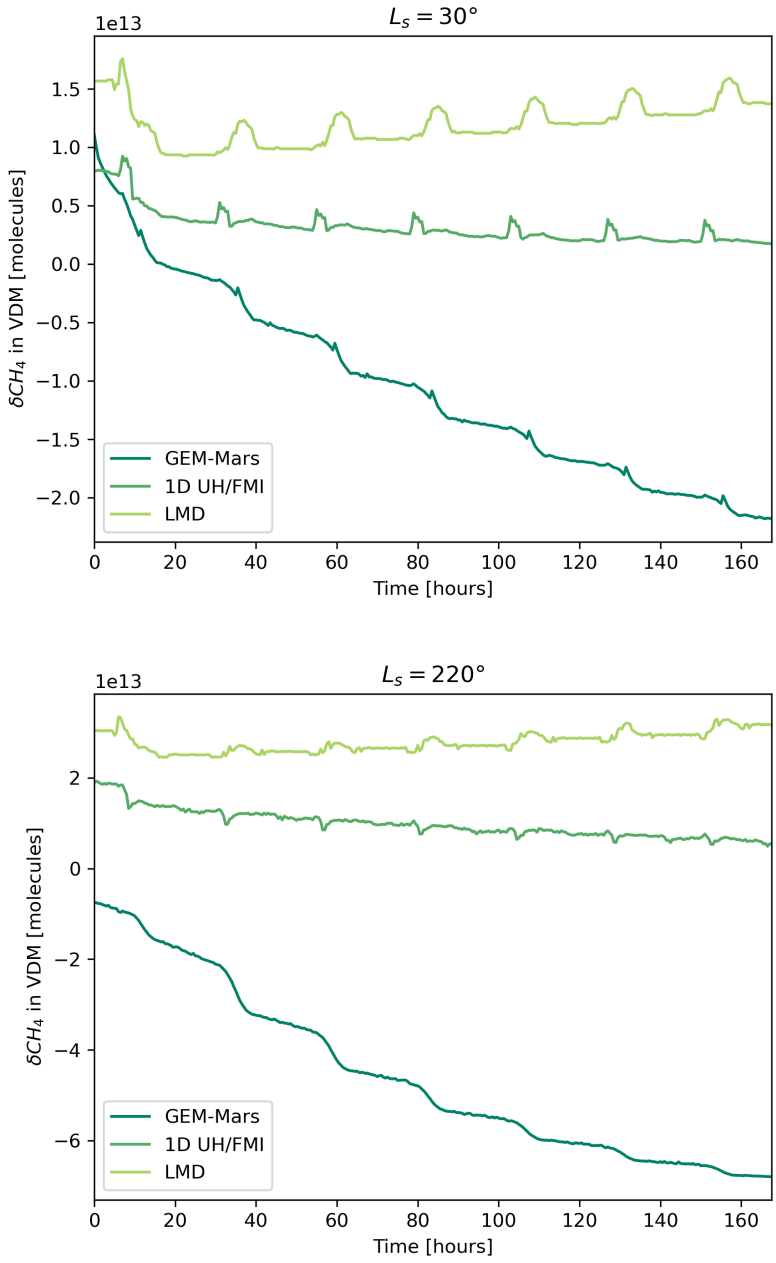


Figure 3.14: The relative number of methane molecules the VDM repeated over the same 7 sols of simulation without the methane destruction mechanism in comparison to the VDM with the methane destruction mechanism shown for a well-mixed profile. Positive values reflect more methane in the simulation without reduction and negative values correspond with more methane in the VDM when the destruction mechanism is active. For all three atmospheric models, the total number of methane molecules is unstable shown by the gradually increasing amount of methane when using the 1D UH/FMI and LMD models, and decreasing amount of methane for the GEM-Mars model.

In contrast, the overall methane within the VDM decreases when using the GEM-Mars atmo-

spheric model. This too, is unsurprising. The eddy diffusivity values at the top of the VDM are relatively high. Without a methane destruction mechanism, methane is transported into the box model faster than the overall destruction mechanism. This occurs because the gradient between the top of the VDM and box model is much larger than when the methane destruction mechanism is active. I can infer that the GEM-Mars relative decrease in methane will persist until the concentration in the box model and at the top of the VDM will be in equilibrium (as with the other two atmospheric models). This results in a build up in methane in the box model over time. Methane in the VDM using the GEM-Mars model will decrease until the top of the VDM is in equilibrium with the box model and then the methane within the VDM will begin to increase (Fig. 3.14).

It is evident that including the rapid methane destruction mechanism strongly affects the transport of methane in the atmosphere and would affect the estimated methane flux from the surface if I were to repeat this exercise without the destruction mechanism. Additionally, the model would not reach steady state until the box model concentration and top of the VDM are in equilibrium such that the box model concentration would likely be significantly higher than the TGO detection threshold.

3.4 Discussion and Implications

The results in this work demonstrate that a fast destruction mechanism can be used to explain some of the apparent methane concentration discrepancies between the Curiosity rover and TGO orbiter measurements. Furthermore, I demonstrated that a plume-like detection of methane such as the 21 ppbv methane concentration measurement can be reduced quickly in the atmosphere. However, there are still areas in this work that can be improved upon. In this section, I review the use of eddy diffusivity coefficients and our reliance upon them for simulating atmospheric processes, address the limitations of the methane plume investigation, comment on some caveats to the model used in this work, and address whether the simulations using Gale Crater are appropriate to represent the rest of Mars. Lastly, I comment on potential future measurements that can be taken by SAM-TLS to test the performance of the destruction mechanism and atmospheric models.

3.4.1 Eddy Diffusivity Coefficients

The eddy diffusivities used in the 1D VDM are assumed to describe the overall transport of atmospheric constituents throughout the atmosphere. These eddy diffusivity coefficients were derived from a variety of atmospheric models. However, these values are not necessarily representative of the overall mixing that occurs. In particular, atmospheric mixing at higher altitudes such as above 100 m may be underestimated by eddy diffusivity values (Millour). This is likely the case with the LMD model, where the eddy diffusivities fall to the molecular diffusivity limit around 5 km during the daytime. Methane is removed faster than it is transported into the higher layers. When methane is emitted from the surface, the partial pressure of methane is low for the 1D UH/FMI and LMD models, thereby minimizing the destruction and allowing methane to be transported before becoming trapped in a layer around 2000 - 5000 m. This scenario where the transport above 5 km is solely dependent on molecular diffusion is highly unlikely. Thus, my simulation of 0 ppbv in the box model is likely also unrealistic.

However, I can infer from the 1D UH/FMI results where the box model methane concentration is on the order of ∼1E-20 ppbv that the low methane flux for the LMD model would likely not lead to a methane concentration greater than of 0.02 ppbv even with a modestly increased eddy diffusivity. More broadly, if one assumes that all of the atmospheric models, including GEM-Mars, underestimate the eddy diffusivity, then one can assume that the methane concentration in the box model where TGO would typically observe would be higher than my results. In this instance, the values would not be consistent with both SAM-TLS and TGO observations. Overall, eddy diffusivities are a proxy for mixing in the atmosphere and are poorly constrained for the Martian atmosphere above the surface due to the lack of data at higher altitudes.

Eddy diffusivity values begin at varying heights for the different models and do not capture the detailed dynamics from the surface (Figs. 3.3 and 3.4). Differences between the atmospheric models are apparent as low as 10 m in the atmosphere. However, I reasonably cover a full range of scenarios for the Martian atmosphere over Gale Crater and find that my general conclusions remain the same. With two of the three atmospheric models I used, it is possible to both achieve a SAM-TLS methane measurement near the surface while methane falls below 0.02 ppbv where the atmosphere is measured by TGO. The GEM-Mars atmospheric model does lead to an excess of 0.02 ppbv

at altitudes observed by TGO, with a simulated maximum value of 0.033 ppbv, though this value remains below the detection threshold for measurements by TGO taken near Gale Crater. However, Neary, the developers of GEM-Mars have also noted that the eddy diffusivity coefficients derived from GEM-Mars may also be an underrepresentation of the mixing higher in the atmosphere.

Underestimation of atmospheric mixing has been demonstrated in past work, such as in Toigo and Richardson (2002), where they found it necessary to increase vertical diffusivity in their model by an order of magnitude to match surface wind speeds in a mesoscale model and in Haberle et al. (1993) where they suspected the errors in their turbulence scheme were the cause of a mismatch between observed and simulated wind speeds at the surface and during descent of the Viking 1 and Viking 2 landers using a 1D atmospheric model. The discrepancy between LMD model simulations, the MarsWRF model, and observed wind activity on Mars between 2 and 10 km has been previously reported by Paton et al. (2024) during the descent of the Perseverance rover. Winds on the order of several meters per second were inferred during the descent between 5 and 10 km during the daytime, which suggest that the eddy diffusivities at these altitudes are greater than zero (in contrast to the values I retrieved from the MCD). It is likely that atmospheric mixing also takes place over Gale Crater at these altitudes, unlike the values estimated by the LMD model I used in this work. Near the surface, wind speeds measured by Ingenuity within a few meters of the surface were higher than those predicted by both the LMD model and MarsWRF (Jackson et al., 2025). In Paton et al. (2021), they find that the 1D UH/FMI model was broadly able to replicate wind speeds at the surface as observed by the InSight lander during the daytime. However, surface winds at the Viking 1 lander site were higher than expected when using the LMD model (Paton et al., 2021). Overall, there is substantial evidence that the LMD model underestimates wind speeds and likely eddy diffusivity near the surface and higher in the atmosphere during the daytime. As both the 1D UH/FMI model and GEM-Mars have similar or lower eddy diffusivity coefficients near the surface, one infers that perhaps all of these values during the daytime are an underestimate of atmospheric mixing. It is worth noting that Fonseca et al. (2018) reports that MarsWRF simulations closely match Curiosity rover REMS measurements for temperature and pressure, but does not perform as well in terms of wind speed and direction as expected.

In spite of the differences between the three atmospheric models used in this work, they share similar eddy diffusivity coefficients between 10 m and 2 km during the daytime, before once again

diverging dramatically above 2 km. Eddy diffusivity coefficients stay relatively high in the GEM-Mars model, while decreasing sharply in the LMD and 1D UH/FMI models. Given the large gap between eddy diffusivity coefficients between models in the first few meters of the surface, and between 2 - 10 km shown in this work and in Paton et al. (2024), this suggests the need for further investigation of atmospheric dynamics Mars at these altitudes.

Furthermore, the atmospheric models used in this work have been noted by previous authors to demonstrate an overall underestimation of mixing and wind speed estimates. I caution that the simulations in this work should be taken as an exercise in investigating the impact of methane destruction and interactions with atmospheric models. Results from the 1D UH/FMI and LMD model should not be taken as a realistic representation, as it is unlikely that the transport of trace gases such as methane is entirely cutoff at 3 km during the daytime as winds are expected at such altitudes.

3.4.2 Plumes of Methane

How quickly does a large injection of methane get removed from the atmosphere? I found that a 21 ppbv plume reaching 10 m from the surface would be quickly diluted and the methane concentration falls to background levels (in the case of GEM-Mars, within a few hours). Additionally, the contribution to the surface methane at 1 m on the following morning is between 0.02 and 0.05 ppbv. This rapid removal of a methane plume is partially due to the efficiency of the destruction mechanism. When I consider the increased methane concentration from the plume due to increased methane adsorption, methane can be removed relatively quickly once it becomes daytime. This is evident in the plume simulation using the LMD atmospheric model where the plume is not diluted overnight. When I consider the other end member of my mixing models, GEM-Mars, a 21 ppbv plume is diluted by two orders of magnitude within half an hour (our mixing time step). If the GEM-Mars model reasonably represents the near-surface in Gale Crater at night, high concentrations of methane would have to be sustained by a high methane flux. In contrast, if mixing is nearly non-existent overnight, then it is both possible to observe the 21 ppbv methane concentration over a several hour ingest time span and subsequently measure an methane concentration decrease by two orders of magnitude during the day time. Note that this extreme example is unlikely unless the source of such a high methane concentration occurs nearby SAM-TLS as horizontal transport would

also be limited during the night. Future work can consider simulating the horizontal transport of a methane plume using higher resolution atmospheric models than those used in this work.

3.4.3 Model Limitations

In addition to uncertainty arising from the eddy diffusivity values, the GEM-Mars and LMD models also do not account for localized dynamics from topographical effects. The MOLA topography used in the GCMs are smoothed over larger areas, with a resolution of 0.25° x 0.25° in GEM-Mars, and presumably a similar resolution in the LMD model. These assumptions may influence the overall estimates of methane mixing in the atmosphere. Additionally, I do not account for the possibility that methane originates from outside of Gale Crater nor for methane leaving Gale Crater. While these assumptions are reasonable given the data limitations, future measurements of methane and atmospheric activity outside of Gale Crater would be necessary to support that methane can be present at the surface and not easily observed at higher altitudes.

An additional caveat to my simulations is the assumption that the vertical diffusion model is sufficient to represent the average atmospheric transport throughout Gale Crater. In my 1D VDM, I do not explicitly account for horizontal transport. In this work, I was mostly interested in the background concentration of methane near the surface and assumed that the surface of Gale Crater equally contributed to the methane flux. In reality, microseepage may be present at in some locations but not others on Mars. Nonetheless, I was able to provide an initial explanation for how methane could readily build up near the surface during the night time and become rapidly removed in the morning, even near the surface. Further, I demonstrate that despite increased daytime mixing and higher flux estimates than Moores et al. (2019b), I find that the methane concentration at higher altitudes observable by TGO result in less than 0.02 ppbv for two out of three atmospheric models, and only during select times of the year do my simulations show that methane exceeds TGO's detection threshold. As it pertains to Gale Crater specifically, mesoscale modelling suggests that the atmosphere within Gale Crater is replaced by external air within 1 sol (Pla-Garcia et al., 2019). Thus, I would expect horizontal mixing in and out of Gale Crater to be more impactful than localized differences in methane concentration within the crater. Generally, my model can estimate the upper limit of methane concentration using the atmospheric models if there is horizontal homogeneity.

My model can be used to investigate the impact of horizontal transport in specific cases where methane is added into the VDM. For example, I simulated the effects of a plume in Section 3.4.2 where one can conceive that a large source of methane was released and was transported into the vertical column. The plume needs to be sufficiently large that horizontal effects of dispersion out of the column do not need to be considered. This investigation is limited to how quickly the plume is removed and does not provide insight into how the plume was added into the vertical column, nor how the evolution of the plume changes if horizontal transport were explicitly modelled.

Additionally, I assumed that the methane flux from the surface is at a fixed value. While I iterated my solution for the methane flux, the value itself was consistent from the surface. As the source of methane is still undetermined, it is difficult to say how representative this stable flux is. Previous works have evaluated how much methane can be drawn into the subsurface as part of adsorption processes (Gough et al., 2011, Ortiz et al., 2024). If the primary mechanism for methane flux into the surface is from barometric pumping, then a realistic methane flux at the surface would be dependent on the surface pressure. Future work could consider a methane flux that is variable within an individual sol and could also include processes that vary over the course of a single sol such as barometric pumping from the subsurface. Moreover, investigations of how much methane flux is required to achieve methane on the order of 10s of ppbv could also provide insight into the surface and atmospheric interactions and processes on Mars.

3.4.4 Gale Crater as a Proxy for All of Mars

I focus on Gale Crater as my location for modelling the methane diffusion and destruction. However, I note that Gale Crater is unlikely to be the sole source of methane emissions and similar methods can be applied elsewhere on Mars. I choose Gale Crater as my study location as there are surface measurements at this site. While I am interested in testing whether the destruction of methane resolves the apparent discrepancy between SAM-TLS and TGO, this research also provides some insight into methane processes elsewhere on Mars, such as the large plumes of methane observed by telescopes and orbiters (Formisano et al., 2004, Mumma et al., 2009, Geminale et al., 2008). Notably, there has been perchlorate measurements made at different latitudes outside of craters on Mars, such as that at the Viking and Phoenix landing sites (high latitudes) and at Gale Crater and Jezero Crater (low latitudes) (Clark and Kounaves, 2016, McKay et al., 2025, Wiens et al.,

2022). Additionally, oxychlorine and chlorine species have been measured at higher altitudes by TGO (Faggi et al., 2025). This suggests that the overall methane destruction mechanism can be active all over Mars while methane remains difficult to detect from orbit. However, measurements elsewhere at the surface of Mars would be necessary to validate this proposal to demonstrate whether or not Gale Crater is unique in terms of potential methane sources (Oehler and Etiope, 2017).

3.4.5 Atmospheric Mixing in the Daytime

While I did not simulate $L_s = 120°$ and $L_s = 134°$, the methane concentration in the GEM-Mars model from $L_s = 100°$ and $L_s = 140°$ come closest to the ∼0.05 ppbv reported for noon, with values from the LMD model exceeding even 1 SEM of the daytime measurements. Given the disparity in methane concentration near the surface in the afternoon, I suggest taking additional methane measurements around 1500 LTST near $L_s = 130°$. The sole daytime measurements are taken between $L_s = 120°$ and 134°, and measurements taken in the afternoon would provide a way to identify if one of the atmospheric models tends to perform better near the surface during daytime. Both the 1D UH/FMI and LMD models indicate that methane should build up in the afternoon, whereas the GEM-Mars model shows a decrease in methane near the surface during the daytime, continually decreasing towards the afternoon. Ideally, measurements around 0000 LTST and 1200 LTST can also be taken around the same time of year.

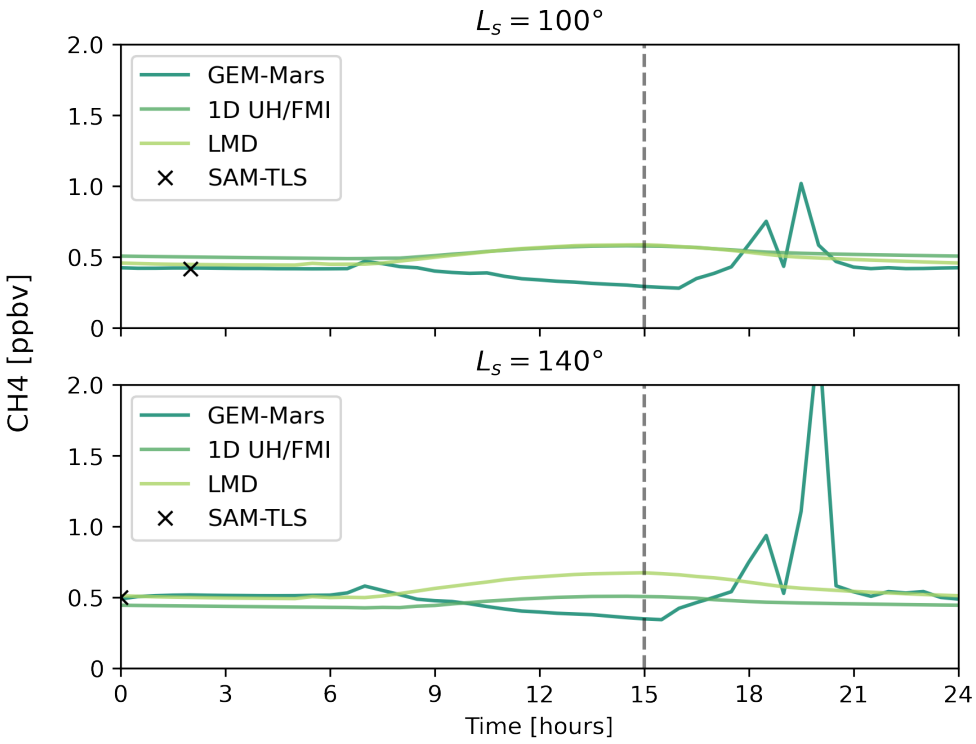


Figure 3.15: Methane concentration at 1 m above the surface for simulated sols $L_s = 100°$ and 140°for a well-mixed dust profile. The dashed line at 1500 LTST indicates the ideal sample time to compare expected methane concentration from the atmospheric models. Measurements taken at 0000 LTST and 1200 LTST would be useful to compare relative increase or decrease in methane concentration.

3.5 Conclusions

I demonstrated that the presence of UV-activated perchlorate as a methane destruction mechanism can explain the difference in methane concentration observations at the surface of Gale Crater and from orbit. I used a vertical diffusion model to reproduce the methane concentration as observed by SAM-TLS at the surface and updated the model from Walters (2023) to use a realistic boundary condition for the VDM by adding a box model. As part of the vertical diffusion model, I added the destruction mechanism from Zhang et al. (2022) that is dependent on the local pressure, temperature, perchlorate availability, and photon flux. I incorporated three atmospheric models as part of this work, including a column model that was calibrated to Curiosity REMS measurements. These atmospheric models provided eddy diffusivities, temperature, and pressure profiles for my simulations. In my simulations, methane destruction requires adsorption onto dust particles. Thus, I

considered two different dust profiles which also affect the available flux for the methane destruction reaction. I found that the dust distribution profiles did not lead to significant differences between the overall behaviour of methane in the atmosphere and the methane flux from the surface.

I represented the observable atmosphere for TGO by means of a box model that includes the entire atmospheric column above 10 km. From my results, I find that methane in the box model typically falls below the detection threshold of TGO. Additionally, I found that depending on the atmospheric model used in the VDM, methane can build up throughout the day at the surface. The methane fluxes required for these simulations range from 1.77×10^{-12} - 1.82×10^{-9} kg/m^2/sol. I found that the choice of atmospheric model from which diffusivity values were obtained does affect whether methane at TGO observable altitudes falls below the TGO detection threshold. Specifically, when considering GEM-Mars, the methane concentration at 10 km is greater than 0.02 ppbv for half of MY35 in my simulations (up to 0.033 ppbv), which is slightly above the detection threshold of TGO. However, based measurements from TGO nearby Gale Crater, the specific detection threshold (0.065 ppbv at best) exceeded the concentration within the box model. Overall, this work demonstrates that it is possible to explain the disappearance of methane from the surface before it is measured by orbital assets by means of interactions with perchlorate during the daytime. SAM-TLS and TGO measurements of methane are not necessarily in contradiction.

Chapter 4

Titan Airbursts

The work in this chapter has been published previously as the following:

Elisa Dong, Catherine D. Neish, John E. Moores, Shigeru Wakita, Gareth S. Collins, Peter G. Brown, Ralph D. Lorenz, Benjamin Fernando, Mark P. Panning, "Signal characteristics of potential airbursts in Titan's atmosphere", in *Icarus*, [2025]

and has been updated and extended here for the purposes of this document. CRediT: Elisa Dong: Writing – original draft, Validation, Methodology, Investigation, Formal analysis. Catherine D. Neish: Writing – review & editing, Supervision, Project administration, Conceptualization. John E. Moores: Writing – review & editing, Supervision, Resources. Shigeru Wakita: Writing – original draft, Writing – review & editing, Validation, Software. Gareth S. Collins: Writing – review & editing, Methodology. Peter G. Brown: Writing – review & editing, Methodology. Ralph D. Lorenz: Writing – review & editing. Benjamin Fernando: Writing – review & editing. Mark P. Panning: Writing – review & editing.

4.1 Introduction

Our knowledge of the solar system improves with proximity to Earth. The upcoming Dragonfly mission will launch in 2027 to visit one of the few planetary bodies in our solar system where we can better understand prebiotic chemistry.

Little is known about the population distribution of the small (meter-sized) cometary objects that reside in the outer solar system (Bottke et al., 2023, Nesvorný et al., 2023). Our current knowledge of cometary objects and their properties is restricted to comets that are km or more in size (e.g. Aspahug and Benz (1994), Richardson et al. (2007). As such, meteor population in the outer solar system is constrained by very few observations. Current population estimates are based on crater counts made on the Jovian and Saturnian moons and observed flashes in Jupiter's atmosphere (Bottke et al., 2023, Korycansky and Zahnle, 2005). However, most of these events are attributed to large impactors, and the meter-scale impactor population is poorly constrained due to lack of sufficiently high resolution observations. Additionally, they may be part of a population that has been contaminated by nearby meteoroids, such as the Taurids (Borovička and Spurný, 2020). As such, the properties of studied comets may not be representative of smaller cometary objects in the outer solar system. The arrival of Dragonfly to Titan in the mid-2030s (Barnes et al., 2021, Lorenz et al., 2018, Turtle and Lorenz, 2024) could be an excellent platform for learning more about the small impactor population in the outer solar system. While the Dragonfly mission is primarily focused on prebiotic chemistry, it is also equipped with a suite of meteorological and geophysical instruments known as DraGMet (Barnes et al., 2021, Lorenz et al., 2018, Rafkin et al., 2018). DraGMet's science goals include characterization of Titan's atmospheric methane abundance, surface atmospheric exchange, and moisture transport as part of understanding the history of Titan's atmospheric methane (Barnes et al., 2021). As part of the DraGMet suite, there are 3 microphones, a pressure sensor, and a seismometer, among other instruments (Barnes et al., 2021, Turtle and Lorenz, 2024). Similar instruments have been used on Earth and Mars to track the passage of impactors (meteors) through their atmospheres (Brown et al., 2007, Daubar et al., 2023, Edwards et al., 2006, Lognonné et al., 2019).

Currently, the most optimistic estimate of impactor rate for impactors larger than a radius of 1 m is $\sim$0.077 events/year when using estimations from (Bottke et al., 2023) following the equations

derived in (Zahnle et al., 2003). Thus, we would expect less than one event over the course of the ∼3 year Dragonfly mission. In addition, high quality data from DraGMet will be limited due to data-constraints, so it is unlikely an event will be captured within routine data returns. However, we could increase the odds of finding such an event if the onboard computer has a reference signal and range of characteristics to flag, so it can make a better-informed decision regarding the return of additional data. Such signals would include predicted overpressure events with their corresponding amplitude and length, as well as any subsequent seismic signals.

Meteors descend through Titan's atmosphere at hypervelocity (> several km/s), which creates extreme stresses on the meteor body. During the descent, the meteor experiences friction from the atmosphere that results in ablation of its surface (Ip, 1990), and the increase in atmospheric pressure during descent may cause the meteor to break up into smaller fragments along its path. Impactors that survive the descent to the surface can leave craters on the surface as long-lived traces of their presence, but only large impactors are able to do so. As a result, Titan has few obvious impact craters below ∼20 km diameter (Hedgepeth et al., 2020), as predicted from pre-Cassini models of atmospheric shielding (e.g. Lorenz (1997)). However, larger impactors are far less common than smaller impactors (Bottke et al., 2023, Nesvorný et al., 2023, Tremaine and Dones, 1993, Zahnle et al., 2003). Smaller impactors often never reach the surface, and may terminate by burning up rapidly, possibly leading to a localized explosion. When a sufficiently rapid breakup of a meteor occurs, the corresponding explosion is referred to as an airburst, and is accompanied by a shockwave (Ceplecha et al., 1998, Revelle, 2005).

Instead of waiting for the limited data return from Dragonfly and searching for signs of airbursts in the pressure sensor and seismometer data, we can plan in advance by describing the potential acoustic and seismic signals. For the hypothetical signal to be recorded, the amplitude of the signal must be greater than the detection threshold of the instrument, and the signal length must be longer than instrument sampling rate. Estimating the bounds of the signal amplitude and length will help us determine if we can detect airbursts on Titan, and if we can distinguish them from other phenomena.

Airbursts have been successfully detected using infrasound networks and seismometers on Earth, supporting the visual identification and confirmation of meteors as observed by telescopes and the naked eye (Brown et al., 2011, 2007, Edwards et al., 2006). Together, this has resulted in better

understanding of the physics of airbursts and their energy propagation to the surface (Edwards et al., 2009, 2006, Wheeler et al., 2017). Several authors have been able to use this information to successfully reconstruct the back trajectory of various impactors, describing their descent sequence and the height of impactor break-ups. Some commonly used models describing the descent of meteors and their associated airbursts have been developed and are detailed in Lyne et al. (1996), Popova (2004), Register et al. (2017), ReVelle (1976), Romig (1965). Several of these models have also been used to replicate crater populations. For example, Korycansky and Zahnle (2005) used a modified version of the pancake model to describe the spread of fragments during descent to estimate the cratering distribution on the surface of Titan.

In this dissertation, I use the code package of Schwarz et al. (2022) to simulate the disruption of icy meteoroids in Titan's atmosphere. This code package includes implementations of the Fragment Cloud Model (FCM) by Wheeler et al. (2017, 2018) and the similar Separate Fragments model (SFM) (Artemieva and Shuvalov, 2001, Bland and Artemieva, 2006, Passey and Melosh, 1980), which was used by Collins et al. (2022) to simulate stony meteoroid breakup in the Martian atmosphere. The FCM is an expansion of the SFM, where a fraction of material from each breakup event explicitly includes a cloud-debris component. This cloud fraction was included to better match complex events (Wheeler et al., 2017). However, Wheeler et al. (2017) note that pancake or discrete fragmentation models are sufficient for the simple flares in which we are interested.

The relationship between the overpressure from the blast wave and the subsequent seismic displacement has also been investigated by several authors (Brown et al., 2007, Edwards et al., 2006, ReVelle et al., 2005, Silber et al., 2018). They find that theoretical estimates approximate the recorded peak displacement within an order of magnitude (Edwards et al., 2007). These studies are supported by blast waves from explosives testing and observations of human-made objects where the velocities are well constrained, such as returning space shuttles travelling faster than the speed of sound. Both produce sonic booms, resulting in blast waves and subsequent ground displacement (Edwards et al., 2008, Glasstone and Dolan, 1977, Kanamori et al., 1992, Silber et al., 2024).

Further from Earth, the use of a seismometer on Mars as part of the InSight mission has proven useful for the detection of meteoroid impacts. The meteoroid impacts detected by InSight produced a seismic signal from surface impact, but also produced seismoacoustic signals where the atmospheric disturbance generated by the impact propagated through the atmosphere and

coupled with the ground at the seismometer (Daubar et al., 2018, Garcia et al., 2022). The impacts were effectively distinguished from other endogenic seismic sources on the basis of this distinct seismoacoustic chirp signal that arrived much later than the very high frequency seismic signal from the impact. Following the positive confirmation of craters in high-resolution optical imagery of the surface, the InSight team has since detected at least nine total impact events (Bickel et al., 2025, Charalambous et al., 2025, Daubar et al., 2023, 2024, Garcia et al., 2022), although other seismic events recorded by InSight have been attributed to impacts based on their similarity in frequency content and size-frequency distribution (Zenhäusern et al., 2024). Among the confirmed impacts, four produced a cluster of craters (as opposed to a single crater) implying that the meteoroid fragmented in the atmosphere. For one of these events, S0986c, multiple chirp arrivals were detected. These have been interpreted as signals produced by the meteoroid during entry and break up, indicating the potential for seismic detection of an airburst (Garcia et al., 2022). However, there has been no confirmed detection of a meteoroid airburst or meteoroid break-up event on Mars that did not produce a crater or craters on the ground.

It is noteworthy that no pressure perturbation events directly associated with impacts were detected by the InSight pressure sensor. The pressure sensor was only in operation during the first apparent airburst on the seismometer and was later not in use due to lander power constraints (Garcia et al., 2022). For later impacts, the estimated overpressure was between 1.5 and 45 mPa, potentially below the noise threshold of around 10 mPa in the 0.5 – 1.5 Hz band. It is possible airbursts from later events would not have been detected regardless (Garcia et al., 2022).

In this work, I conduct a first order investigation to determine whether airbursts could be detected on Titan by Dragonfly. I simulate the descent of small impactors through Titan's atmosphere using the Separate Fragments Model to track the breakup of the meteor and identify the airburst heights. I then describe the airburst signals in terms of overpressure and seismic displacement at the surface. These simulated pressure and seismic signals will provide a point of reference for comparison to data collected during the Dragonfly mission. As data return will be limited, it is not feasible to consistently retrieve high-fidelity time series data for the pressure and seismic sensors and airburst events may be missed. Knowing the unique characteristics of airburst signals will help mission planners to determine the best sampling and signal processing strategy for different instruments.

4.2 Methods

I simulate the descent of various meteor bodies using the Separate Fragments Model (SFM), which has been validated for the Martian atmosphere and combines several models of breakup and dust cloud production (Collins et al., 2022, Wheeler et al., 2017). The physical characteristics of the meteor bodies were retrieved from a range of studies to infer meteor velocities, ice and void fractions, and dynamic strengths (Biele et al., 2022, Borovička and Spurný, 2020, Ceplecha et al., 1998, Nesvorný et al., 2023, Zahnle et al., 2003). The radius of the meteors was selected to range between 1 and 5 m. Atmospheric pressures are extrapolated for use in the SFM from an atmospheric profile of Titan obtained by the Huygens probe (Fulchignoni et al., 2005).

To track meteor descent, fragmentation events, and subsequent child fragment evolution, we simulated meteor progression through the Titanian atmosphere using the SFM as implemented by Collins et al. (2022). The SFM was applied to Mars to simulate the descent of rocky impactors in the Martian atmosphere (Collins et al., 2022). To adjust the SFM for Titan-like conditions, I used the atmospheric density profile retrieved from the Huygens probe using Figures 1 and 2 from (Fulchignoni et al., 2005) and applied an interpolation to create a grid with consistent altitude intervals of 2 km. I note that the FCM might be more applicable when considering icy meteors, as it accounts for a cloud fraction that might be expected from weak meteor bodies. However, the use of a cloud fraction introduces additional variables to the model whose constraints are not well defined by the existing literature. As I am only interested in the upper limit of detectability and the incorporation of a cloud fraction would result in weaker airbursts, the SFM is sufficient for my simulations.

The SFM uses typical equations of atmospheric drag and ablation to track the change in the descent velocity and the change in the mass of the meteor bodies as they experience friction from the descent and increasing ram pressure from the atmosphere (Baldwin and Sheaffer, 1971, Collins et al., 2022, Passey and Melosh, 1980)

$$\frac{dv}{dt} = -\frac{C_D \rho_a v^2 \pi r^2}{2m} + g \sin\theta \tag{4.1}$$

$$\frac{dm}{dt} = -\frac{\sigma \rho_a v^3 \pi r^2}{2} \tag{4.2}$$

$$\frac{d\theta}{dt} = \frac{g \cos\theta}{v} - \frac{C_L \rho_a \pi r^2 v}{2m} - \frac{v \cos\theta}{R_p + z} \tag{4.3}$$

$$\frac{dz}{dt} = -v \sin\theta \tag{4.4}$$

Here, $\frac{dv}{dt}$, $\frac{dm}{dt}$, $\frac{d\theta}{dt}$, $\frac{dz}{dt}$ are the changes to velocity, mass, descent angle, and altitude with respect to time t, where v, m, z are the velocity, mass, and height from the surface. θ is the descent angle (Fig. 4.1). These factors are coupled together in Equations 1 – 4, where $C_D = 1.5$ is the drag coefficient, noting that a drag coefficient of 1 is the Newtonian value and 2 is the free-molecule value (Romig, 1965), ρ_a is the atmospheric density at the current time step, r is the radius of the meteor body (I assume a spherical body), $\sigma = 5 \times 10^{-9}$ kg/J is the ablation parameter, $C_L = 5 \times 10^{-4}$ is the lift coefficient (Collins et al., 2022), and $R_p = 2574.7$ km is the radius of the planet. The gravitational constant at the surface is $g_0 = 1.352$ kg m^{-3}.

In the SFM, the meteor body experiences changes in velocity and mass during the descent using equations of drag and ablation (Artemieva and Shuvalov, 2001, Wheeler et al., 2017). When ram pressure is reached – i.e., when the external pressure exceeds the internal strength of the body, the parent body breaks up and results in child fragments that are also tracked in the SFM. The strength of the child fragment is derived from a Weibull-like distribution (Weibull, 1951). Tracking each of the steps in the SFM simulation results in the energy release curve, which can then be used to estimate burst height and energy available for the airburst.

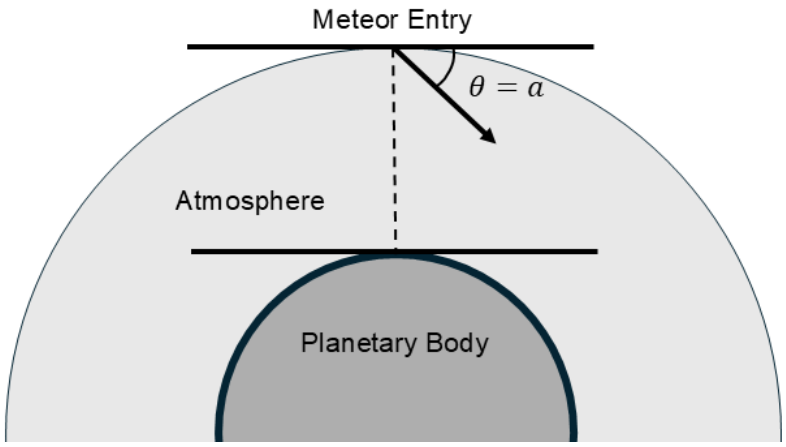


Figure 4.1: Illustration of the meteor entry geometry showing the descent angle a with respect to the atmosphere and planetary body.

Fragmentation occurs when ram pressure, P_R, exceeds the internal strength of the body S as in Equation 4.5.

$$P_R = \rho_a v^2 > S \tag{4.5}$$

In these simulations, the fragmentation results in 2 child fragments, each with a mass of m_f, equal to half of the parent mass m_p. The distribution of fragment mass was chosen so that general fragmentation trends and effects could be understood, such as in the case of Wheeler et al. (2017), Revelle (2005), ReVelle (2007), Baldwin and Sheaffer (1971). The resultant dynamic strength of the child fragments are typically stronger than the parent fragment (Artemieva and Shuvalov, 2001), following a Weibull-like scaling relationship (Wheeler et al., 2017, 2018) with a strength scalar of $\alpha = 0.25$ which is then scaled by a random strength scaling factor from a log-normal distribution by drawing an exponential factor x from a normal distribution with a mean of 0 and standard deviation of $\delta = 0.5$ so that the child fragment can occasionally be allowed to be weaker than the parent fragment as shown in Equation 4.6.

$$Y_f = Y_P(\frac{m_p}{m_f})^{\alpha}10^x, x \sim \mathcal{N}(0, \delta) \tag{4.6}$$

Each of the child fragments is also tracked in the simulation using Equations 4.1 - 4.4 This is the Independent Wakes model presented in Passey and Melosh (1980) which describes the travel of each individual fragment and their breakup condition. The SFM differs from the Independent Wakes model by prescribing the resultant masses and strengths of the meteor fragments following breakup. Ablation of the meteor is described using the Chain Reaction model (Avramenko et al., 2014). For each step in the simulation, the height step is 10 m.

The SFM then outputs the energy that the meteor releases for each height step during its descent, $\frac{dE}{dz}$. For my purposes, I define the airburst height z_{burst} as the maximum $\frac{dE}{dz}$ value and the peak of the energy release curve. This corresponds to rapid and successive fragmentation. This method also corresponds with the general practice of identifying the airburst height by the peak flare in brightness as observed during meteor descent (Brown et al., 2007, Ceplecha et al., 1998). To visualize this, I plot the energy released in each simulated time step against the height as an energy release curve (Fig. 4.2). I note that our criteria for airburst height assumes that each of the simulations results in an airburst. However, not all meteors in our simulations will necessarily result in an airburst, such as the case with meteors that quickly exit the atmosphere at a shallow angle.

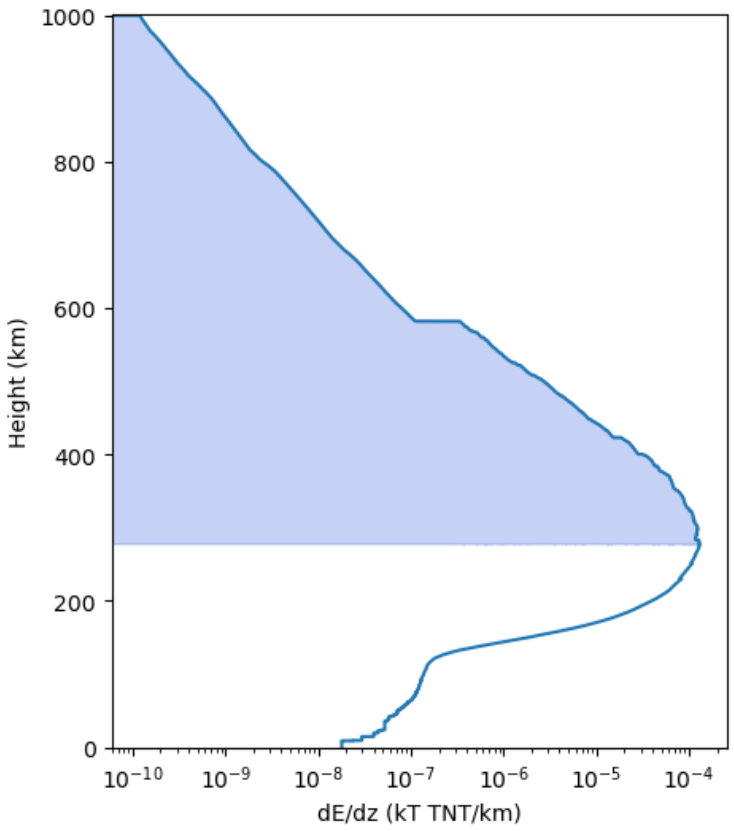


Figure 4.2: Example output of an energy release curve from the Separate Fragments Model for a meteor initiated with the following parameters: $v = 11$ km s^{-1}, $S_0 = 1.0$ kPa, $\rho = 500$ kg m^{-3}, $r = 1$ m, $a = 45°$. We assume that the peak in the curve where we observe the maximum dE/dz value corresponds with the instant of airburst. The shaded area corresponds to the cumulative energy prior to the airburst.

I select the burst height by identifying the peak of the energy release curve corresponding to the maximum energy release. I then use empirical equations that have been validated for a Martian atmosphere to estimate the overpressure at the surface (Collins et al., 2022, Glasstone and Dolan, 1977). These equations take into account the burst height, energy, and atmospheric densities at the burst height and surface. Due to the lack of a standardized method of estimating energy from airbursts, I use the following: (a) 100% of the initial kinetic energy of the incoming body, and (b) the cumulative energy released from the energy release curve as estimated until the burst height. Approach (a) provides the best-case scenario for detection, as the maximum energy in the system is used to generate the overpressure. Approach (b) describes a scenario where we estimate that all the energy lost during the initial descent until airburst contributes to the blast wave.

From the overpressure, I can estimate the seismic surface response due to the blast wave coupling

with the ground. The vertical velocity of the ground is estimated from the overpressure, incident angle and density of the air and ground (Ben-Menahem and Singh, 1981, Edwards et al., 2009, Xu et al., 2022). The duration of the signals will likewise be estimated from Glasstone and Dolan (1977), and the respective seismic generation methods either via simulation or analytical solutions Edwards et al. (2009), Martire et al. (2021), ReVelle and Edwards (2007). For both the overpressure and seismic response, I will also describe how the amplitude of the airburst signals decreases with increasing distance from the source to identify a distance limit.

4.2.1 Meteor Properties

To initialize the simulations in the SFM, I selected a range of meteor sizes between 1 to 5 meters in radius. The number of events $N(> d)$ expected to occur can be estimated using the equation from Zahnle et al. (2003) for objects of diameter less than 1.5 km.

$$N(> d) = P_{EC} N_J(> d), d < 1.5\text{km} \tag{4.7}$$

Here, d is the diameter of the comet, P_{EC} is the ecliptic cometary impact probability relative to Jupiter, and N_J is the number of comets estimated to impact Jupiter each year. Using Bottke et al. (2023)'s estimates for N_J where $N_J(> 2m) \sim 1424$ comets and $N_J(> 10m) \sim 24$ comets, and scaling the number of events impacting Jupiter to Titan with Zahnle et al. (2003)'s value of $P_{EC} = 5.4 \times 10^{-5}$, I find that $N(> 2\text{m}) = 0.077$ events/year for meteors of radius 1 m. This corresponds to one such meteor every ∼13.0 years. Similarly, we find that $N(> 10\text{m}) = 1.30 \times 10^{-3}$ events/year for meteors of radius 5 m, corresponding to one strike every 771.6 years. Over the roughly 3-year lifetime of Dragonfly, I can estimate k, the probability of one 1-m object impacting Titan, if I assume that the expected impact rate of λ events follows a Poisson distribution over the same time interval. I find that the probability that $k = 1$ for one event during the three-year timeframe is $\sim 18.3\%$ for an average of $\lambda = 0.231$ events over three years. For two such events, the probability becomes $\sim 2.1\%$.

$$P_N = \frac{\lambda^k e^{-\lambda}}{k!} \tag{4.8}$$

In ny model, I set the entry velocities between 10 – 12 km/s, where 10.5 km/s is the average entry

velocity for Titan (Zahnle et al., 2003), and initialized entry angles between $15-75°$, where a $0°$ entry would immediately exit the atmosphere and a $90°$ entry is vertical to the surface. Outer solar system impactors are likely cometary in nature (i.e. from the Trojans or Centaurs), so we set densities of $250 - 750\ \mathrm{kg\,m^{-3}}$ to describe icy bodies corresponding with porosity (void space fraction) between 75% and 25% (Borovička and Spurný, 2020). In Groussin et al. (2019), they summarize the general properties of cometary nuclei and found they have densities of 480 +/- 220 $\mathrm{kg\,m^{-3}}$, with porosities of 70 - 80%, and of global tensile strengths < 100 Pa. However, the dynamic internal strength of the meteor body is poorly constrained for cometary bodies. Icy bolides are loosely bound porous icy-rock mixtures, with lower strength than that of rocky bodies (Borovička, 2005). Compressive strengths as high as 1.5 kPa have been observed for comet Churyumov–Gerasimenko/67P from the Rosetta mission and an upper limit of 12 kPa was inferred for Comet 9P/Tempel 1 from the Deep Impact mission (Biele et al., 2022). Recent estimates from Biele et al. (2022) show that unevolved cometary materials can have a tensile strength as low as 1×10^{-3} kPa. However, these estimates are derived from observed cometary bodies, and the smallest of these were $>$ 10s of meters in diameter. Given that strength tends to inversely scale with diameter (Biele et al., 2022, Bryson et al., 2018, Housen and Holsapple, 1999), it is reasonable to assume strengths for our simulations should be greater than the lowest estimated tensile strengths, as my chosen meteor radii are smaller than those investigated by Biele et al. (2022). However, I note that Attree et al. (2018) estimated that the tensile strength of the likely homogeneous 67P/Churyumov-Gerasimenko may range between 1 - 5 Pa at the meter-scale, and strong heterogenities on the scale of a few meters were considered unlikely on 67P (Groussin et al., 2019). To account for the uncertainty of estimated strengths for cometary materials, I investigated strengths between 0.001 and 10 kPa such that the dynamic strength encompasses the range of potential tensile and compressive strengths for cometary meteors. All my initializing parameters are described in Table 4.1, with other SFM settings remaining the same as in the default settings.

Table 4.1: Initiating parameters for the Separate Fragments Model.

Symbols	Meteor Parameter	Value	Additional Values
	Entry Altitude[1]	1000 km	
a	Entry Angle	45 °	[15, 30, 60, 75] °
v	Entry Velocity	[10, 11, 12] $\mathrm{km\,s^{-1}}$	
r	Radius	[1, 2, 3, 4, 5] m	
ρ	Density	500 $\mathrm{kg\,m^{-3}}$	[250, 750] $\mathrm{kg\,m^{-3}}$
S_0	Internal Strength	[0.001, 0.01, 0.1, 1.0, 10.0] kPa	

To estimate variability in our results, I simulated three additional runs using different random seeds for the following cases: $v = 11$ km/s, $a = 45°$, $\rho = 500\mathrm{kg\,m^{-3}}$ for all radius and internal strength ranges to retrieve the standard deviation in burst height and cumulative burst energy. I then converted these values to percentage deviation to be applied to other cases and the subsequent overpressure and seismic amplitude calculations. For overpressures that were estimated using the kinetic energy from the initial meteor parameters, I only used the burst height to propagate errors.

4.2.2 Overpressure Estimations

To determine the overpressure at the surface, the energy release from the airburst itself must be estimated. As there are no standard methods to estimate the energy of the airburst, I calculate the energy release using three different methods. 1) The maximum energy available for the airburst is calculated by assuming the initial kinetic energy of the incoming meteor would be entirely converted into the airburst energy, $E_{Kmax} = \frac{1}{2}mv^2$. E_{Kmax} is used to constrain the maximum overpressure that we can anticipate. As this value is overly optimistic, I also consider 2), half of E_{Kmax}, E_{K50}, based on observations that half of the energy from bursts in nuclear tests was radiated away (Glasstone and Dolan, 1977). Previous work by Boslough and Crawford (2008) has shown that an equivalent point source explosion at the altitude of the airburst may lead to an underestimation of the overpressure at the surface. Thus, my estimates using kinetic energy may also be an underestimation of the maximum overpressure. Finally, I consider 3), the cumulative energy released until the point of airburst, E_{cum}. This approximation reasonably aligns with the equivalent yield energy

[1]The entry altitude is fixed at 1000 km for each of the simulations. I used a random seed of 0 for the base cases. I sampled the entire parameter space of the listed entry velocity, radius, and internal strength of the meteors for an entry angle of 45 °as listed under the Value column. For meteors with entry velocity of 11 km/s and density of 500 $\mathrm{kg\,m^{-3}}$, I additionally simulated different entry angles as listed under Additional Values. I also simulated varying densities listed under Additional Values for $v = 11$ km/s, $a = 45°$. To estimate errors, I also randomly selected three additional random seeds for each of the $v = 11$ km/s base case simulations.

inferred from infrasound records of observed events on Earth (e.g. Ens et al. (2012), Gi and Brown (2017)). Additionally, this approach was previously used to estimate the equivalent airburst energy from the Chelyabinsk event. The resulting energy estimate was similar to that derived from other methods, including estimates using the seismic and infrasound recordings (Brown et al., 2013).

To convert the airburst energy into overpressure at the surface, I use an approach based on empirical data and equations previously developed for a 1 kt nuclear blast in the Earth's atmosphere (Glasstone and Dolan, 1977). This adaptation is supported by the similarities between Titan and Earth's atmospheric pressure profile, with an exponential decrease in pressure until the stratosphere where these equations derived by Glasstone and Dolan (1977) are typically considered applicable.

Collins et al. (2017) provides an empirical overpressure equation experienced at Earth's surface, with constants derived from fits to the nuclear test data on Earth:

$$P_{Earth} = 3.14 \times 10^{11} d_{slant}^{2.6} + 1.8 \times 10^{7} d_{slant}^{-1.13} \tag{4.9}$$

Here, d_{slant} is the slant distance from the burst to the receiver. I use the scaling relations from Glasstone and Dolan (1977) to scale the equations from the 1 kt case to the ambient pressures at Titan's surface. The full derivation is included in Appendix A of (Dong et al., 2026). The resultant overpressure at the surface P_{Titan} is provided by Equations 4.10 and 4.11

$$P_{Titan} = (3.14 \times 10^{11} d_{scale}^{2.6} + 1.8 \times 10^{7} d_{scale}^{-1.13}) \left(\frac{P_{ambT}}{P_{Earth}} \right) \tag{4.10}$$

$$d_{scale} = \frac{d_{slant}}{\left(\frac{W_{burst}}{ktTNT}\right)^{\frac{1}{3}} \left(\frac{P_{Earth}}{P_{ambT}}\right)^{\frac{1}{3}}} = \frac{z_{burst}}{\left(\frac{W_{burst}}{ktTNT}\right)^{\frac{1}{3}} \left(\frac{P_{Earth}}{P_{ambT}}\right)^{\frac{1}{3}}} \tag{4.11}$$

Here, $P_{ambT} = 147$ kPa is the ambient pressure at Titan's surface, and $P_{Earth} = 101.325$ kPa is the ambient pressure at Earth's surface. d_{scale} provides the scaling factor for converting burst distance from Earth to Titan's atmosphere, where W_{burst} is the airburst energy in ktTNT. To maximize the likelihood of detection, I assume that the airburst takes place directly above Dragonfly such that $d_{slant} = z_{burst}$ in km.

As with past work, I validate the overpressure estimates with hydrodynamical simulations with support from coauthors. After determining the burst heights and their corresponding energies,

we numerically investigate the overpressure caused by a static energy release using the iSALE-2D shock physics code (Amsden et al., 1980, Collins et al., 2004, 2016, Wünnemann et al., 2006). For iSALE-2D, both the burst height and burst energy are required inputs to investigate the expansion of the blast energy. To describe Titan's atmosphere, we use the Huygens Atmospheric Structure Instrument (HASI) temperature profile to set the atmospheric temperature (Huber, 2019). We use the simplified Tillotson equation of state (EOS) of an ideal gas for the atmosphere (Collins et al., 2016). We set the maximum height in the computational domain to 300 km to prevent any reflection of the shock wave caused by the airburst, and investigate horizontal distances up to 300 km from the burst point. Note that we also use the same EOS for the spherical static source. In contrast to the temperature profile, iSALE cannot directly incorporate the pressure profile from the instrumental data. Thus, we adjust the pressure in iSALE to match the observed data at the ground (i.e., 147 kPa), as the surface pressure is important in estimating an overpressure for the empirical method (see Eq. 4.10). While iSALE calculates the pressure from the top of the atmosphere towards the surface, the pressure profile deviates from the observed data in the upper region possibly due to the numerical limitation and/or usage of simplified EOS (Fig. 4.3). Nevertheless, this deviation will not significantly affect our results since our interest is from the burst location towards the ground.

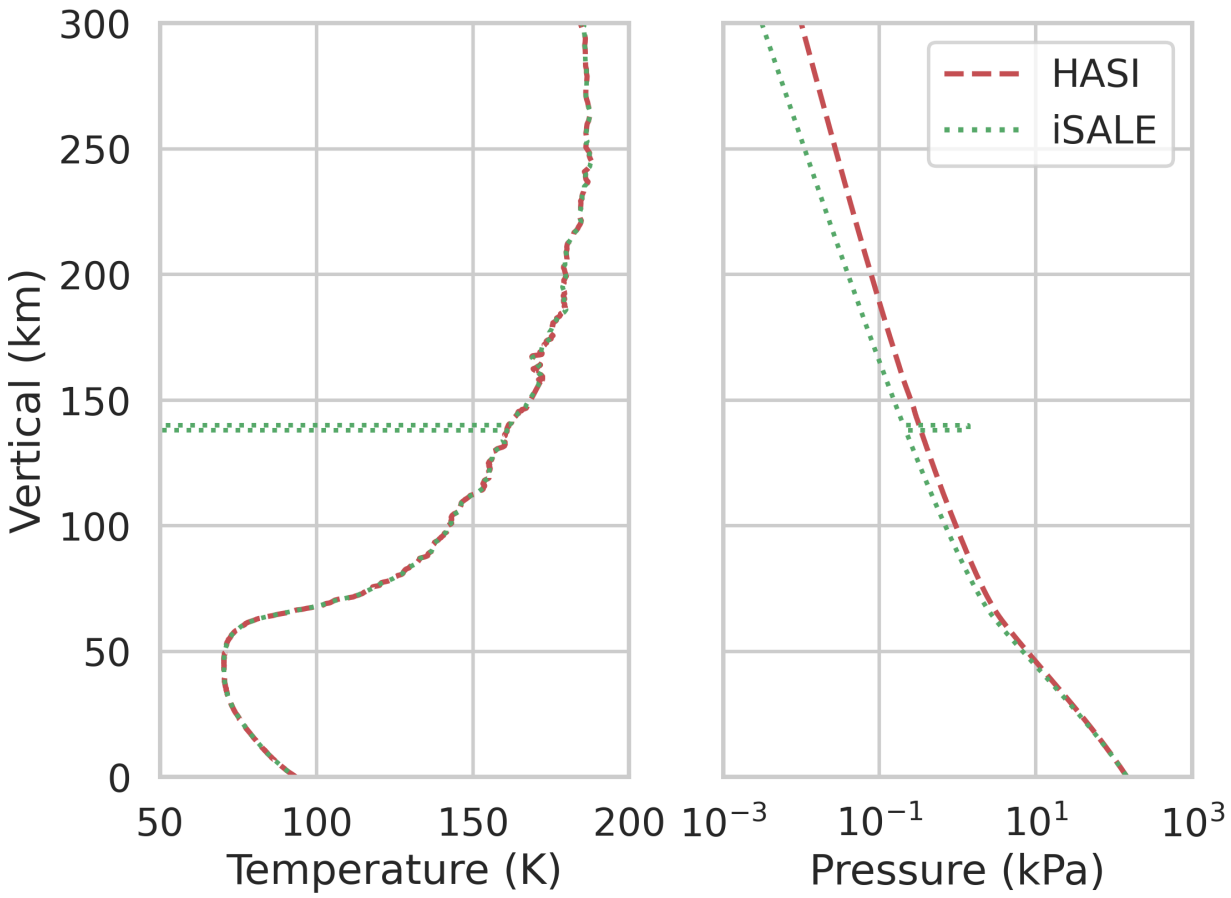


Figure 4.3: Temperature and pressure profile used in iSALE. Red dashed lines depict HASI data. Green dotted lines indicate the initial profiles in iSALE, assuming a burst point of 139 km. The discontinuous horizontal lines illustrate the burst point at 139 km.

In this work, we consider a Titan airburst as a spherical static source with a radius of 1000 m. To reasonably simulate a Titan airburst, we use a resolution of 100 m which corresponds to 10 cells per projectile radius. Collins et al. (2017) used much smaller sources comparable with the size of meteor. However, if we implemented a static source with the same size as our meteors with radii of a few meters, the simulation would be computationally expensive. We require at least 10 cells to resolve a static source and the burst heights in our case are beyond 100 km, so we consider a larger static source than the meteor. Although our initial burst size is much larger than the meteor, we use the same initial energy. Therefore, we expect our model results to align with our evaluation to within an order of magnitude. Note that assuming a static source model can result in two times smaller overpressure compared to the other models (e.g., the moving-source model, Collins et al. (2017)). We opt to use iSALE as a validation method rather than the sole

overpressure estimation method due to the immense computational time and resources required to generate iSALE simulations.

I then estimate the travel time the blast wave takes between the onset of the airburst to the overpressure signal at the surface, t_{Titan}. I assume that the airburst travels directly from source to receiver in a vertical path at the local speed of sound, c_{Titan}

$$t_{Titan} = \int_0^z \frac{dz}{c_{Titan}} \tag{4.12}$$

I can retrieve the speed of sound estimates from the Huygens Atmospheric Structure Instrument (HASI) temperature profile from Huber (2019) by relating the speed of sound to the temperature (Eq. 4.13). The HASI temperature profile showed a surface temperature of $T_0 = 93.5$ K at the Huygens landing site, and I use an approximate speed of sound at the surface of $c_0 = 194 \mathrm{m\,s^{-1}}$ (Hagermann et al., 2007). Thus, for each of the sample height intervals, I can estimate the representative speed of sound assuming that the ideal gas law holds with a stable atmospheric composition. Further discussion on the variability of methane concentration in the atmosphere can be found in Hagermann et al. (2007). I retrieve the temperature at each height step T_z from the temperature profile using Equation 4.13.

$$c_{Titan}(T_z) = c_0 \sqrt{\frac{T_0}{T_z}} \tag{4.13}$$

I can additionally estimate the length of the overpressure signal τ_{Titan} using the scaling laws derived by (Glasstone and Dolan, 1977) using reference values for pulse lengths on Earth (Eq. 4.14, with full derivation in Appendix A in Dong et al. (2026)). I am interested in the positive pulse phase, which is the initial wave of positive overpressure from the blast wave. This length does not include the subsequent negative pressure that follows the initial overpressure (Fig. 4.4).

$$\tau_{Titan} = \tau_1 \left(\frac{W_{burst}}{ktTNT}\right)^{\frac{1}{3}} \left(\frac{P_{ambT}}{P_T}\right)^{\frac{1}{3}} \left(\frac{T_{ambT}}{T_T}\right)^{\frac{1}{2}} \tag{4.14}$$

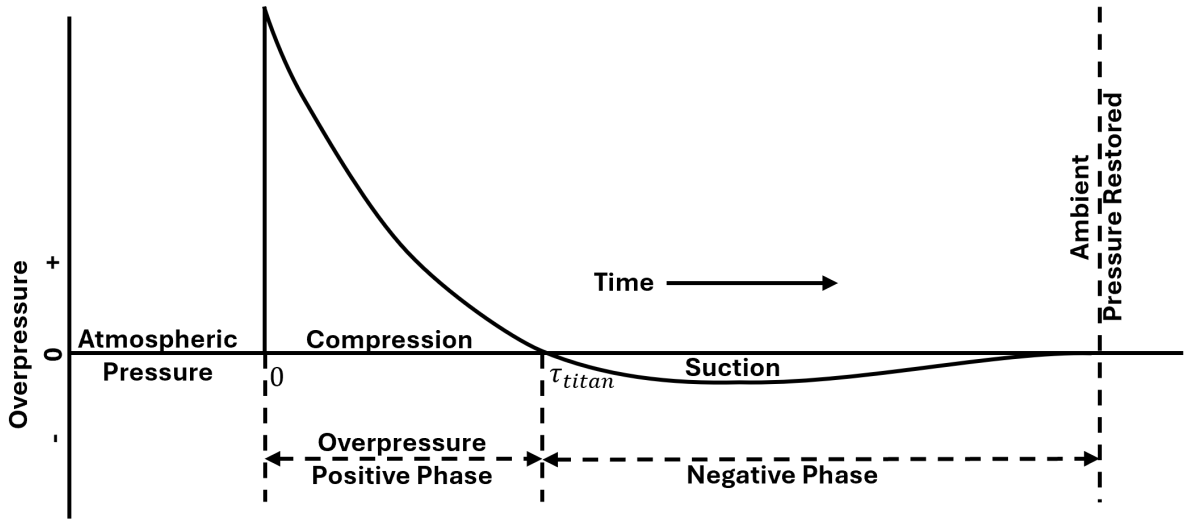


Figure 4.4: Illustration of the overpressure pulse from a single point source recreated from Glasstone and Dolan (1977)'s Figure 3.11. Upon arrival, the pressure increases sharply to a peak, before decaying and the atmosphere is restored to its previous pressure. The first phase where the increase in pressure is positive is the positive pulse phase.

τ_1 is the time for a reference 1-ktTNT blast as retrieved from the positive pulse phase plot in Glasstone and Dolan (1977)'s Figure 3.76. $T_0 = 288.15$ K and T_{Titan}=93.5 K are the temperatures at standard sea level on Earth, and the surface of Titan, respectively. P_T and T_T are the pressure and temperature at the burst height in Titan's atmosphere.

However, this extrapolation is limited, as the maximum burst height shown in Glasstone and Dolan (1977)'s Figure 3.76 is 0.3 km. ReVelle (1976) derived an equation to evaluate the change in pulse frequency, and thereby pulse length, as the shock transitions from the initial highly nonlinear ballistic shock to a weakly nonlinear shockwave where the waveform experiences distortion (Cotten et al., 1971)

$$\tau = 0.526 \left(\frac{1}{\tau_1} \right) z_{burst}^{0.25} \tag{4.15}$$

Using Equation 4.15, I can extend the reference positive pulse phase length to relevant burst heights for an Earth-like atmosphere, then convert this to the equivalent overpressure signal length for a Titan atmosphere using the scaling laws in Equation 4.14 for the weakly nonlinear phase. Alternatively, I can directly estimate the period of the blast τ_0 by calculating the fundamental frequency f_0 (ReVelle, 1976) at the burst height

$$f_0 = \frac{1}{\tau_0} = \frac{c_{Titan}}{2.81 R_0} \tag{4.16}$$

$$R_0 = \left(\frac{W_{burst}}{4\pi P_T} \right)^{\frac{1}{3}} \tag{4.17}$$

Where R_0 is the blast radius for a spherical blast (Sakurai, 1964), calculated with reference to the local atmospheric pressure for a burst energy of W_{burst} (joules). Note that Edwards et al. (2008) formulates the blast radius as $R_0 = \left(\frac{3W_{burst}}{4\pi P_T} \right)^{\frac{1}{3}}$.

Following the weakly nonlinear phase, the blast wave may transition to a linear phase where the period and length of the positive pulse phase becomes fixed. I estimate this transition distance by following the procedure described in Edwards et al. (2008) in section 12.13, where linearity occurs when the distortion distance is greater than the remaining distance the pulse needs to travel. This distortion distance, $d\prime$, where the fundamental period f_0 is distorted by 10% is shown by

$$d\prime = \frac{C_s \tau_0}{34.3 \left(\frac{\Delta p}{p} \right)} \tag{4.18}$$

for the local speed of sound C_s, fundamental period τ_0, and the overpressure to local pressure ratio at a given height $\frac{\Delta p}{p}$ (Edwards, 2009b, Towne, 1967). To describe the transition between the weak shock and linear regimes and the final burst period, I implemented the code provided in the Supracenter package (McFadden et al., 2021) and replaced the atmospheric conditions with the HASI atmospheric profiles for temperature and pressure. Here the speed of sound is calculated using

$$C_s = c_{Titan} = \sqrt{\frac{\gamma R T}{M_0}} \tag{4.19}$$

where I set $\gamma = 1.4$ as the heat capacity ratio, R is the ideal gas constant, T is the temperature at the burst height in Kelvin, and $M_0 = 28.3$ g/mol is the molar mass of the air at 94 K (Samuelson et al., 1981). To run the simulation, I chose to evenly divide the distance between the burst height and the surface distance by 10000 intervals for the calculations. The estimate for the positive phase pulse length is simply half of the period.

In this work, I used three methods to estimate the positive phase length. The first is extending Glassstone and Dolan's values in Equation 4.14 to Titan's atmosphere and accounting for weakly nonlinear behaviour (Eq. 4.15). Second, I directly estimate the fundamental frequency (Eq. 4.16) at the start of the blast wave and assume it travels as a weakly nonlinear wave to the surface, again applying Equation 4.15. Third, I consider that the wave may shift from weakly nonlinear to linear and the period of the wave becomes fixed. I simulate the final period of the wave for this method using the Supracentre package.

I additionally considered the effects of atmospheric attenuation that would be expected for higher altitude airbursts. However, I estimated the expected attenuation in Titan's atmosphere for acoustic frequencies lower than 10 Hz (Petculescu and Lueptow, 2007) and find the atmospheric attenuation coefficient is less than $5.65 \times 10^{-10}\mathrm{m}^{-1}$ and is several orders of magnitude less than the atmospheric attenuation on Earth. Thus, I do not include the effects of atmospheric attenuation in our results.

4.2.3 Seismic Response

When the blast wave reaches the surface, the compressive wave will provide an impulse onto the surface, resulting in a coupling response.Ie can describe the surface response independent of the instrument by treating the atmosphere and the surface interface as a fluid and solid half-space. Using equations derived by Ben-Menahem and Singh (1981), I estimate the vertical velocity of the surface in response to an impulsive force using the following equation from Edwards et al. (2009).

$$V_z(t) = P_0 \left(\frac{m_2}{m_1}\right)\left(\frac{\cos e}{\rho_a C_s}\right)\exp(i\chi(t)) \tag{4.20a}$$

$$m_1 = \cos e \left[\left(\frac{V_s}{V_p}\right)^{\frac{1}{2}} \sin 2e\prime \sin 2f\prime + \cos 2f\prime^2\right] \tag{4.20b}$$

$$m_2 = \left(\frac{\rho_a C_s}{\rho_s V_p}\right)\cos e\prime \tag{4.20c}$$

$$\hat{c} = \frac{C_s}{\sin e}, x = z_{burst}\tan e \tag{4.20d}$$

$$V_z(t) = \frac{P_0}{\rho_s V_p}\exp\left(i\chi(t)\right) \tag{4.20e}$$

Here e is the incident angle from the overpressure wave, where $e\prime$, and $f\prime$ are angles of the refracted P and S-wave components into the surface. The sound speed in air at the surface is described by C_s, with the apparent horizontal particle velocity (trace velocity) of $\hat{c}$ where x is the horizontal distance. The P- and S-wave velocities in the surface are V_p and V_s, respectively. The density of the atmosphere and surface are ρ_a and ρ_s, respectively. For this work, I consider the best-case scenario, where the burst occurs directly overhead, maximizing the signal we would detect in comparison to less favourable geometries. Thus, the incident angle of the overpressure is $e = 0°$, which also leads to $e\prime = 0°$, then Equation 4.20a simplifies to 4.20e. The seismic pulse amplitude is described by the incident overpressure P_0 and the phase shift from the overpressure pulse into the surface is $\exp(i\chi(t))$ where the shape of the overpressure pulse is described as a function of time, $\chi(t)$. To investigate the maximum amplitude of the vertical velocity and corresponding length of the seismic signal, I describe the overpressure at the surface in the form of half of a sine wave, such that

$$\chi(t) = \sin 2\tau_{Titan} \forall t, 0 \leq t \leq \tau_{Titan} \tag{4.21}$$

The surface is assumed to consist of organic polymers with a corresponding density range of 500 – 1500 $\mathrm{kg\,m^{-3}}$ to account for the wide range of densities determined in previous Titan analogue experiments (Burr et al., 2006, Hörst and Tolbert, 2013, Imanaka et al., 2012, Trainer et al., 2004). The atmospheric parameters are fixed for surface level values with a speed of sound of $C_s = 194$ m/s and a density of approximately $\rho_a = 5.0\mathrm{kg\,m^{-3}}$ as extrapolated from the HASI data (Huber, 2019).

I consider a range of material velocities (Table 4.2). These include sandstone and sand to provide some sense of granular materials at the surface with varying compactness and saturation. Till is included to represent poorly sorted materials at the surface. I also consider water ice to represent the icy shell of Titan's surface (Sotin et al., 2021).

Material	V_p range (km/s)	V_s range (km/s)
Basalt	5.2 – 6.2	3.3 – 4.0
Sandstone	3.0 – 5.0	1.4 – 2.5
Wet Sand	1.5 – 2.2	0.7 – 0.8
Till	1.9 – 2.6	0.8 – 1.0
Water Ice at 94 K	2.9 – 3.0	1.3 – 1.7

Table 4.2: Average compressional velocities of common materials on Earth (Earle and Panchuk, 2019) and approximate Martian regolith and bedrock properties (Lognonné et al., 2020). To estimate the water ice velocities at Titan surface temperatures, we use equations from Kohnen (1974). Note that the inclusion of methane clathrates would decrease the velocity of a water ice shell by around 4.6% (Marusiak et al., 2022). Seismic velocities are further modified by factors such as pressure, porosity, temperature, fluid saturation (Bykov, 1994), and for sandstone, clay percentage (Eberhart-Phillips et al., 1989).

I estimated the standard deviation for our airburst heights and energies by simulating 3 additional runs using random seeds for our base cases of $v = 11\text{km}\,\text{s}^{-1}$, $\rho = 500\text{kg}\,\text{m}^{-3}$, $a = 45°$, radius between $r = 1 - 5$ m and $S_0 = 0.001 - 10.0$ kPa.

4.3 Simulation Results

4.3.1 Burst Heights

I first evaluated the effect of strength, radius (and by proxy, mass), and incidence angles on burst height (defined in Section 4.2). I found that objects with low strength (0.1 Pa) resulted in burst heights at the top of the atmosphere. Thus, I removed these simulations from the general discussion as the bursts occur well above the troposphere and the scaling relationships dependent on the exponentially decreasing pressure profile were not validated above the troposphere (Glasstone and Dolan, 1977).

For meteors with shallower incident angles of 15 °and 30 °, I found that they consistently produced energy release curves with peaks at the same altitudes, regardless of their initial strength or radius. This is likely a consequence of the meteor travelling through the atmosphere at a shallow angle, with most of the meteor eventually exiting the atmosphere (Fig. 4.5). I also remove these simulations from further discussion. For our remaining simulations, we can observe that burst heights generally decreased with increased strength and increased radius regardless of the incident angle (Fig. 4.6).

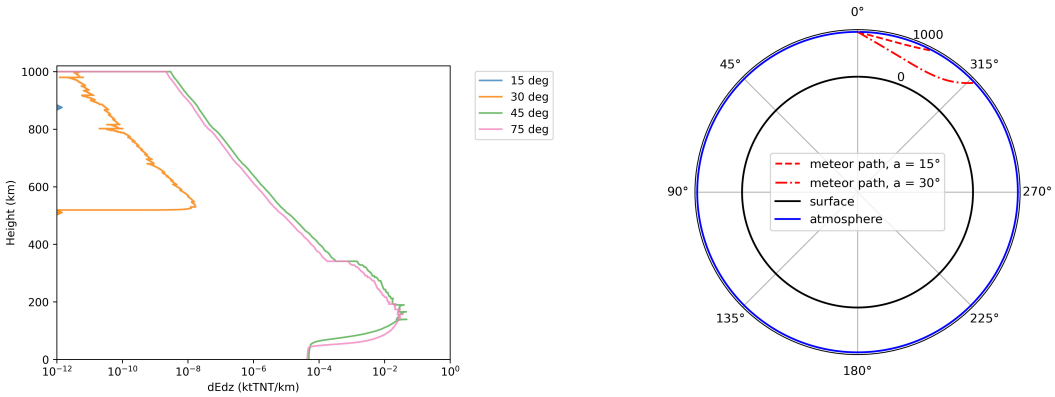


Figure 4.5: Left: Energy release curve example for $v = 11$ km s^{-1}, $S_0 = 10.0$ kPa, $r = 5$ m, and $\rho = 500$ kg m^{-3}. Negative energy contributions to the atmosphere where the meteor gains kinetic energy are not shown. The height at which the 15 °and 30 °meteor changes its trajectory to be upwards is indicated by a blue and yellow triangle on the y-axis, respectively. Right: Plot of the 15 °and 30 °meteor trajectories through the atmosphere. Note that they exit the atmosphere before producing an airburst.

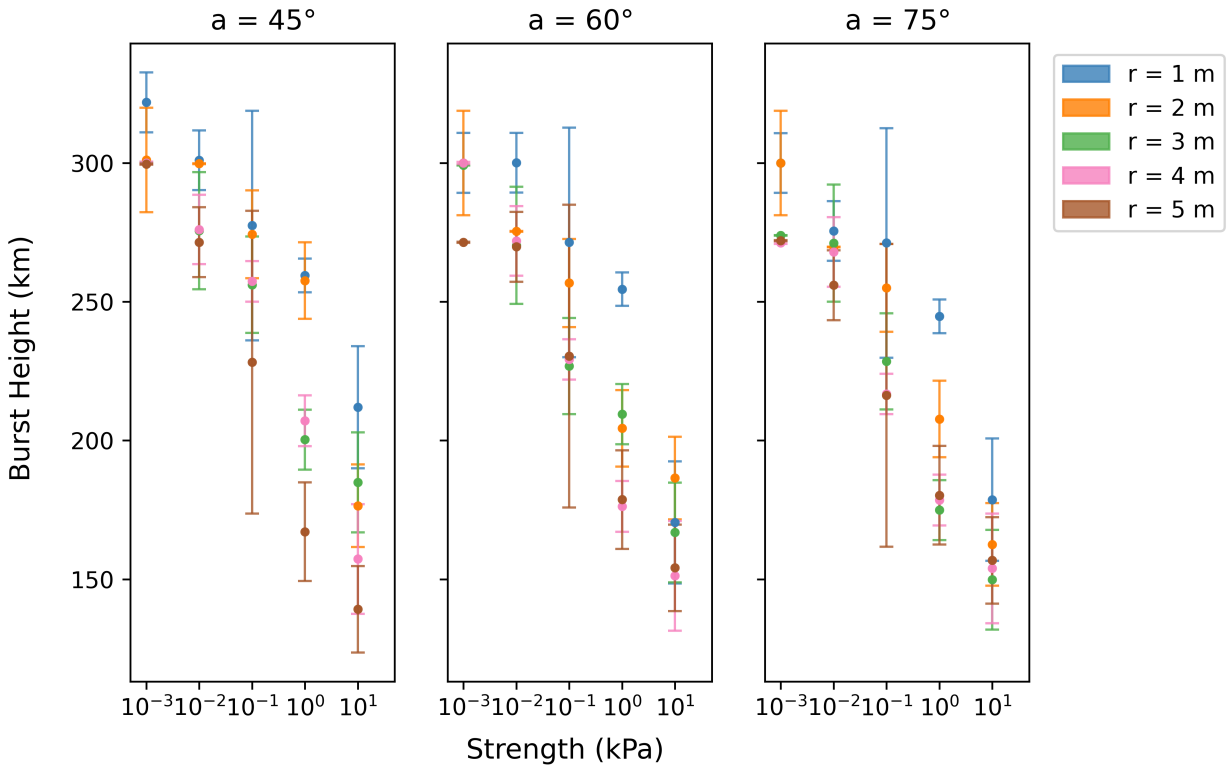


Figure 4.6: Burst height at a variety of incoming meteor incident angles, radii, and strengths for an incident velocity of $v = 11$ km s^{-1} and $\rho = 500$ kg m^{-3}. The error bars are the standard deviation as estimated from additional simulations with different random seeds. The colour of the markers corresponds to the radius of the initial meteor. For a fixed meteor strength, airburst heights are within 50 km of each other regardless of the initial radius. Entry incident angle affects burst height as well. Generally we can observe that an increase in incident angle decreases the burst height for smaller strength meteors. However, this relationship is not consistent for all of our simulations. The variability in airburst height based on the change in entry angle was around 50 km, keeping all other variables constant.

Contrary to expectations, increasing the incident entry angles does not clearly correspond to lower burst altitude in my simulations (Fig. 4.6) (Robertson and Mathias, 2019). For example, in Figure 4.6, we can observe that the meteor with $r = 5$ m, $S_0 = 10.0$ kPa had the lowest airburst height at 45 °in comparison to similar meteors with steeper entry angles. When I consider the large uncertainty in burst height however, the difference between the simulations for different incident angles is insignificant. If we only consider meteors with initial strength $S_0 = 0.1$ Pa, then the burst height does appear to correspond with incident entry angle with a decrease in burst height with an increase in entry angle.

Further inspection of the individual simulations shows that in several of my simulations with

steeper descent angle and higher strength, there were multiple distinct peaks in the energy release curve, suggesting an airburst with multiple major fragmentation events (Fig. 4.7). I note that the magnitude of the additional peaks is of the same order as what we determine to be the airburst peak, with strong peaks spaced $\sim$ 25 km higher than the next peak. Thus, for these simulations with multiple large peaks, I can estimate the specific overpressure contribution from those additional events and evaluate whether they arrive as distinct waves to the surface.

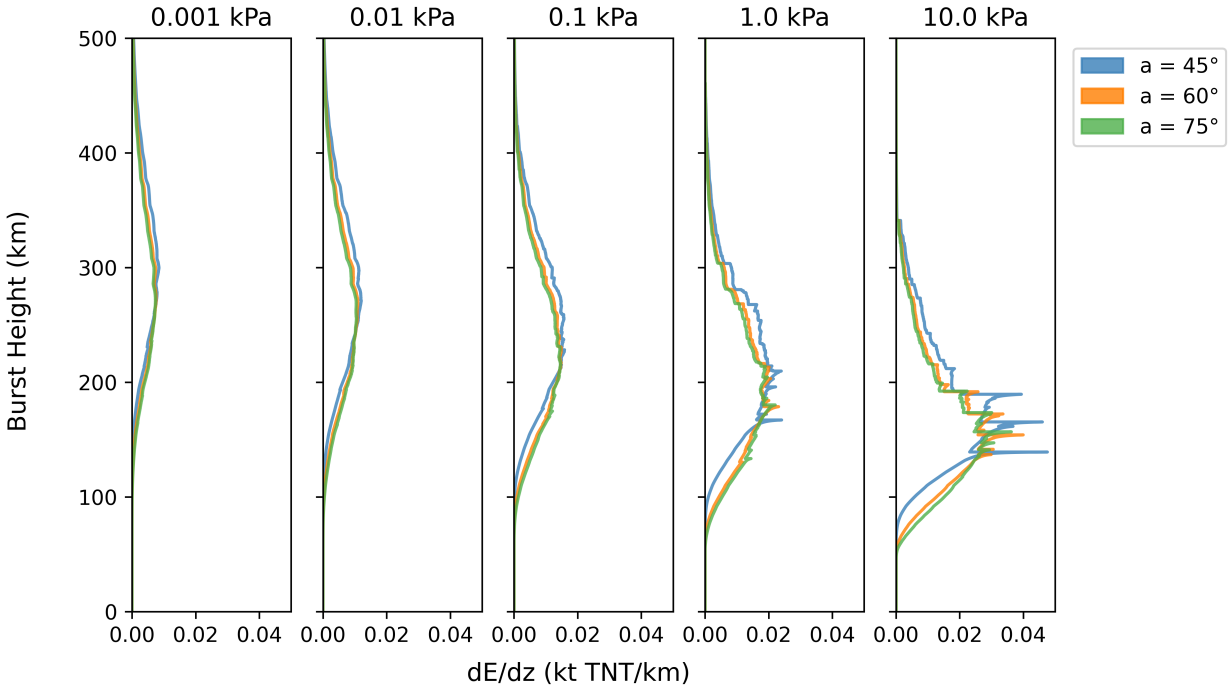


Figure 4.7: Energy release curves for varying incidence angles with increasing incident strength. $v = 11$ km s^{-1}, $r = 5$ m, $\rho = 500$ kg m^{-3}. Note that the simulations with incident strength $S_0 = 1.0$ and 10.0 kPa show multiple potential airburst peak locations. For energy release curves with multiple peaks, the maximum peak height is taken to be the airburst height.

I found that the effect of entry velocity on burst height was not immediately apparent (Fig. 4.8). Burst heights for low strength objects $\leq$ 0.01 kPa were independent of the meteor's initial velocity. As with the incident angle of the meteor, there is an unexpected absence of a clear trend in burst height with initial meteor velocity. This may be partly due to the simulation procedure that involves the use of random seeds for the fragmentation procedure. We can observe that the variability in burst height is 10s of kms. However, for smaller and stronger meteors, I found a difference of around 50 km in burst height for varying velocities with the highest burst heights for

the $v = 12\text{km}\,\text{s}^{-1}$ case. Again, we can observe that for meteors with initially higher strengths, the energy curves displayed multiple potential airburst peaks.

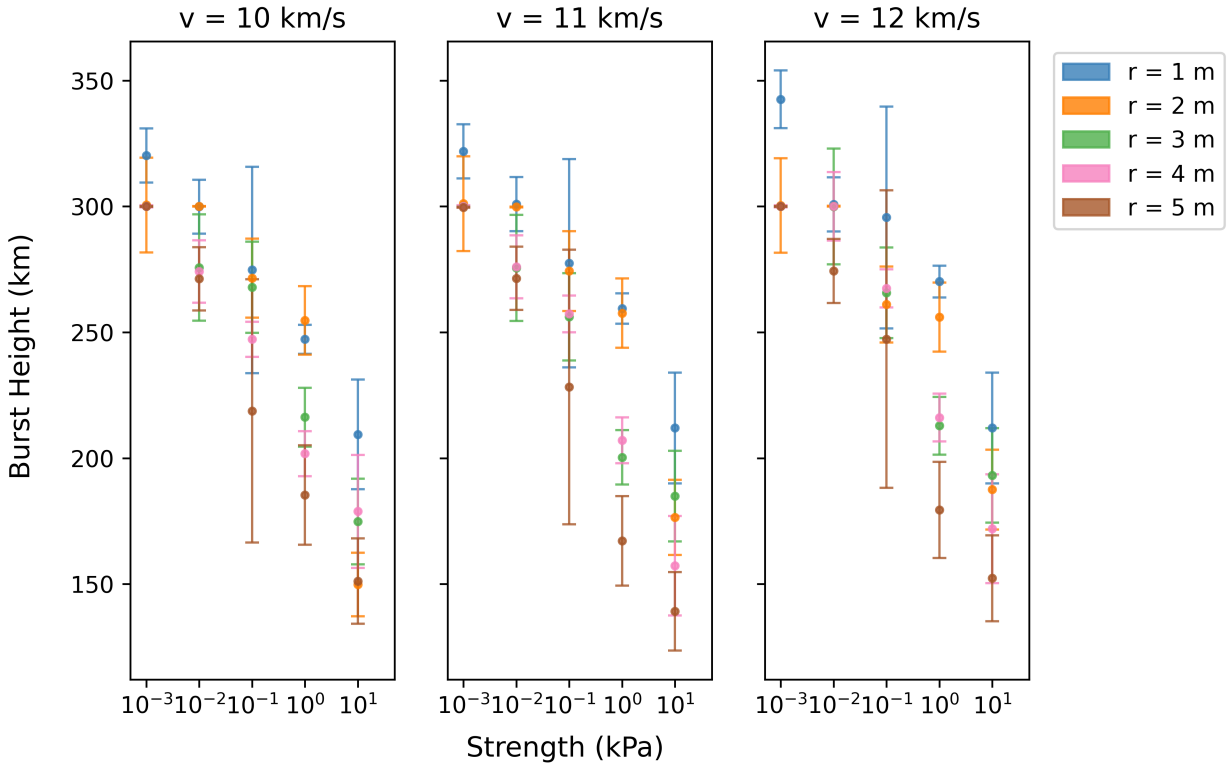


Figure 4.8: Examining the relationship between entry velocity and burst height. From left to right, we plot the airburst heights as estimated from the maximum $\frac{dE}{dz}$ value in the energy curve for variable initial velocity, radius, and strength at incident angle $a = 45°$, $\rho = 500\ \text{kg}\,\text{m}^{-3}$. The colour of the markers corresponds to the radius of the initial meteor. There is no clear trend between the incident velocity and the burst height.

The effect of density did not appear to be significant in terms of the burst height either, though for lower strength and smaller radius meteors there was a decrease in burst altitude with increasing density (Fig. 4.9). This is not surprising as the mass loss progression is more dependent on strength than total mass.

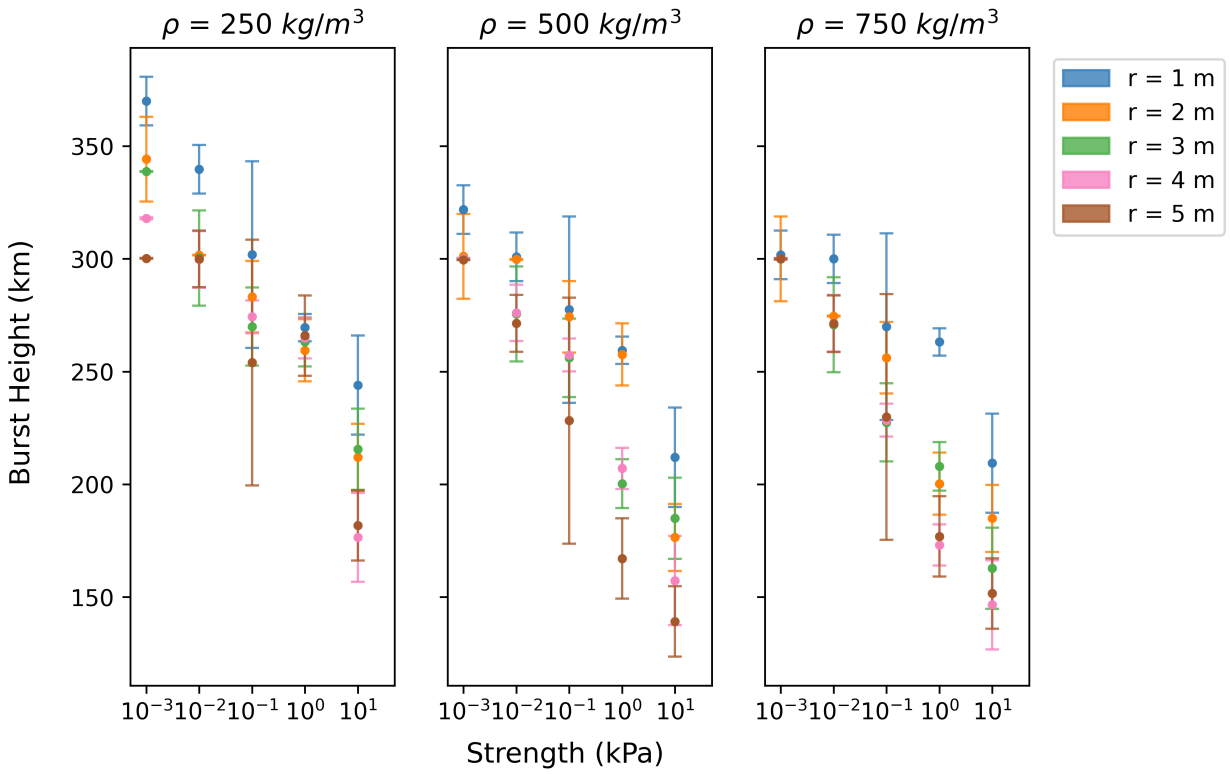


Figure 4.9: Examining the relationship between density and burst height. From left to right, we plot the burst heights for $v = 11$ km s^{-1} at incident angle 45 °with variable strength, radius, and density. The size and colour of the markers correspond to the radius of the initial meteor. The lowest density of $\rho = 250$ kg m^{-3} corresponds with a void space for an icy comet of 75%. This results in the highest burst height produced by the SFM in our range of simulations. Generally, the burst heights are correspondingly higher for lower density. However, this trend does not continue when simulating a higher density of 750 kg m^{-3} in comparison to the 500 kg m^{-3} case.

4.3.2 Overpressure Estimations

Overpressures on the ground are greater when the airburst is close to the surface, and the available burst energy is higher (Eqn. 4.10, Fig. 4.10). The three different methods of estimating burst energy are shown in Figure 4.10. Generally, we also observe that an increase in meteoroid radius leads to a slightly lower burst height (Figs. 4.6, 4.7, 4.8). I find that the largest overpressures are produced by meteors with greater radius and density (Fig. 4.11), regardless of the method of burst energy estimation, as all methods are mass dependent. I found that the maximum overpressure on the ground varied between 1.7 – 53.2 Pa across all simulated radii and strengths for an incident angle of 45 °and density of 500 kg m^{-3} (Fig. 4.11), with an overpressure as low as 1.1 Pa for meteors with density of $\rho = 250$kg m^{-3}. Of the three methods used to estimate energy release, I find that

E_{Kmax} results in the greatest overpressure at the surface, where E_{cum} is lower than E_{K50} at lower strength, but results in greater energy available for the overpressure at higher strength. This is consistent with the increased complexity and number of peaks observed in the energy curve for higher strength objects and was found for all simulated incoming velocities.

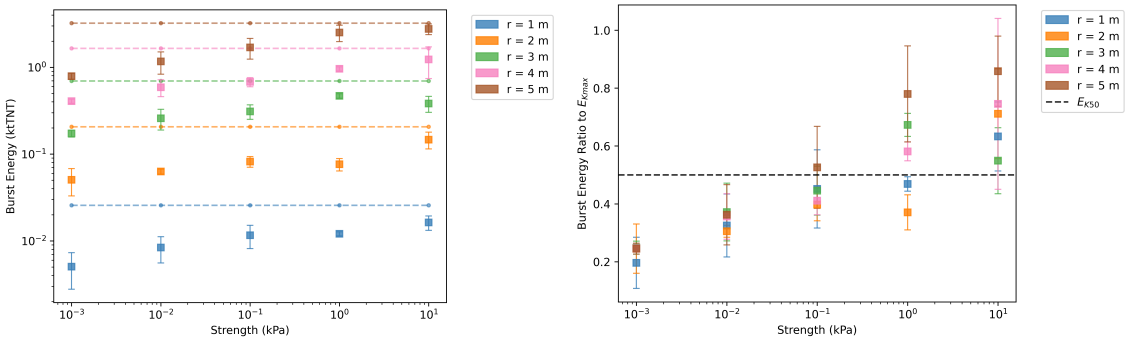


Figure 4.10: Left: Estimates of burst energy in ktTNT using E_{Kmax} (circles, dashed lines) and E_{cum} (squares) for meteors of $v = 11$ km s^{-1}, incident angle $a = 45°$, $\rho = 500$ kg m^{-3}, and varying incident radius and strength. E_{K50} can be inferred to be half of E_{Kmax}. The colour of the markers corresponds to the radius of the initial meteor. Error bars are shown for E_{cum} as estimated from the random seed procedure described in Section 4.2.1. Right: Estimates of burst energy shown as a ratio of E_{cum} (squares) and E_{K50} (dashed line) to the initial kinetic energy E_{Kmax}. The burst energy with E_{Kmax} and E_{K50} are independent of the descent processes and are shown with horizontal lines to more easily distinguish estimates from E_{cum}.

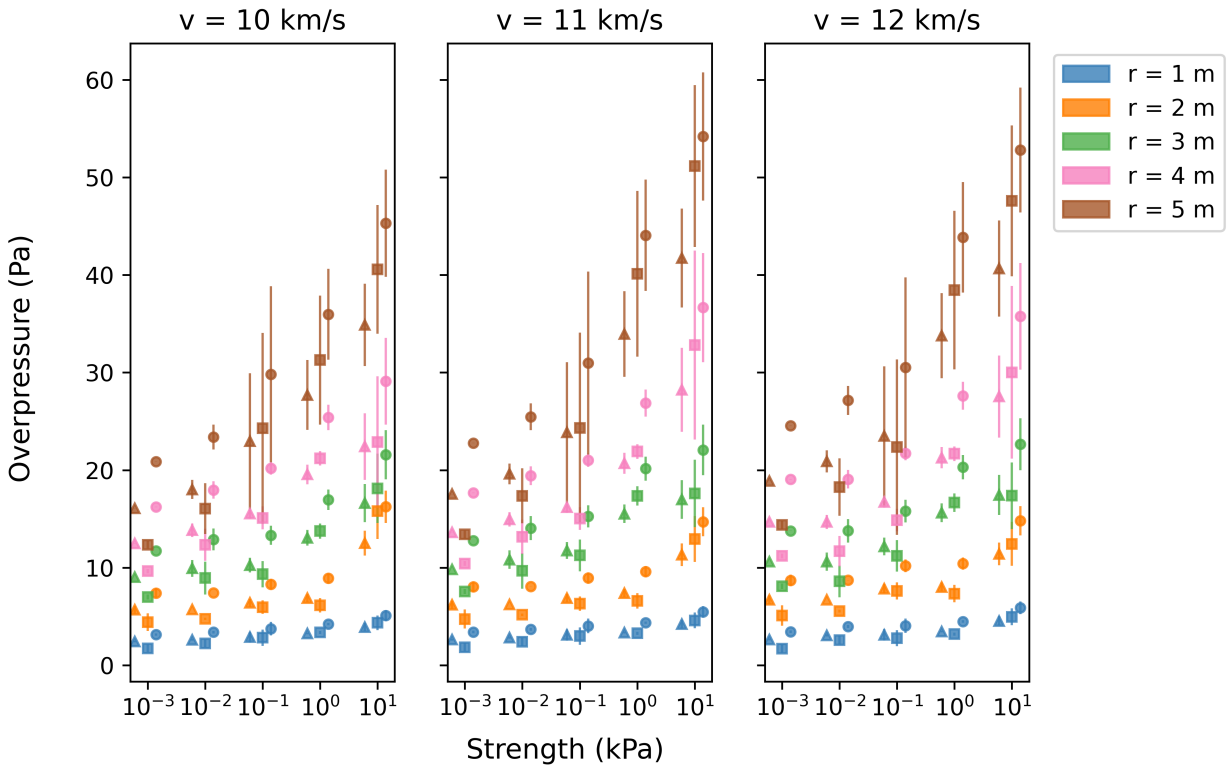


Figure 4.11: Corresponding overpressures for variable velocities, strength, and radius with all other variables fixed at incident angle $a = 45°$, density $\rho = 500$ kg m^{-3}. Overpressure estimates were derived from burst energies from E_{Kmax} (circles), E_{cum} (squares), and E_{K50} (triangles). Despite the increase in maximum kinetic energy for higher incident velocity meteors, the overall contribution to the overpressure is not significant. The values for each of the different burst energy mechanisms are slightly offset for easier interpretation.

At varying incident angles, I do not observe significant deviation in the overpressure from the incident angle of 45 °(Fig. 4.12). Similarly, when varying the density of the meteor bodies, I find that the range of overpressures remains the same (Fig. 4.13). I find that the relative relationship between a density of 250 kg m^{-3} and 500 kg m^{-3} is as expected, with increasing overpressure for a corresponding increase in mass. However, in comparing the density of 500 kg m^{-3} to 750 kg m^{-3}, the relationship is not as straightforward, as the burst heights do not increase notably, and the energy curve takes a different shape. Regardless, the maximum overpressure occurs when the initializing parameters are $\rho = 500$ kg m^{-3} and $a = 45°$.

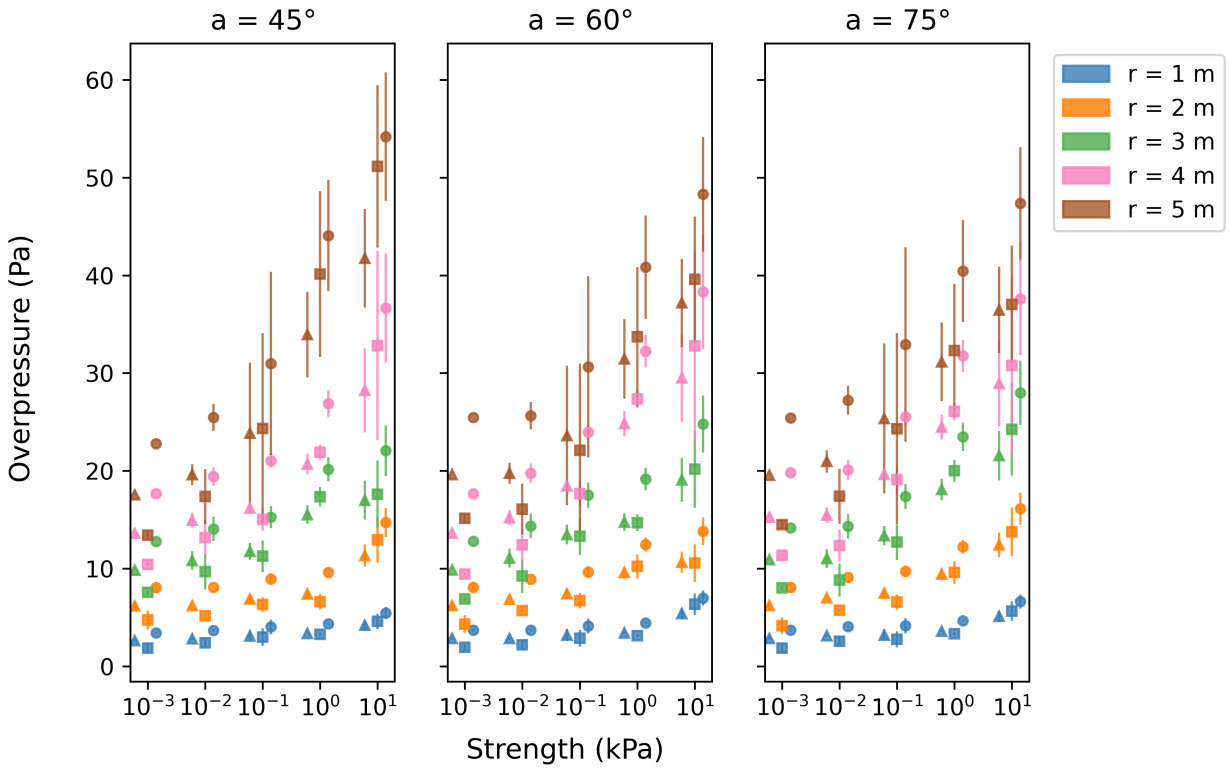


Figure 4.12: Overpressures with varying incident angle, initial strength, and radius with fixed velocity $v = 11$ km s^{-1} and density $\rho = 500$ kg m^{-3}. Overpressure estimates were derived from burst energies from E_{Kmax} (circles), E_{cum} (squares), and E_{K50} (triangles). The overall effect of varying these components does not result in significant deviation from the estimated overpressure range estimated for incident angle $a = 45°$ and density $\rho = 500$ kg m^{-3}. The values for each of the different burst energy mechanisms are slightly offset for easier interpretation.

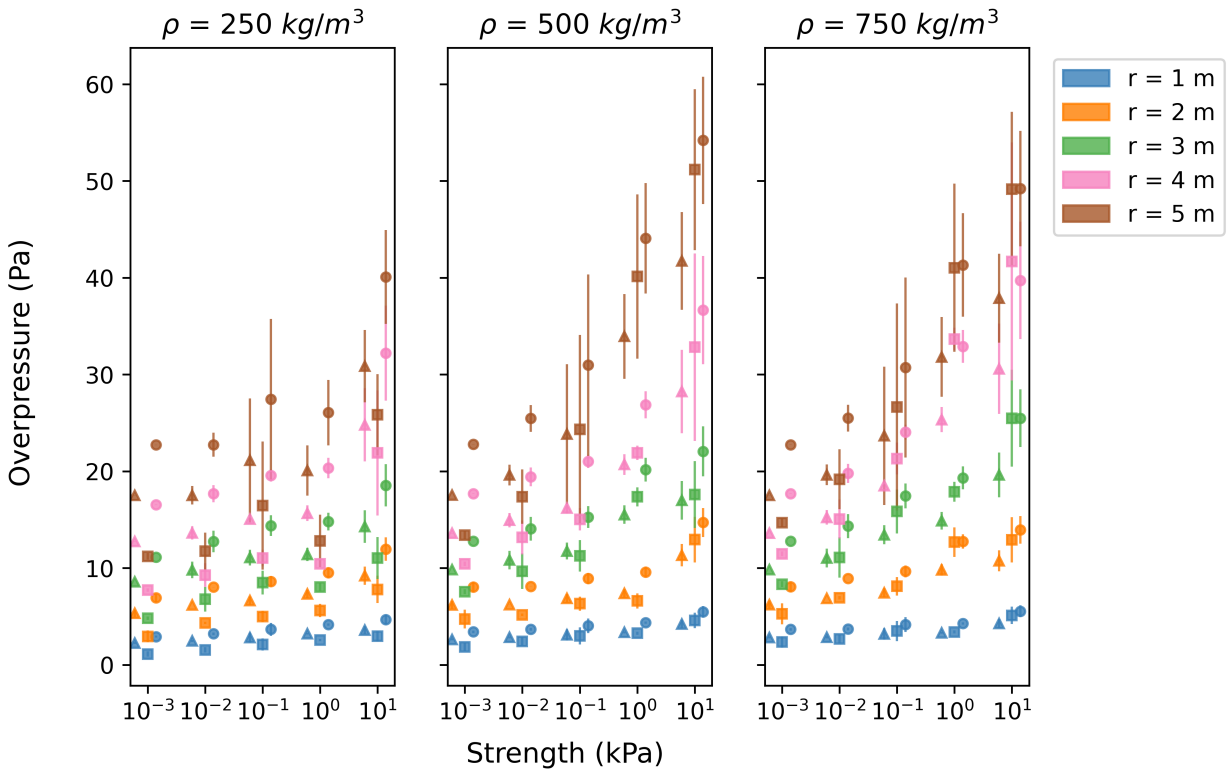


Figure 4.13: Overpressures with varying incident angle, initial strength, and radius with fixed velocity $v = 11$ km s^{-1} incident angle $a = 45°$. Overpressure estimates were derived from burst energies from E_{Kmax} (circles), E_{cum} (squares), and E_{K50} (triangles). The overall effect of varying these components does not result in significant deviation from the estimated overpressure range estimated for incident angle $a = 45°$ and density $\rho = 500$ kg m^{-3}. The values for each of the different burst energy mechanisms are slightly offset for easier interpretation.

4.3.3 Travel Times and Signal Length

I assume that the blast wave travel speed drops to the local speed of sound within a few 10s of wavelengths or $\geq R_0$ from the source, similar to Earth's atmosphere. This occurs when the blast wave moves into the weakly nonlinear regime (ReVelle, 1976). The assumption that a blastwave travels at the speed of sound after the hypersonic regime is consistent with observations of the Cheylabinsk meteor, where the airburst and surface arrival were 87.5 s apart from the town closest to the airburst epicenter for an approximate burst height of 22.5 km; at the speed of sound, 340 m/s, the expected travel time is 73.5 - 91.2 s for a straight-line distance of 25 - 31 km (Heimann et al., 2013). The estimated travel times with our corresponding range of burst heights on Titan (minimum 139.2 km and maximum of 342.5 km) are 781.2 s to 2257.2 s when using the values

derived from the HASI profile. The estimated travel times are similar to that of the 900 s iSALE-2D time for maximum overpressure in Section 4.3.5 for two test cases.

I also estimated the positive pulse phase length using the initial kinetic energy of the meteors (Fig. 4.4 and 4.14). By extending Glasstone and Dolan's empirical values to our burst heights using Equation 4.14 and assuming an entirely weakly linear regime for the entire travel from burst to surface, we can estimate positive phase pulse lengths of 3.9 to 38.4 seconds, depending on the burst height, strength, and the associated energy release. For the second method, I estimated the positive pulse phase length from the fundamental frequency of the blast and find a length of 2.4 to 13.8 s. On the same figure, I also plot estimates from the Supracenter code for meteors with burst radius between 1000 and 1500 m, and burst heights between 125 and 225 km. I found that the positive pulse phases were between 9.5 and 14.9 s, with longer positive pulse phases corresponding to higher burst heights and greater burst radius. From the different methods of estimation, we can assume that the positive pulse length will be on the order of $\sim$10 s if we consider the total kinetic energy of the meteor. The length of the positive phase of the pulse is slightly decreased with other methods of estimating energy as part of the airburst.

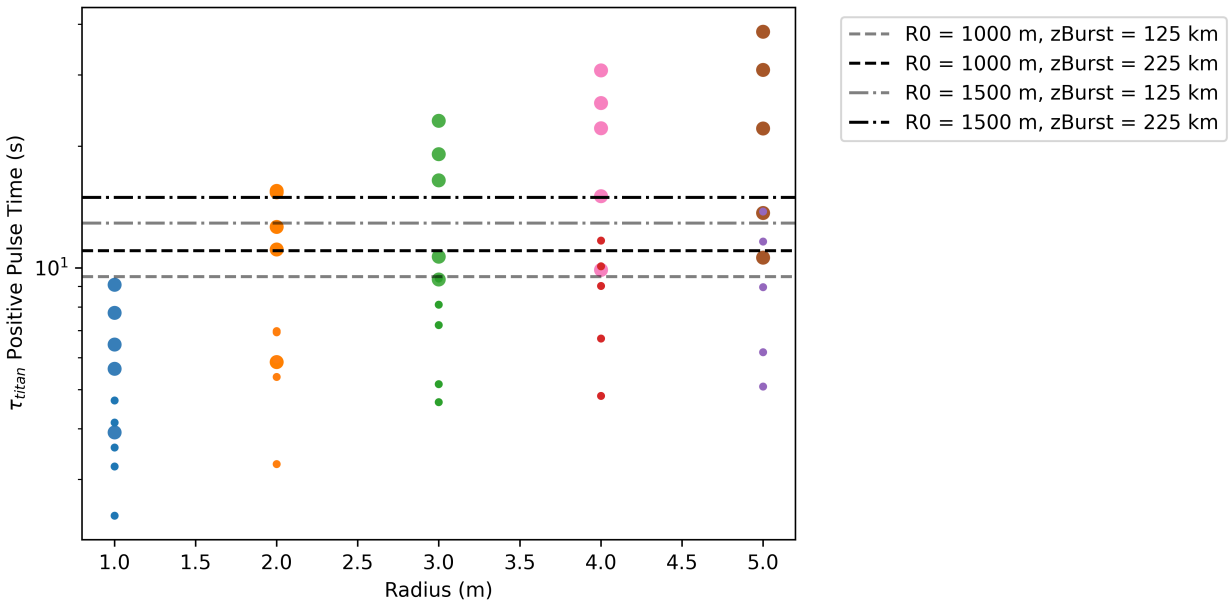


Figure 4.14: Overpressure signal length for the positive phase. The large circles represent estimates using Glasstone and Dolan (1977)'s values for a Titan atmosphere and the small circles represent estimates using the fundamental frequency calculated for the airburst. These estimates use the initial kinetic energy E_{Kmax} for burst height simulations from $v = 11\text{km}\,\text{s}^{-1}$, $a = 45°$, $\rho = 500\text{kg}\,\text{m}^{-3}$ and assuming the blast wave propagates as a weakly nonlinear wave. The dashed and dash-dotted lines represent the positive pulse phase estimation using the simulation from the Supracenter package for a weakly nonlinear to linear regime estimation for blast radii of $R_0 = 1000$ m and 1500 m at burst heights of 125 km and 225 km.

4.3.4 Additional Peaks

For simulations that resulted in multiple strong airburst peaks (e.g. Figure 4.15), I extracted the burst heights and calculated their associated overpressures by taking the cumulative energy between the peaks for each event. The burst events are between 25 - 50 km apart, and at hypervelocities, will be separated by a few seconds in time. By the time the multiple bursts reach the surface, I find that the arrival times are minutes apart. In the example shown in Figure 4.15, I find that the two dominant peaks would arrive approximately 210 s apart.

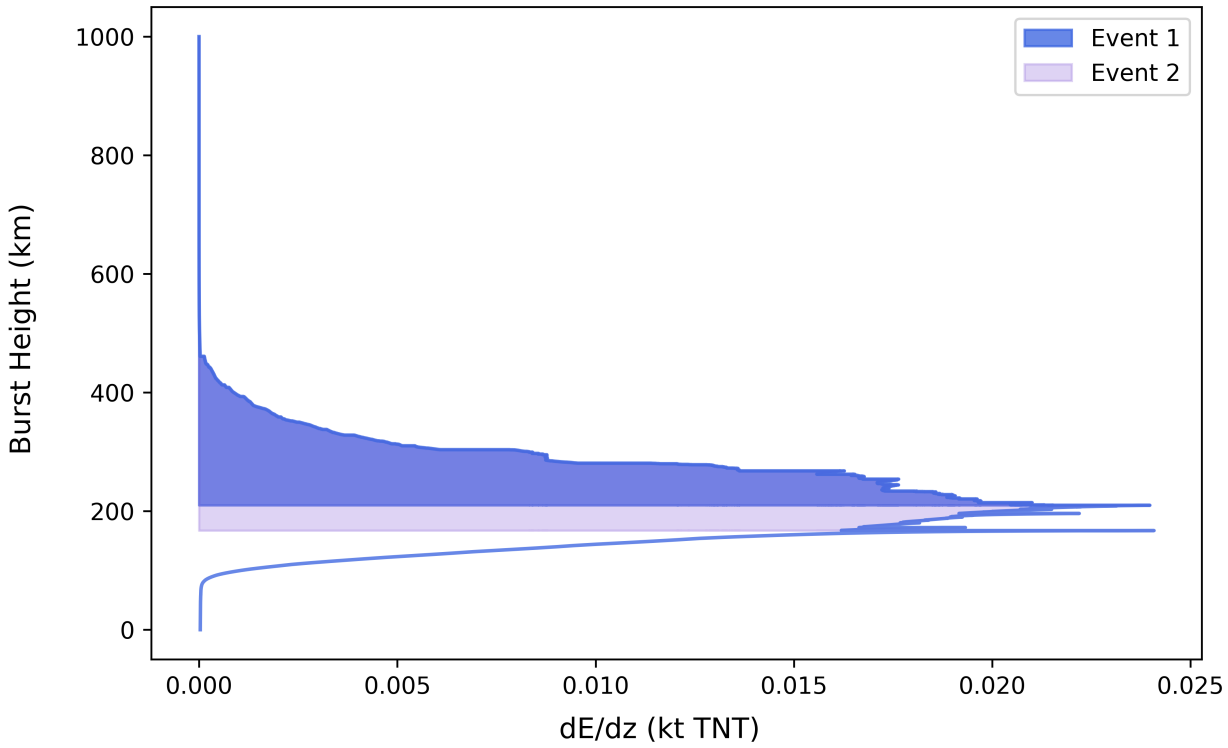


Figure 4.15: Example of energy release curve with two apparent airburst peaks can be observed for the $v = 11$ km s^{-1}, $a = 45°$, $\rho = 500$ kg m^{-3}, and $S_0 = 1.0$ kPa case. In this instance, the two peaks are 42 km apart in the simulation. The cumulative energy released between at the second airburst (∼0.9 ktTNT) shown in the lilac shaded area is half of that of the first airburst (∼1.7 ktTNT) shown in the blue shaded area.

4.3.5 Overpressure Estimations using iSALE-2D

I consider two cases from our SFM simulations using the burst energy and burst height with an initial blast radius of 1000 m to numerically calculate the overpressure at the surface using iSALE-2D. Case 1 uses a burst height of 139.2 km with an energy of 3.22 ktTNT (1.35×10^{13} J) from a meteor with $r = 5$ m, $\rho = 500$km m^{-3}, $v = 11$km s^{-1}, $S_0 = 10.0$ kPa, and an incident angle of $a = 45°$. Case 2 uses a burst height of 151.2 km with an energy of $E_{Kmax} = 2.57$ ktTNT (1.07E13 J) from a meteor with $r = 5$ m, $\rho = 500$km m^{-3}, $v = 10$km s^{-1}, $S_0 = 10.0$ kPa, and an incident angle of $a = 45°$. Note that these burst energies result in a blast radii of ≈ 1000 m (Eq. 4.17), which is comparable with our initial burst radius in our iSALE models. We did not use $r = 1$ m SFM results as they exceed our iSALE simulation domain. Our iSALE results show that the maximum overpressure at 900 s after the burst is 43.2 Pa for Case 1 and 23.4 Pa for Case 2. For

Case 1 and Case 2, it would take approximately 800 s to reach the surface immediately below the burst where the overpressures are 32.2 and 12.0 Pa respectively (see Section 4.3.3). Since this time increases as the distance from the burst point increases, we consider 900 s to represent overpressure profiles from the burst point to a point on the surface at a 200 km horizontal distance from the point immediately below the burst (see Section 4.4.1). Note that we confirm that the overpressures between 900 – 1200 s are the same. Our numerical values are about 50 – 80% of my estimates using (Glasstone and Dolan, 1977)'s empirical methods, which are 54.1 Pa for Case 1 and 45.2 Pa for Case 2, respectively. Nevertheless, these values are within an order of magnitude, which is sufficient for this initial work. I will discuss this further in Section 4.4.1.

4.3.6 Seismic Response

The seismic response is directly related to the overpressure and the P-wave velocity of the surface material (Eq. 4.20). For a surface density $\rho_s = 500\text{kg}\,\text{s}^{-3}$, I can calculate a peak vertical velocity as a function of overpressure to be 0.32 to 1.33 $\mu\text{m}\,\text{s}^{-1}\,\text{Pa}^{-1}$ (Fig. 4.16). This results in a range of 0.59 $\mu\text{m}\,\text{s}^{-1}$ – 72.26 $\mu\text{m}\,\text{s}^{-1}$ for a meteor of $\rho = 500\text{kg}\,\text{m}^{-3}$ (Fig. 4.16), and as low as 0.36 $\mu\text{m}\,\text{s}^{-1}$ for meteors with a density of $\rho = 250\text{kg}\,\text{m}^{-3}$. For variable surface densities, I found vertical velocities as a function of overpressure ranging between 0.11 and 1.33 $\mu\text{m}\,\text{s}^{-1}\,\text{Pa}^{-1}$ (Fig. 4.17).

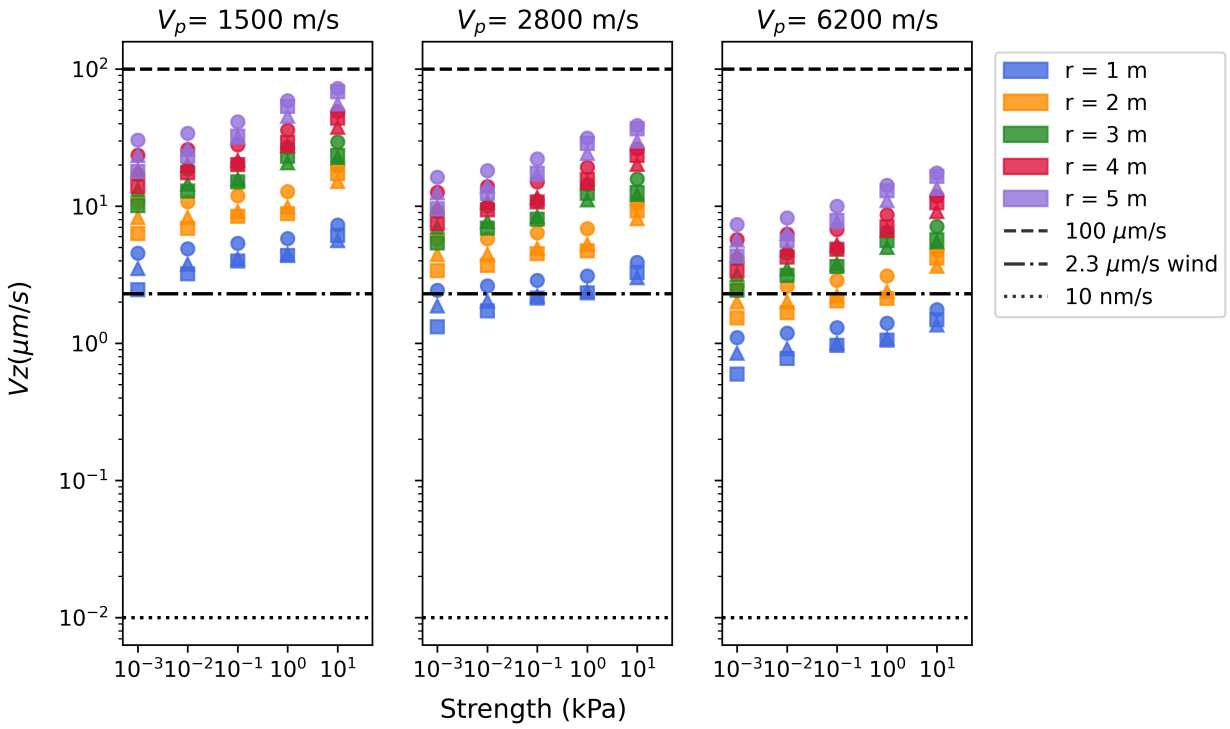


Figure 4.16: Peak vertical velocity of the surface. Simulations are shown for SFM initiating parameters $v = 11$ km s^{-1}, entry angle $a = 45°$, $\rho = 500$ kg m^{-3} and varying strength and radius of the meteor. Vertical velocity estimates were derived from overpressures and burst energies from E_{Kmax} (circles), E_{cum} (squares), and E_{K50} (triangles) for $V_p = 1500$ m s^{-1} for wet sand, $V_p = 3000$ m s^{-1} for an intermediate between till, sandstone, and water-ice at 94 K, and $V_p = 6200$ m s^{-1} for basalt, spanning the range of potential Titan surface velocities as described in Table 4.2. As the surface P-wave velocity increases, the smaller the surface response to overpressure. I also indicate potential sample rates and thresholds (10 nm s^{-1} at 10 Hz, and 100 μm s^{-1} at 0.1 Hz if we assume similar capabilities to the Very Broad Band seismometer onboard InSight (Lognonné et al., 2019)) and the expected wind noise on Titan (0.01 μm s^{-1} at 0.01 Hz (Lorenz et al., 2021)) with dashed lines.).

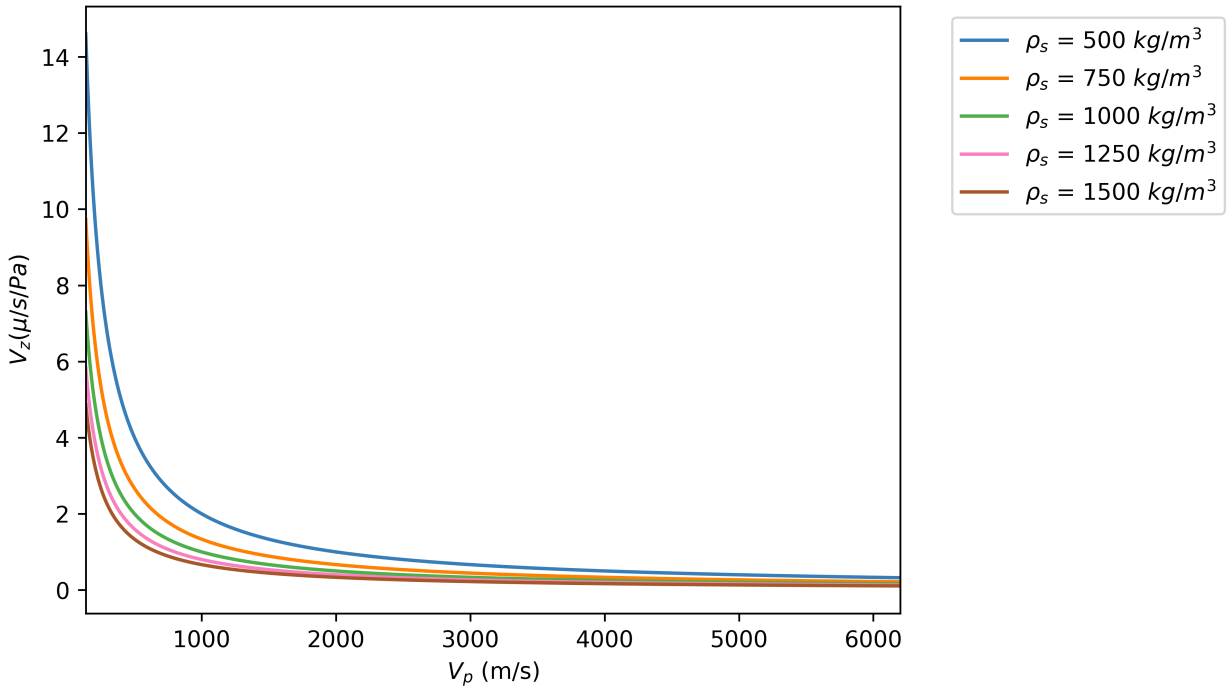


Figure 4.17: Vertical velocity for varying surface density ρ_s and surface P-wave velocity V_p. A lower surface density and P-wave velocity corresponds with a greater vertical velocity response from the surface.

I also estimated the length of the seismic impulse corresponding to the initial overpressure blast at the surface by considering a noise threshold of 1 $\mu m\,s^{-1}$, and find that the length of the pulse is between 0.5 – 1.4 s for $V_p = 1500\ m\,s^{-1}$ for all of our simulations or 0.7 – 1.5 s for a noise threshold of 0.1 $\mu m\,s^{-1}$ (Fig. 4.18). In practice, the length of the seismic response will be dependent on the entirety of the overpressure blast and the sensitivity of the instrument at a given frequency.

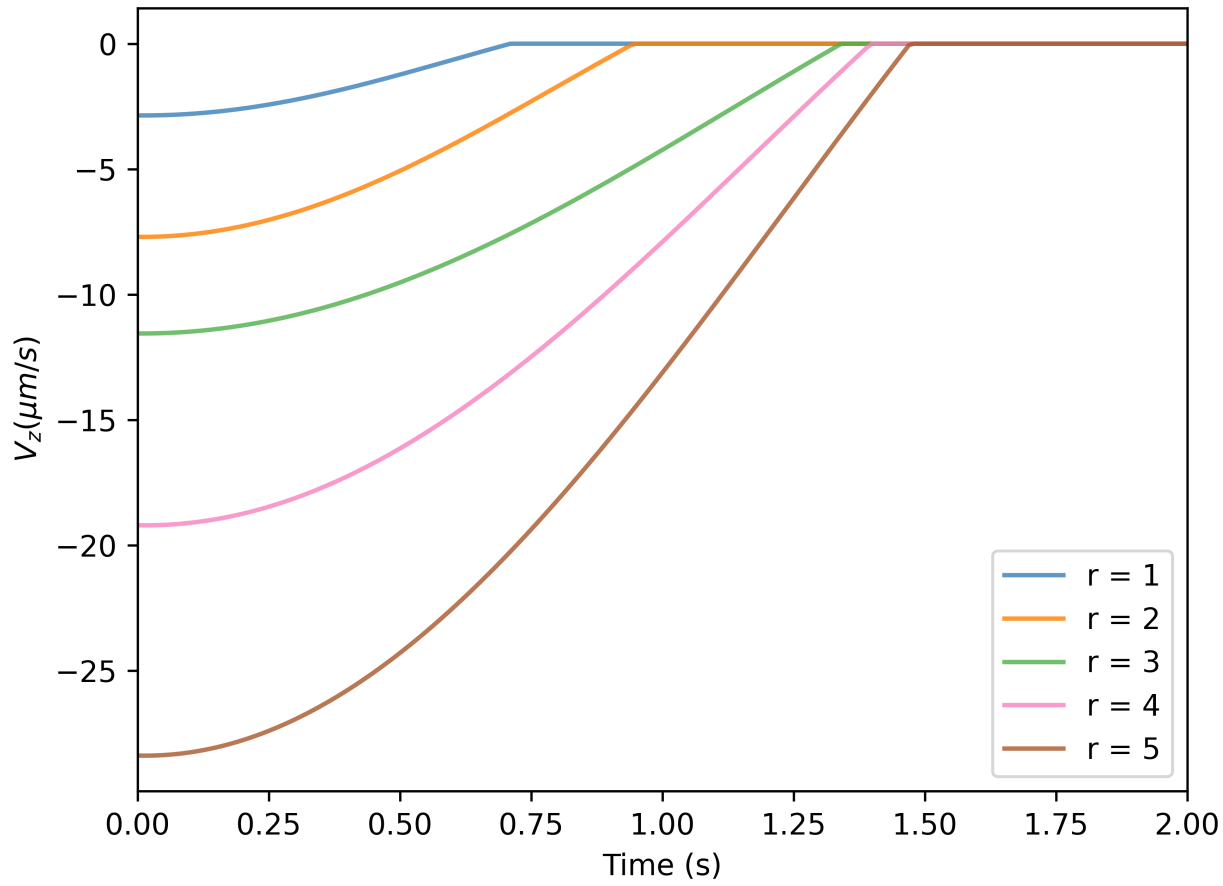


Figure 4.18: Vertical velocity generated for a wet sand surface using an exponentially decaying function for impactors of $v = 11$ km s^{-1}, $\rho = 500$ kg m^{-3}, $a = 45°$, $S_0 = 10.0$ kPa, and $r = 1 - 5$ m generated from the overpressure pulse length τ_{Titan} derived by Equations 4.14 and 4.15. To estimate the length of the peak seismic response, we set a cutoff of 1 µm s^{-1} and 0.1 µm s^{-1} and find that the lengths vary between 0.5 - 1.4 s and 0.7 - 1.5 s, respectively.

4.4 Discussion

I note that my results are intended to be a first order investigation of the most optimistic scenario for airburst detection on Titan, as the meteor properties and surface properties of Titan are still poorly constrained. I estimated the overpressure, length of the overpressure signal, coupled seismic displacement, and length of the seismic signal that result from an airburst occurring in Titan's atmosphere. This work provides initial predictions when considering future interpretations of the pressure sensor and seismometer data from Dragonfly. It also provides recommendations for signal acquisition and processing parameters that could be used to identify airbursts on Titan.

4.4.1 Overpressure

Previous research has shown that the terminal height of meter-scale meteors is related to their strength (Ceplecha and McCrosky, 1976, Brown et al., 2016). My results demonstrate there is a general relationship between the burst height and the material properties of the impactor. Larger and more cohesive meteoroids penetrate further into the atmosphere before an airburst occurs, as would be expected from previous work done by Robertson and Mathias (2019) using a different meteor entry mode. My observations are also in line with Ceplecha and McCrosky (1976) who noted that meteors with lower strengths tended to have higher terminal heights. Brown et al. (2016) observed a very weak correlation between shallower entry angles and higher peak height. In contrast, my results suggest that it is difficult to describe a relationship between entry angle and burst height. While Borovička et al. (2017) demonstrated that meteors with different properties can have similar peak heights, I found consistent trends with size (and therefore, mass) and strength. Overall, the resultant surface overpressures are also larger for larger and stronger impactors.

In all simulations, the overpressure at the ground was greater than 0.1 Pa when the burst occurs directly overhead. However, airbursts are unlikely to occur directly overhead Dragonfly, so I can also consider what the effective range of detection may be. The effect of increasing horizontal distance is shown in Figure 4.19 for select events without accounting for the effects of atmospheric attenuation and curvature of the planet. This fall off is likely to be steeper as the energy from the blast is dissipated due to effects such as attenuation and transmission loss from reflection and refraction of the wave due to temperature and pressure changes throughout the atmosphere. It is likely that the decrease in overpressure at several hundred km is unphysical, and the Glasstone and Dolan (1977) empirical equations do not hold at large slant distances. I also note that I removed simulations with initial starting strengths of less than 0.1 Pa. While we expect cometary meteors to have strengths of several Pascals at the m-scale, we have yet to observe and evaluate the strength of such objects. As such, it is possible for the meteors to be sufficiently weak that airbursts will take place several hundreds of km above the surface and the detection of the corresponding blastwave highly unlikely.

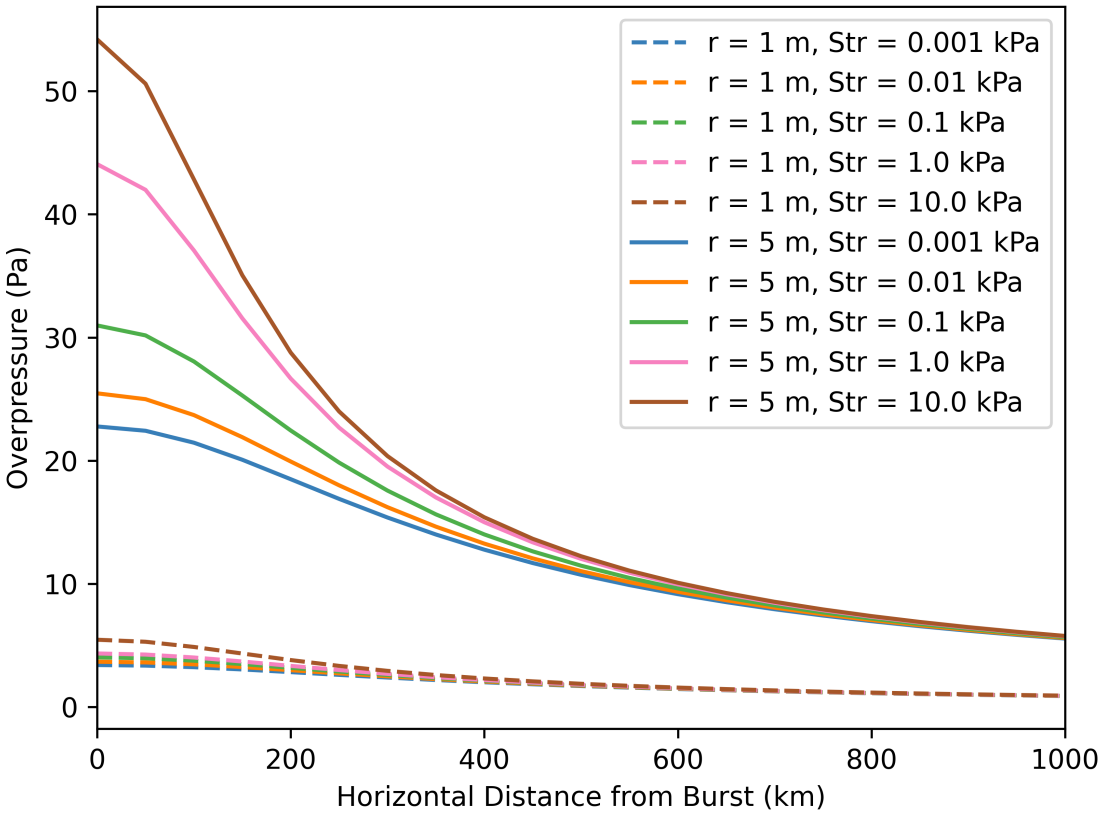


Figure 4.19: Peak overpressure fall-off with increasing horizontal distance from burst solely due to the distance using Equation 4.10. This plot includes simulations from $v = 11$ km s^{-1}, $r = 1$ and 5 m, $\rho = 500$ kg m^{-3}, and $a = 45°$ with varying initial strength. This plot does not account for the curvature of Titan's surface nor reflection and refraction in the atmosphere.

I also observed that, in our simulations, low strength objects burst higher up in the atmosphere regardless of the other variables we changed. This suggests that if we are to detect an airburst of notable magnitude, it is likely to be a strong (> 1.0 kPa) cometary body coming in at a steep angle (> 45 °).

In terms of travel time to the surface, it is likely that the event takes several minutes to reach the surface considering the speed of sound and the total distance the blast wave needs to travel. While I did not consider the momentum of the impactor itself (this would decrease the overall travel time by effectively lowering the burst height (Boslough and Crawford, 2008)), I do not expect this effect to be significant over several hundred kms. I also noted that there were some cases in our simulations where there were multiple peaks in the energy release curve. These peaks were spaced

around 25 – 50 km apart. With the Supracenter code, I found that the transition height from a weakly nonlinear regime to a linear regime was around 10 km from each burst, thus, we would expect to see these events reach the surface as independent blast waves and potentially differentiate between multiple separate airbursts from the same meteor.

I also estimated the duration of the initial positive phase pulse three different ways, and found consistent estimates for the length. It was surprising that assuming a fully weakly linear regime resulted in a similar estimate as a step-wise propagation and tracking of the pulse through the atmosphere using Supracenter where the transition between weakly nonlinear to linear is close to the airburst. Additionally, I found that the Glasstone and Dolan (1977) empirical extrapolation and use of the fundamental frequency estimation also resulted in similar values for pulse length.

The overpressures from Glasstone and Dolan (1977) empirical methods and iSALE-2D have the same order of magnitude, though the numerical values are somewhat smaller than the empirical values (see Section 4.3.5). If the numerical values are accurate, the initial burst energy contribution to the overpressure with the empirical method needs to be reduced between 75 - 83% (estimated from Eqs. 4.10 and 4.11) through processes such as conversion into light. However, the typical estimated loss is only 1 - 5%, thus this is unlikely. Instead, the energy from the blast wave can be split into separate parcels as it travels through the atmosphere. In the empirical estimations, I assume that all of the energy from the blast wave moves as a single unit. When the split happens in the numerical simulation, it can reduce the overall overpressure. Alternatively, if the empirical values are accurate, the discrepancy could be because our numerical model treats the burst as a static source. Since the iSALE static source simulation results in an overpressure of about half of the moving source simulation (Collins et al., 2017), Glasstone and Dolan's empirical equations better represent a moving source. This effect could be significant for the case with a higher burst point (Case 2 at 151 km). We can observe that the discrepancy between the numerical results and the empirical values are larger for Case 2 in comparison to the lower burst point (Case 1 at 139 km), despite similar burst energies. The initial pressure profile may also influence the iSALE results (see Section 4.2.2 and Fig. 4.3). However, simply increasing resolution in the numerical models could resolve the discrepancy in the pressure profile. Increased resolution could also mitigate the difference between the meteor sizes and the initial burst radii, whereby the results of both methods would converge. As such, this initial work may have room for improvement, however, both methods

are well suited to estimate overpressure on Titan. We also note that we did not run a simulation with iSALE-2D for the more likely scenario of $r = 1$ m due to computational costs. However, as my empirical estimates are not dissimilar to the results from the hydrodynamical simulation for the cases we did consider, the validation from iSALE-2D is sufficient to demonstrate that the empirical method is a suitable first order estimation.

4.4.2 Seismicity

With respect to the seismic response, we can be reasonably confident that the peak velocity estimates are similar to the estimates presented based on previous work done for Earth (Edwards et al., 2009, ReVelle and Edwards, 2007), unless the surface materials vary outside of the properties listed in Table 4.2. In covering a wide range of surface materials, I found a similar scale of response, under the optimal situation where the airburst occurs overhead. In comparing our results to those estimated by Edwards et al. (2009) for the Stardust shuttle return over playa, I find that our surface response is of the same order despite the different atmospheric conditions. For their measured ground coupling coefficients at a clay-rich soil for the hypervelocity shockwave produced from the Stardust shuttle return, they found $7.3 \pm 0.2 \mu m\,s^{-1}\,Pa^{-1}$. This corresponds with a seismic period of 0.165 ± 0.003 s and 0.144 ± 0.011 s at their two measuring sites, which are on the order of our estimates for seismic pulse length after the acoustic wave fully couples into the ground. Previous studies for events measured at acoustic frequencies of 20 - 25 Hz estimate between 6 - 7 $\mu m\,s^{-1}\,Pa^{-1}$ for silty loam and loess, and 14 $\mu m\,s^{-1}\,Pa^{-1}$ for sandy soil (Edwards et al., 2007). They also note that their observations were approximately twice the amplitude as predicted from theoretical results, which suggests my results may be an underestimation. However, for airbursts at some horizontal distance from Dragonfly, the seismic signal will attenuate with distance as it travels along refractive paths.

Although I am most interested in an order of magnitude estimation of overpressures and seismicity for this initial study, I note that our overpressure estimations may be off by a factor of 2. I did not account for the downwards momentum of the meteor (Boslough and Crawford, 2008), and previous work estimating the vertical velocity of the surface was also off by an order of magnitude in comparison to field measurements (Edwards et al., 2009). Much of this work is inspired by testing done as part of nuclear tests several decades ago, where equations and relationships were

predominantly empirical. One consideration is the fundamental frequency of a quasi-point source explosion. To date, this value has not been estimated directly (e.g. Edwards et al. (2008)), despite my use of Sakurai (1964)'s relationship, and may affect the travel times and pulse length of blast waves. However, with our additional iSALE simulations, I find that the empirical equations for overpressure are on the same order of magnitude. Additionally, with respect to compliance efficiency, the recent OSIRIS-REx reentry showed that estimating the seismic response from the overpressure at the surface is appropriate within an order of magnitude (Fernando et al., 2024).

4.4.3 Applications to DraGMet

If we assume that the threshold for detection for the pressure sensor onboard Dragonfly is 1 Pa, we should be able to detect airbursts from bolides with physical properties that are similiar to our most optimistic simulations with the pressure sensor alone. This is a fraction of the sensitivity of InSight's pressure sensor (0.01 Pa at in the 0.5 – 1.5 Hz band (Garcia et al., 2022)). Sample frequencies are expected to be around 1 Hz for typical measurements throughout the day, and up to 10 samples per second during high data collection times. The length of our pulses is likely on the order of seconds to fractions of a second. If the overpressure signal decays rapidly, these events are unlikely to be detected during typical background measurements. However, if a sufficiently large overpressure is detected by the DraGMet instrumentation, and we observe a steep fall off as a function of time, then it is possibly an airburst. The detection is thus most likely to be constrained by the frequency at which the sensor is operating.

Other events that may cause pressure inflections include diurnal effects and winds. The difference between pressure changes due to an airburst and regular weather effects is that we are more likely to see several instances of winds. If there is a general front moving through, we would expect that this signal would be several orders of magnitude longer than that of an airburst, and would not necessarily have the negative overpressure component following. However, the passage of dust devils could produce similar magnitude sharp pressure drops of a few Pa to tens of Pa over the span of a few seconds (Lorenz, 2021). In distinguishing the two events, dust devils should result in a larger negative pressure drop, whereas airbursts should have a relatively large positive pressure increase in the wave form.

With the seismic response, if the sensor has a noise threshold above 10s of $\mu m\,s^{-1}$, the surface

has a P-wave velocity close to sand, and we can sample at sub-second frequencies, then it is also likely that an airburst event with a sufficiently energetic blast wave can be registered with the onboard seismometer. As a point of reference, the Very Broad Band seismometer onboard InSight had the capability of returning sample rates between 20 and 100 samples per second (Lognonné et al., 2019). We would expect the onboard sample rate to be similar, at around 10 $\mathrm{nm\,s^{-1}}$ at 10 Hz, and 100 $\mathrm{\mu m\,s^{-1}}$ at 0.1 Hz. The sensitivity of the 10 Hz band would be sufficient to identify the peak and decay of the event. As is the case with overpressure detection, our main constraint is the regularity at which the instrument operates. Additionally, I note that the ground displacement from the airburst exceeds that of the anticipated wind noise of up to 2.3 $\mathrm{\mu m\,s^{-1}}$ at 3 Hz and that of atmospheric pressure noise which is on the order of 0.01 $\mathrm{\mu m\,s^{-1}}$ at 0.01 Hz (Lorenz et al., 2021). However, if the surface P-wave velocity is on the order of several $\mathrm{km\,s^{-1}}$, then it is possible we will be unable to detect any but the strongest of meteors we simulated.

The length of the overpressure and seismic signals are long enough to be sampled several times as part of high-frequency sampling operations. The overpressure signal is potentially several tens of seconds, though we note this calculation required significant interpolation. Nonetheless, we should expect the positive phase of the overpressure from the blast wave to extend over several seconds, well within typical sampling frequencies. Similarly, we should expect to be able to detect the seismic response at frequencies at around 10 Hz or lower. Based on my simulation from the exponentially decaying overpressure pulse, I find that the duration of the positive phase of the event is on the order of 0.1 s. Thus, if we are interested in capturing these transient events, the frequency at which seismic velocity sampling occurs will need to be more frequent to detect these events. Given that our seismic signals have a period of less than 1.0 s, it is unlikely to conflict with microseisms from the sea, though it may overlap with the background tidal cracking and atmospheric noise (Panning et al., 2020). Another potential signal conflict is the booming dunes of Titan (Hunt and Vriend, 2010).

I note that Equation 4.20 can be written in a way that relates V_p and V_s directly. If both overpressure and seismic velocity are obtained for a single burst that is at some horizontal distance to Dragonfly, it is possible to infer the material properties of Titan's surface, such as the $\frac{V_p}{V_s}$ ratio.

The methods presented in this paper are applicable to all planetary bodies with atmospheres with the noted caveats. With respect to my simulations, I chose to use the SFM model, and enforced

a consistent fragmentation pattern where each fragment would produce two child fragments. The use of the SFM limits the potential effects of cloud-debris formation and overall travel of the fragments that might be better described in the Fragment Cloud Model or pancake models. While the SFM and our initial parameters are justified for a first-order investigation, I caution that my results can only be considered upper limits. For example, I examined simulations where the meteor split into four child fragments, rather than just two. In these situations, the burst height was 25% higher and the burst energy was 20% lower. Alternative fragmentation and meteor descent models should be taken into consideration in future studies. With respect to Titan, the material properties of comets themselves are not well understood, nor are they likely well represented by perfect spheres as assumed by my model. It may be meaningful to consider alternative shape parameters for comets and their fragments. Lastly, this work could be modified to further include additional atmospheric effects, such as ducting effects that may occur during the night from a stronger temperature inversion, additional signals from reflection from topographical features, the formation of Rayleigh waves across the surface, and super rotating winds expected between 75 and 200 km altitude effects on the blast wave propagation.

4.5 Conclusions and Future Work

I investigated airburst characteristics in Titan's atmosphere using the Separate Fragments Model to track the progression of a hypothetical meteor. I estimated the overpressure at the surface using empirical equations, and the seismic velocity from seismoacoustic coupling. In the optimistic scenario and meteor properties I considered here, I expect that airburst events can be detected given the predicted instrument sensitivity and sampling rate for Dragonfly. Additionally, I have provided the anticipated characteristics of airbursts for both the pressure sensor and seismometer so we can distinguish airburst events from other pressure and seismic signals on Titan. I find that the expected overpressure ranges between 1.1 – 53.2 Pa, and the peak seismic velocity is between 0.1 and 1.33 $\mu m\,s^{-1}\,Pa^{-1}$ (0.1 and 72.26 $\mu m\,s^{-1}$). Current outer solar system cometary population distributions suggest it is unlikely that such impactors will enter Titan airspace over the course of the Dragonfly mission, so any positive detections during the lifetime of the Dragonfly mission would require a revision to these population estimates and size frequency distributions.

Chapter 5

Conclusions

An atmosphere is the interface between a planetary surface and space. Particles, light, and sound propagate through the atmosphere over varying spatial and temporal scales. A strategically placed instrument at the surface of a planetary body can thus infer information about the present day activity of the planet, and its interactions with space. However, launching of a space mission equipped with instruments that measure atmospheric constituents and distortions is costly and typically infrequent. As such, leveraging equipment from ongoing missions and planned upcoming missions can be explored for additional science return. This is particularly relevant when an investigation can be conducted with minimal impact to the main mission goal.

An example where a single instrument has made significant discoveries about a planetary atmosphere is Curiosity's SAM-TLS, which acquired methane measurements at the surface of Mars (Webster et al., 2018, 2021). While numerous methane measurements exist from Mars orbit, data points near the surface are limited and spatially constrained. However, in conjunction with the orbital data, the measurements suggest a strong disparity between methane concentration at the surface and that measured from orbit (Korablev et al., 2019, Montmessin et al., 2021, Knutsen et al., 2021). Additionally, the day and night measurements from the surface indicate a potential diurnal variability. As methane is of astrobiological significance, these reported methane values inspired further investigation of the differences in methane abundance within a few km and hours of each other. My contributions to these investigations were two-fold, the first being the investigation of methane diffusion through a simulated Martian atmosphere whilst incorporating a relatively new methane destruction mechanism that could be present on Mars; and the second, an analog study

demonstrating how methane spatial variability can be measured in the context of the precision of the currently deployed methane spectrometer (SAM-TLS) on the surface of Mars.

In Chapter 2, I conducted an analog study demonstrating that the current instruments on Mars would be sufficient to detect meter-scale variability, and thereby locate areas of high and low concentrations of methane. Identifying these locations would narrow the candidates for methane source and sink mechanisms. However, I also indicated that future measurements would need to be more frequent and spatially distributed.

In Chapter 3, I found that it is possible to have relatively low fluxes of methane by investigating the detailed dynamics within Gale Crater when coupled with a rapid destruction mechanism. This provides a potential solution for the apparent discrepancies between methane concentrations observed within Gale Crater and those observed from orbit. I found that the incorporation of both diffusion (dilution) of methane from the surface and destruction by means of UV-activated perchlorate could satisfy both the measurements near the surface, and those from orbit. However, the specific transport of methane varies depending on the atmospheric models used. Investigations of the atmospheric dynamics within a few km of the surface would support refined simulations. Additionally, in a few select simulations, methane above 10 km exceeds the detection threshold of the Trace Gas Orbiter. The best time of year to measure this high-altitude methane would be around $L_s = 220°$ or $L_s = 330°$. I also identified the need to measure methane at the surface during the afternoon to better understand atmospheric dynamics near the surface.

In Chapter 4, I investigated the signals that could be produced by airbursts in Titan's atmosphere. I found that the occurrence of airbursts with initial meteor radii greater than 1 m can readily be detected by the upcoming Dragonfly mission. The impactor rate is quite poorly constrained in the outer Solar Syste, so by conducting this study, we establish the signal for a given impactor and prepare for data return in advance, allowing us to better refine observation strategies. This investigation provides additional science return without requiring changes to an existing suite of instrumentation. I suggested that all future missions to planets with atmospheres equipped with seismometers should also include this preliminary investigation prior to launch.

Overall, this body of work considers how information is propagated through the atmosphere, and the subsequent inferences we can make about planetary bodies. By evaluating the required sensitivity of measurements, we can inform instrument development and mission observation plan-

ning.

Chapter 6

Future Work

In the previous three chapters, I provided an overview into three projects evaluating planetary atmospheres. Here I expand upon interesting avenues of research that naturally arose from those chapters.

6.1 Next Steps in Understanding Martian Methane

In the conclusion of the Martian Methane Analog chapter, I indicated that future measurements of methane on Mars would perform best by either continuously monitoring the same location at regular intervals, or by implementing distributed measurement devices across an area of interest to track the spatial and temporal differences. Key locations to place methane measuring instruments on Mars would be aligned with geological features such as surface cracks, sedimentary basins, and ancient volcanoes (Oehler and Etiope, 2017). Realistically, the number future instruments deployed on Mars will likely be limited and an array of instruments will not be feasible. Thus, continuous monitoring would be the next future step for an analog study.

Future analog studies would be best accompanied by a suite of meteorological instruments in addition to a methane measurement device. These include an anemometer, pressure sensor, and temperature sensor much like the REMS instrument suite on the Curiosity rover. Wind direction and speed could provide context on increases and decreases in the local methane concetration for relatively nearby effects. Pressure and temperature changes could be used to relate the overall diurnal cycle of methane, if there is one. Measurements taken by these instruments in conjunction

with modelling of the atmosphere could be used to locate sources of methane and the rate of transport. This exercise would closely align to the work conducted by Luo et al. (2021) who was able to infer the origin of a methane plume-like source. The difference in this proposed study would include capturing a longer time series of methane concentrations that would provide more constraints on the simulation. Furthermore, returning to the same study site of the polygonal terrain would provide context on microseepage origins rather than plume-like sources. This work could be done entirely within a simulation, but as noted in Chapter 3, atmospheric models tend to underestimate transport and mixing near the surface.

It is worth noting that the future development of MAGE includes the ability to measure different isotops of carbon in the methane molecules. Doing so will constrain the potential sources of methane as well as the isotopic ratio of carbon can be indicative of the origin of methane.

In Chapter 3, I was unable to get access to models such as MarsWRF and the NASA-Ames GCM model at the time of writing. It is important to consider a wide range of atmospheric models as none of the atmospheric models truly represent the entire Martian atmosphere and the atmospheric dynamics. In particular, evidence from inferred wind speeds and directions from mission landings and Ingenuity flights tend to diverge from modelled values predicted by GCMs and 1D models of the Martian atmosphere. These differences are most noticeable in the first few meters of the surface, and between 2 and 10 km altitude. I suggest future work incorporate a wider range of models to better evaluate the effect of choosing between different atmospheric models on diffusion and destruction and their limitations.

Overall, it is likely that the atmospheric models tend to underestimate atmospheric mixing in the models I used. In terms of the divergence from model simulations and observations, future Mars missions can be considered to better constrain the lower few kilometers of the atmosphere. With additional measurements, it may be possible to adjust the diffusivity values such as in Toigo and Richardson (2002) to better match the atmospheric behaviour. Another area of improvement for the atmospheric models is to better constrain nighttime mixing. Eddy diffusivity coefficients varied over several orders of magnitude in the three atmospheric models I did consider. While the atmospheric models were validated agianst surface temperatures and pressures over full day cycles, very little data exists on atmospheric mixing during the nighttime except from that of Pathfinder (Paton et al., 2023).

The methane destruction mechanisms used in Chapter 3 can also be refined. In this work, two methane destruction mechanisms are used, the generally quoted 330 year methane lifetime for an e-fold reduction, and the relatively rapid methane destruction that involves the reaction of perchlorate with methane when perchlorate is UV-activated (Zhang et al., 2022). However, other processes in the Martian atmosphere can contribute to methane removal, such as the adsorption reaching into the subsurface and triboelectric charging of dust grains near the surface during dust events Atreya et al. (2007), Ortiz et al. (2024), Moores et al. (2019b), Thøgersen et al. (2021), Chide et al. (2025). There may also be competing reactions to slow the Zhang et al. (2022) methane destruction mechanism. In my simulations, I did not consider satisfying the overall atmospheric chemistry of the Martian atmosphere, such as accounting for various levels of CO_2 and CO, both of which are produced when methane is oxidized (Zhang et al., 2022), or the expected byproduct of HCl observable by orbiter when the chlorine ion reacts with the UV dissociated components of H_2O. Furthermore, it would be interesting to track the total amount of chlorate produced by the destruction mechanism and estimate its relative impact on reactions with say, ferrous oxides (Mitra et al., 2020).

One of the assumptions of the methods used in the model described in Chapter 3 was that methane flux is constant throughout the sol. This is likely not an accurate representation of methane flux if methane comes from the subsurface. As demonstrated by Ortiz et al. (2024), adsorption and desorption of methane within the subsurface (where the Zhang et al. (2022) methane destruction mechanism is not active) can affect the total methane concentration near the surface. Incorporating a barometric pumping model into the existing VDM and box model framework could produce estimates of methane reservoirs in the subsurface.

6.2 Next Steps in Undestanding Airbursts in Titan's Atmosphere

In Chapter 4, I assumed a variety of meteor properties such as composition, porosity, and internal strengths. However, these values are not well constrained for the outer Solar System to described airburst signals on Titan. Estimates of the meteor properties we used were based on cometary objects within the Inner Solar System, with the majority of data coming from the investigation of Comet 67P and Deep Impact (e.g. (Biele et al., 2022, Attree et al., 2018)). While we expect

that cometary objects are similar in composition in the outer solar system, the general internal strengths are not well constrained. Further investigation and simulation of cometary properties could be useful. In particular, it is possible that the strength range that I used does not accurately reflect the real range of cometary objects.

The internal strength of the cometary objects can be refined by future missions to explore cometary bodies such as the Rosetta and Philae missions. However, is not necessarily easy to conduct a mission to a cometary object in the near future. It is perhaps possible to simulate some of the processes in a laboratory environment such as the strength of ice grains travelling at several kilmeters per second, such as the gas gun at the University of Kent (Price et al., 2024) or the aerosol impact spetrometer at the University of California, San Diego (Adamson et al., 2017). Overall, there are still avenues of research to better understand the material properties of comets and their interactions in the atmosphere.

Another avenue of future research would be to consider whether the meteor descent simulation accurately reflects the breakup processes for comets. The Separate Fragments Model was developed for rocky meteors and has been shown to match the observed descent of impactors in Earth's atmosphere. It is meaningful to also test the performance of the SFM against cometary impactors in Earth's atmosphere as part of validating my approach.

References

Nasa: Mars fact sheet, 2020. URL `https://nssdc.gsfc.nasa.gov/planetary/factsheet/marsfact.html`.

B. D. Adamson, M. E. C. Miller, and R. E. Continetti. The aerosol impact spectrometer: a versatile platform for studying the velocity dependence of nanoparticle-surface impact phenomena. *EPJ Techniques and Instrumentation*, 4, 1 2017. doi: 10.1140/epjti/s40485-017-0037-6.

A. A. Amsden, H. M. Ruppel, and C. W. Hirt. Sale: a simplified ale computer program for fluid flow at all speeds. Technical report, Los Alamos National Laboratory (LANL), 6 1980. URL `http://www.osti.gov/servlets/purl/5176006/`.

N. Artemieva and J. Lunine. Cratering on titan: impact melt, ejecta, and the fate of surface organics. *Icarus*, 164:471–480, 8 2003. ISSN 0019-1035. doi: 10.1016/S0019-1035(03)00148-9.

N. Artemieva and J. I. Lunine. Impact cratering on titan ii. global melt, escaping ejecta, and aqueous alteration of surface organics. *Icarus*, 175:522–533, 6 2005. ISSN 0019-1035. doi: 10.1016/J.ICARUS.2004.12.005.

N. A. Artemieva and V. V. Shuvalov. Motion of a fragmented meteoroid through the planetary atmosphere. *Journal of Geophysical Research: Planets*, 106:3297–3309, 2 2001. ISSN 2156-2202. doi: 10.1029/2000JE001264.

S. P. Arya. *Introduction to micrometeorology*, volume 79. Academic Press, 2 edition, 4 2001. ISBN 9780080489261.

E. Aspahug and W. Benz. Density of comet shoemaker-levy 9 deduced by modelling breakup of the parent 'rubble pile'. *Nature: Letters*, 370:120–123, 1994.

S. K. Atreya, P. R. Mahaffy, and A. S. Wong. Methane and related trace species on mars: Origin, loss, implications for life, and habitability. *Planetary and Space Science*, 55:358–369, 2 2007. ISSN 0032-0633. doi: 10.1016/J.PSS.2006.02.005.

S. K. Atreya, O. Witasse, V. F. Chevrier, F. Forget, P. R. Mahaffy, P. B. Price, C. R. Webster, and R. W. Zurek. Methane on mars: Current observations, interpretation, and future plans. *Planetary and Space Science, Special Issue on Methane on Mars*, 2011. doi: 10.1016/j.pss.2010.10.008.

N. Attree, O. Groussin, L. Jorda, D. Nébouy, N. Thomas, Y. Brouet, E. Kührt, F. Preusker, F. Scholten, J. Knollenberg, P. Hartogh, H. Sierks, C. Barbieri, P. Lamy, R. Rodrigo, D. Koschny, H. Rickman, H. U. Keller, M. F. A'Hearn, A. T. Auger, M. A. Barucci, J. L. Bertaux, I. Bertini, D. Bodewits, S. Boudreault, G. Cremonese, V. D. Deppo, B. Davidsson, S. Debei, M. D. Cecco, J. Deller, M. R. El-Maarry, S. Fornasier, M. Fulle, P. J. Gutiérrez, C. Güttler, S. Hviid, W. H.

Ip, G. Kovacs, J. R. Kramm, M. Küppers, L. M. Lara, M. Lazzarin, J. J. L. Moreno, S. Lowry, S. Marchi, F. Marzari, S. Mottola, G. Naletto, N. Oklay, M. Pajola, I. Toth, C. Tubiana, J. B. Vincent, and X. Shi. Tensile strength of 67p/churyumov–gerasimenko nucleus material from overhangs. *Astronomy & Astrophysics*, 611:A33, 3 2018. ISSN 0004-6361. doi: 10.1051/0004-6361/201732155.

M. I. Avramenko, I. V. Glazyrin, G. V. Ionov, and A. V. Karpeev. Simulation of the airwave caused by the chelyabinsk superbolide. *Journal of Geophysical Research: Atmospheres*, 119:7035–7050, 6 2014. ISSN 2169-8996. doi: 10.1002/2013JD021028.

B. Baldwin and Y. Sheaffer. Ablation and breakup of large meteoroids during atmospheric entry. *Journal of Geophysical Research*, 76:4653–4668, 7 1971. ISSN 2156-2202. doi: 10.1029/JA076I019P04653.

J. W. Barnes, E. P. Turtle, M. G. Trainer, R. D. Lorenz, S. M. MacKenzie, W. B. Brinckerhoff, M. L. Cable, C. M. Ernst, C. Freissinet, K. P. Hand, A. G. Hayes, S. M. Horst, J. R. Johnson, E. Karkoschka, D. J. Lawrence, A. L. Gall, J. M. Lora, C. P. McKay, R. S. Miller, S. L. Murchie, C. D. Neish, C. E. Newman, J. Nunez, M. P. Panning, A. M. Parsons, P. N. Peplowski, L. C. Quic, J. Radebaugh, S. C. Rafkin, H. Shiraishi, J. M. Soderblom, K. S. Sotzen, A. M. Stickle, E. R. Stofan, C. Szopa, T. Tokano, T. Wagner, C. Wilson, R. A. Yingst, K. Zacny, and S. C. Stahler. Science goals and objectives for the dragonfly titan rotorcraft relocatable lander. *The Planetary Science Journal*, 2:130, 7 2021. ISSN 2632-3338. doi: 10.3847/PSJ/ABFDCF.

M. Battalio and H. Wang. The mars dust activity database (mdad): A comprehensive statistical study of dust storm sequences. *Icarus*, 354:114059, 1 2021. ISSN 0019-1035. doi: 10.1016/J.ICARUS.2020.114059.

A. Ben-Menahem and S. J. Singh. *Seismic Waves and Sources*. 1981. ISBN 9781461258582.

V. T. Bickel, I. J. Daubar, G. Zenhäusern, G. Doran, C. Charalambous, B. Fernando, A. Sokolowska, K. L. Wagstaff, T. Pike, S. C. Stähler, J. Clinton, and D. Giardini. New impacts on mars: Systematic identification and association with insight seismic events. *Geophysical Research Letters*, 52, 2 2025. ISSN 19448007. doi: 10.1029/2024GL109133.

J. Biele, J. B. Vincent, and J. Knollenberg. Mechanical properties of cometary surfaces. *Universe*, 8:487, 9 2022. ISSN 22181997. doi: 10.3390/UNIVERSE8090487/S1.

G. Bischof, S. D. Guzewich, J. E. Moores, M. T. Lemmon, J. M. Battalio, C. W. Hayes, A. C. Innanen, and C. L. Smith. Dust dynamics in gale crater observed using the line-of-sight extinction through 3,663 sols of the mars science laboratory mission. *Journal of Geophysical Research: Planets*, 129:e2024JE008349, 10 2024. ISSN 21699100. doi: 10.1029/2024JE008349.

A. K. Blackadar. The vertical distribution of wind and turbulent exchange in a neutral atmosphere. *Journal of Geophysical Research*, 67:3095–3102, 7 1962. ISSN 2156-2202. doi: 10.1029/JZ067I008P03095.

P. A. Bland and N. A. Artemieva. The rate of small impacts on earth. *Meteoritics & Planetary Science*, 41:607–631, 4 2006. ISSN 1945-5100. doi: 10.1111/J.1945-5100.2006.TB00485.X.

J. Borovička. Physical and chemical properties of meteoroids as deduced from observations. *Proceedings of the International Astronomical Union*, 1:249–271, 2005. ISSN 1743-9221. doi: 10.1017/S1743921305006782.

J. Borovička and P. Spurný. Physical properties of taurid meteoroids of various sizes. *Planetary and Space Science*, 182:104849, 2020. ISSN 00320633. doi: 10.1016/j.pss.2020.104849.

J. Borovička, P. Spurný, V. I. Grigore, and J. Svoreň. The january 7, 2015, superbolide over romania and structural diversity of meter-sized asteroids. *Planetary and Space Science*, 143: 147–158, 9 2017. ISSN 0032-0633. doi: 10.1016/J.PSS.2017.02.006.

M. B. E. Boslough and D. A. Crawford. Low-altitude airbursts and the impact threat. *International Journal of Impact Engineering*, 35:1441–1448, 2008. doi: 10.1016/j.ijimpeng.2008.07.053.

W. F. Bottke, D. Vokrouhlický, R. Marshall, D. Nesvorný, A. Morbidelli, R. Deienno, S. Marchi, L. Dones, and H. F. Levison. The collisional evolution of the primordial kuiper belt, its destabilized population, and the trojan asteroids. *The Planetary Science Journal*, 4:168, 9 2023. ISSN 2632-3338. doi: 10.3847/PSJ/ACE7CD.

P. Brown, P. J. Mccausland, M. Fries, E. Silber, W. N. Edwards, D. K. Wong, R. J. Weryk, J. Fries, and Z. Krzeminski. The fall of the grimsby meteorite—i: Fireball dynamics and orbit from radar, video, and infrasound records. *Meteoritics & Planetary Science*, 46:339–363, 3 2011. ISSN 1945-5100. doi: 10.1111/J.1945-5100.2010.01167.X.

P. Brown, P. Wiegert, D. Clark, and E. Tagliaferri. Orbital and physical characteristics of meter-scale impactors from airburst observations. *Icarus*, 266:96–111, 3 2016. ISSN 0019-1035. doi: 10.1016/J.ICARUS.2015.11.022.

P. G. Brown, W. N. Edwards, D. O. ReVelle, and P. Spurny. Acoustic analysis of shock production by very high-altitude meteors—i: infrasonic observations, dynamics and luminosity. *Journal of Atmospheric and Solar-Terrestrial Physics*, 69:600–620, 4 2007. ISSN 1364-6826. doi: 10.1016/J.JASTP.2006.10.011.

P. G. Brown, J. D. Assink, L. Astiz, R. Blaauw, M. B. Boslough, J. Borovička, N. Brachet, D. Brown, M. Campbell-Brown, L. Ceranna, W. Cooke, C. D. Groot-Hedlin, D. P. Drob, W. Edwards, L. G. Evers, M. Garces, J. Gill, M. Hedlin, A. Kingery, G. Laske, A. L. Pichon, P. Mialle, D. E. Moser, A. Saffer, E. Silber, P. Smets, R. E. Spalding, P. Spurny, E. Tagliaferri, D. Uren, R. J. Weryk, R. Whitaker, and Z. Krzeminski. A 500-kiloton airburst over chelyabinsk and an enhanced hazard from small impactors. *Nature*, 503:238–241, 11 2013. ISSN 1476-4687. doi: 10.1038/NATURE12741.

K. L. Bryson, D. R. Ostrowski, and A. Blasizzo. Meteorite flaws and scaling for atmospheric entry. *Planetary and Space Science*, 164:85–90, 12 2018. ISSN 00320633. doi: 10.1016/j.pss.2018.06.018.

D. M. Burr, J. P. Emery, R. D. Lorenz, G. C. Collins, and P. A. Carling. Sediment transport by liquid surficial flow: Application to titan. *Icarus*, 181:235–242, 3 2006. ISSN 0019-1035. doi: 10.1016/J.ICARUS.2005.11.012.

V. G. Bykov. V p /v s ratio and physico-mechanical properties of rocks. *Geol. of Pac. Ocean*, 11: 135–150, 1994.

M. L. Cable, S. M. Hörst, R. Hodyss, P. M. Beauchamp, M. A. Smith, and P. A. Willis. Titan tholins: Simulating titan organic chemistry in the cassini-huygens era. *Chemical Reviews*, 112: 1882–1909, 3 2011. ISSN 00092665. doi: 10.1021/CR200221X.

Z. Ceplecha and R. E. McCrosky. Fireball end heights: A diagnostic for the structure of meteoric material. *Journal of Geophysical Research*, 81:6257–6275, 12 1976. ISSN 2156-2202. doi: 10.1029/JB081I035P06257.

Z. Ceplecha, J. Borovička, W. G. Elford, D. O. ReVelle, R. L. Hawkes, V. Porubčan, and M. Šimek. Meteor phenomena and bodies. *Space Science Reviews*, 84:327–471, 1998. ISSN 00386308. doi: 10.1023/A:1005069928850.

C. Charalambous, W. T. Pike, B. Fernando, N. Wójcicka, D. Kim, M. Froment, P. Lognonné, S. Woodley, L. Ojha, V. T. Bickel, J. McNeil, G. S. Collins, I. J. Daubar, A. Horleston, and B. Banerdt. New impacts on mars: Unraveling seismic propagation paths through a cerberus fossae impact detection. *Geophysical Research Letters*, 52, 2 2025. ISSN 19448007. doi: 10.1029/2024GL110159.

B. Charnay and S. Lebonnois. Two boundary layers in titan's lower troposphere inferred from a climate model. *Nature Geoscience*, 5:106–109, 1 2012. ISSN 1752-0908. doi: 10.1038/ngeo1374.

E. Chassefière. Metastable methane clathrate particles as a source of methane to the martian atmosphere. *Icarus*, 204(1):137–144, nov 2009. ISSN 0019-1035. doi: 10.1016/J.ICARUS.2009.06.016.

B. Chide, R. D. Lorenz, F. Montmessin, S. Maurice, Y. Parot, R. Hueso, G. Martinez, A. Vicente-Retortillo, X. Jacob, M. Lemmon, B. Dubois, P. Y. Meslin, C. Newman, T. Bertrand, G. Deprez, D. Toledo, A. S. 'anchez Lavega, A. Cousin, and R. C. Wiens. Detection of triboelectric discharges during dust events on mars. *Nature*, 647:865–869, 11 2025. ISSN 1476-4687. doi: 10.1038/s41586-025-09736-y.

P. R. Christensen, J. L. Bandfield, V. E. Hamilton, S. W. Ruff, H. H. Kieffer, T. N. Titus, M. C. Malin, R. V. Morris, M. D. Lane, R. L. Clark, B. M. Jakosky, M. T. Mellon, J. C. Pearl, B. J. Conrath, M. D. Smith, R. T. Clancy, R. O. Kuzmin, T. Roush, G. L. Mehall, N. Gorelick, K. Bender, K. Murray, S. Dason, E. Greene, S. Silverman, and M. Greenfield. Mars global surveyor thermal emission spectrometer experiment: Investigation description and surface science results. *Journal of Geophysical Research: Planets*, 106:23823–23871, 10 2001. ISSN 01480227. doi: 10.1029/2000JE001370.

T. R. Christensen. Methane emission from Arctic tundra. *Biogeochemistry*, 21(2):117–139, jun 1993. ISSN 01682563. doi: 10.1007/BF00000874.

R. T. Clancy, B. J. Sandor, M. J. Wolff, P. R. Christensen, M. D. Smith, J. C. Pearl, B. J. Conrath, and R. J. Wilson. An intercomparison of ground-based millimeter, mgs tes, and viking atmospheric temperature measurements: Seasonal and interannual variability of temperatures and dust loading in the global mars atmosphere. *Journal of Geophysical Research: Planets*, 105:9553–9571, 4 2000. ISSN 01480227. doi: 10.1029/1999JE001089.

B. Clark and S. Kounaves. Evidence for the distribution of perchlorates on mars. *International Journal of Astrobiology*, 15:311–318, 10 2016. ISSN 1473-5504. doi: 10.1017/S1473550415000385.

A. Colaïtis, A. Spiga, F. Hourdin, C. Rio, F. Forget, and E. Millour. A thermal plume model for the martian convective boundary layer. *Journal of Geophysical Research: Planets*, 118:1468–1487, 7 2013. ISSN 21699100. doi: 10.1002/JGRE.20104.

G. S. Collins, H. J. Melosh, and B. A. Ivanov. Modeling damage and deformation in impact simulations. *Meteoritics & Planetary Science*, 39:217–231, 2 2004. ISSN 1945-5100. doi: 10.1111/J.1945-5100.2004.TB00337.X.

G. S. Collins, D. Elbeshausen, T. M. Davison, K. Wünnemann, B. Ivanov, and H. J. Melosh. isale-dellen manual. Technical report, 7 2016.

G. S. Collins, E. Lynch, R. McAdam, and T. M. Davison. A numerical assessment of simple airblast models of impact airbursts. *Meteoritics & Planetary Science*, 52:1542–1560, 8 2017. ISSN 1945-5100. doi: 10.1111/MAPS.12873.

G. S. Collins, E. L. Newland, D. Schwarz, M. Coleman, S. McMullan, I. J. Daubar, K. Miljkovic, T. Neidhart, and E. Sansom. Meteoroid fragmentation in the martian atmosphere and the formation of crater clusters. *Journal of Geophysical Research: Planets*, 127:1–22, 2022. ISSN 21699100. doi: 10.1029/2021JE007149.

B. J. Conrath. Thermal structure of the martian atmosphere during the dissipation of the dust storm of 1971. *Icarus*, 24:36–46, 1 1975. ISSN 0019-1035. doi: 10.1016/0019-1035(75)90156-6.

D. E. Cotten, W. L. Donn, and A. Oppenheim. On the generation and propagation of shock waves from apollo rockets at orbital altitudes. *Geophysical Journal of the Royal Astronomical Society*, 26:149–159, 1971. ISSN 1365246X. doi: 10.1111/j.1365-246X.1971.tb03388.x.

A. P. Crósta, E. A. Silber, R. M. Lopes, B. C. Johnson, E. Bjonnes, M. J. Malaska, S. D. Vance, C. Sotin, A. Solomonidou, and J. M. Soderblom. Modeling the formation of menrva impact crater on titan: Implications for habitability. *Icarus*, 370:114679, 12 2021. ISSN 0019-1035. doi: 10.1016/J.ICARUS.2021.114679.

F. Daerden, J. A. Whiteway, L. Neary, L. Komguem, M. T. Lemmon, N. G. Heavens, B. A. Cantor, E. Hébrard, and M. D. Smith. A solar escalator on mars: Self-lifting of dust layers by radiative heating. *Geophysical Research Letters*, 42:7319–7326, 9 2015. ISSN 19448007. doi: 10.1002/2015GL064892.

R. E. Danielson, J. J. Caldwell, and D. R. Larach. An inversion in the atmosphere of titan. *Icarus*, 20:437–443, 12 1973. ISSN 0019-1035. doi: 10.1016/0019-1035(73)90016-X.

I. Daubar, P. Lognonné, N. A. Teanby, K. Miljkovic, J. Stevanovic, J. Vaubaillon, B. Kenda, T. Kawamura, J. Clinton, A. Lucas, M. Drilleau, C. Yana, G. S. Collins, D. Banfield, M. Golombek, S. Kedar, N. Schmerr, R. Garcia, S. Rodriguez, T. Gudkova, S. May, M. Banks, J. Maki, E. Sansom, F. Karakostas, M. Panning, N. Fuji, J. Wookey, M. van Driel, M. Lemmon, V. Ansan, M. Böse, S. Stähler, H. Kanamori, J. Richardson, S. Smrekar, and W. B. Banerdt. Impact-seismic investigations of the insight mission. *Space Science Reviews*, 214:1–68, 12 2018. ISSN 15729672. doi: 10.1007/S11214-018-0562-X.

I. J. Daubar, B. A. Fernando, R. F. Garcia, P. M. Grindrod, G. Zenhäusern, N. Wójcicka, N. A. Teanby, S. C. Stähler, L. Posiolova, A. C. Horleston, G. S. Collins, C. Charalambous, J. Clinton, M. E. Banks, M. Froment, P. Lognonné, M. Panning, and W. B. Banerdt. Two seismic events from insight confirmed as new impacts on mars. *The Planetary Science Journal*, 4:175, 9 2023. ISSN 2632-3338. doi: 10.3847/PSJ/ACE9B4.

I. J. Daubar, R. F. Garcia, A. E. Stott, B. Fernando, G. S. Collins, C. M. Dundas, N. Wójcicka, G. Zenhäusern, A. S. McEwen, S. C. Stähler, M. Golombek, C. Charalambous, D. Giardini,

P. Lognonné, and W. B. Banerdt. Seismically detected cratering on mars: Enhanced recent impact flux? *Science Advances*, 10, 6 2024. ISSN 23752548. doi: 10.1126/SCIADV.ADK7615.

E. De and K. Leffingwell. Ground-Ice Wedges: The Dominant Form of Ground-Ice on the North Coast of Alaska. *The Journal of Geology*, 23(7):635–654, oct 1915. ISSN 0022-1376. doi: 10.1086/622281.

E. Dong, J. E. Moores, H. M. Sapers, L. B. V. Stofer, and A. C. Innanen. A martian analog for spatially varying methane microseepage - polygons at expedition strip, axel heiberg island. *Acta Astronautica*, 237:84–95, 12 2025. ISSN 0094-5765. doi: 10.1016/J.ACTAASTRO.2025.07.050. URL `https://www.sciencedirect.com/science/article/pii/S0094576525004801`.

E. Dong, C. D. Neish, J. E. Moores, S. Wakita, G. S. Collins, P. G. Brown, R. D. Lorenz, B. Fernando, and M. P. Panning. Signal characteristics of potential airbursts in titan's atmosphere. *Icarus*, 445:116855, 2 2026. ISSN 0019-1035. doi: 10.1016/J.ICARUS.2025.116855.

P. M. Douglas, D. A. Stolper, D. A. Smith, K. M. Walter Anthony, C. K. Paull, S. Dallimore, M. Wik, P. M. Crill, M. Winterdahl, J. M. Eiler, and A. L. Sessions. Diverse origins of Arctic and Subarctic methane point source emissions identified with multiply-substituted isotopologues. *Geochimica et Cosmochimica Acta*, 188:163–188, sep 2016. ISSN 0016-7037. doi: 10.1016/J.GCA.2016.05.031.

S. Earle and K. Panchuk. Physical geology. page 807, 2019.

D. Eberhart-Phillips, D. H. Han, and M. D. Zoback. Empirical relationships among seismic velocity, effective pressure, porosity, and clay content in sandstone. *Geophysics*, 54:82–89, 1989. ISSN 00168033. doi: 10.1190/1.1442580.

W. N. Edwards. *Meteor generated infrasound: Theory and observation*, pages 361–414. Springer Netherlands, 2009a. ISBN 9781402095078. doi: 10.1007/978-1-4020-9508-5_12.

W. N. Edwards. *Meteor generated infrasound: Theory and observation*, pages 361–414. Springer Netherlands, 2009b. ISBN 9781402095078. doi: 10.1007/978-1-4020-9508-5_12.

W. N. Edwards, P. G. Brown, and D. O. ReVelle. Estimates of meteoroid kinetic energies from observations of infrasonic airwaves. *Journal of Atmospheric and Solar-Terrestrial Physics*, 68:1136–1160, 6 2006. ISSN 1364-6826. doi: 10.1016/J.JASTP.2006.02.010.

W. N. Edwards, D. W. Eaton, P. J. McCausland, D. O. ReVelle, and P. G. Brown. Calibrating infrasonic to seismic coupling using the stardust sample return capsule shockwave: Implications for seismic observations of meteors. *Journal of Geophysical Research: Solid Earth*, 112:1–13, 2007. ISSN 21699356. doi: 10.1029/2006JB004621.

W. N. Edwards, D. W. Eaton, and P. G. Brown. Seismic observation of meteors: Coupling theory and obervations. *Reviews of Geophysics*, 46, 2008. ISSN 87551209. doi: 10.1029/2007RG000253.

W. N. Edwards, P. G. Brown, and D. W. Eaton. Frequency-dependent acoustic–seismic coupling of meteor shock waves. *Bulletin of the Seismological Society of America*, 99:3055–3066, 10 2009. ISSN 0037-1106. doi: 10.1785/0120080226.

C. Elachi, S. Wall, M. Allison, Y. Anderson, R. Boehmer, P. Callahan, P. Encrenaz, E. Flamini, G. Franceschetti, Y. Gim, G. Hamilton, S. Hensley, M. Janssen, W. Johnson, K. Kelleher, R. Kirk,

R. Lopes, R. Lorenz, J. Lunine, D. Muhleman, S. Ostro, F. Paganelli, G. Picardi, F. Posa, L. Roth, R. Seu, S. Shaffer, L. Soderblom, B. Stiles, E. Stofan, S. Vetrella, R. West, C. Wood, L. Wye, and H. Zebker. Cassini radar views the surface of titan. *Science*, 308:970–974, 5 2005. ISSN 00368075. doi: 10.1126/SCIENCE.1109919.

T. A. Ens, P. G. Brown, W. N. Edwards, and E. A. Silber. Infrasound production by bolides: A global statistical study. *Journal of Atmospheric and Solar-Terrestrial Physics*, 80:208–229, 2012. ISSN 13646826. doi: 10.1016/j.jastp.2012.01.018.

ESA. Esa - esa's mars orbiters did not see latest curiosity methane burst, 2019. URL `https://www.esa.int/Science_Exploration/Human_and_Robotic_Exploration/Exploration/ExoMars/ESA_s_Mars_orbiters_did_not_see_latest_Curiosity_methane_burst`.

G. Etiope and D. Z. Oehler. Methane spikes, background seasonality and non-detections on mars: A geological perspective, 4 2019. ISSN 00320633.

S. Faggi, S. Aoki, G. Liuzzi, G. Villanueva, H. Sagawa, M. J. Mumma, A. C. Vandaele, F. Daerden, and S. Viscardy. Following the hcl cycle over three martian seasons in mars year 36. *Journal of Geophysical Research: Planets*, 130:e2025JE009105, 11 2025. ISSN 21699100. doi: 10.1029/2025JE009105.

B. Fernando, C. Charalambous, C. Saliby, E. Sansom, C. Larmat, D. Buttsworth, D. Hicks, R. Johnson, K. Lewis, M. McCleary, G. Petricca, N. Schmerr, F. Zander, and J. Inman. Seismoacoustic measurements of the osiris-rex re-entry with an off-grid raspberry pishake. *Seismica*, 3, 2024. doi: 10.26443/seismica.v3i1.1154.

R. M. Fonseca, M. P. Zorzano-Mier, and J. Martín-Torres. Planetary boundary layer and circulation dynamics at gale crater, mars. *Icarus*, 302:537–559, 3 2018. ISSN 0019-1035. doi: 10.1016/J.ICARUS.2017.11.036.

S. Fonti, F. Mancarella, G. Liuzzi, T. L. Roush, M. C. Frouard, J. Murphy, and A. Blanco. Astrophysics revisiting the identification of methane on mars using tes data. *A&A*, 581:136, 2015. doi: 10.1051/0004-6361/201526235.

F. Forget, F. Hourdin, R. Fournier, C. Hourdin, O. Talagrand, M. Collins, S. R. Lewis, P. L. Read, and J. P. Huot. Improved general circulation models of the martian atmosphere from the surface to above 80 km. *Journal of Geophysical Research: Planets*, 104:24155–24175, 10 1999. ISSN 01480227. doi: 10.1029/1999JE001025.

V. Formisano, S. Atreya, T. Encrenaz, N. Ignatiev, and M. Giuranna. Detection of methane in the atmosphere of mars. *Science*, 306:1758–1761, 12 2004. ISSN 00368075. doi: 10.1126/SCIENCE.1101732.

M. Fulchignoni, F. Ferri, F. Angrilli, A. J. Ball, A. Bar-Nun, M. A. Barucci, C. Bettanini, G. Bianchini, W. Borucki, G. Colombatti, M. Coradini, A. Coustenis, S. Debei, P. Falkner, G. Fanti, E. Flamini, V. Gaborit, R. Grard, M. Hamelin, A. M. Harri, B. Hathi, I. Jernej, M. R. Leese, A. Lehto, P. F. L. Stoppato, J. J. Lopez-Moreno, T. Makinen, J. A. McDonnell, C. P. McKay, G. Molina-Cuberos, F. M. Neubauer, V. Pirronello, R. Rodrigo, B. Saggin, K. Schwingenschuh, A. Seiff, F. S. oes, H. Svedhem, T. Tokano, M. C. Towner, R. Trautner, P. Withers, and J. C. Zarnecki. In situ measurements of the physical characteristics of titan's environment. *Nature*, 438:785–791, 11 2005. ISSN 1476-4687. doi: 10.1038/nature04314.

J. Gõmez-Elvira, C. Armiens, I. Carrasco, M. Genzer, F. Gõmez, R. Haberle, V. E. Hamilton, A. M. Harri, H. Kahanpää, O. Kemppinen, A. Lepinette, J. M. Soler, J. Martín-Torres, J. Martínez-Frías, M. Mischna, L. Mora, S. Navarro, C. Newman, M. A. D. Pablo, V. onica Peinado, J. Polkko, S. C. Rafkin, M. Ramos, N. O. R. o, M. Richardson, J. A. Rodríguez-Manfredi, J. J. R. P. o, E. Sebastián, M. D. L. T. Juárez, J. Torres, R. Urquí, A. R. Vasavada, J. Verdasca, and M. P. Zorzano. Curiosity's rover environmental monitoring station: Overview of the first 100 sols. *Journal of Geophysical Research: Planets*, 119:1680–1688, 7 2014. ISSN 2169-9100. doi: 10.1002/2013JE004576.

R. F. Garcia, I. J. Daubar, Éric Beucler, L. V. Posiolova, G. S. Collins, P. Lognonné, L. Rolland, Z. Xu, N. Wójcicka, A. Spiga, B. Fernando, G. Speth, L. Martire, A. Rajšić, K. Miljković, E. K. Sansom, C. Charalambous, S. Ceylan, S. Menina, L. Margerin, R. Lapeyre, T. Neidhart, N. A. Teanby, N. C. Schmerr, M. Bonnin, M. Froment, J. F. Clinton, O. Karatekin, S. C. Stähler, N. L. Dahmen, C. Durán, A. Horleston, T. Kawamura, M. Plasman, G. Zenhäusern, D. Giardini, M. Panning, M. Malin, and W. B. Banerdt. Newly formed craters on mars located using seismic and acoustic wave data from insight. *Nature Geoscience*, 15:774–780, 9 2022. ISSN 1752-0908. doi: 10.1038/s41561-022-01014-0.

A. Geminale, V. Formisano, and M. Giuranna. Methane in martian atmosphere: Average spatial, diurnal, and seasonal behaviour. *Planetary and Space Science*, 56:1194–1203, 7 2008. ISSN 0032-0633. doi: 10.1016/J.PSS.2008.03.004.

N. Gi and P. Brown. Refinement of bolide characteristics from infrasound measurements. *Planetary and Space Science*, 143:169–181, 2017. ISSN 00320633. doi: 10.1016/j.pss.2017.04.021.

E. Gillen, P. B. Rimmer, and D. C. Catling. Statistical analysis of curiosity data shows no evidence for a strong seasonal cycle of martian methane. *Icarus*, 336:113407, 1 2020. ISSN 0019-1035. doi: 10.1016/J.ICARUS.2019.113407.

S. Glasstone and P. J. Dolan. *The Effects of Nuclear Weapons*. United States Department of Defense and Energy Research and Development Adminitration, 3 edition, 1977. doi: 10.2307/j.ctt5hjpq2.37.

J. Gómez-Elvira, C. Armiens, L. C. ner, M. Domínguez, M. Genzer, F. Gómez, R. Haberle, A. M. Harri, V. Jiménez, H. Kahanää, L. Kowalski, A. Lepinette, J. Martín, J. Martínez-Frías, I. McEwan, L. Mora, J. Moreno, S. Navarro, M. A. D. Pablo, V. Peinado, A. P. na, J. Polkko, M. Ramos, N. O. Renno, J. Ricart, M. Richardson, J. Rodríguez-Manfredi, J. Romeral, E. Sebastián, J. Serrano, M. D. L. T. Juárez, J. Torres, F. Torrero, R. Urquí, L. Vázquez, T. Velasco, J. Verdasca, M. P. Zorzano, and J. Martín-Torres. Rems: The environmental sensor suite for the mars science laboratory rover. *Space Science Reviews*, 170:583–640, 8 2012. ISSN 1572-9672. doi: 10.1007/S11214-012-9921-1.

R. V. Gough, M. A. Tolbert, C. P. McKay, and O. B. Toon. Methane adsorption on a martian soil analog: An abiogenic explanation for methane variability in the martian atmosphere. *Icarus*, 207:165–174, 5 2010. ISSN 0019-1035. doi: 10.1016/J.ICARUS.2009.11.030.

R. V. Gough, J. J. Turley, G. R. Ferrell, K. E. Cordova, S. E. Wood, D. O. Dehaan, C. P. McKay, O. B. Toon, and M. A. Tolbert. Can rapid loss and high variability of martian methane be explained by surface h2o2? *Planetary and Space Science*, 59:238–246, 2 2011. ISSN 0032-0633. doi: 10.1016/J.PSS.2010.09.018.

C. A. Griffith, L. Doose, M. G. Tomasko, P. F. Penteado, and C. See. Radiative transfer analyses of titan's tropical atmosphere. *Icarus*, 218:975–988, 4 2012. ISSN 0019-1035. doi: 10.1016/J.ICARUS.2011.11.034.

J. P. Grotzinger, J. Crisp, A. R. Vasavada, R. C. Anderson, Charles, J. Baker, R. Barry, D. F. Blake, P. Conrad, K. S. Edgett, B. Ferdowski, R. Gellert, J. B. Gilbert, M. Golombek, J. Gómez-Elvira, D. M. Hassler, L. Jandura, M. Litvak, P. Mahaffy, J. Maki, M. Meyer, M. C. Malin, I. Mitrofanov, J. J. Simmonds, D. Vaniman, R. V. Welch, and R. C. Wiens. Mars science laboratory mission and science investigation. *Space Science Reviews*, 170:5–56, 7 2012. ISSN 1572-9672. doi: 10.1007/S11214-012-9892-2. URL `https://link.springer.com/article/10.1007/s11214-012-9892-2`.

O. Groussin, N. Attree, Y. Brouet, V. Ciarletti, B. Davidsson, G. Filacchione, H. H. Fischer, B. Gundlach, M. Knapmeyer, J. Knollenberg, R. Kokotanekova, E. Kührt, C. Leyrat, D. Marshall, I. Pelivan, Y. Skorov, C. Snodgrass, T. Spohn, and F. Tosi. The thermal, mechanical, structural, and dielectric properties of cometary nuclei after rosetta. *Space Science Reviews*, 215:1–51, 6 2019. ISSN 15729672. doi: 10.1007/S11214-019-0594-X.

S. D. Guzewich, E. R. Talaat, A. D. Toigo, D. W. Waugh, and T. H. McConnochie. High-altitude dust layers on mars: Observations with the thermal emission spectrometer. *Journal of Geophysical Research: Planets*, 118:1177–1194, 6 2013. ISSN 21699100. doi: 10.1002/JGRE.20076.

S. D. Guzewich, C. E. Newman, M. de la Torre Juárez, R. J. Wilson, M. Lemmon, M. D. Smith, H. Kahanpää, and A. M. Harri. Atmospheric tides in gale crater, mars. *Icarus*, 268:37–49, 4 2016. ISSN 0019-1035. doi: 10.1016/J.ICARUS.2015.12.028.

S. D. Guzewich, C. E. Newman, M. D. Smith, J. E. Moores, C. L. Smith, C. Moore, M. I. Richardson, D. Kass, A. Kleinböhl, M. Mischna, F. J. Martín-Torres, M. P. Zorzano-Mier, and M. Battalio. The vertical dust profile over gale crater, mars. *Journal of Geophysical Research: Planets*, 122:2779–2792, 12 2017. ISSN 2169-9100. doi: 10.1002/2017JE005420.

S. D. Guzewich, M. Lemmon, C. L. Smith, G. Martínez, de Vicente-Retortillo, C. E. Newman, M. Baker, C. Campbell, B. Cooper, J. Gómez-Elvira, A. M. Harri, D. Hassler, F. J. Martin-Torres, T. McConnochie, J. E. Moores, H. Kahanpää, A. Khayat, M. I. Richardson, M. D. Smith, R. Sullivan, M. de la Torre Juarez, A. R. Vasavada, D. Viúdez-Moreiras, C. Zeitlin, and M. P. Z. Mier. Mars science laboratory observations of the 2018/mars year 34 global dust storm. *Geophysical Research Letters*, 46:71–79, 1 2019. ISSN 19448007.

R. M. Haberle. Solar system/sun, atmospheres, evolution of atmospheres — planetary atmospheres: Mars. *Encyclopedia of Atmospheric Sciences: Second Edition*, pages 168–177, 1 2015. doi: 10.1016/B978-0-12-382225-3.00312-1.

R. M. Haberle, H. C. Houben, R. Hertenstein, and T. Herdtle. A boundary-layer model for mars: Comparison with viking lander and entry data. *Journal of the Atmospheric Sciences*, 50, 1993.

R. M. Haberle, J. Gõmez-Elvira, M. D. L. T. Juárez, A. M. Harri, J. L. Hollingsworth, H. Kahanpää, M. A. Kahre, M. Lemmon, F. J. Martín-Torres, M. Mischna, J. E. Moores, C. Newman, S. C. Rafkin, N. R. o, M. I. Richardson, J. A. Rodríguez-Manfredi, A. R. Vasavada, and M. P. Zorzano-Mier. Preliminary interpretation of the rems pressure data from the first 100 sols of the msl mission. *Journal of Geophysical Research: Planets*, 119:440–453, 3 2014. ISSN 2169-9100. doi: 10.1002/2013JE004488.

A. Hagermann, P. D. Rosenberg, M. C. Towner, J. R. Garry, H. Svedhem, M. R. Leese, B. Hathi, R. D. Lorenz, and J. C. Zarnecki. Speed of sound measurements and the methane abundance in titan's atmosphere. *Icarus*, 189:538–543, 2007. ISSN 00191035. doi: 10.1016/j.icarus.2007.02.004.

A. M. Harri, M. Genzer, O. Kemppinen, J. Gõmez-Elvira, R. Haberle, J. Polkko, H. Savijärvi, N. R. o, J. A. Rodriguez-Manfredi, W. Schmidt, M. Richardson, T. Siili, M. Paton, M. D. la Torre-Juarez, T. Mäkinen, C. Newman, S. Rafkin, M. Mischna, S. Merikallio, H. Haukka, J. Martin-Torres, M. Komu, M. P. Zorzano, V. Peinado, L. Vazquez, and R. Urqui. Mars science laboratory relative humidity observations: Initial results. *Journal of geophysical research. Planets*, 119:2132–2147, 2014. ISSN 2169-9097. doi: 10.1002/2013JE004514.

P. O. Hayne, D. A. Paige, and N. G. Heavens. The role of snowfall in forming the seasonal ice caps of mars: Models and constraints from the mars climate sounder. *Icarus*, 231:122–130, 3 2014. ISSN 0019-1035. doi: 10.1016/J.ICARUS.2013.10.020.

C. He and M. A. Smith. Identification of nitrogenous organic species in titan aerosols analogs: Implication for prebiotic chemistry on titan and early earth. *Icarus*, 238:86–92, 8 2014. ISSN 0019-1035. doi: 10.1016/J.ICARUS.2014.05.012.

N. G. Heavens, M. I. Richardson, A. Kleinbhöl, D. M. Kass, D. J. McCleese, W. Abdou, J. L. Benson, J. T. Schofield, J. H. Shirley, and P. M. Wolkenberg. The vertical distribution of dust in the martian atmosphere during northern spring and summer: Observations by the mars climate sounder and analysis of zonal average vertical dust profiles. *Journal of Geophysical Research: Planets*, 116, 2011. ISSN 01480227. doi: 10.1029/2010JE003691.

E. Hébrard, C. Listowski, P. Coll, B. Marticorena, G. Bergametti, A. Määttänen, F. Montmessin, and F. Forget. An aerodynamic roughness length map derived from extended martian rock abundance data. *Journal of Geophysical Research: Planets*, 117:4008, 4 2012. ISSN 01480227. doi: 10.1029/2011JE003942I.

M. H. Hecht, S. P. Kounaves, R. C. Quinn, S. J. West, S. M. Young, D. W. Ming, D. C. Catling, B. C. Clark, W. V. Boynton, J. Hoffman, L. P. DeFlores, K. Gospodinova, J. Kapit, and P. H. Smith. Detection of perchlorate and the soluble chemistry of martian soil at the phoenix lander site. *Science*, 325:64–67, 7 2009. ISSN 00368075. doi: 10.1126/SCIENCE.1172466.

J. E. Hedgepeth, C. D. Neish, E. P. Turtle, B. W. Stiles, R. Kirk, and R. D. Lorenz. Titan's impact crater population after cassini. *Icarus*, 344:113664, 7 2020. ISSN 0019-1035. doi: 10.1016/J.ICARUS.2020.113664.

S. Heimann, Àlvaro Gonzàlez, R. Wang, S. Cesca, and T. Dahm. Seismic characterization of the chelyabinsk meteor's terminal explosion. *Seismological Research Letters*, 84:1021–1025, 2013. ISSN 08950695. doi: 10.1785/0220130042.

D. P. Hinson, M. Pätzold, S. Tellmann, B. Häusler, and G. L. Tyler. The depth of the convective boundary layer on mars. *Icarus*, 198:57–66, 11 2008. ISSN 0019-1035. doi: 10.1016/J.ICARUS.2008.07.003.

J. V. Hogancamp, B. Sutter, R. V. Morris, P. D. Archer, D. W. Ming, E. B. Rampe, P. Mahaffy, and R. Navarro-Gonzalez. Chlorate/fe-bearing phase mixtures as a possible source of oxygen and chlorine detected by the sample analysis at mars instrument in gale crater, mars. *Journal of Geophysical Research: Planets*, 123:2920–2938, 11 2018. ISSN 21699100. doi: 10.1029/2018JE005691.

A. A. Holtslag and B. A. Boville. Local versus nonlocal boundary-layer diffusion in a global climate model. *Journal of Climate*, 6:1825–1842, 10 1993. ISSN 0894-8755. doi: 10.1175/1520-0442(1993)006.

S. M. Hörst. Titan's atmosphere and climate. *Journal of Geophysical Research: Planets*, 122: 432–482, 3 2017. ISSN 2169-9100. doi: 10.1002/2016JE005240.

S. M. Hörst and M. A. Tolbert. In situ measurements of the size and density of titan aerosol analogs. *The Astrophysical Journal Letters*, 770:L10, 5 2013. ISSN 2041-8205. doi: 10.1088/2041-8205/770/1/L10.

S. M. Hörst, R. V. Yelle, A. Buch, N. Carrasco, G. Cernogora, O. Dutuit, E. Quirico, E. Sciamma-O'Brien, M. A. Smith, A. Somogyi, C. Szopa, R. Thissen, and V. Vuitton. Formation of amino acids and nucleotide bases in a titan atmosphere simulation experiment. *Astrobiology*, 12:809–817, 9 2012. ISSN 15311074. doi: 10.1089/AST.2011.0623.

F. Hourdin, P. le Van, F. Forget, and O. Talagrand. Meteorological variability and the annual surface pressure cycle on mars. *Journal of the Atmospheric Sciences*, 11 1993.

K. R. Housen and K. A. Holsapple. Scale effects in strength-dominated collisions of rocky asteroids. *Icarus*, 142:21–33, 11 1999. ISSN 00191035. doi: 10.1006/icar.1999.6206.

L. Huber. Huygens atmosphere structure instrument (hasi) bundle. 2019. doi: 10.17189/23e7-zw13.

M. L. Hunt and N. M. Vriend. Booming sand dunes. *Annual Review of Earth and Planetary Sciences*, 38:281–301, 5 2010. ISSN 00846597. doi: 10.1146/ANNUREV-EARTH-040809-152336/1.

H. Imanaka, D. P. Cruikshank, B. N. Khare, and C. P. McKay. Optical constants of titan tholins at mid-infrared wavelengths (2.5–25 μm) and the possible chemical nature of titan's haze particles. *Icarus*, 218:247–261, 3 2012. ISSN 0019-1035. doi: 10.1016/J.ICARUS.2011.11.018.

W. H. Ip. Meteoroid ablation processes in titan's atmosphere. *Nature*, 345:511–512, 1990. ISSN 1476-4687. doi: 10.1038/345511a0.

B. Jackson, L. Fenton, T. Brown, A. Munguira, G. Martinez, C. Newman, D. Viúdez-Moreiras, M. Golombek, R. Lorenz, M. D. Paton, and D. Conway. Profiling near-surface winds on mars using attitude data from mars 2020 ingenuity. *The Planetary Science Journal*, 6:21, 1 2025. ISSN 2632-3338. doi: 10.3847/PSJ/AD8B41.

L. D. Jaffe and L. M. Herrell. Cassini/huygens science instruments, spacecraft, and mission. *Journal of Spacecraft and Rockets*, 34:509–521, 1997. ISSN 15336794. doi: 10.2514/2.3241.

B. M. Jakosky and C. B. Farmer. The seasonal and global behavior of water vapor in the mars atmosphere: Complete global results of the viking atmospheric water detector experiment. *Journal of Geophysical Research: Solid Earth*, 87:2999–3019, 4 1982. ISSN 2156-2202. doi: 10.1029/JB087IB04P02999.

P. B. James, H. H. Kieffer, D. A. Paige, P. B. James, H. H. Kieffer, D. A. Paige, James, P. B., Kieffer, H. H., Paige, and D. A. *The seasonal cycle of carbon dioxide on Mars.*, pages 934–968. 1992.

S. J. K. Jensen, J. Skibsted, H. J. Jakobsen, I. L. ten Kate, H. P. Gunnlaugsson, J. P. Merrison, K. Finster, E. Bak, J. J. Iversen, J. C. Kondrup, and P. Nørnberg. A sink for methane on mars? the answer is blowing in the wind. *Icarus*, 236:24–27, 7 2014. ISSN 0019-1035. doi: 10.1016/J.ICARUS.2014.03.036.

H. Kanamori, J. Mori, B. Sturtevant, D. L. Anderson, and T. Heaton. Seismic excitation by space shuttles. *Shock Waves*, 2:89–96, 1992. ISSN 09381287. doi: 10.1007/BF01415896.

D. M. Kass, A. Kleinböhl, D. J. McCleese, J. T. Schofield, and M. D. Smith. Interannual similarity in the martian atmosphere during the dust storm season. *Geophysical Research Letters*, 43: 6111–6118, 6 2016. ISSN 1944-8007. doi: 10.1002/2016GL068978.

E. W. Knutsen, G. L. Villanueva, G. Liuzzi, M. M. Crismani, M. J. Mumma, M. D. Smith, A. C. Vandaele, S. Aoki, I. R. Thomas, F. Daerden, S. Viscardy, J. T. Erwin, L. Trompet, L. Neary, B. Ristic, M. A. Lopez-Valverde, J. J. Lopez-Moreno, M. R. Patel, O. Karatekin, and G. Bellucci. Comprehensive investigation of mars methane and organics with exomars/nomad. *Icarus*, 357: 114266, 3 2021. ISSN 0019-1035. doi: 10.1016/J.ICARUS.2020.114266.

H. Kohnen. The temperature dependence of seismic waves in ice. *Journal of Glaciology*, 13:144–147, 1974. ISSN 0022-1430. doi: 10.3189/S0022143000023467.

O. Korablev, A. C. Vandaele, F. Montmessin, A. A. Fedorova, A. Trokhimovskiy, F. Forget, F. Lefèvre, F. Daerden, I. R. Thomas, L. Trompet, J. T. Erwin, S. Aoki, S. Robert, L. Neary, S. Viscardy, A. V. Grigoriev, N. I. Ignatiev, A. Shakun, A. Patrakeev, D. A. Belyaev, J. L. Bertaux, K. S. Olsen, L. Baggio, J. Alday, Y. S. Ivanov, B. Ristic, J. Mason, Y. Willame, C. Depiesse, L. Hetey, S. Berkenbosch, R. Clairquin, C. Queirolo, B. Beeckman, E. Neefs, M. R. Patel, G. Bellucci, J. J. López-Moreno, C. F. Wilson, G. Etiope, L. Zelenyi, H. Svedhem, J. L. Vago, G. Alonso-Rodrigo, F. Altieri, K. Anufreychik, G. Arnold, S. Bauduin, D. Bolsée, G. Carrozzo, R. T. Clancy, E. Cloutis, M. Crismani, F. D. Pieve, E. D'Aversa, N. Duxbury, T. Encrenaz, T. Fouchet, B. Funke, D. Fussen, M. Garcia-Comas, J. C. Gérard, M. Giuranna, L. Gkouvelis, F. Gonzalez-Galindo, D. Grassi, S. Guerlet, P. Hartogh, J. Holmes, B. Hubert, J. Kaminski, O. Karatekin, Y. Kasaba, D. Kass, I. Khatuntsev, A. Kleinböhl, N. Kokonkov, V. Krasnopolsky, R. Kuzmin, G. Lacombe, O. Lanciano, E. Lellouch, S. Lewis, M. Luginin, G. Liuzzi, M. López-Puertas, M. López-Valverde, A. Määttänen, A. Mahieux, E. Marcq, J. Martin-Torres, I. Maslov, A. Medvedev, E. Millour, B. Moshkin, M. J. Mumma, H. Nakagawa, R. E. Novak, F. Oliva, D. Patsaev, A. Piccialli, C. Quantin-Nataf, E. Renotte, B. Ritter, A. Rodin, F. Schmidt, N. Schneider, V. Shematovich, M. D. Smith, N. A. Teanby, E. Thiemann, N. Thomas, J. V. Auwera, L. Vazquez, G. Villanueva, M. Vincendon, J. Whiteway, V. Wilquet, M. J. Wolff, P. Wolkenberg, R. Yelle, R. Young, L. Zasova, and M. P. Zorzano. No detection of methane on mars from early exomars trace gas orbiter observations. *Nature*, 568:517–520, 4 2019. ISSN 1476-4687. doi: 10.1038/s41586-019-1096-4.

D. G. Korycansky and K. J. Zahnle. Modeling crater populations on venus and titan. *Planetary and Space Science*, 53:695–710, 6 2005. ISSN 00320633. doi: 10.1016/J.PSS.2005.03.002.

S. P. Kounaves, M. H. Hecht, J. Kapit, K. Gospodinova, L. Deflores, R. C. Quinn, W. V. Boynton, B. C. Clark, D. C. Catling, P. Hredzak, D. W. Ming, Q. Moore, J. Shusterman, S. Stroble, S. J. West, and S. M. Young. Wet chemistry experiments on the 2007 phoenix mars scout lander mission: Data analysis and results. *Journal of Geophysical Research: Planets*, 115:0–10, 1 2010. ISSN 01480227. doi: 10.1029/2009JE003424.

V. A. Krasnopolsky, J. P. Maillard, and T. C. Owen. Detection of methane in the martian atmosphere: evidence for life? *Icarus*, 172:537–547, 12 2004. ISSN 0019-1035. doi: 10.1016/J.ICARUS.2004.07.004.

G. P. Kuiper, Kuiper, G. P., Kuiper, and G. P. Titan: a satellite with an atmosphere. *ApJ*, 100: 378, 11 1944. ISSN 0004-637X. doi: 10.1086/144679.

M. C. Lau, B. T. Stackhouse, A. C. Layton, A. Chauhan, T. A. Vishnivetskaya, K. Chourey, J. Ronholm, N. C. Mykytczuk, P. C. Bennett, G. Lamarche-Gagnon, N. Burton, W. H. Pollard, C. R. Omelon, D. M. Medvigy, R. L. Hettich, S. M. Pfiffner, L. G. Whyte, and T. C. Onstott. An active atmospheric methane sink in high Arctic mineral cryosols. *The ISME Journal*, 9(8): 1880–1891, apr 2015. ISSN 1751-7370. doi: 10.1038/ismej.2015.13.

F. Lefèvre and F. Forget. Observed variations of methane on mars unexplained by known atmospheric chemistry and physics. *Nature*, 460:720–723, 8 2009. ISSN 1476-4687. doi: 10.1038/nature08228.

C. B. Leovy and R. W. Zurek. Thermal tides and martian dust storms: Direct evidence for coupling. *Journal of Geophysical Research: Solid Earth*, 84:2956–2968, 6 1979. ISSN 2156-2202. doi: 10.1029/JB084IB06P02956.

J. S. Levy, D. R. Marchant, and J. W. Head. Thermal contraction crack polygons on Mars: A synthesis from HiRISE, Phoenix, and terrestrial analog studies. *Icarus*, 206(1):229–252, 2010. ISSN 00191035. doi: 10.1016/j.icarus.2009.09.005.

J. S. Lewis. Satellites of the outer planets: Their physical and chemical nature. *Icarus*, 15:174–185, 10 1971. ISSN 0019-1035. doi: 10.1016/0019-1035(71)90072-8.

S. R. Lewis, M. Collins, and F. Forget. Mars climate database v3.0 detailed design document. Technical report, 4 2001.

S. Liebner, K. Rublack, T. Stuehrmann, and D. Wagner. Diversity of aerobic methanotrophic bacteria in a permafrost active layer soil of the Lena Delta, Siberia. *Microbial Ecology*, 57(1): 25–35, jan 2009. ISSN 00953628. doi: 10.1007/S00248-008-9411-X.

G. F. Lindal, G. E. Wood, H. B. Hotz, D. N. Sweetnam, V. R. Eshleman, and G. L. Tyler. The atmosphere of titan: An analysis of the voyager 1 radio occultation measurements. *Icarus*, 53: 348–363, 2 1983. ISSN 0019-1035. doi: 10.1016/0019-1035(83)90155-0.

D. Y. Lo, S. K. Atreya, M. H. Wong, M. G. Trainer, H. B. Franz, T. H. McConnochie, D. Viúdez-Moreiras, P. R. Mahaffy, and C. A. Malespin. Evaluating atmospheric and surface drivers for o2 variations at gale crater as observed by msl sam. *The Planetary Science Journal*, 5:65, 3 2024. ISSN 2632-3338. doi: 10.3847/PSJ/AD251B.

P. Lognonné, W. B. Banerdt, D. Giardini, W. T. Pike, U. Christensen, P. Laudet, S. de Raucourt, P. Zweifel, S. Calcutt, M. Bierwirth, K. J. Hurst, F. Ijpelaan, J. W. Umland, R. Llorca-Cejudo, S. A. Larson, R. F. Garcia, S. Kedar, B. Knapmeyer-Endrun, D. Mimoun, A. Mocquet, M. P. Panning, R. C. Weber, A. Sylvestre-Baron, G. Pont, N. Verdier, L. Kerjean, L. J. Facto, V. Gharakanian, J. E. Feldman, T. L. Hoffman, D. B. Klein, K. Klein, N. P. Onufer, J. Paredes-Garcia, M. P. Petkov, J. R. Willis, S. E. Smrekar, M. Drilleau, T. Gabsi, T. Nebut, O. Robert, S. Tillier, C. Moreau, M. Parise, G. Aveni, S. B. Charef, Y. Bennour, T. Camus, P. A. Dandonneau, C. Desfoux, B. Lecomte, O. Pot, P. Revuz, D. Mance, J. tenPierick, N. E. Bowles,

C. Charalambous, A. K. Delahunty, J. Hurley, R. Irshad, H. Liu, A. G. Mukherjee, I. M. Standley, A. E. Stott, J. Temple, T. Warren, M. Eberhardt, A. Kramer, W. Kühne, E. P. Miettinen, M. Monecke, C. Aicardi, M. André, J. Baroukh, A. Borrien, A. Bouisset, P. Boutte, K. Brethomé, C. Brysbaert, T. Carlier, M. Deleuze, J. M. Desmarres, D. Dilhan, C. Doucet, D. Faye, N. Faye-Refalo, R. Gonzalez, C. Imbert, C. Larigauderie, E. Locatelli, L. Luno, J. R. Meyer, F. Mialhe, J. M. Mouret, M. Nonon, Y. Pahn, A. Paillet, P. Pasquier, G. Perez, R. Perez, L. Perrin, B. Pouilloux, A. Rosak, I. S. de Larclause, J. Sicre, M. Sodki, N. Toulemont, B. Vella, C. Yana, F. Alibay, O. M. Avalos, M. A. Balzer, P. Bhandari, E. Blanco, B. D. Bone, J. C. Bousman, P. Bruneau, F. J. Calef, R. J. Calvet, S. A. D'Agostino, G. de los Santos, R. G. Deen, R. W. Denise, J. Ervin, N. W. Ferraro, H. E. Gengl, F. Grinblat, D. Hernandez, M. Hetzel, M. E. Johnson, L. Khachikyan, J. Y. Lin, S. M. Madzunkov, S. L. Marshall, I. G. Mikellides, E. A. Miller, W. Raff, J. E. Singer, C. M. Sunday, J. F. Villalvazo, M. C. Wallace, D. Banfield, J. A. Rodriguez-Manfredi, C. T. Russell, A. Trebi-Ollennu, J. N. Maki, E. Beucler, M. Böse, C. Bonjour, J. L. Berenguer, S. Ceylan, J. Clinton, V. Conejero, I. Daubar, V. Dehant, P. Delage, F. Euchner, I. Estève, L. Fayon, L. Ferraioli, C. L. Johnson, J. Gagnepain-Beyneix, M. Golombek, A. Khan, T. Kawamura, B. Kenda, P. Labrot, N. Murdoch, C. Pardo, C. Perrin, L. Pou, A. Sauron, D. Savoie, S. Stähler, E. Stutzmann, N. A. Teanby, J. Tromp, M. van Driel, M. Wieczorek, R. Widmer-Schnidrig, and J. Wookey. Seis: Insight's seismic experiment for internal structure of mars. *Space Science Reviews*, 215:1–170, 1 2019. ISSN 1572-9672. doi: 10.1007/S11214-018-0574-6.

P. Lognonné, W. B. Banerdt, W. T. Pike, D. Giardini, U. Christensen, R. F. Garcia, T. Kawamura, S. Kedar, B. Knapmeyer-Endrun, L. Margerin, F. Nimmo, M. Panning, B. Tauzin, J. R. Scholz, D. Antonangeli, S. Barkaoui, E. Beucler, F. Bissig, N. Brinkman, M. Calvet, S. Ceylan, C. Charalambous, P. Davis, M. van Driel, M. Drilleau, L. Fayon, R. Joshi, B. Kenda, A. Khan, M. Knapmeyer, V. Lekic, J. McClean, D. Mimoun, N. Murdoch, L. Pan, C. Perrin, B. Pinot, L. Pou, S. Menina, S. Rodriguez, C. Schmelzbach, N. Schmerr, D. Sollberger, A. Spiga, S. Stähler, A. Stott, E. Stutzmann, S. Tharimena, R. Widmer-Schnidrig, F. Andersson, V. Ansan, C. Beghein, M. Böse, E. Bozdag, J. Clinton, I. Daubar, P. Delage, N. Fuji, M. Golombek, M. Grott, A. Horleston, K. Hurst, J. Irving, A. Jacob, J. Knollenberg, S. Krasner, C. Krause, R. Lorenz, C. Michaut, R. Myhill, T. Nissen-Meyer, J. ten Pierick, A. C. Plesa, C. Quantin-Nataf, J. Robertsson, L. Rochas, M. Schimmel, S. Smrekar, T. Spohn, N. Teanby, J. Tromp, J. Vallade, N. Verdier, C. Vrettos, R. Weber, D. Banfield, E. Barrett, M. Bierwirth, S. Calcutt, N. Compaire, C. L. Johnson, D. Mance, F. Euchner, L. Kerjean, G. Mainsant, A. Mocquet, J. A. R. Manfredi, G. Pont, P. Laudet, T. Nebut, S. de Raucourt, O. Robert, C. T. Russell, A. Sylvestre-Baron, S. Tillier, T. Warren, M. Wieczorek, C. Yana, and P. Zweifel. Constraints on the shallow elastic and anelastic structure of mars from insight seismic data. *Nature Geoscience 2020 13:3*, 13:213–220, 2 2020. ISSN 1752-0908. doi: 10.1038/s41561-020-0536-y.

R. D. Lorenz. Cratering on titan: A pre-cassini perspective. 45:1009–1019, 1997. ISSN 00320633.

R. D. Lorenz. Dust devil winds: Assessing dry convective vortex intensity limits at planetary surfaces. *Icarus*, 354:114062, 2021. doi: 10.1016/j.icarus.2020.114062.

R. D. Lorenz, E. P. Turtle, J. W. Barnes, M. G. Trainer, D. S. Adams, K. E. Hibbard, C. Z. Sheldon, K. Zacny, P. N. Peplowski, D. J. Lawrence, M. A. Ravine, T. G. Mcgee, K. S. Sotzen, S. M. Mackenzie, J. W. Langelaan, S. Schmitz, L. S. Wolfarth, and P. D. Bedini. Dragonfly: A rotorcraft lander concept for scientific exploration at titan. *Johns Hopkins APL Technical Digest*, 34, 2018.

R. D. Lorenz, M. Panning, S. C. Stähler, H. Shiraishi, R. Yamada, and E. P. Turtle. Titan seismology with dragonfly : Probing the internal structure of the most accessible ocean world. In *LPI Contrib. No. 2132*, 2019.

R. D. Lorenz, H. Shiraishi, M. Panning, and K. Sotzen. Wind and surface roughness considerations for seismic instrumentation on a relocatable lander for titan. *Planetary and Space Science*, 206: 105320, 2021. ISSN 00320633. doi: 10.1016/j.pss.2021.105320.

Y. Luo, M. A. Mischna, J. C. Lin, B. Fasoli, X. Cai, and Y. L. Yung. Mars methane sources in northwestern gale crater inferred from back trajectory modeling. *Earth and Space Science*, 8: e2021EA001915, 11 2021. ISSN 23335084. doi: 10.1029/2021EA001915.

J. E. Lyne, M. Tauber, and R. Fought. An analytical model of the atmospheric entry of large meteors and its application to the tunguska event. *Journal of Geophysical Research: Planets*, 101:23207–23212, 10 1996. ISSN 2156-2202. doi: 10.1029/96JE02047.

A. Määttänen, C. Listowski, F. Montmessin, L. Maltagliati, A. Reberac, L. Joly, and J. L. Bertaux. A complete climatology of the aerosol vertical distribution on mars from mex/spicam uv solar occultations. *Icarus*, 223:892–941, 4 2013. ISSN 0019-1035. doi: 10.1016/J.ICARUS.2012.12.001.

J. R. Mackay. Ice-Wedge Cracks, Garry Island, Northwest Territories. *Canadian Journal of Earth Sciences*, 11(10), oct 1974. ISSN 0008-4077. doi: 10.1139/E74-133.

J. B. Madeleine, F. Forget, E. Millour, L. Montabone, and M. J. Wolff. Revisiting the radiative impact of dust on mars using the lmd global climate model. *Journal of Geophysical Research: Planets*, 116:11010, 11 2011. ISSN 01480227. doi: 10.1029/2011JE003855.

C. Martín-Rubio, A. Vicente-Retortillo, G. Martínez-Esteve, F. Gómez, and J. A. Rodríguez-Manfredi. Global characterization of the early-season dust storm of mars year 36. *Icarus*, 426: 116369, 1 2025. ISSN 0019-1035. doi: 10.1016/J.ICARUS.2024.116369.

C. Martineau, Y. Pan, L. Bodrossy, E. Yergeau, L. G. Whyte, and C. W. Greer. Atmospheric methane oxidizers are present and active in Canadian high Arctic soils. *FEMS Microbiology Ecology*, 89(2):257–269, aug 2014. ISSN 0168-6496. doi: 10.1111/1574-6941.12287.

G. M. Martínez, C. N. Newman, A. D. Vicente-Retortillo, E. Fischer, N. O. Renno, M. I. Richardson, A. G. Fairén, M. Genzer, S. D. Guzewich, R. M. Haberle, A. M. Harri, O. Kemppinen, M. T. Lemmon, M. D. Smith, M. de la Torre-Juárez, and A. R. Vasavada. The modern near-surface martian climate: A review of in-situ meteorological data from viking to curiosity. *Space Science Reviews*, 212:295–338, 4 2017. ISSN 1572-9672. doi: 10.1007/S11214-017-0360-X.

L. Martire, R. Martin, and Q. Brissaud. Specfem2d-dg, an open-source software modelling mechanical waves in coupled solid–fluid systems: the linearized navier–stokes approach. *Geophysical Journal International*, 228:664–697, 9 2021. ISSN 0956-540X. doi: 10.1093/GJI/GGAB308.

A. G. Marusiak, S. Vance, M. P. Panning, A. S. Bryant, M. A. Hesse, E. Carnahan, and B. Journaux. The effects of methane clathrates on the thermal and seismic profile of titan's icy lithosphere. *The Planetary Science Journal*, 3:167, 7 2022. ISSN 2632-3338. doi: 10.3847/PSJ/AC787E.

C. K. McCalley, B. J. Woodcroft, S. B. Hodgkins, R. A. Wehr, E. H. Kim, R. Mondav, P. M. Crill, J. P. Chanton, V. I. Rich, G. W. Tyson, and S. R. Saleska. Methane dynamics regulated by microbial community response to permafrost thaw. *Nature*, 514(7523):478–481, oct 2014. ISSN 1476-4687. doi: 10.1038/nature13798.

L. McFadden, P. Brown, D. Vida, and P. Spurn y. Fireball characteristics derivable from acoustic data. *Journal of Atmospheric and Solar-Terrestrial Physics*, 216:105587, 2021. ISSN 13646826. doi: 10.1016/j.jastp.2021.105587.

C. P. McKay, R. C. Quinn, and C. R. Stoker. The viking biology experiments on mars revisited. *Icarus*, 431:116466, 5 2025. ISSN 0019-1035. doi: 10.1016/J.ICARUS.2025.116466.

M. T. Mellon, R. E. Arvidson, J. J. Marlow, R. J. Phillips, and E. Asphaug. Periglacial landforms at the Phoenix landing site and the northern plains of Mars. *Journal of Geophysical Research: Planets*, 113(E3):0–23, mar 2008. ISSN 2156-2202. doi: 10.1029/2007JE003039.

M. T. Mellon, M. C. Malin, R. E. Arvidson, M. L. Searls, H. G. Sizemore, T. L. Heet, M. T. Lemmon, H. U. Keller, and J. Marshall. The periglacial landscape at the Phoenix landing site. *Journal of Geophysical Research: Planets*, 114(E1):0–06, jan 2009. ISSN 2156-2202. doi: 10.1029/2009JE003418.

L. Metcalfe, M. Aberasturi, E. Alonso, R. Álvarez, M. Ashman, I. Barbarisi, J. Brumfitt, A. Cardesín, D. Coia, M. Costa, R. Fernández, D. Frew, J. Gallegos, J. J. G. Beteta, B. Geiger, D. Heather, T. Lim, P. Martin, C. M. noz Crego, M. M. noz Fernandez, A. Villacorta, and H. Svedhem. Exomars trace gas orbiter (tgo) science ground segment (sgs). *Space Science Reviews*, 214:78–, 6 2018. ISSN 1572-9672. doi: 10.1007/S11214-018-0511-8.

E. Millour. personal communication.

M. A. Mischna, M. Allen, M. I. Richardson, C. E. Newman, and A. D. Toigo. Atmospheric modeling of mars methane surface releases. *Planetary and Space Science*, 59:227–237, 2 2011. ISSN 0032-0633. doi: 10.1016/J.PSS.2010.07.005.

K. Mitra, E. L. Moreland, and J. G. Catalano. Capacity of chlorate to oxidize ferrous iron: Implications for iron oxide formation on mars. *Minerals*, 10:729, 8 2020. ISSN 2075-163X. doi: 10.3390/MIN10090729.

F. Montmessin, O. I. Korablev, A. Trokhimovskiy, F. Lefèvre, A. A. Fedorova, L. Baggio, A. Irbah, G. Lacombe, K. S. Olsen, A. S. Braude, D. A. Belyaev, J. Alday, F. Forget, F. Daerden, J. Pla-Garcia, S. Rafkin, C. F. Wilson, A. Patrakeev, A. Shakun, and J. L. Bertaux. A stringent upper limit of 20 pptv for methane on mars and constraints on its dispersion outside gale crater. *Astronomy & Astrophysics*, 650:A140, 6 2021. ISSN 0004-6361. doi: 10.1051/0004-6361/202140389.

C. A. Moore, J. E. Moores, M. T. Lemmon, S. C. Rafkin, R. Francis, J. Pla-García, R. M. Haberle, M. P. Zorzano, F. J. Martín-Torres, and J. R. Burton. A full martian year of line-of-sight extinction within gale crater, mars as acquired by the msl navcam through sol 900. *Icarus*, 264: 102–108, 1 2016. ISSN 0019-1035. doi: 10.1016/J.ICARUS.2015.09.001.

J. E. Moores and A. C. Schuerger. Uv degradation of accreted organics on mars: Idp longevity, surface reservoir of organics, and relevance to the detection of methane in the atmosphere. *Journal of Geophysical Research: Planets*, 117, 8 2012. ISSN 01480227. doi: 10.1029/2012JE004060.

J. E. Moores, M. T. Lemmon, H. Kahanpää, S. C. Rafkin, R. Francis, J. Pla-Garcia, K. Bean, R. Haberle, C. Newman, M. Mischna, A. R. Vasavada, M. de la Torre Juárez, N. Rennö, J. Bell, F. Calef, B. Cantor, T. H. Mcconnochie, A. M. Harri, M. Genzer, M. H. Wong, M. D. Smith, F. J. Martín-Torres, M. P. Zorzano, O. Kemppinen, and E. McCullough. Observational evidence of a suppressed planetary boundary layer in northern gale crater, mars as seen by the navcam

instrument onboard the mars science laboratory rover. *Icarus*, 249:129–142, 3 2015. ISSN 0019-1035. doi: 10.1016/J.ICARUS.2014.09.020.

J. E. Moores, C. L. Smith, and A. C. Schuerger. Uv production of methane from surface and sedimenting idps on mars in light of rems data and with insights for tgo. *Planetary and Space Science*, 147:48–60, 11 2017. ISSN 0032-0633. doi: 10.1016/J.PSS.2017.09.008.

J. E. Moores, R. V. Gough, G. M. Martinez, P. Y. Meslin, C. L. Smith, S. K. Atreya, P. R. Mahaffy, C. E. Newman, and C. R. Webster. Methane seasonal cycle at gale crater on mars consistent with regolith adsorption and diffusion. *Nature Geoscience*, 12:321–325, 3 2019a. ISSN 1752-0908. doi: 10.1038/s41561-019-0313-y.

J. E. Moores, P. L. King, C. L. Smith, G. M. Martinez, C. E. Newman, S. D. Guzewich, P. Y. Meslin, C. R. Webster, P. R. Mahaffy, S. K. Atreya, and A. C. Schuerger. The methane diurnal variation and microseepage flux at gale crater, mars as constrained by the exomars trace gas orbiter and curiosity observations. *Geophysical Research Letters*, 46:9430–9438, 8 2019b. ISSN 1944-8007. doi: 10.1029/2019GL083800.

J. E. Moores, H. M. Sapers, and A. C. Schuerger. Exogenous carbon is unlikely to be the source of methane microseepage emissions on mars. *Research Notes of the AAS*, 8:120, 5 2024. ISSN 2515-5172. doi: 10.3847/2515-5172/AD454D.

V. I. Moroz. Chemical composition of the atmosphere of mars. *Advances in Space Research*, 22: 449–457, 1 1998. ISSN 0273-1177. doi: 10.1016/S0273-1177(98)00085-4.

S. L. Mouélic, T. Cornet, S. Rodriguez, C. Sotin, B. Seignovert, J. W. Barnes, R. H. Brown, K. H. Baines, B. J. Buratti, R. N. Clark, P. D. Nicholson, J. Lasue, V. Pasek, and J. M. Soderblom. The cassini vims archive of titan: From browse products to global infrared color maps. *Icarus*, 319:121–132, 2 2019. ISSN 0019-1035. doi: 10.1016/J.ICARUS.2018.09.017.

M. J. Mumma, G. L. Villanueva, R. E. Novak, T. Hewagama, B. P. Bonev, M. A. DiSanti, A. M. Mandell, and M. D. Smith. Strong release of methane on mars in northern summer 2003. *Science*, 323:1041–1045, 2 2009. ISSN 00368075.

I. naki Ordonez-Etxeberria, R. Hueso, and A. Sánchez-Lavega. A systematic search of sudden pressure drops on gale crater during two martian years derived from msl/rems data. *Icarus*, 299: 308–330, 1 2018. ISSN 0019-1035. doi: 10.1016/J.ICARUS.2017.07.032.

I. naki Ordonez-Etxeberria, R. Hueso, A. Sánchez-Lavega, E. Millour, and F. Forget. Meteorological pressure at gale crater from a comparison of rems/msl data and mcd modelling: Effect of dust storms. *Icarus*, 317:591–609, 1 2019. ISSN 0019-1035. doi: 10.1016/J.ICARUS.2018.09.003.

L. Neary. personal communication.

L. Neary and F. Daerden. The gem-mars general circulation model for mars: Description and evaluation. *Icarus*, 300:458–476, 1 2018. ISSN 0019-1035. doi: 10.1016/J.ICARUS.2017.09.028.

C. Neish, M. J. Malaska, C. Sotin, R. M. Lopes, C. A. Nixon, A. Affholder, A. Chatain, C. Cockell, K. K. Farnsworth, P. M. Higgins, K. E. Miller, and K. M. Soderlund. Organic input to titan's subsurface ocean through impact cratering. *Astrobiology*, 24:177–189, 2 2024. ISSN 15311074. doi: 10.1089/AST.2023.0055.

C. D. Neish and R. D. Lorenz. Titan's global crater population: A new assessment. *Planetary and Space Science*, 60:26–33, 1 2012. ISSN 0032-0633. doi: 10.1016/J.PSS.2011.02.016.

D. Nesvorný, L. Dones, M. D. Prá, M. Womack, and K. J. Zahnle. Impact rates in the outer solar system. *The Planetary Science Journal*, 4:139, 8 2023. ISSN 2632-3338. doi: 10.3847/PSJ/ACE8FF.

C. E. Newman, H. Kahanpää, M. I. Richardson, G. M. Martínez, A. Vicente-Retortillo, and M. T. Lemmon. Marswrf convective vortex and dust devil predictions for gale crater over 3 mars years and comparison with msl-rems observations. *Journal of Geophysical Research: Planets*, 124: 3442–3468, 12 2019. ISSN 21699100.

H. B. Niemann, S. K. Atreya, J. E. Demick, D. Gautier, J. A. Haberman, D. N. Harpold, W. T. Kasprzak, J. I. Lunine, T. C. Owen, and F. Raulin. Composition of titan's lower atmosphere and simple surface volatiles as measured by the cassini-huygens probe gas chromatograph mass spectrometer experiment. *Journal of Geophysical Research: Planets*, 115, 12 2010. ISSN 01480227. doi: 10.1029/2010JE003659.

D. Z. Oehler and G. Etiope. Methane seepage on mars: where to look and why. *Astrobiology*, 17 (12), dec 2017. ISSN 15311074. doi: 10.1089/AST.2017.1657.

J. P. Ortiz, H. Rajaram, P. H. Stauffer, K. W. Lewis, R. C. Wiens, and D. R. Harp. Sub-diurnal methane variations on mars driven by barometric pumping and planetary boundary layer evolution. *Journal of Geophysical Research: Planets*, 129:e2023JE008043, 1 2024. ISSN 21699100. doi: 10.1029/2023JE008043.

G. R. Osinski, R. Léveillé, A. Berinstain, M. Lebeuf, and M. Bamsey. Terrestrial analogues to mars and the moon: Canada's role. *Geoscience Canada*, 33, 2006. ISSN 1911-4850.

T. Owen, K. Biemann, D. R. Rushneck, J. E. Biller, D. W. Howarth, and A. L. Lafleur. The composition of the atmosphere at the surface of mars. *Journal of Geophysical Research*, 82: 4635–4639, 9 1977. ISSN 2156-2202. doi: 10.1029/JS082I028P04635.

C. Oze and M. Sharma. Have olivine, will gas: Serpentinization and the abiogenic production of methane on Mars. *Geophysical Research Letters*, 32(10):1–4, may 2005. ISSN 1944-8007. doi: 10.1029/2005GL022691.

M. P. Panning, R. Lorenz, H. Shiraishi, R. Yamada, S. Stähler, E. P. Turtle, T. Hurford, N. Murdoch, and S. Vance. Seismology on titan: A seismic signal and noise budget in preparation for dragonfly. *SEG Technical Program Expanded Abstracts*, 2020-October:3539–3542, 2020. ISSN 19494645. doi: 10.1190/SEGAM2020-3426937.1.

Q. R. Passey and H. J. Melosh. Effects of atmospheric breakup on crater field formation. *Icarus*, 42:211–233, 1980. doi: 10.1016/0019-1035(80)90072-X.

M. D. Paton, J. Leino, A. M. Harri, and H. Savijärvi. Martian boundary layer wind profiles during the landings of viking and insight. *Icarus*, 367:114581, 10 2021. ISSN 0019-1035. doi: 10.1016/J.ICARUS.2021.114581.

M. D. Paton, H. Savijärvi, P. Grindrod, A. M. Harri, J. Leino, and D. Ellison. Martian wind and surface conditions during the night-time descent and landing of pathfinder. *Icarus*, 390:115318, 1 2023. ISSN 0019-1035. doi: 10.1016/J.ICARUS.2022.115318.

M. D. Paton, H. Savijärvi, A. M. Harri, J. Leino, T. Bertrand, D. Viúdez-Moreiras, R. D. Lorenz, and C. Newman. Inferred wind speed and direction during the descent and landing of perseverance on mars. *Icarus*, 415:116045, 6 2024. ISSN 0019-1035. doi: 10.1016/J.ICARUS.2024.116045.

A. Petculescu and R. M. Lueptow. Atmospheric acoustics of titan, mars, venus, and earth. *Icarus*, 186:413–419, 2 2007. ISSN 0019-1035. doi: 10.1016/J.ICARUS.2006.09.014.

A. Petrosyan, B. Galperin, S. E. Larsen, S. R. Lewis, A. Määttänen, P. L. Read, N. Renno, L. P. Rogberg, H. Savijrvi, T. Siili, A. Spiga, A. Toigo, and L. Vázquez. The martian atmospheric boundary layer. *Reviews of Geophysics*, 49:3005, 9 2011. ISSN 1944-9208. doi: 10.1029/2010RG000351.

C. Pilger, L. Ceranna, J. O. Ross, A. L. Pichon, P. Mialle, and M. A. Garcés. Ctbt infrasound network performance to detect the 2013 russian fireball event. *Geophysical Research Letters*, 42: 2523–2531, 4 2015. ISSN 19448007. doi: 10.1002/2015GL063482.

J. Pla-Garcia, S. C. Rafkin, Ö. Karatekin, and E. Gloesener. Comparing MSL Curiosity Rover TLS-SAM Methane Measurements With Mars Regional Atmospheric Modeling System Atmospheric Transport Experiments. *Journal of Geophysical Research: Planets*, 124(8):2141–2167, aug 2019. ISSN 2169-9100. doi: 10.1029/2018JE005824.

W. Pollard, T. Haltigin, L. Whyte, T. Niederberger, D. Andersen, C. Omelon, J. Nadeau, M. Ecclestone, and M. Lebeuf. Overview of analogue science activities at the McGill Arctic Research Station, Axel Heiberg Island, Canadian High Arctic. *Planetary and Space Science*, 57(5-6): 646–659, may 2009. ISSN 0032-0633. doi: 10.1016/J.PSS.2009.01.008.

O. Popova. Meteoroid ablation models. *Earth, Moon and Planets*, 95:303–319, 12 2004. ISSN 01679295. doi: 10.1007/S11038-005-9026-X.

M. C. Price, M. J. Cole, K. H. Harriss, L. S. Alesbrook, M. J. Burchell, and P. J. Wozniakiewicz. A new compact, self-compressing, vertical one and two-stage gas gun at the university of kent. *International Journal of Impact Engineering*, 184:104828, 2 2024. ISSN 0734-743X. doi: 10.1016/J.IJIMPENG.2023.104828.

N. E. Putzig, M. T. Mellon, K. A. Kretke, and R. E. Arvidson. Global thermal inertia and surface properties of mars from the mgs mapping mission. *Icarus*, 173:325–341, 2 2005. ISSN 0019-1035. doi: 10.1016/J.ICARUS.2004.08.017.

S. C. Rafkin, J. Pla-Garcia, M. Kahre, J. Gomez-Elvira, V. E. Hamilton, M. Marín, S. Navarro, J. Torres, and A. Vasavada. The meteorology of gale crater as determined from rover environmental monitoring station observations and numerical modeling. part ii: Interpretation. *Icarus*, 280:114–138, 12 2016. ISSN 0019-1035. doi: 10.1016/J.ICARUS.2016.01.031.

S. C. R. Rafkin, R. D. Lorenz, E. P. Turtle, J. W. Barnes, M. G. Trainer, A. L. Gall, J. M. Lora, C. P. McKay, C. E. Newman, M. P. Panning, T. Tokano, C. Wilson, and D. S. Team. Exploring titan's meteorology with dragonfly. *EPSC Abstracts*, 12, 2018.

F. Raulin, P. Bruston, P. Coll, D. Coscia, M. C. Gazeau, L. Guez, and E. de Vanssay. Exobiology on titan - a reference laboratory for studying prebiotic chemistry on a planetary scale. *Journal of Biological Physics*, 20:39–53, 3 1995. ISSN 00920606. doi: 10.1007/BF00700419.

P. J. Register, D. L. Mathias, and L. F. Wheeler. Asteroid fragmentation approaches for modeling atmospheric energy deposition. *Icarus*, 284:157–166, 2017. ISSN 10902643. doi: 10.1016/j.icarus.2016.11.020.

D. O. ReVelle. on meteor-generated infrasound. *Journal of Geophysical Research*, 81:1217–1230, 3 1976. ISSN 2156-2202. doi: 10.1029/JA081I007P01217.

D. O. Revelle. Recent advances in bolide entry modeling: A bolide potpourri. *Earth, Moon and Planets*, 95:441–476, 12 2005. ISSN 01679295. doi: 10.1007/1-4020-5075-5_43.

D. O. ReVelle. Neo fireball diversity: energetics-based entry modeling and analysis techniques. *Proceedings of the International Astronomical Union*, 2:95–106, 8 2007. ISSN 1743-9221. doi: 10.1017/S1743921307003122.

D. O. ReVelle and W. N. Edwards. Stardust—an artificial, low-velocity "meteor" fall and recovery: 15 january 2006. *Meteoritics & Planetary Science*, 42:271–299, 2 2007. ISSN 1945-5100. doi: 10.1111/J.1945-5100.2007.TB00232.X.

D. O. ReVelle, W. Edwards, and T. D. Sandoval. Genesis—an artificial, low velocity "meteor" fall and recovery: September 8, 2004. *Meteoritics & Planetary Science*, 40:895–916, 6 2005. ISSN 1945-5100. doi: 10.1111/J.1945-5100.2005.TB00162.X.

J. E. Richardson, H. J. Melosh, C. M. Lisse, and B. Carcich. A ballistics analysis of the deep impact ejecta plume: Determining comet tempel 1's gravity, mass, and density. *Icarus*, 191:176–209, 1 2007. ISSN 0019-1035. doi: 10.1016/J.ICARUS.2007.08.033.

D. K. Robertson and D. L. Mathias. Hydrocode simulations of asteroid airbursts and constraints for tunguska. *Icarus*, 327:36–47, 7 2019. ISSN 0019-1035. doi: 10.1016/J.ICARUS.2018.10.017.

M. F. Romig. Physics of meteor entry. *AIAA*, 3, 1965. doi: 10.2514/3.2877.

A. Sakurai. Blast wave theory. Technical report, 1964.

R. E. Samuelson, R. A. Hanel, V. G. Kunde, and W. C. Maguire. Mean molecular weight and hydrogen abundance of titan's atmosphere. *Nature*, 292:688–693, 1981. ISSN 1476-4687. doi: 10.1038/292688a0.

C. J. Savage, J. Radebaugh, E. H. Christiansen, and R. D. Lorenz. Implications of dune pattern analysis for titan's surface history. *Icarus*, 230:180–190, 2 2014. ISSN 0019-1035. doi: 10.1016/J.ICARUS.2013.08.009.

H. Savijarvi. On surface temperature and moisture prediction in atmospheric models. *Contributions to Atmospheric Physics*, 65:281–292, 1992. ISSN 00058173.

H. Savijarvi. A model study of the atmospheric boundary layer in the mars pathfinder lander conditions. *Quarterly Journal of the Royal Meteorological Society*, 125:483–493, 1 1999. ISSN 0035-9009. doi: 10.1002/qj.49712555406.

H. I. Savijärvi, G. M. Martinez, E. Fischer, N. O. Renno, L. K. Tamppari, A. Zent, and A. M. Harri. Humidity observations and column simulations for a warm period at the mars phoenix lander site: Constraining the adsorptive properties of regolith. *Icarus*, 343:113688, 2020. ISSN 10902643. doi: 10.1016/j.icarus.2020.113688.

H. Savijäärvi. Mechanisms of the diurnal cycle in the atmospheric boundary layer of mars. *Quarterly Journal of the Royal Meteorological Society*, 138:552–560, 1 2012. ISSN 00359009.

P. J. Schinder, F. M. Flasar, E. A. Marouf, R. G. French, C. A. McGhee, A. J. Kliore, N. J. Rappaport, E. Barbinis, D. Fleischman, and A. Anabtawi. The structure of titan's atmosphere from cassini radio occultations. *Icarus*, 215:460–474, 10 2011. ISSN 0019-1035. doi: 10.1016/J.ICARUS.2011.07.030.

D. Schwarz, G. S. Collins, E. L. Newland, and M. Coleman. Fragment-cloud model, 2022.

J. Shah, C. D. Neish, and S. Trozzo. An analogue study of impact craters on titan: Implications for titan's surface age. *Icarus*, 433:116536, 6 2025. ISSN 0019-1035. doi: 10.1016/J.ICARUS.2025.116536.

E. A. Silber, M. Boslough, W. K. Hocking, M. Gritsevich, and R. W. Whitaker. Physics of meteor generated shock waves in the earth's atmosphere – a review. *Advances in Space Research*, 62:489–532, 8 2018. ISSN 0273-1177. doi: 10.1016/J.ASR.2018.05.010.

E. A. Silber, D. C. Bowman, C. G. Carr, D. P. Eisenberg, B. R. Elbing, B. Fernando, M. A. Garcés, R. Haaser, S. Krishnamoorthy, C. A. Langston, Y. Nishikawa, J. Webster, J. F. Anderson, S. Arrowsmith, S. Bazargan, L. Beardslee, B. Beck, J. W. Bishop, P. Blom, G. Bracht, D. L. Chichester, A. Christe, J. Clarke, K. Cummins, J. Cutts, L. Danielson, C. Donahue, K. Eack, M. Fleigle, D. Fox, A. Goel, D. Green, Y. Hasumi, C. Hayward, D. Hicks, J. Hix, S. Horton, E. Hough, D. P. Huber, M. A. Hunt, J. Inman, S. M. A. Islam, J. Izraelevitz, J. D. Jacob, J. Johnson, R. J. Kc, A. Komjathy, E. Lam, J. Lapierre, K. Lewis, R. D. Lewis, P. Liu, L. Martire, M. Mccleary, E. A. Mcghee, I. Mitra, A. Nag, L. Ocampo, G. 16, K. Pearson, M. Plaisir, S. K. Popenhagen, H. Rassoul, M. R. Giannone, M. Samnani, N. Schmerr, K. Spillman, G. Srinivas, S. K. Takazawa, A. Tempert, R. Turley, C. V. Beek, L. Viens, O. A. Walsh, N. Weinstein, R. White, B. Williams, T. C. Wilson, S. Wyckoff, M.-Y. Yamamoto, Z. Yap, T. Yoshiyama, and C. Zeiler. Geophysical observations of the 2023 september 24 osiris-rex sample return capsule reentry. *The Planetary Science Journal*, 5:213, 9 2024. ISSN 2632-3338. doi: 10.3847/PSJ/AD5B5E.

C. L. Smith, J. E. Moores, M. Lemmon, S. D. Guzewich, C. A. Moore, D. Ellison, and A. S. Khayat. Visibility and line-of-sight extinction estimates in gale crater during the 2018/my34 global dust storm. *Geophysical Research Letters*, 46:9414–9421, 8 2019. ISSN 1944-8007. doi: 10.1029/2019GL083788.

C. L. Smith, M. Lemmon, J. E. Moores, S. D. Guzewich, T. H. McConnochie, C. E. Newman, A. S. Khayat, M. Battalio, C. A. Moore, and D. Ellison. The line of sight extinction record at gale crater as observed by msl's mastcam and navcam through ∼2500 sols. *Journal of Geophysical Research: Planets*, 125:e2020JE006465, 11 2020. ISSN 2169-9100. doi: 10.1029/2020JE006465.

M. D. Smith. Spacecraft observations of the martian atmosphere. *Annual Review of Earth and Planetary Sciences*, 36:191–219, 5 2008. ISSN 00846597. doi: 10.1146/ANNUREV.EARTH.36.031207.124334.

M. D. Smith, M. J. Wolff, N. Spanovich, A. Ghosh, D. Banfield, P. R. Christensen, G. A. Landis, and S. W. Squyres. One martian year of atmospheric observations using mer mini-tes. *Journal of Geophysical Research: Planets*, 111, 12 2006. ISSN 01480227.

J. C. Solá. Observations des satellites principaux de jupiter et de titan. *Astronomische Nachrichten*, 179:289–290, 1 1908. ISSN 15213994. doi: 10.1002/ASNA.19081791807.

C. Sotin, K. Kalousovaacute, and G. Tobie. Titan's interior structure and dynamics after the cassini-huygens mission. *Annual Review of Earth and Planetary Sciences*, 49:579–607, 5 2021. ISSN 00846597. doi: 10.1146/ANNUREV-EARTH-072920-052847.

B. Stackhouse, M. C. Lau, T. Vishnivetskaya, N. Burton, R. Wang, A. Southworth, L. Whyte, and T. C. Onstott. Atmospheric CH4 oxidation by Arctic permafrost and mineral cryosols as a function of water saturation and temperature. *Geobiology*, 15(1):94–111, jan 2017. ISSN 1472-4669. doi: 10.1111/GBI.12193.

C. Stroud, P. Makar, T. Karl, A. Guenther, C. Geron, A. Turnipseed, E. Nemitz, B. Baker, M. Potosnak, and J. D. Fuentes. Role of canopy-scale photochemistry in modifying biogenic-atmosphere exchange of reactive terpene species: Results from the celtic field study. *Journal of Geophysical Research D: Atmospheres*, 110:149–162, 2005. ISSN 01480227. doi: 10.1029/2005JD005775.

M. E. Summers, B. J. Lieb, E. Chapman, and Y. L. Yung. Atmospheric biomarkers of subsurface life on mars. *Geophysical Research Letters*, 29:24–1, 12 2002. ISSN 19448007. doi: 10.1029/2002GL015377.

B. Sutter, R. C. Quinn, P. D. Archer, D. P. Glavin, T. D. Glotch, S. P. Kounaves, M. M. Osterloo, E. B. Rampe, and D. W. Ming. Measurements of oxychlorine species on mars. *International Journal of Astrobiology*, 16:203–217, 7 2017. ISSN 1473-5504. doi: 10.1017/S1473550416000057.

N. A. Teanby, M. Sylvestre, J. Sharkey, C. A. Nixon, S. Vinatier, and P. G. Irwin. Seasonal evolution of titan's stratosphere during the cassini mission. *Geophysical Research Letters*, 46:3079–3089, 3 2019. ISSN 19448007. doi: 10.1029/2018GL081401;PAGE:STRING:ARTICLE/CHAPTER.

J. Thøgersen, P. Nørnberg, K. Finster, and S. J. K. Jensen. Greenhouse gas capture by triboelectric charging. *Chemical Physics Letters*, 783:139069, 11 2021. ISSN 0009-2614. doi: 10.1016/J.CPLETT.2021.139069.

C. L. Tien. On the eddy diffusivities for momentum and heat. *Applied Scientific Research*, 8:345–348, 1 1959. ISSN 00036994. doi: 10.1007/BF00411759.

A. D. Toigo and M. Richardson. A mesoscale model for the martian atmosphere. *Journal of Geophysical Research: Planets*, 107:3–1, 7 2002. ISSN 01480227. doi: 10.1029/2000JE001489.

M. G. Tomasko. Preliminary results of polarimetry and photometry of titan at large phase angles from pioneer 11. *Journal of Geophysical Research: Space Physics*, 85:5937–5942, 11 1980. ISSN 2156-2202. doi: 10.1029/JA085IA11P05937.

M. G. Tomasko, L. R. Doose, M. Lemmon, P. H. Smith, and E. Wegryn. Properties of dust in the martian atmosphere from the imager on mars pathfinder. *Journal of Geophysical Research: Planets*, 104:8987–9007, 1999. ISSN 01480227. doi: 10.1029/1998JE900016.

D. H. Towne. *Wave Phenomena*. Addison-Wesley Publishing Company, 1967.

M. G. Trainer, A. A. Pavlov, D. B. Curtis, C. P. McKay, D. R. Worsnop, A. E. Delia, D. W. Toohey, O. B. Toon, and M. A. Tolbert. Haze aerosols in the atmosphere of early earth: Manna from heaven. *Astrobiology*, 4:409–419, 12 2004. ISSN 15311074. doi: 10.1089/AST.2004.4.409.

M. G. Trainer, M. H. Wong, T. H. Mcconnochie, H. B. Franz, S. K. Atreya, P. G. Conrad, F. Lefèvre, P. R. Mahaffy, C. A. Malespin, H. L. K. Manning, J. Martín-Torres, G. M. Martínez, C. P. Mckay, R. Navarro-González, Á. Vicente-Retortillo, C. R. Webster, and M.-P. Zorzano. Seasonal Variations in Atmospheric Composition as Measured in Gale Crater, Mars. *Journal of Geophysical Research: Planets*, 124:3000–3024, 2019. doi: 10.1029/2019JE006175.

S. Tremaine and L. Dones. On the statistical distribution of massive impactors. *Icarus*, 106:335–341, 1993.

E. P. Turtle and R. D. Lorenz. Dragonfly: In situ aerial exploration to understand titan's prebiotic chemistry and habitability. In *2024 IEEE Aerospace Conference*, pages 1–5. Institute of Electrical and Electronics Engineers (IEEE), 5 2024. ISBN 9798350304626. doi: 10.1109/AERO58975.2024.10521151.

E. P. Turtle, J. E. Perry, J. M. Barbara, A. D. D. Genio, S. Rodriguez, S. L. Mouélic, C. Sotin, J. M. Lora, S. Faulk, P. Corlies, J. Kelland, S. M. MacKenzie, R. A. West, A. S. McEwen, J. I. Lunine, J. Pitesky, T. L. Ray, and M. Roy. Titan's meteorology over the cassini mission: Evidence for extensive subsurface methane reservoirs. *Geophysical Research Letters*, 45:5320–5328, 6 2018. ISSN 19448007. doi: 10.1029/2018GL078170.

A. C. Vandaele, S. Aoki, S. Bauduin, F. Daerden, A. Fedorova, M. Giuranna, O. Korablev, F. Lefèvre, A. Määtänen, F. Montmessin, M. R. Patel, M. Smith, L. Trompet, S. Viscardy, Y. Willame, and N. Yoshida. Composition and chemistry of the martian atmosphere as observed by mars express and exomars trace gas orbiter. *Space Science Reviews*, 220:75–, 9 2024. ISSN 1572-9672. doi: 10.1007/S11214-024-01109-7.

A. R. Vasavada, J. P. Grotzinger, R. E. Arvidson, F. J. Calef, J. A. Crisp, S. Gupta, J. Hurowitz, N. Mangold, S. Maurice, M. E. Schmidt, R. C. Wiens, R. M. Williams, and R. A. Yingst. Overview of the mars science laboratory mission: Bradbury landing to yellowknife bay and beyond. *Journal of Geophysical Research: Planets*, 119:1134–1161, 6 2014. ISSN 21699100. doi: 10.1002/2014JE004622.

S. Viscardy, F. Daerden, and L. Neary. Formation of layers of methane in the atmosphere of mars after surface release. *Geophysical Research Letters*, 43:1868–1875, 3 2016. ISSN 1944-8007. doi: 10.1002/2015GL067443.

S. Viscardy, D. C. Catling, and K. Zahnle. Questioning the reliability of methane detections on mars by the curiosity rover. *Journal of Geophysical Research: Planets*, 130:e2024JE008441, 4 2025. ISSN 21699100. doi: 10.1029/2024JE008441.

C. Voigt, A. M. Virkkala, G. Hould Gosselin, K. A. Bennett, T. A. Black, M. Detto, C. Chevrier-Dion, G. Guggenberger, W. Hashmi, L. Kohl, D. Kou, C. Marquis, P. Marsh, M. E. Marushchak, Z. Nesic, H. Nykänen, T. Saarela, L. Sauheitl, B. Walker, N. Weiss, E. J. Wilcox, and O. Sonnentag. Arctic soil methane sink increases with drier conditions and higher ecosystem respiration. *Nature Climate Change*, 13(10):1095–1104, aug 2023. ISSN 1758-6798. doi: 10.1038/s41558-023-01785-3.

J. H. Waite, D. T. Young, T. E. Cravens, A. J. Coates, F. J. Crary, B. Magee, and J. Westlake. Planetary science: The process of tholin formation in titan's upper atmosphere. *Science*, 316: 870–875, 5 2007. ISSN 00368075. doi: 10.1126/SCIENCE.1139727.

S. Wakita, B. C. Johnson, J. M. Soderblom, and C. D. Neish. A youthful titan implied by improved impact simulations. *Geophysical Research Letters*, 53:e2025GL116041, 2 2026. ISSN 19448007. doi: 10.1029/2025GL116041L.

M. Walters, J. E. Moores, F. Grandmont, M. Gordon, and H. Sapers. Water vapor condensation in optical instruments on Mars. *Acta Astronautica*, 218:232–239, may 2024. ISSN 0094-5765. doi: 10.1016/J.ACTAASTRO.2024.02.031.

M. E. Walters. *Quantifying methane fluxes on Mars: Modeling the vertical evolution of martian methane for improved detection and analysis*. PhD thesis, York University, 2023.

C. R. Webster and P. R. Mahaffy. Determining the local abundance of martian methane and its' 13c/12c and d/h isotopic ratios for comparison with related gas and soil analysis on the 2011 mars science laboratory (msl) mission. *Planetary and Space Science*, 59:271–283, 2 2011. ISSN 0032-0633. doi: 10.1016/J.PSS.2010.08.021.

C. R. Webster, P. R. Mahaffy, S. K. Atreya, G. J. Flesch, K. A. Farley, O. Kemppinen, N. Bridges, J. R. Johnson, M. Minitti, D. Cremers, J. F. Bell, L. Edgar, J. Farmer, A. Godber, M. Wadhwa, D. Wellington, I. McEwan, C. Newman, M. Richardson, A. Charpentier, L. Peret, P. King, J. Blank, G. Weigle, M. Schmidt, S. Li, R. Milliken, K. Robertson, V. Sun, M. Baker, C. Edwards, B. Ehlmann, K. Farley, J. Griffes, J. Grotzinger, H. Miller, M. Newcombe, C. Pilorget, M. Rice, K. Siebach, K. Stack, E. Stolper, C. Brunet, V. Hipkin, R. Léveillé, G. Marchand, P. S. Sánchez, L. Favot, G. Cody, A. Steele, L. Flückiger, D. Lees, A. Nefian, M. Martin, M. Gailhanou, F. Westall, G. Israël, C. Agard, J. Baroukh, C. Donny, A. Gaboriaud, P. Guillemot, V. Lafaille, E. Lorigny, A. Paillet, R. Pérez, M. Saccoccio, C. Yana, C. A. Aparicio, J. C. Rodríguez, I. C. Blázquez, F. G. Gómez, J. G. Elvira, S. Hettrich, A. L. Malvitte, M. M. Jiménez, J. Martínez-Frías, J. M. Soler, F. J. Martín-Torres, A. M. Jurado, L. Mora-Sotomayor, G. M. Caro, S. N. López, V. Peinado-González, J. Pla-García, J. A. Rodriguez Manfredi, J. J. Romeral-Planelló, S. A. Sans Fuentes, E. S. Martinez, J. T. Redondo, R. Urqui-O'Callaghan, M. P. Z. Mier, S. Chipera, J. L. Lacour, P. Mauchien, J. B. Sirven, H. Manning, A. Fairén, A. Hayes, J. Joseph, S. Squyres, R. Sullivan, P. Thomas, A. Dupont, A. Lundberg, N. Melikechi, A. Mezzacappa, J. DeMarines, D. Grinspoon, G. Reitz, B. Prats, E. Atlaskin, M. Genzer, A. M. Harri, H. Haukka, H. Kahanpää, J. Kauhanen, O. Kemppinen, M. Paton, J. Polkko, W. Schmidt, T. Siili, C. Fabre, J. Wray, M. B. Wilhelm, F. Poitrasson, K. Patel, S. Gorevan, S. Indyk, G. Paulsen, S. Gupta, D. Bish, J. Schieber, B. Gondet, Y. Langevin, C. Geffroy, D. Baratoux, G. Berger, A. Cros, C. D'Uston, O. Forni, O. Gasnault, J. Lasue, Q. M. Lee, S. Maurice, P. Y. Meslin, E. Pallier, Y. Parot, P. Pinet, S. Schröder, M. Toplis, É. Lewin, W. Brunner, E. Heydari, C. Achilles, D. Oehler, B. Sutter, M. Cabane, D. Coscia, G. Israël, C. Szopa, G. Dromart, F. Robert, V. Sautter, S. Le Mouélic, N. Mangold, M. Nachon, A. Buch, F. Stalport, P. Coll, P. François, F. Raulin, S. Teinturier, J. Cameron, S. Clegg, A. Cousin, D. DeLapp, R. Dingler, R. S. Jackson, S. Johnstone, N. Lanza, C. Little, T. Nelson, R. C. Wiens, R. B. Williams, A. Jones, L. Kirkland, A. Treiman, B. Baker, B. Cantor, M. Caplinger, S. Davis, B. Duston, K. Edgett, D. Fay, C. Hardgrove, D. Harker, P. Herrera, E. Jensen, M. R. Kennedy, G. Krezoski, D. Krysak, L. Lipkaman, M. Malin, E. McCartney, S. McNair, B. Nixon, L. Posiolova, M. Ravine, A. Salamon, L. Saper, K. Stoiber, K. Supulver, J. Van Beek, T. Van Beek, R. Zimdar, K. L. French, K. Iagnemma, K. Miller, R. Summons, F. Goesmann, W. Goetz, S. Hviid, M. Johnson, M. Lefavor, E. Lyness, E. Breves, M. Darby Dyar, C. Fassett, D. F. Blake, T. Bristow, D. DesMarais, L. Edwards, R. Haberle, T. Hoehler, J. Hollingsworth, M. Kahre, L. Keely, C. McKay, M. B. Wilhelm, L. Bleacher, W. Brinckerhoff, D. Choi, P. Conrad, J. P. Dworkin,

J. Eigenbrode, M. Floyd, C. Freissinet, J. Garvin, D. Glavin, D. Harpold, A. Jones, P. Mahaffy, D. K. Martin, A. McAdam, A. Pavlov, E. Raaen, M. D. Smith, J. Stern, F. Tan, M. Trainer, M. Meyer, A. Posner, M. Voytek, R. C. Anderson, A. Aubrey, L. W. Beegle, A. Behar, D. Blaney, D. Brinza, F. Calef, L. Christensen, J. A. Crisp, L. DeFlores, B. Ehlmann, J. Feldman, S. Feldman, G. Flesch, J. Hurowitz, I. Jun, D. Keymeulen, J. Maki, M. Mischna, J. M. Morookian, T. Parker, B. Pavri, M. Schoppers, A. Sengstacken, J. J. Simmonds, N. Spanovich, M. de la Torre Juarez, A. R. Vasavada, C. R. Webster, A. Yen, P. D. Archer, F. Cucinotta, J. H. Jones, D. Ming, R. V. Morris, P. Niles, E. Rampe, T. Nolan, M. Fisk, L. Radziemski, B. Barraclough, S. Bender, D. Berman, E. N. Dobrea, R. Tokar, D. Vaniman, R. M. Williams, A. Yingst, K. Lewis, L. Leshin, T. Cleghorn, W. Huntress, G. Manhès, J. Hudgins, T. Olson, N. Stewart, P. Sarrazin, J. Grant, E. Vicenzi, S. A. Wilson, M. Bullock, B. Ehresmann, V. Hamilton, D. Hassler, J. Peterson, S. Rafkin, C. Zeitlin, F. Fedosov, D. Golovin, N. Karpushkina, A. Kozyrev, M. Litvak, A. Malakhov, I. Mitrofanov, M. Mokrousov, S. Nikiforov, V. Prokhorov, A. Sanin, V. Tretyakov, A. Varenikov, A. Vostrukhin, R. Kuzmin, B. Clark, M. Wolff, S. McLennan, O. Botta, D. Drake, K. Bean, M. Lemmon, S. P. Schwenzer, R. B. Anderson, K. Herkenhoff, E. M. Lee, R. Sucharski, M. Á. de Pablo Hernández, J. J. Blanco Ávalos, M. Ramos, M. H. Kim, C. Malespin, I. Plante, J. P. Muller, R. Navarro-González, R. Ewing, W. Boynton, R. Downs, M. Fitzgibbon, K. Harshman, S. Morrison, W. Dietrich, O. Kortmann, M. Palucis, D. Y. Sumner, A. Williams, G. Lugmair, M. A. Wilson, D. Rubin, B. Jakosky, T. Balic-Zunic, J. Frydenvang, J. K. Jensen, K. Kinch, A. Koefoed, M. B. Madsen, S. L. Svane Stipp, N. Boyd, J. L. Campbell, R. Gellert, G. Perrett, I. Pradler, S. VanBommel, S. Jacob, T. Owen, S. Rowland, E. Atlaskin, H. Savijärvi, E. Boehm, S. Böttcher, S. Burmeister, J. Guo, J. Köhler, C. M. García, R. Mueller-Mellin, R. Wimmer-Schweingruber, J. C. Bridges, T. McConnochie, M. Benna, H. Franz, H. Bower, A. Brunner, H. Blau, T. Boucher, M. Carmosino, S. Atreya, H. Elliott, D. Halleaux, N. Rennó, M. Wong, R. Pepin, B. Elliott, J. Spray, L. Thompson, S. Gordon, H. Newsom, A. Ollila, J. Williams, P. Vasconcelos, J. Bentz, K. Nealson, R. Popa, L. C. Kah, J. Moersch, C. Tate, M. Day, G. Kocurek, B. Hallet, R. Sletten, R. Francis, E. McCullough, E. Cloutis, I. L. ten Kate, R. Kuzmin, R. Arvidson, A. Fraeman, D. Scholes, S. Slavney, T. Stein, J. Ward, J. Berger, and J. E. Moores. Low upper limit to methane abundance on Mars. *Science*, 342(6156):355–357, oct 2013. ISSN 10959203. doi: 10.1126/SCIENCE.1242902.

C. R. Webster, P. R. Mahaffy, S. K. Atreya, G. J. Flesch, M. A. Mischna, P. Y. Meslin, K. A. Farley, P. G. Conrad, L. E. Christensen, A. A. Pavlov, J. Martín-Torres, M. P. Zorzano, T. H. McConnochie, T. Owen, J. L. Eigenbrode, D. P. Glavin, A. Steele, C. A. Malespin, P. D. Archer, B. Sutter, P. Coll, C. Freissinet, C. P. McKay, J. E. Moores, S. P. Schwenzer, J. C. Bridges, R. Navarro-Gonzalez, R. Gellert, and M. T. Lemmon. Mars methane detection and variability at Gale crater. *Science*, 347(6220):415–417, jan 2015. ISSN 10959203. doi: 10.1126/SCIENCE.1261713.

C. R. Webster, P. R. Mahaffy, S. K. Atreya, J. E. Moores, G. J. Flesch, C. Malespin, C. P. McKay, G. Martinez, C. L. Smith, J. Martin-Torres, J. Gomez-Elvira, M. P. Zorzano, M. H. Wong, M. G. Trainer, A. Steele, D. Archer, B. Sutter, P. J. Coll, C. Freissinet, P. Y. Meslin, R. V. Gough, C. H. House, A. Pavlov, J. L. Eigenbrode, D. P. Glavin, J. C. Pearson, D. Keymeulen, L. E. Christensen, S. P. Schwenzer, R. Navarro-Gonzalez, J. Pla-García, S. C. Rafkin, Á. Vicente-Retortillo, H. Kahanpää, D. Viudez-Moreiras, M. D. Smith, A. M. Harri, M. Genzer, D. M. Hassler, M. Lemmon, J. Crisp, S. P. Sander, R. W. Zurek, and A. R. Vasavada. Background levels of methane in Mars' atmosphere show strong seasonal variations. *Science*, 360(6393): 1093–1096, jun 2018. ISSN 10959203. doi: 10.1126/SCIENCE.AAQ0131.

C. R. Webster, P. R. Mahaffy, J. Pla-Garcia, S. C. Rafkin, J. E. Moores, S. K. Atreya, G. J. Flesch, C. A. Malespin, S. M. Teinturier, H. Kalucha, C. L. Smith, D. Viúdez-Moreiras, and A. R. Vasavada. Day-night differences in mars methane suggest nighttime containment at gale crater. *Astronomy & Astrophysics*, 650:A166, 6 2021. ISSN 0004-6361. doi: 10.1051/0004-6361/202040030.

W. Weibull. A statistical distribution function of wide applicability. *Journal of Applied Mechanics*, pages hal–03112318, 1951.

L. F. Wheeler, P. J. Register, and D. L. Mathias. A fragment-cloud model for asteroid breakup and atmospheric energy deposition. *Icarus*, 295:149–169, 10 2017. ISSN 0019-1035. doi: 10.1016/J.ICARUS.2017.02.011.

L. F. Wheeler, D. L. Mathias, E. Stokan, and P. G. Brown. Atmospheric energy deposition modeling and inference for varied meteoroid structures. *Icarus*, 315:79–91, 2018. doi: 10.1016/j.icarus.2018.06.014.

R. C. Wiens, A. Udry, O. Beyssac, C. Quantin-Nataf, N. Mangold, A. Cousin, L. Mandon, T. Bosak, O. Forni, S. M. McLennan, V. Sautter, A. Brown, K. Benzerara, J. R. Johnson, L. Mayhew, S. Maurice, R. B. Anderson, S. M. Clegg, L. Crumpler, T. S. Gabriel, P. Gasda, J. Hall, B. H. Horgan, L. Kah, C. L. IV, J. M. Madariaga, P. Y. Meslin, A. M. Ollila, F. Poulet, C. Royer, S. K. Sharma, S. Siljeström, J. I. Simon, T. E. Acosta-Maeda, C. Alvarez-Llamas, S. M. Angel, G. Arana, P. Beck, S. Bernard, T. Bertrand, B. Bousquet, K. Castro, B. Chide, E. Clavé, E. Cloutis, S. Connell, E. Dehouck, G. Dromart, W. Fischer, T. Fouchet, R. Francis, J. Frydenvang, O. Gasnault, E. Gibbons, S. Gupta, E. M. Hausrath, X. Jacob, H. Kalucha, E. Kelly, E. Knutsen, N. Lanza, J. Laserna, J. Lasue, S. L. Mouélic, R. Leveille, G. L. Reyes, R. Lorenz, J. A. Manrique, J. Martinez-Frias, T. McConnochie, N. Melikechi, D. Mimoun, F. Montmessin, J. Moros, N. Murdoch, P. Pilleri, C. Pilorget, P. Pinet, W. Rapin, F. Rull, S. Schröder, D. L. Shuster, R. J. Smith, A. E. Stott, J. Tarnas, N. Turenne, M. Veneranda, D. S. Vogt, B. P. Weiss, P. Willis, K. M. Stack, K. H. Williford, and K. A. Farley. Compositionally and density stratified igneous terrain in jezero crater, mars. *Science Advances*, 8:3399, 8 2022. ISSN 23752548. doi: 10.1126/SCIADV.ABO3399.

M. J. Wolff, M. D. Smith, R. T. Clancy, R. Arvidson, M. Kahre, F. S. IV, S. Murchie, and H. Savijärvi. Wavelength dependence of dust aerosol single scattering albedo as observed by the compact reconnaissance imaging spectrometer. *Journal of Geophysical Research: Planets*, 114, 2 2009. ISSN 2156-2202. doi: 10.1029/2009JE003350.

A. S. Wong, S. K. Atreya, and T. Encrenaz. Chemical markers of possible hot spots on mars. *Journal of Geophysical Research: Planets*, 108:5026, 4 2003. ISSN 2156-2202. doi: 10.1029/2002JE002003.

C. A. Wood, R. Lorenz, R. Kirk, R. Lopes, K. Mitchell, and E. Stofan. Impact craters on titan. *Icarus*, 206:334–344, 3 2010. ISSN 0019-1035. doi: 10.1016/J.ICARUS.2009.08.021.

K. Wünnemann, G. S. Collins, and H. J. Melosh. A strain-based porosity model for use in hydrocode simulations of impacts and implications for transient crater growth in porous targets. *Icarus*, 180:514–527, 2 2006. ISSN 0019-1035. doi: 10.1016/J.ICARUS.2005.10.013.

Z. Xu, M. Froment, R. F. Garcia, Éric Beucler, K. Onodera, T. Kawamura, P. Lognonné, and W. B. Banerdt. Modeling seismic recordings of high-frequency guided infrasound on mars. *Journal of Geophysical Research: Planets*, 127:e2022JE007483, 11 2022. ISSN 2169-9100. doi: 10.1029/2022JE007483.

Y. L. Yung, P. Chen, K. Nealson, S. Atreya, P. Beckett, J. G. Blank, B. Ehlmann, J. Eiler, G. Etiope, J. G. Ferry, F. Forget, P. Gao, R. Hu, A. Kleinböhl, R. Klusman, F. Lefèvre, C. Miller, M. Mischna, M. Mumma, S. Newman, D. Oehler, M. Okumura, R. Oremland, V. Orphan, R. Popa, M. Russell, L. Shen, B. Sherwood Lollar, R. Staehle, V. Stamenković, D. Stolper, A. Templeton, A. C. Vandaele, S. Viscardy, C. R. Webster, P. O. Wennberg, M. L. Wong, and J. Worden. Methane on Mars and Habitability: Challenges and Responses. *Astrobiology*, 18(10): 1221–1242, oct 2018. ISSN 15311074. doi: 10.1089/AST.2018.1917.

K. Zahnle, P. Schenk, H. Levison, and L. Dones. Cratering rates in the outer solar system. *Icarus*, 163:263–289, 2003. ISSN 00191035. doi: 10.1016/S0019-1035(03)00048-4.

K. Zahnle, R. S. Freedman, and D. C. Catling. Is there methane on mars? *Icarus*, 212:493–503, 4 2011. ISSN 0019-1035. doi: 10.1016/J.ICARUS.2010.11.027.

G. Zenhäusern, N. Wójcicka, S. C. Stähler, G. S. Collins, I. J. Daubar, M. Knapmeyer, S. Ceylan, J. F. Clinton, and D. Giardini. An estimate of the impact rate on mars from statistics of very-high-frequency marsquakes. *Nature Astronomy*, 8:1138–1147, 6 2024. ISSN 2397-3366. doi: 10.1038/s41550-024-02301-z.

X. Zhang, D. Berkinsky, C. R. Markus, S. R. Chitturi, F. J. Grieman, M. Okumura, Y. Luo, Y. L. Yung, and S. P. Sander. Reaction of methane and uv-activated perchlorate: Relevance to heterogeneous loss of methane in the atmosphere of mars. *Icarus*, 376:114832, 2022. ISSN 10902643. doi: 10.1016/j.icarus.2021.114832.

R. W. Zurek and C. B. Leovy. Thermal tides in the dusty martian atmosphere: A verification of theory. *Science*, 213:437–439, 7 1981. ISSN 0036-8075. doi: 10.1126/SCIENCE.213.4506.437.

R. W. Zurek, A. Chicarro, M. A. Allen, J. L. Bertaux, R. T. Clancy, F. Daerden, V. Formisano, J. B. Garvin, G. Neukum, and M. D. Smith. Assessment of a 2016 mission concept: The search for trace gases in the atmosphere of mars. *Planetary and Space Science*, 59:284–291, 2 2011. ISSN 0032-0633. doi: 10.1016/J.PSS.2010.07.007.

Appendix A

Atmospheric Dynamics and Eddy Diffusivity

This appendix is a detailed accounting of dynamical atmospheric modelling theory that are used to estimate eddy diffusivity values. I also include brief comments for each of the three atmospheric models mentioned in Chapter 3 where they differ from the typical equations.

A.1 Dynamical Atmospheric Modelling Theory

Eddy diffusivity coefficients are not a physical value that can be measured. However, they are generally used to simulate the effects of transport in atmospheres. In general, the atmospheric models estimate the eddy diffusivity coefficients in the following manner. The atmospheric model is divided into the area below the planetary boundary layer, and above the planetary boundary layer. Below the planetary boundary layer, the surface eddy diffusivity for all the models follows the Monin-Obukhov similarity theory, such that momentum and heat are dependent on the stability of the function of the local gradient Richardson number $F_m(R_i)$. In this section I present how to calculate estimate the gradiant Richardson number, the stability function, and the eddy diffusivity coefficients at the surface (Monin-Obhukov similarity theory). There are two methods for estimating mixing above the surface (Blackadar mixing theory, and the methods presented by Haberle et al. (1993)). Where the atmospheric models further differ from the following equations, they are described in their respective sections.

At the surface, turbulent transport from the surface typically follows Monin-Obhukov simlarity theory and eddy diffusivity is calculated as

$$\kappa_m(\frac{\delta_u}{\delta z}, \frac{\delta_v}{\delta z}) = c_d(u_s^2 + v_s^2) \tag{A.1}$$

where c_d is the drag coeffient and is a function of stability $F_m(Ri)$ and surface roughness z_0. In Haberle et al. (1993), the gradiant Richardson number is calculated as

$$R_i = \frac{\beta g \frac{\delta\theta}{\delta z}}{(\frac{\delta u}{\delta z})^2 + \frac{\delta v}{\delta z})^2} \tag{A.2}$$

where g is the gravitational acceleration and β is the volume expansion coefficient. u and v correspond to wind in horizontal and vertical directions, θ is the potential temperature, and z is the altitude. Haberle et al. (1993) chose their critical Richardson number to be $Ri_c = 0.19$, where values above Ri_c correpond to non turbulent mixing.

Above the surface, the eddy diffusivity for momentum is can be described following Haberle et al. (1993), where

$$\kappa_m = l^2((\frac{\delta u}{\delta z})^2 + (\frac{\delta v}{\delta z})^2)^{0.5} G_M^{-0.5} S_m. \tag{A.3}$$

Here, G_m and S_m are stability functions from **?**. The mixing length l comes from Blackadar (1962) such that

$$l = l_0 \frac{kz}{kz + l_0} \tag{A.4}$$

where $k = 0.4$ is the von Kármán constant and l_0 is the maximum mixing length with the PBL estimated using

$$l_0 = 0.2 \frac{\int_0^\infty qz dz}{\int_0^\infty q dz} \tag{A.5}$$

where q is the radiative heating rate.

An alternative formulation for eddy diffusivity above the surface (, Holtslag1993) denoted κ_c, is as follows:

$$\kappa_c = l_c^2 S F_c(Ri). \tag{A.6}$$

Here, S is the local shear, $l_c = \frac{1}{kz} + \frac{1}{\lambda_c}$ and $F_c(Ri)$ is an alternative stability function of the gradient Richardson number. Holtslag and Boville (1993) set the asymptotic mixing length $\lambda_c = 300m$ when below 1 km, and otherwise define

$$\lambda_c = 30 + 270 \exp(1 - \frac{z}{1000}) \tag{A.7}$$

such that λ_c reaches the free atmospheric value of 30 m. The gradient Richardson number used here is

$$Ri = \frac{g}{\theta_v} \frac{\frac{\delta\theta_v}{\delta z}}{S^2}. \tag{A.8}$$

where θ_v is the virtual potential temperature. The stability functions follow **?**, where

$$F_c(Ri) = (1 - 18Ri)^{0.5}, Ri < 0$$
$$F_c(Ri) = 1 - 5Ri, Ri \geq 0. \tag{A.9}$$

A.1.1 GEM-Mars

Convective transport above the surface is described by Holtslag and Boville (1993) such that

$$(\overline{w'u'})_0 = -C_m(V_1, u_1)(\overline{w'v'})_0 = -C_m(V_1, v_1) \tag{A.10}$$

where C_m is the surface exchange coefficient

$$C_m = C_n f_m(Ri_{b0}). \tag{A.11}$$

Here, C_n is the neutral exchange coefficient and depends V_1, the horizontal veloity vector and u_1 and v_1, the zonal and meridonal wind components at the first level. C_n also depends on the von Kármán coefficient, the height of the next model level, and the surface roughness length. Exchanges to the next level from the surface use a roughless length for momentum (assumed to be the same roughness length as heat). or GEM-Mars, the surface roughness length is 0.324 m (Neary and Daerden, 2018). f_m is a function that modifies the neutral exchange coefficient and Ri_{b0} is the surface bulk Richardson number, defined by

$$Ri_{b0} = \frac{gz_1(\theta_{v0} - \theta_{v1})}{\theta_1 |V_1|^2}. \tag{A.12}$$

When the bulk Richardson number is unstable ($Ri_{b0} < 0$), then

$$f_m(Ri_{b0}) = 1 - \frac{Ri_0}{1 + 75C_n(\frac{z_1 + z_{0m}}{z_{0m}})^{0.5}}. \tag{A.13}$$

When $Ri_{b0} \geq 0$,

$$f_m(Ri_{b0}) = \frac{1}{1 + 10Ri_0(1 + 8Ri_0)}. \tag{A.14}$$

Above the surface, Holtslag and Boville (1993) uses a non-local scheme that deviates from the one described in A.1. Flux is described as

$$\overline{w'C'} = -\kappa_m \frac{\delta C}{\delta z}. \tag{A.15}$$

Note that the countergradient term γ_c is not included following Daerden et al. (2015). The eddy diffusivity coefficient is

$$\kappa_m = k w_t z (1 - \frac{z}{h})^2. \tag{A.16}$$

w_t is the characteristic turbulent velocity scale and h is the boundary layer height. $w_t = \frac{u_*}{\phi_h}$ where u_* is the friction velocity and ϕ_h is a dimensionless vertical temperature gradient for $0 \leq \frac{z}{L} \leq 1$, where L is the Obhukov length. For $\frac{z}{L} > 1$, $\phi_h = 5 + \frac{z}{L}$. When unstable, $\phi_h = (1 - 15\frac{z}{L})^{-0.5}$.

h can explicitly be calculated using

$$h = \frac{Ri_{cr}(u(h)^2 + v(h)^2)}{(\frac{g}{\theta_s})(\theta_v(h) - \theta_s)}\theta_s = \theta_v(z_s) + b\frac{\overline{w'\theta'_{v0}}}{w_m} \tag{A.17}$$

where the critical bulk Richardson number is $Ri_{cr} = 0.5$, b is a constant, $\bar{w'\theta'_{v0}}$ is the virtual heat flux at the surface, and $\theta_v(z_s)$ is the virtual temperature at a given layer from the surface. When $\bar{w'\theta'_{v0}} > 0$, the conditions are unstable. When conditions are stable, $\theta_s = \theta_v(z_s)$, where θ_s is the approximate temperature at the surface and $z_s = 10$ m.

A.1.2 1D University Helsinki/Finnish Meteorological Institute (1D UH/FMI) Model

The surface-layer scheme for the 1D UH/FMI model follows Monin-Obhukov similarity theory where the stability function depends on the local Richardson number Ri such that

$$\begin{aligned} F_m(Ri) &= (1 - 16Ri)^{0.5}, Ri < 0 \\ F_m(Ri) &= (1 + 5Ri + 44Ri^2)^{-2}, Ri \geq 0. \end{aligned} \tag{A.18}$$

The stability terms were first shown in (Savijarvi, 1992) and updated in (Savijarvi, 1999). Above the surface, the gradiant Richardson number is calculated using Blackadar (1962) with an asymptotic mixing length of 300 m.

A.1.3 Laboratoire de Météorologie Dynamic Mars GCM - The LMD Model

Mixing within the PBL utilises a thermal plume model described in Colaïtis et al. (2013). Turbulence is described as

$$\bar{w'\phi'} = \frac{F_u}{\rho}(\phi_u - \bar{ph}i) + \frac{F_d}{\rho}(\phi_d - \bar{ph}i). \tag{A.19}$$

Here, u and d subscripts represent upwards and downards for the following variables. $F_u = \alpha_u \rho w_u$ is the updraft mass flux, $F_d = \alpha_d \rho w_d$ is the downdraft mass flux. α is the fractional coverage, w is the vertical velocity , ϕ_u and ϕ_d represent the conserved variable for the updraft and downdraft averaged values, while $\bar{\phi} = \alpha\phi_u + (1 - \alpha)\phi_e$ where ϕ_e represents the conserved environment-averaged values.

Appendix B

Effect of Varying Dust Distributions for Methane Diffusion and Destruction

In Chapter 3, I noted that I prescribed two different dust profiles for the VDM. I found that the overall effect was minimal and did not affect my interpretations of the results. As such, Chapter 3 figures primarily show the results using the well-mixed dust profile. In this appendix, I demonstrate the effect of different dust models. I also comment on why I believe changing the dust distribution does not meaningfully change my results.

B.1 Varying Dust Distributions

I show the same main results for methane concentrations measured at 1 m in the VDM and in the box model (Fig. B.1). I observe few difference in the overall behaviour of methane in my simulations when I adjusted the dust profile to be a well-mixed profile. Methane is generally more dilute higher in the VDM on the surface, particularly in the daytime. However, in the $\nu = 3$ Conrath profile, dust is distributed more densely towards the surface. Thus, at higher altitudes, the destruction mechanism is less active as there is less perchlorate available to remove methane.

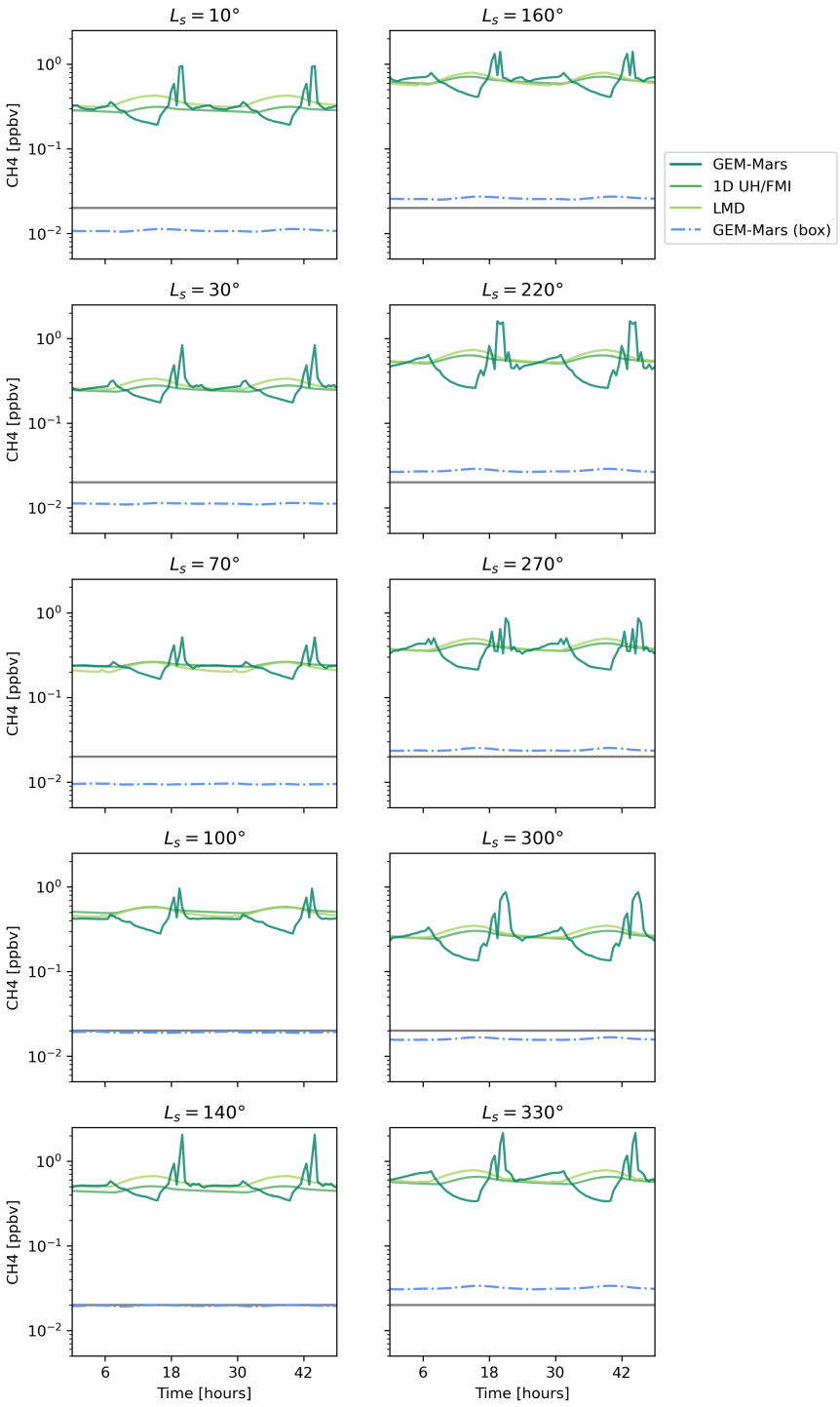


Figure B.1: Examples of surface methane concentration at 1 m (green) and box model (blue) concentration for the last 48 hours in the simulation for a Conrath profile of $\nu = 3$. The grey line corresponds to 0.02 ppbv. The methane concentrations shown for each model repeats over 24 Martian hours, reflective of the diurnal nature of atmospheric mixing. Note that the 1D UH/FMI box model concentrations not shown as their values fall well below the methane concentration range plotted. However, the behaviour of the 1D UH/FMI methane concentration in the box model mimic that of the GEM-Mars methane concentration within the box model with a slight increase during the afternoon. Additionally, the LMD box model value is consistent 0 ppbv and is not plotted.

For the GEM-Mars model where the methane flux is the same in both the well-mixed dust profile and in the Conrath profile (Table 3.4), I find that the methane is more efficiently removed in the well-mixed profile (Fig. B.2). I also find no major difference in the 1D UH/FMI and LMD model (Fig. B.3). This is unsurprising as the 1D UH/FMI and LMD atmospheric models tends to retain methane closer to the surface and methane mixing is limited or inhibited during the night. Overall, this leads to rapid removal of methane during the daytime.

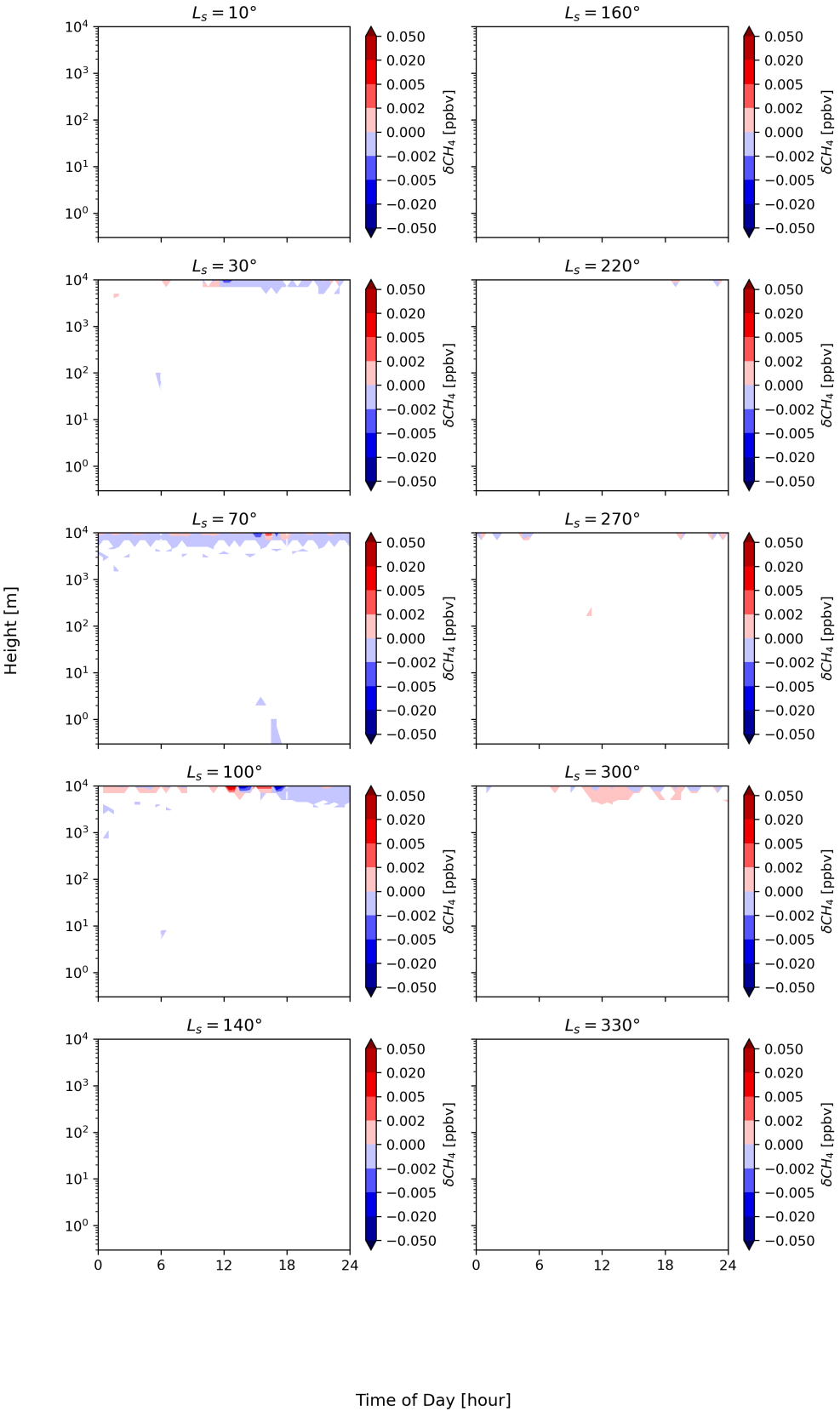


Figure B.2: Difference between the well-mixed dust profile and the Conrath profile for the GEM-Mars atmospheric model. A negative value (blue) corresponds with less methane in the well-mixed dust profile, which is consistently shown in all of the difference plots for GEM-Mars. The difference between the two dust profiles is less impactful in the top few km of the VDM.

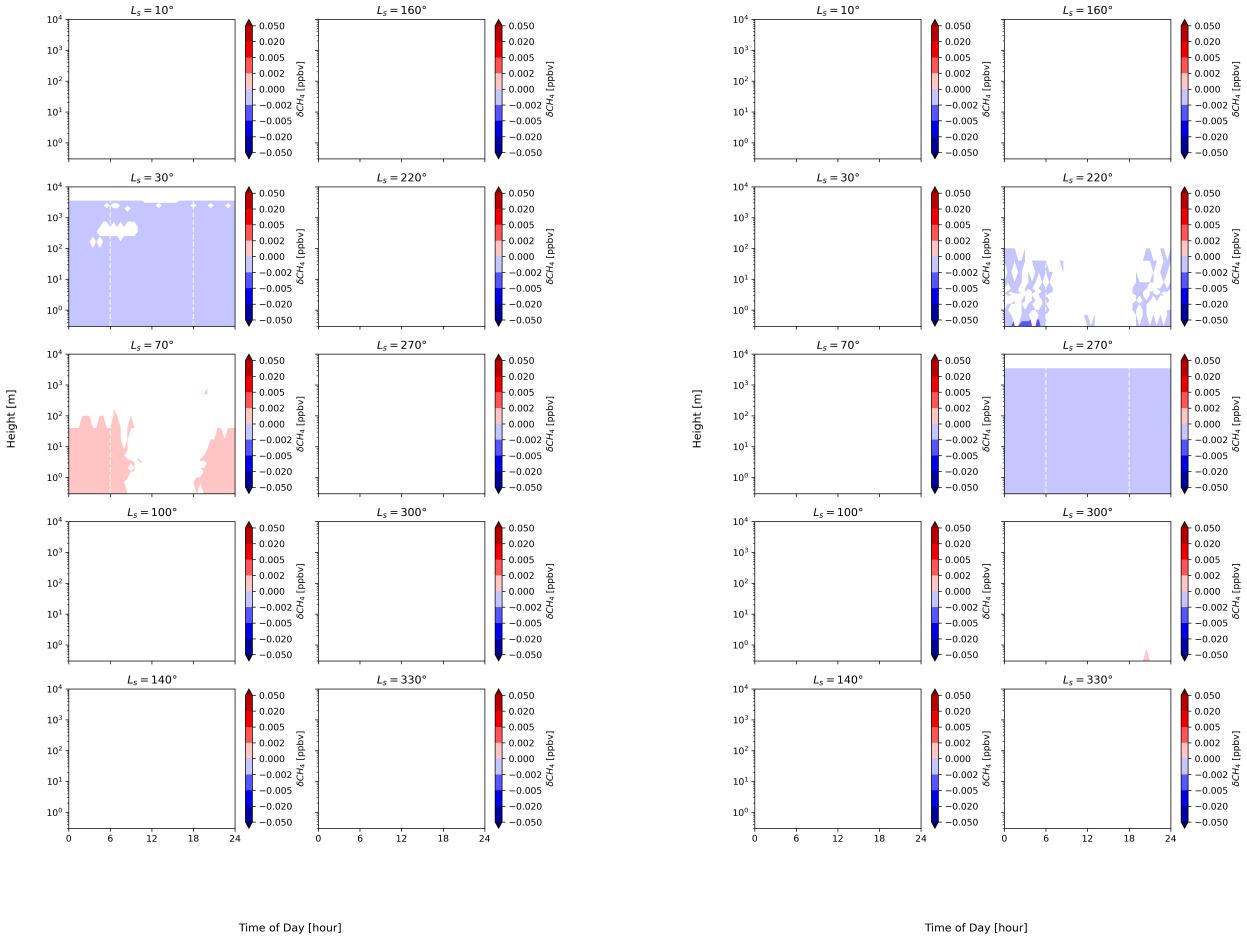


Figure B.3: Difference between the well-mixed dust profile and the Conrath profile for the 1D UH/FMI (left) and LMD (right) atmospheric models. A negative value corresponds with less methane in the well-mixed dust profile. The difference between the two dust profiles is minimal.

B.2 Discussion of Dust Profiles

I found that the dust profile (well-mixed or exponentially increasing towards the surface) did not generally affect my results nor the overall methane profile in the atmosphere. This is surprising when one considers that there is more dust and a higher methane partial pressure to allow for destruction closer to the surface. However, recall that the photon flux availability is also dependent on the dust concentration. Thus, there is likely an "even" trade-off between the increase in photon flux and the decrease in surface area available for the reaction when comparing the two different dust profiles.